2004

Carbon nanotubes and conducting polymer composites

May Tahhan
University of Wollongong

CARBON NANOTUBES AND CONDUCTING POLYMER COMPOSITES

A thesis submitted in fulfillment of the requirements for the award of the degree

DOCTOR OF PHILOSOPHY

from the

UNIVERSITY OF WOLLONGONG

by

May Tahhan,

B.Sc. Chemistry, M.Sc. Chemistry, Grad. Cert. Buss.

INTELLIGENT POLYMERS RESEARCH INSTITUTE

DEPARTMENT OF CHEMISTRY

December 2004

CERTIFICATION

I, May Tahhan, declare that this thesis, submitted in fulfillment of the requirements for the award of Doctor of Philosophy, in the Department of Chemistry, University of Wollongong, is wholly my own work unless otherwise referenced or acknowledged. The document has not been submitted for qualifications at any other academic institute.

May Tahhan

6 December 2004

Table of Contents

List of Tables

List of Figures

List of Schemes

List of Abbreviations

1D	One Dimension
2D	Two Dimensions
1,2-DCB	1,2-Dichlorobenzene
AA12BE	Allyl alcohol 1,2-butoxylate ethoxylate
Abs.	Absorbance
AC	Alternating Current
AFM	Atomic Force Microscopy
Ag/AgCl	Silver/Silver-chloride
AHFP	Ammonium hexaflurophosphate
AIBN	2,2`-azobisisobutyronitrile
Au	Gold
BC	Benzalkonium chloride
C	Carbon
CNT	Carbon Nanotubes
CO	Carbon monoxide
CO_2	Carbon dioxide
CV	Cyclic Voltammetry
CV	Cyclic Voltammogrames
DDAB	Didodecyldimethyl ammonium bromide
Dex	Dextran sulfate
DNA	Deoxyribose Nucleic Acid

DOS	Density Of State
E	Chemical Potential
Fe	Iron
FMWCNT	Functionalized Mutli-Walled Carbon Nanotubes
G.C.	Glassy Carbon
HCl	Hydrochloric acid
HCNT	HiPco Nanotubes
H_2SO_4	Sulfuric acid
ITO	Indium Tin Oxide
KCl	Potassium chloride
$K_4Fe(CN)_6$	Potassium ferrocyanide
LVDT	Linear Variable Distance Transducer
MMA	Methyl methaacrylate
M.W	Molecular Weight
MWCNT	Multi-Walled Carbon Nanotubes
N_2	Nitrogen
N0.15	Noxamium 0.15®
NaCl	Sodium chloride
$NaNO_3$	Sodium nitrate
NaOH	Sodium hydroxide
NH_4OH	Ammonium hydroxide
NIPPAm-AMPS	N-isopropylacrylamide 2-acrylamido-2-methyl-1-propanesulfonic acid

NMP	N-methyl pyrrolidone
P3HT	Poly(3-hexylthiophene)
PA	Polyacetylene
PAn	Polyaniline
PCS	Particle Coagulation Spinning
PET	Poly(ethylene terephtalate)
PMAS	Poly(methoxyaniline-5-sulfonic acid)
PMMA	Poly(methyl methacrylatye)
PmPV	Poly(m-phenylenevinylene-co-2,5-dioctyloxy-p-phenylenevinylene)
PPA	Poly(phenylacetylene)
PPEI-EI	Poly(propionylethylenimine-co-ethylenimine)
PPV	Poly(p-phenylene vinylene)
PPy	Polypyrrole
PSS	Poly(styrene sulfonate)
Pt	Platinum
PTh	Polythiophene
PVA	Poly(vinyl alcohol)
PVDF	Polyvinylidene fluoride
PVP	Polyvinyl pyrrolidone
Py	Pyrrole
RBM	Radial Breathing Mode
RCNT	Rice Carbon Nanotube

SCE	Saturated Calomel Electrode
SDS	Sodium dodecyl sulfate
SEM	Scanning Electron Microscopy
SO_3H	Sulfonic acid
SWCNT	Single-Walled Carbon Nanotubes
TCNQ	Tetracyanoquinodimethane
TDM	Tangential Displacement Mode
TEM	Transmission Electron Microscopy
TGA	Thermogravimetric Analysis
TTF	Tetrathiofulvalene
TX100	Triton X 100®
UV-Vis	Ultraviolet and Visible Absorption spectroscopy
VHS	Van Hove Singularities

List of Measurement Units

Å	Angstroms
λ	Wavelength
°C	Celsius degree
C	Coulomb
mC	Millicoulomb
Ω	Ohm
mΩ	Milliohm
KΩ	Kiloohm
A	Amp
mA	Milliamp
μA	Microamp
cm	Centimeter
Da	Dalton
F	Faraday
mF	Millifaraday
g	Gram
mg	milligram
L	Liter
mL	Milliliter

m	Meter
mm	Milliliter
μm	Micrometer
nm	Nanometer
min	Minute
M	Molar
mol	Mole
mmol	Millimole
N	Newton
Pa	Pascal
KPa	Kilopascal
GPa	Gigapascal
MPa	Megapascal
TPa	Terapascal
s	Second
S	Siemen
sccm	Standard cubic centimeter
V	Volt
mV	Millivolt
μV	Microvolt

Abstract

A nanocomposite is defined as a material of more than one solid phase, where at least one dimension falls in the nanometer range. The combination of carbon nanotubes (CNT) and conducting polymers offers an attractive route for the production of novel compounds that can be used in a variety of application such as sensors, actuators, and molecular scale electronic devices. The ultimate goal of this work is to develop and investigate CNT composites that provide a structural functionality together with one or more other key functions.

A variety of novel CNT dispersions were prepared using commercially available CNT systems such as Rice single-walled carbon nanotubes (RCNT), HiPco single-walled carbon nanotubes (HCNT), and Multi-walled carbon nanotube (MWCNT). This study explored the application of novel functional dispersing agents. Deoxyribose Nucleic Acid (DNA) a biological molecule, N-isopropylacrylamide 2-acrylamido-2-methyl-1-propanesulfonic acid (NIPPAm-AMPS) a polyelectrolyte, Didodecyldimethyl ammonium bromide (DDAB) a polymerizable compound, Poly(methoxyaniline-5-sulfonic acid) (PMAS) an inherently conducting polymer, and PVA an insulating polymer were some of the agents used to disperse the CNT. These dispersions were then evaluated in term of their stability and ability to effectively disperse the CNT. Solid-state CNT composites (mats) were then prepared by means of pressure filtration of the CNT/dispersant solutions. These mats were characterized using a variety of different techniques to determine their viability to be used as mechanical actuators or electrochemical devices. The characterization methods included cyclic voltammetry, conductivity, capacitance, atomic force microscopy, scanning electron microscopy, Young's modulus, and actuation measurements.

Abstract

RCNT/conducting polymer composites were prepared by the electropolymerization of Pyrrole with a range of different dopant anions in the presence of different RCNT dispersions. In these composites, the RCNT were completely covered by the polymer, consequently the electrochemical responses of these composites were dominated by the electrochemistry of the polymers with the CNT functioning as a conductor element.

Polypyrrole was also electropolymerized using functionalized multi-walled carbon nanotubes (FMWCNT) as dopant. Electropolymerization was carried out using galvanostatic and potentiostatic techniques on gold-coated Mylar and ITO-glass. It was determined that PPy/FMWCNT composites deposited on either electrode using potentiostatic deposition exhibited redox peaks. This redox behavior was not observed when the galvanostatic deposition was employed.

HCNT/Polyaniline (PAn) composites were prepared by either casting a film from a solution of HCNT and PAn in 1,2-Dichlorobenzene, or by casting a film of PAn onto an existing HCNT mat. The latter exhibited the highest conductivity. The actuation behavior of these CNT composites was investigated and it was determined that the PAn component contributes to the actuation strain while the HCNT component contributes to Young's modulus. The combination of the HCNT (with their mechanical properties) and PAn (with its actuator behavior) offers and attractive route not only to reinforce the polymer film but also to introduce new electronic properties based on morphological modifications or electronic interactions between the two components giving a robust blend of optimum properties. These results open the door for these composites to be used in a variety of applications that require a combination of the above characteristics such as mechanically reinforced actuator devices, robotics, optical fiber switches, prosthetic devices, and anti-vibration systems.

In addition, PPy with a range of dopant anions was electrodeposited galvanostatically, potentiostatically, and potentiodynamically on the surface of four different carbon electrodes, RCNT mat (unannealed), RCNT mat (annealed), glassy carbon, and carbon foil. It was found that the method of electrodeposition was crucial to the electroactivity of the deposited polymers, particularly when deposited onto a RCNT mat due to the different interaction between the deposited polymer and the RCNT mat

Finally, HCNT/SDS, HCNT/PMAS, and HCNT/DNA fibers were prepared using the Particle Coagulating Spinning method (PCS). The annealing process resulted in a dramatic increase in conductivity of up to 2600 times higher compared to the unannealed fibers. However, the annealing process did not play any role in keeping the fibers together or modifying the alignment of the carbon nanotubes ropes within the fibers. The HCNT/DNA fibers, with their biocompatibility, high conductivity, and good mechanical properties can be used as artificial muscles, bioelectronic sensors, or even as platforms to support the growth of nerve cells.

This thesis delineates the methods of successful production of solid sate CNT mats and fibers, utilizing traditional polymeric and more novel multi-functional dispersant materials. Thereby, providing a series of new framework for which future device structures can be fabricated.

Acknowledgements

I would first like to acknowledge the guidance and support of my supervisors, Prof. Gordon G. Wallace and Dr. Joseph N. Barisci over the course of my Ph. D.

I would like to thank Prof. Gordon Wallace for his financial support and opportunities that he has provided me with, and I would like to acknowledge his continuous council and encouragement.

I would like to thank the staff and students at the Intelligent Polymer Research Institute, working with them was defiantly a memorable experience and one that I will never forget.

I would like to thank Dr. Philippe Poulin for his invitation to Centre de Recherche Paul Pascal-CNRS laboratories, France. I would like to acknowledge his financial support but more importantly I would like to thank him for his unrestricted advice and help. I would also like to thank Stephane Badairre for his time and technical assistant with my work that was carried at the CNRS.

I would also like to thank Dr. Van-Tan Truong at the Defence Science and Technology Organization, Melbourne, Australia. I would like to thank him for offering me the chance to work with him and I would like to acknowledge his guidance and help.

I would like to thank Dr. Violeta Misoska for her help with the SEM images. I would also like to thank Dr. Chee Too and Dr. Simon Moulton for their help with the proof reading of my thesis.

Finally, I would like to offer the biggest thank you to Dr. Peter Innis for all the time that he spent reading my thesis and all the work that he did in helping me present this thesis. I would further like to thank him for his unconditional help and technical advice throughout the three years of my experimental work. Thank you for being such a generous and patient person, I have learned so much from you.

I would like to thank all my friends for being there for me, through the good times and the bad times. Whenever I doubted it, you managed to prove to me that friendship is the most important thing, thank you guys.

I would also like to thank my family for their help, encouragement, support and patience over the course of this Ph. D thesis. This work would not have been possible without you and I am forever in your debt.

I would like to dedicate this thesis to the most important person in my life now and forever…

Nadia

My Mother

CHAPTER ONE

CARBON NANOTUBES AND CONDUCTING POLYMERS

1.1- CARBON NANOTUBES

One goal of device science is miniaturization; hence nanotechnology has received considerable attention. The possibility that the unique properties of nanostructures will result in novel applications and devices is an enticing goal (1). Another reason for the great popularity of this field is that phenomenas occurring on this length scale are of interest to physicists, chemists, biologists, electrical and mechanical engineers, and computer scientists. Although many nanostructures such as large molecules and quantum dots are of interest, at present, one of the most active areas is the study of nanotubes.

1.1.1 Carbon nanotubes, what are they?

Iijima discovered carbon nanotubes in 1991 (2), and a method for the large-scale synthesis of nanotubes by Ebbesen and Ajayan was introduced in 1992 (3). This opened up a new era in material science and nanotechnology. Since then various nanotubes, with or without encapsulated metals, having a straight, curved, planar spiral, single and double helical shape have been experimentally produced either by the arc-discharge method or by vapor deposition of organic chemicals (4 - 19). These elongated tubes consist of carbon hexagons arranged in a concentric manner with both ends of the tubes normally capped by fullerene-like structures. They usually

have a diameter of the order of tens of Angstroms and the length of up to several micrometers, and can behave as semi-conductors or metal depending on the diameter and helicity of the arrangement of graphitic rings in the walls.

Two distinct types of carbon nanotubes have been recognized. The first is Multi-walled carbon nanotubes (MWCNT) that consist of more than one concentric cylindrical shell of graphene sheets, which are coaxially arranged around a central hollow with a constant interlayer separation of 3.4 Å. The second is Single-walled carbon nanotubes (SWCNT) that are made of single layers of graphene cylinders. The SWCNT have some distinct advantages over their MWCNT counterparts. For example, SWCNT are transparent to electromagnetic radiation including light, and furthermore, SWCNT show truly one-dimensional quantum effects.

The smallest SWCNT can be viewed as a fullerene molecule that has been bisected at the equator, and the two resulting hemispheres joined with a monolayer graphene tube of the same diameter as C_{60}. Because the graphene sheet can be rolled up with varying degrees of twist along its length, SWCNT can have a variety of chiral structures (20 - 22). If the C_{60} molecule is bisected normal to a five-fold axis, the so-called armchair nanotube (Fig 1.1a) is formed. Likewise, a zigzag nanotube (Fig 1.1b) results if the C_{60} molecule is bisected normal to a three-fold axis. Armchair and zigzag are achiral. The so-called chiral nanotubes (Fig 1.1c) can be produced when the C_{60} is bisected to a variety of other fold-axis other than a five or three-fold axis.

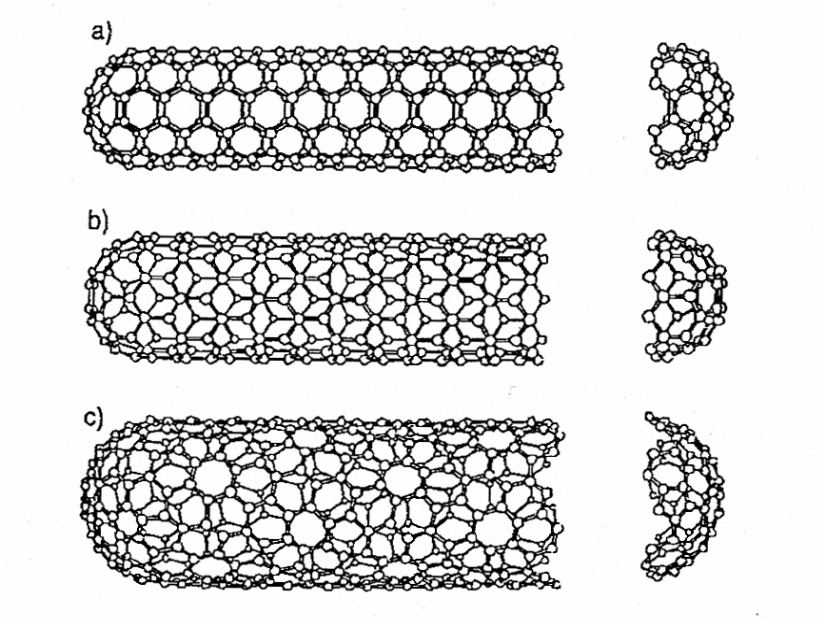

Fig 1.1 Schematic representation of SWCNT, a) Armchair, b) Zigzag, and c) Chiral (23).

In general, carbon nanotubes can be specified mathematically in terms of the unit cell, the smallest group of atoms that defines its structure through the so-called chiral vector of the nanotube C_h and the chiral angle θ. The C_h is given by $C_h = na_1 + ma_2$ where a_1 and a_2 are unit vectors in the two dimensional hexagonal lattice and *n* and *m* are integers. The chiral angle θ is then the angle between C_h and a_1 (24).

The limiting achiral cases (n, 0) zigzag, and (n, n) armchair are indicated with dashed lines in (Fig 1.2). The translation vector T is along the tube axis and the orthogonal to C_h. The rolled up area swept out by T and C_h corresponds to the repeat unit of an (n, m) tube, hence a nanotube (n, m) symmetry determines the size of its unit cell, which can vary greatly among tubes (23, 25).

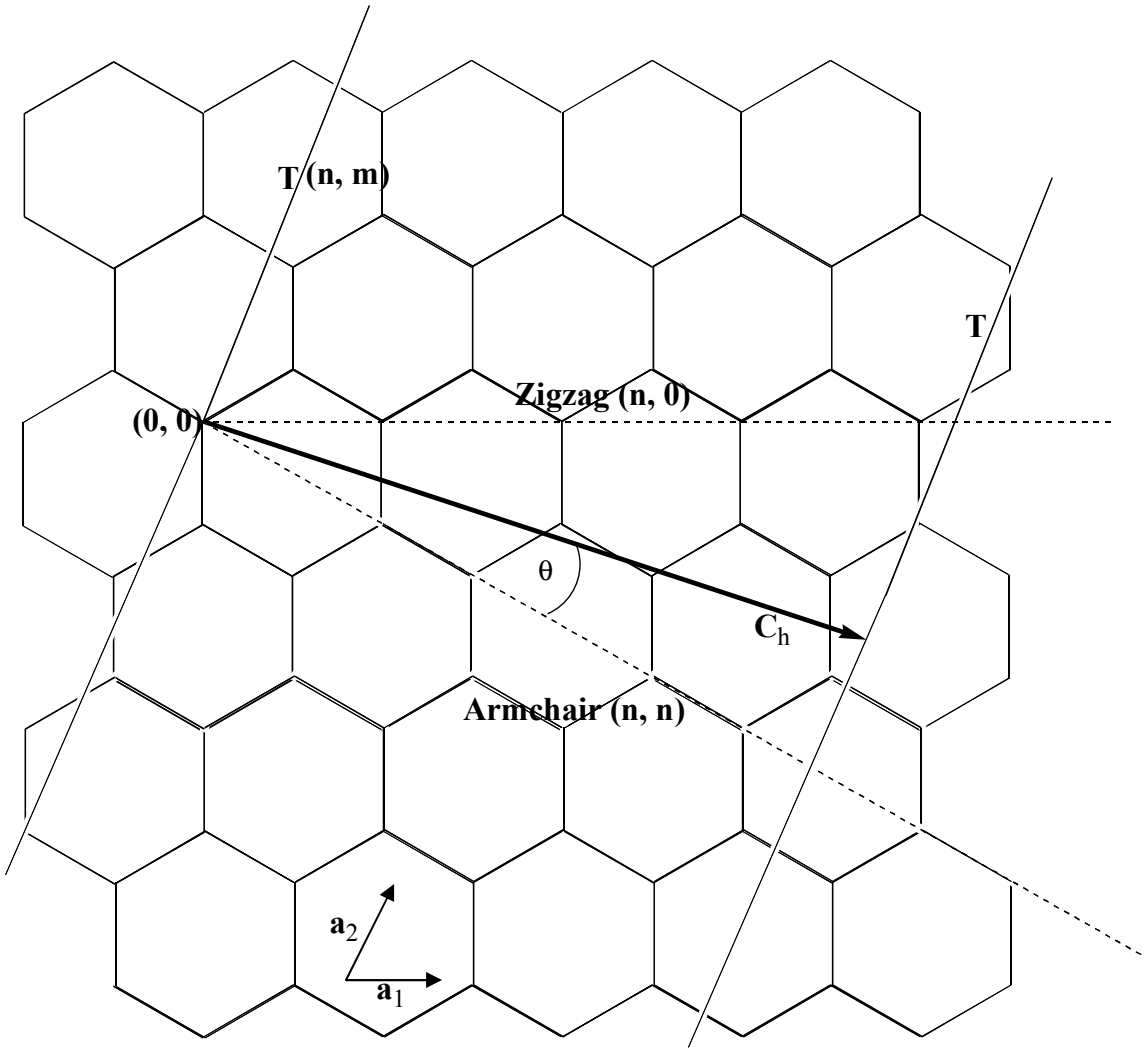

Fig 1.2 A graphene sheet that can be rolled into a SWCNT. a_1 and a_2 are the unit vectors of the graphene lattice. The dashed lines denote the main symmetry directions in the graphene sheet, the zigzag (n, 0) and armchair (n, n). T is the translation vector and defines the one dimensional (1D) unit cell. The (n, m) along the T represent achiral nanotubes. C_h the chiral vector, and θ the chiral angle.

When the graphene sheet is rolled up to form the cylindrical part of the nanotube, the chiral vector forms the circumference of the nanotubes circular cross-section with its ends meeting each other. Armchair nanotubes are formed when $n = m$ and the chiral

angle is 30°, whereas zigzag nanotubes correspond to either *n* or *m* = 0 and θ = 0. All other chiral nanotubes have the chiral angle intermediate between 0° and 30°.

The properties of nanotubes are determined by their diameter and chiral angle, which in turn depend on *n* and *m*. Theoretical studies have indicated that all armchair nanotubes are metallic, as are one-third of all possible zigzag nanotubes depending on their diameter and chiral angle (26). Graphite is semi-metal or zero gap semiconductor whose valence and conductance bands touch and are degenerate at six K (K_f) points, these six positions define the corners of the first Brilluion zone. As a finite piece of the two dimensional (2D) graphene sheet is rolled up to form a 1D tube, the periodic boundary conditions imposed by C_h can be used to enumerate the allowed 1D sub-bands, and the quantenized states resulting from radial confinements (27). If one of these allowed sub-bands passes through one or more of the K points, the nanotube will be metallic otherwise semiconducting. Thus zigzag (n, 0) or chiral (n, m) are metallic when (n-m)/3 is an integer and otherwise semiconducting. Therefore, independent of helicity, the energy gaps of semiconducting (n, 0) and (n, m) should depend inversely on diameter (27, 28). The semiconducting energy gap corresponds to the vertical separation between π and π* bands at the same K position of the 1D sub-band closest to K. Because the separation of 1D sub-bands is inversely proportional to diameter, larger semiconducting tubes will have an allowed state closer to K and have a correspondingly smaller energy gap. In addition, the finite curvature of the tubes also leads to mixing of π/σ bonding and π*/σ* antibonding orbitals on carbon (27, 29).

The chirality of the carbon nanotubes has significant implications on the material properties. In particular tube chirality is known to have a strong impact on the electronic properties of carbon nanotubes. Graphene is considered to be semiconducting, but it has been shown that nanotubes can be either metallic or semiconducting, depending on the tube chirality (30). MWCNT are essentially concentric SWCNT, where each individual tube can have different chirality. These concentric nanotubes are held together by secondary van der Waals forces (31).

Signature features in the Density Of State (DOS) of a material appears at the band edges and are commonly referred to as Van Hove Singularities (VHS). In three dimensions VHS are kinks due to the increased degeneracy of the available phase space, while in two dimensions the VHS appear as stepwise discontinuities with increasing energy. Unique to one-dimensional systems the VHS are manifest as peaks. Hence, SWCNT are expected to exhibit spikes in the DOS due to the 1D nature of their band structure (27). One important fact is that the first set of VHS in the DOS for similar diameter tubes is three times larger for metallic tubes than for semiconducting tubes.

In addition, in order to maximize Van Der Waals contact and lower their free energy, individual SWCNT align themselves with each other to form ropes. It was found that if the SWCNT comprising a rope are well aligned and packed closely together they often exhibit helicities similar to each other (27). Bernaerts *et al* have shown that SWCNT within ropes are found to comprise largely tubes of armchair chirality (32).

1.1.2 Synthesis

In general, the most robust way of making carbon nanotubes is by electric arc-discharge between two pure graphite electrodes in a helium atmosphere. During the arc-discharge, a deposit is grown on the cathode surface from plasma created by the evaporation of the anode. The deposit formed on the cathode has a soft core, which contains randomly oriented carbon nanotubes and polyhedral carbon particles (33).

The carbon arc-discharge method as employed for fullerenes was first used to produce MWCNT (3). Carbon nanotubes grow in bundles along with the formation of well-ordered carbon particles and other disordered carbonaceous material. Typically, the smallest bundle consists of 10 to 100 aligned nanotubes of nearly the same length. Later, it was discovered that MWCNT could also be produced by decomposition of hydrocarbon both in the presence and absence of metal catalysts; this was termed as vapor grown carbon nanotubes. The vapor grown carbon nanotubes exist also in bundles and often show internal bamboo-shaped structures, suggesting the capping of the inner layers along the length and tubular diameter (34). Also, the vaporizing of carbon in vacuum with either an electron beam or resistive heating followed by deposition on a cold surface, and electrolysis of molten alkali halide salts using carbon electrodes under an argon atmosphere have recently been reported (35 - 38). MWCNT have also been produced by high-temperature-graphitizing of the polyacrylonitrile nanotubes prepared within the pores of alumina template membrane or zeolite nanochannels (39, 40). Uniform hollow MWCNT with open ends were generated by chemical vapor deposition of organic hydrocarbons compounds directly within the pores of an alumina template membrane incorporated with or without a Ni catalyst. (41).

In 1993 SWCNT were observed for the first time in soot generated by the carbon arc-discharge using metals containing carbon electrodes (42, 43). To produce the SWCNT, a pure carbon cathode and a carbon anode containing a mixture of a transient metal and graphite powder in a hole are normally used. Co-vaporization of carbon and the metal catalyst in the arc generator results in the formation of web-like deposits of SWCNT in the fullerene containing soot. However, this produced a low yield of SWCNT and the samples lack structural uniformity. It was the efficient synthesis of ordered SWCNT bundles by pulsed laser vaporization of carbon target by Thess *et al* in 1996, that made the goal of testing the properties of SWCNT possible (44, 45).

Carbon nanotubes can be conveniently prepared via a new chemical approach by pyrolizing the composite fibers consisting of a pyrrole skin layer and a poly(ethylene terephtalate) PET core fiber at 1000 °C under a nitrogen (N_2) atmosphere (46) (Fig 1.3).

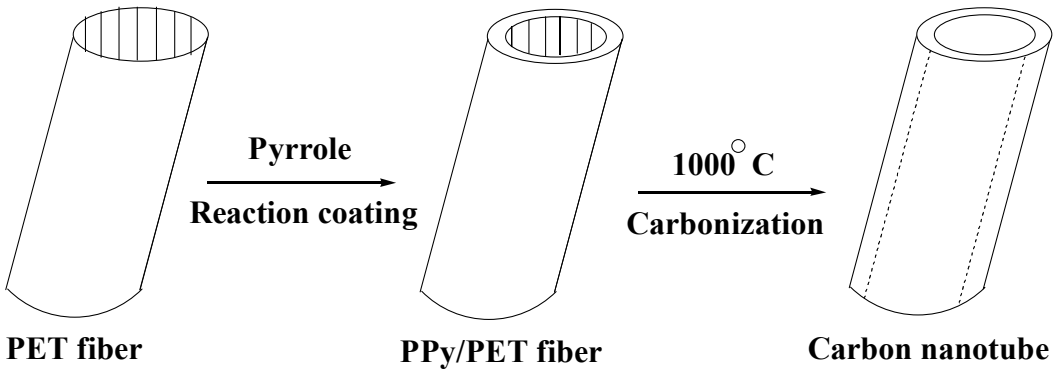

Fig 1.3 Pyrolization of composite fibers consisting of a pyrrole skin layer and a PET core fiber at 1000 °C under nitrogen (N_2) atmosphere.

The basic idea is to utilize a thermally removable polymer fiber such as PET, as the growing template for a thermally more stable material such as conjugated polymer like Polypyrrole (PPy) (47). The resulting fiber is then subjected to thermal treatment to remove the PET template by thermal degradation, while the PPy skin layer is simultaneously carbonized to form a carbon tube.

The tube wall thickness can be controlled by controlling the thickness of the PPy skin layer. Furthermore, the tube diameter can also be varied by changing the diameter of the PET core fiber. Interestingly, this method enables the preparation of well organized two or three-dimensional structure assemblies of carbon nanotubes via the use of appropriate woven templates. These carbon nanotubes are shown to be mostly amorphous in structure while the arc-discharge carbon nanotubes show a highly ordered cylindrical layer-stacking structure.

Carbon nanotubes synthesized by most of the common techniques, such as arc-discharge and catalytic pyrolysis, often exist in a randomly entangled state. However, aligned carbon nanotubes have been prepared either by post-synthesis fabrication (48 - 49), and by synthesis induced alignment such as template synthesis (50 - 51). Aligned carbon nanotubes have also been prepared either by slicing nanotubes-dispersed polymer composite or by rubbing a nanotube-deposited plastic surface with a thin Teflon sheet or aluminum foil (52, 53). Other researchers have prepared aligned carbon nanotubes by pyrolysis (54 - 56). In addition, Tans *et al* synthesized large arrays of aligned carbon nanotubes by radio frequency sputter coating (57).

1.1.3 Purification

In order to remove the amorphous carbon and catalytic particles many researchers heat the SWCNT material in nitric acid. The acid treated SWCNT and ropes of SWCNT are covered by debris, which consists of decomposition products. Due to the presence of carboxylic acid groups, the debris can be washed away by a basic aqueous solution. The washed material is then suspended in water with the aid of a non-ionic surfactant. To prevent the blocking of pores, cross-flow filtration systems are employed. In order to remove the surfactant residues subsequent to filtration, the tubes are annealed under nitrogen at 350 °C for 24 hours; this is followed by a treatment for 24 hours at 1600 °C to remove the remaining metal particles. This is a very long procedure in which the carbon nanotubes might be damaged and the purity of the final product is not significantly higher than that when the filtration method is applied. Oxidative methods have the advantage that metal particles and amorphous carbon are almost completely removed. More over, they are cheap and capable of purifying large quantities of material. On the other hand, there are several indications that the SWCNT are at least partially attacked during the acid treatment. The material loss during oxidation is larger than the content of impurities, which means that some SWCNT are destroyed, and the damaged SWCNT in the purified samples have different properties than the undamaged SWCNT (58).

Reproducible high yield purification process of SWCNT was developed by Moon *et al* (59); this process combines thermal annealing in air and acid treatment. Control of the temperature and annealing times is crucial for high yield results. It was also noted that the acid treatment enhanced the bundling of SWCNT as compared to samples

that were only annealed without further acid treatment (59), this was attributed to the fact that the entangled SWCNT bundles are released in acid and aggregated themselves by van der Waals interactions. A similar procedure was also applied by Tohji and co-workers (60).

Colomer *et al* proposed a purification method for carbon nanotubes produced by catalytic decomposition (61). This method involves the separation of nanotubes and catalytic particles by fluorhydric acid treatment. Then two ways of amorphous carbon elimination were applied: firstly, oxidation in air at high temperatures, secondly, oxidation in liquid phase at a given temperature by potassium permanganate. Li *et al* also developed a procedure for the purification of SWCNT produced by catalytic decomposition (62). This procedure involves washing with benzene, then acid, followed by ultrasonication and filtration, then the sample is frozen in liquid nitrogen, this is then followed by a second ultrasonication and filtration, finally the sample is washed with de-ionized water. It is believed that the ultrasonication treatment is able to remove the catalyst particles and amorphous carbon from the SWCNT bundles.

Bandow *et al* (63), reported a method mainly based on microfiltration under high pressure. A major advantage of this process is that it is driven by pure physicochemical interactions of the carbon products with the amphilic molecules and the filter membrane, leaving the nanotubes undamaged. The most serious drawback is the dependence of this procedure on the quality of the starting material. It is known that sonicating SWCNT for long periods of time at high frequencies can cause damage by breaking the nanotubes into smaller pieces.

Dujardin *et al* presented a one step method for the purification of SWCNT that does not appear to be sensitive to the quality of the starting material (64), moreover it

eliminates at the same time the carbonaceous material and most of the catalytic metal content. The SWCNT were produced by laser oven ablation, the sample was boiled in nitric acid, then refluxed for 4 hours in nitric acid at 129 °C. Transmission Electron Microscopy (TEM) pictures revealed no severe damage to the walls of the SWCNT. The nitric acid did not only react preferentially with the particles but left most of the SWCNT in the bundles intact. It was suggested that after the removal of the particles the acid reacts with the outermost nanotubes in the bundles, in other words the outer tubes protect the inner tubes within the bundle.

A purification method for the extraction of iron (Fe) metal catalyst and non-SWCNT from nanotubes produced by the HiPco process was proposed by Chiang *et al* (65). Metal catalyzed oxidation at low temperature has been shown to selectively remove non-SWCNT and permit extraction of iron with concentrated hydrochloric acid (HCl). Prolonged catalyzed oxidation has been found to preferentially remove smaller diameter tubes. In addition, Raman spectroscopy indicated that small diameter tubes are preferentially lost during the annealing process. Thermogravimetric analysis (TGA) data for purified HiPco SWCNT illustrates that the SWCNT are able to withstand oxidation temperatures as high as 500 °C. However, it was suggested that oxidation above 325 °C provides little additional air stability, most likely because little iron remains after the 325 °C. In addition, Chiang reported that the dispersibility of the HiPco SWCNT before high temperature annealing is observed to be just as good as the raw HiPco SWCNT, moreover it was found that the annealed samples were harder to disperse after high temperature annealing; presumably because larger better ordered rope structures are formed at high temperatures.

MWCNT that are obtained by the arc-discharge method are usually well garphtized and have a lower density of defects or strained sites than most of the other carbon species in the raw sample. Consequently, several methods have been made at selectively oxidizing the carbon impurities, since an attack should preferentially take place on strained site or defects (58). During gas oxidation the soot is exposed to air or pure oxygen at high temperatures (66, 67), whereas for liquid phase oxidation the material is attacked by strong oxidizing agents (68, 69). Small nanoparticles are completely decomposed during the oxidative treatment and the MWCNT are also attacked but due to their size, relatively large tubes survive a strong oxidation. The oxidation of the tubes takes place at the tips, but also along the tube body. As a result thinned MWCNT with open caps and chemical functions such as hydroxyl, carbonyl, or carboxylic groups on the outer shell are obtained (58).

Size exclusion chromatography has been successfully employed to purify micellar suspended MWCNT (58, 70, 71). This method is applied to surfactant stabilized dispersions of raw material, besides the removal of carbon nanospheres, metal particles, and amorphous carbon, a length separation of the carbon nanotubes is achieved.

Gas phase oxidation which yields purified MWCNT destroys SWCNT (72). Bonrad *et al* introduced a non-destructive separation method for SWCNT and MWCNT soot (73); the carbon nanotubes are dispersed with the aid of ultrasonication in an aqueous surfactant solution and become incorporated into micelles. This incorporation is reversible and does not alter the tubes chemically. Subsequent centrifugation removes a large fraction of microscopic particles and amorphous carbon; purity of the carbon nanotubes is very high (58, 74).

MWCNT are more suitable to be oxidized than SWCNT because the inner layers can remain unreacted and the essential electronic structure can be retained. Oxidative treatment of catalytically grown carbon nanotubes using aqueous acids, introduces oxygen containing functional groups on the surface. After such treatment the nanotubes form a well dispersed electrostatically stabilized colloid in water, the apparent viscosity which rises as a function of nanotube concentration increases dramatically above the critical entanglement concentration. During continued drying the solvent mediates the formation of dense assemblies of nanotubes which then bond together through the surface groups. If the nanotubes are deposited from a diluted suspension by filtration they are able to maximize the number of intertube contacts by packing into a locally paralyzed structure. At higher concentrations, gels form which can be reversibly redispersed. Once the gel is dried a solid is formed which can swell reversibly (75).

1.1.4 Conductivity of carbon nanotubes

Some SWCNT are metallic (due to the presence of delocalized electrons at the Fermi level) while others are semi-metallic. In SWCNT there are two types of nuclear spins with different spin-lattice relaxation rates. The rapidly relaxing component follows the relaxation behavior expected from metals (76). SWCNT exhibit a decrease in the lifetime in the electrons excited to the π^* bands with an increase in energy relative to the fermi-level. This in turn leads to lifetime-induced broadening of Van Hove singularities in the nanotube density of state (77). In SWCNT, electrical conduction occurs through well separated, discrete electron states that are quantum-mechanically

coherent over long distances (78, 79). Pure MWCNT exhibit a lower work function, while acid-oxidized MWCNT show a higher work function due to the disruption of π-conjugation and the introduction of surface dipole moments (80). Doping is expected to alter the electrical properties of pristine carbon nanotubes. Doping changes the carriers in the ropes from holes to the electron, the majority carriers (electrons) density is similar to that (for holes) in the pristine carbon nanotubes (81). Four-point conductivity measurement on doped carbon nanotubes demonstrate that doping involves charge transfer and that SWCNT are inherently p-type materials because of defects or inadvertent doping by exposure to air (82). Transport properties of SWCNT can also be modified by employing redox reactions (83). Van Hove singularities, characteristic of one-dimensional systems, disappear due to the loss of long-range ordering on intercalation.

Changes in the transport properties of the SWCNT have been predicted in terms of change in the carbon-carbon bonds. However, to produce these changes mechanical stress has to be applied within the atomic structure of the SWCNT, the electronic properties of the nanotube change locally at the deformation point. This is consistent with the theoretical calculations, which indicates that mechanical distortion of the nanotube do not significantly affect the conductance, unless the stress applied is great enough to produce local deformation of the carbon bonds in the nanotubes (84). In addition, investigations of the electrical transport properties of metallic SWCNT containing defects, showed that the defects lead to an increase in resistance, inducing strong barriers for electron transport (85).

The conductivity of an individual rope is reported to be approximately 10000 S/cm (86). A model of a manifold of one-dimension interacting electron system to account for the superconductivity observed in ropes of carbon nanotubes have been proposed by Gonzale (87). He relied on the strong suppression of single-particle hopping between neighboring nanotubes in a disordered rope and concluded that the tunneling takes place in pairs of electrons, which are formed within each nanotube due to the existence of large superconducting correlations.

It is difficult to determine the magnitude of conductivity in SWCNT mats. However, a metallic sample can have conductivity an order of magnitude less than a non-metallic sample. One reason for this is likely to be the existence of samples with metallic conductivity only in a small fraction of their cross-sectional area, and so low overall conductivity. Consequently the conductivity is the result of a metallic on-tube conduction in series with an activated, hopping-like conduction of the contact regions (88, 89). This indicates that the effective conductivity of the mats is more than an order of magnitude less than the conductivity a rope. In addition, if conduction requires either scattering or tunneling then the resistance can be very large (90). This conduction mechanism is described by the heterogeneous model, involving regions of antistrophic metallic conduction coupled with electron hopping or tunneling through small electrical barriers corresponding to defects of various types (91). This model seems appropriate for understanding conduction in the individual ropes separated by tangled regions such as polymer or surfactant materials, and also for mats of tangled bundles of ropes in which inter-rope contact are likely to act as barriers (92).

MWCNT are composed of several cylinders of different helicities, complicating any simple interpretation of transport based on theoretical predictions (93). When relating

the static conductivity of SWCNT to the static in plane conductivity of a graphite sheet it is concluded that isolated SWCNT are excellent conductors. In contrast, in MWCNT the electronic properties of bulk graphite are strongly affected by the outer sheet electron hopping, thus MWCNT may posses conductivities substantially below that of the sum of the constituent tubes. It was reported that the resistance of an individual MWCNT is 85 KΩ (94). For large radius MWCNT, the situation is probably most analogous to turbo-static graphite in which the parallel sheets are orientationally disordered (95), where a decrease in diameter results in an increase in conductivity (96). This means that the MWCNT that have a larger number of concentric cylinders will exhibit lower conductivities. Conduction in MWCNT is restricted to the outermost shell. However, we also have to consider the effect of inter-tube coupling as it promotes charge transfer between shells in the MWCNT (97, 98).

The conductivity of MWCNT mats is a complicated issue as the conductivity measure is a result of the contributing voltage passing through the aligned MWCNT *only* (99). MWCNT are mostly metallic and the main contribution to the conductivity comes from carriers (electrons) that hop directly between localized states via variable-range hopping (96, 100, 101). Four probe measurements on individual MWCNT showed a range of electronic behavior (metallic, and semi-metallic) (93). The electrical conductivity of individual MWCNT was estimated to be 1000-2000 S/cm, and it was found that an enormously large current density of 10^6 A/cm^2 could be passed through an individual MWCNT (102). However, it was also found that the conductivity varies depending on the helicity of the rings in the MWCNT, this

indicates that the MWCNT are not a single character of metallic or semi-conducting but include both types. This means that the current flow through a MWCNT will depend on the type of concentric "shells", whether they are metallic, semi-metallic, or both (103). In addition, the transport might be ballistic, where suppression of backscattering in the metallic nanotubes is possible, transport can be ballistic over several microns in length.

The pentagonal defects on the tips of the MWCNT can induce metallic character by introducing sharp resonance in the local density of state at the Fermi level (93). A weak magneto-resistance in the tubes indicates a very short free path for the conduction of electrons, most likely due to scattering by defects. On the other hand, the conductivity of aligned MWCNT in a film is due to the tunneling electron jump from one conducting tube to another (104), and the defects in the aligned MWCNT result in a decrease in the conductivity (105).

1.1.5 Mechanical properties of carbon nanotubes

While one might expect the axial elastic modules of carbon nanotubes to approach that of the basal plane of graphite crystals ~ 1 TPa., some theoretical predictions have suggested that nanotubes stiffness may be even higher (106 - 108). However, results obtained from theoretical estimations or molecular dynamic simulation present discrepancies, due to different definitions of Young's modulus in these systems (109, 110). From the point of view of the elasticity theory, the definition of the Young's modulus involves the specification of the value of the thickness *h* of the tube wall. It is not clear how to define this width for SWCNT, where the wall is composed only of one shell of atoms. Consistent with the concepts established for graphite sheets,

almost all studies have defined the spacing between adjacent tubes h = 3.4 Å as the representative thickness of the SWCNT, with a corresponding Young's modulus value of 1.1 TPa for individual SWCNT (111 - 115). However, to retain the classic relation D = Eh_3/12 the thickness of SWCNT should be h = 0.06 Å, which is about five times smaller than 3.4 Å. In doing so the corresponding Young's modulus is 5.5 TPa (116 - 118). In addition, some studies were independent of the shell thickness where the results imply that the SWCNT have a Young's modulus of 100-500 GPa (119, 120). Lourie and Wagner suggested that SWCNT have a Young's modulus of 3 TPa (121). Some theoretical estimates report values of the order of 5 TPa based on empirical Keating force-constant model. Applying Cox's theory where the nanotubes is treated as the discontinuous fiber phase suspended in a polymeric matrix, the Young's modulus of the SWCNT has been taken as the modulus of "material" within the thickness of the graphene sheet making up the cylindrical wall of the tube, corresponding to a Young's modulus of 320 to 1470 GPa for an individual SWCNT (122, 123).

Tracy *et al* (124) first investigated the elastic modulus of isolated MWCNT by measuring, in transmission electron microscopy, the amplitude of their intrinsic thermal vibrations, the average value obtained over 11 samples was 1.8 TPa. Wong and co-workers were the first to perform direct measurements of the stiffness and strength of individually isolated MWCNT using atomic-force microscopy. A value of 1.26 TPa was obtained for the elastic modulus, and the average strength measured was 14.2 GPa (125). For SWCNT ropes the Young's modulus is about one half that of diamond (115). There are many potential reasons why a rope might fail at a lower strain than an individual SWCNT. A rope might consist of overlapping nanotubes

that do not span the full width of the rope, in which case the forces between the adjacent tubes may be limiting, the rope might fail by slipping off or breaking its point of attachment. The nanotubes in ropes may contain pre-existing defects, if the rope had a smaller diameter over some portion of its length, that portion would undergo higher strain than the average strain calculated (126). The mechanical properties of SWCNT ropes were measured by Salvetat and co-workers (127), and it was found that as the diameter of the tube bundles increases, the axial and shear moduli decrease significantly. This suggests slipping of the nanotubes within the bundle. Walter *et al* further investigated the elastic strain of SWCNT with Atomic Force Microscopy (AFM) (128). On the basis of their experimental strain measurements and an assumed elastic modulus of 1.25 TPa, they calculated yield strength of 45 GPa for the single-walled nanotube ropes. However, the calculated value for the strength would be much lower if the elastic modulus of the nanotubes bundle is decreased as suggested by Salvetat (127). Yu and co-workers investigated the tensile loading of SWCNT and MWCNT ropes using AFM (129, 130). In their work, the nanotubes were attached between two opposing AFM tips and loaded under tension. For MWCNT the failure of the outermost tubes occurred followed by pullout of the inner tubes. The calculated tensile strength of the outermost layer ranged from 11 to 63 GPa and the elastic modulus ranged from 270 to 950 GPa. For SWCNT it was assumed that only the outermost tubes assembled in the rope carried the load during the experiment and they calculated tensile strength of 13 to 52 GPa, and average elastic moduli of 320 to 1470 GPa.

The theoretical Young's modulus has been calculated for several SWCNT aligned in the direction of the tubular axis. The results show that fibers composed entirely of aligned SWCNT have a high modulus which increases as the tubular radius decreases and as the distance between the closed-packed tubules in the fiber get shorter (131). The results indicate that SWCNT ropes, in fact have a very high strength similar to that of SWCNT fibers, even though the bonding between the ropes is low. The SWCNT ropes may slide with respect to each other in the SWCNT bundles during stress transfer since the inter-rope bonding is always weak in the SWCNT bundle. The Young's modulus of bundles composed of aligned SWCNT ropes is 790 GPa (132).

In SWCNT/polymer composites, the ropes play a very small role in strength enhancement (133). In these systems, there are two distinct deformation modes. Sideways buckling of thick tubes and collapse/fracture of thin tubes without any buckling (134).

A fascinating issue is whether there is interdependence between mechanical properties and the diameter and chirality of the SWCNT. Some studies conclude that the Young's modulus is independent of helicity and radius (121). On the other hand, different studies argues that for a given chirality, the stiffness of SWCNT is predicted to decrease with decreasing diameter, and for a given diameter, the stiffness should increase with increasing chiral angle. For nanotubes that are packed into ropes or that have larger diameters, these dependencies are expected to be more complex, and a sharp decrease in stiffness is predicted for SWCNT with diameters above 1.5 nm (111, 112, 114, 135, 136, 137).

Jishi and co-workers concluded that the elastic properties of nanotubes are insensitive to size and chirality (138). They predicted Young's modulus of ~ 1 TPa, shear modulus ~ 0.45 TPa, and bulk modulus ~ 0.74 TPa that are comparable to those of diamond. Hernandez and co-workers performed similar measurements to those of Jishi and found slightly higher values for Young's modules (139). But unlike Lu, they found that elastic moduli are sensitive to both tube diameter and chirality. Ru presented a modified elastic-honeycomb model to study elastic buckling of SWCNT ropes under high pressure (140). Ru gave a simple formula for the critical pressure as a function of nanotubes, Young's modulus and wall thickness-to-radius ratio. It was concluded that SWCNT ropes are susceptible to elastic buckling under high pressure and elastic buckling is responsible for the pressure induced abnormalities of vibration modes and electrical resistivity of SWCNT. Lu *et al* also calculated the elastic properties of MWCNT by means of the empirical-lattice dynamics model (141). It was found that the elastic properties of MWCNT are insensitive to different combinations of parameters, such as chirality, tube radius and number of layers, and that the elastic properties are the same for all nanotubes with a radius larger than 1 nm. Interlayer van der Waals interactions have a negligible contribution to both the tensile and shear stiffness. Ru, using the elastic-shell model, reached the same conclusion (142).

1.2- CONDUCTING POLYMERS

Despite numerous attempts, it was not until recently that the production of macromolecular materials with conductivities similar to those of metal was possible. Chemists have long attempted to synthesis macromolecules with an extended π-electron system as an integral part of the chain. It was hoped that delocalization of the electrons, assumed to take place in such systems, would necessarily lead to high concentration of charge carriers in the transport of current. However, the first molecules of this type prepared displayed low conductivity (143). It is known today that polymers with polyconjugated structures are usually insulators in the ground state. Electrons cannot move along polymer chains and through materials because of the lack of charge carriers (144). In order for polymers to be conductive they must possess not only charge carriers but also an orbital system that allows the charge carriers to move. Conjugated polymers can meet the second requirement through overlapping π-orbitals which provide reasonable carrier mobility along the polymer backbone. Since most organic polymers do not have intrinsic charge carriers, however, the charge carriers must be provided by an external process called doping (145, 146), namely by partial oxidation (p-doping) of the polymer chain with electron acceptors or by partial reduction (n-doping) with electron donors. Through such a doping process, charge defects (e.g polaron, bipolaron, and solution) are introduced (145, 147), which may then be available as charge carriers along the polymer backbone. The doping level is the most obvious factor that influences the conductivity of conducting polymers.

New insights into conducting polymers were introduced by Heeger and MacDiarmid in 1974 (148). In their work they demonstrated for the first time that Polyacetylene (PA), which is a semiconductor with a relatively large band gap, exhibited a dramatic increase in specific conductivity when treated with strong oxidizing or reducing agents. The behavior of the resulting polymer was comparable to that of classical semiconductors e.g. silicon, which upon doping can be transformed into a conducting state. Reactions of the polymer with for example halides, pseudohalides, alkali metal, or alkali metal derivatives was therefore, termed "doping" which is described in detail below. The most prominent example of such an organic metal is the charge-transfer complex produced from tetrathiofulvalene (TTF) and tetracyanoquinodimethane (TCNQ) (143, 149).

Following the work of Heeger and MacDiarmid, other polymers, that become conducting upon doping, were quickly found. Poly(thio-1,4-phenylene) (PTP) was the first example of a polymer that can be doped, its moldable and soluble (143). Pure PTP is an excellent insulator, but in the course of doping its conductivity characteristics change from that of a semiconductor to that of a semimetal. It is generally accepted that the increase in conductivity originates from a chemical reaction between the polymer and dopant which involves charge transfer from the dopant to the polymer. This results in an ionic polymer, in which the charge is delocalized along the polymer backbone. In addition, counterions which were derived from the dopant are also present in the polymer matrix. Redox reactions result in an increase in conductivity, in these reactions segments of polymer chain of lengths *n* are oxidized and structures are formed having the characteristics of a delocalized

radical cation. Undoubtedly, the most elegant method of doping involves electrochemical oxidation in the presence of a suitable supporting electrolyte (150).

The preparation of Polypyrrole was first reported by Dall *et al* in 1968 (151), and this material was later investigated by Diaz and co-workers in 1979 (152). In 1982 Bull *et al* published the results of both the cyclic voltammetry (CV) and impedance measurements of PPy, which demonstrated that PPy films are porous to solvent and electrolyte, and that electron transfer reactions can occur at the PPy film surface itself (153). In 1982 Burgmayer and co-workers reported that ion movement through neutral polymers containing fixed polymer sites was dependent on the nature and number of such charged sites (154). Changing these factors was stated to change the PPy film ionic resistance. It was also shown that ionic resistance is electrochemically controlled via the oxidation of the redox sites within the polymer. They termed this phenomenon the "ion-gate", since the resistance is varied from high to low and vice versa.

In 1984 a more detailed study of the "ion-gate" phenomena using PPy was conducted by Burgmayer *et al* (148). This study included measurements of alternating current (AC) impedance curves of PPy films in the oxidized and reduced states, analytical permeation studies of chloride ion from potassium chloride (KCl) electrolyte, a study of the ion exchange properties of oxidized PPy, and the effect of electropolymerization parameters on ionic permeability. They concluded that the "ion-gate" phenomena reflected differences in the mobility of ions in oxidized and reduced PPy films. They also provided strong evidence that this was due only to changes in fixed ionic site concentrations within the film caused by the oxidation and reduction of PPy. The possibility that "ion-gate" activity was explained in terms of

the well-known electronic conductivity of PPy was ruled out. A simple experiment was conducted to further demonstrate that oxidized PPy films are permiselective. When used as the cell divider membrane in a concentration cell separating unequal concentrations of the same electrolyte, a potential across the PPy film was sensed between a pair of saturated calomel electrodes (SCE). This indicated that oxidized PPy, independent of its electronic properties, acted as a typical ion exchange membrane.

Naio and co-workers conducted a study into the insertion/expulsion of ions by redox cycling of PPy (155). They concluded that the movement of ions during redox cycling of PPy films was dependent on the size of the anions. The PPy films prepared with small anions showed anion doping during oxidation, which meant that only anions provided charge compensation for oxidized sites in the polymer. The mass change due to the redox process was relatively small compared to that associated with electropolymerization, and the charge decrease corresponded to the mass decrease, which indicated that the film released anions during the reduction process. The films formed with large polymeric anions showed in contrast cation release and solvent motion during the oxidation process. The mass increased during the reduction process, which suggests that the film incorporated cations instead of releasing anions. Films prepared with medium-sized anions showed a somewhat intermediate behavior where both cation and anion movement were observed during the oxidation and reduction processes.

The most common conducting polymers are polypyrrole (PPy), polyaniline (PAn), and polythiophene (PTh) (Fig 1.4). Conducting polymers are synthesized using either chemical or electrochemical polymerization (Fig 1.5).

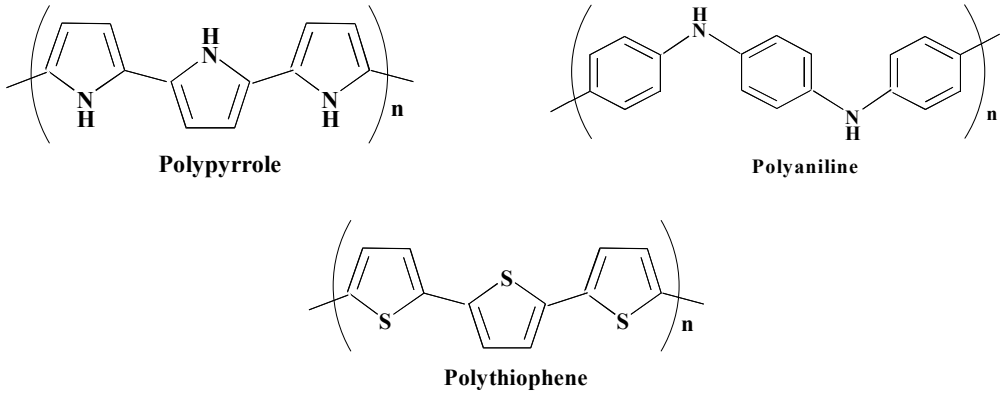

Fig 1.4 Chemical structure of PPy, PAn, and PTh.

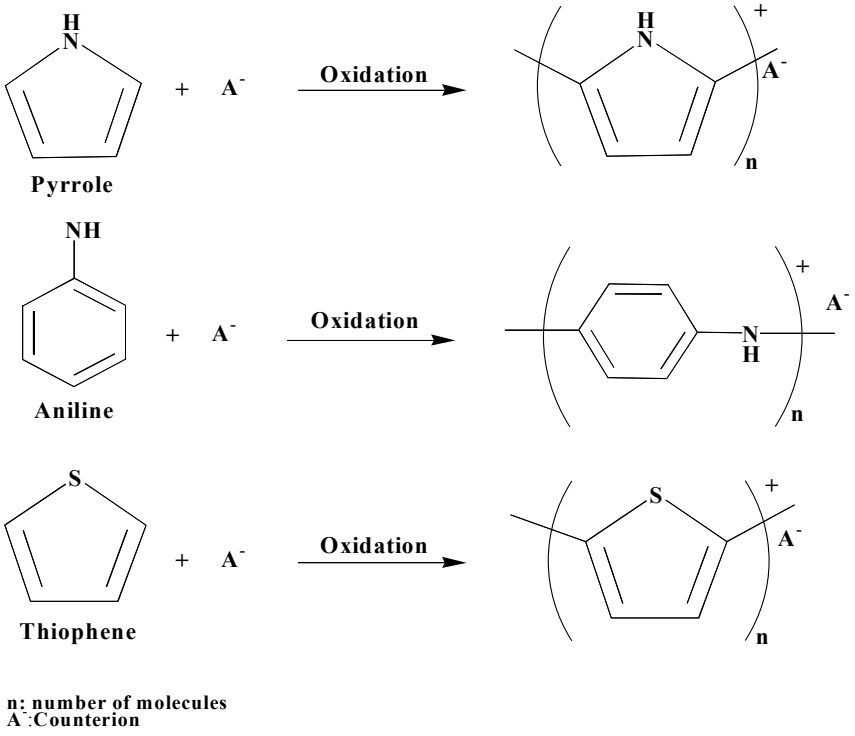

Fig 1.5 Polymerization of PPy, PAn, and PTh.

Electrochemical polymerization is carried out in a two or three electrode cell. A three-electrode cell is more commonly used and it consists of a reference electrode an auxiliary electrode, and a working electrode on which the polymer is deposited. The

electrolyte in this cell consists of the monomer and a dopant. Conducting polymers can be produced electrochemically using constant current (gelvanostatically), constant potential (potentiostatically), or cyclic potential (potentiodynamically). The application of any of the three different methods depends largely on the monomer and dopant used where different polymers are produced with a much higher yield and better properties when different growth condition are applied.

The electrochemical polymerization of PPy proceeds via radical-radical coupling mechanism, in which the repulsion between radicals was assumed to be mediated by the solvent, the counterions and even the monomer (156).

The electrochemical polymerization of aniline to form conducting polymers requires strongly acidic solution conditions for two reasons (157):

1- The aniline monomer is only soluble in water under acidic conditions.
2- The conducting form of PAn only occurs in acidic solutions, as the polymer is doped by protonation as well as oxidation. The electrochemical and chemical doping occur concurrently, and the resulting structure is that of a polaron lattice, which is delocalized over the polymer.

PTh can be synthesized either chemically or electrochemically. As with PPy the mechanism of polymerization involves the formation of radical cations that react with each other or the starting monomer to develop the polymeric structure. However, the potential required to oxidize the thiophene monomer also leads to overoxidation of the polymer itself (158). This is known as the “polythiophene paradox”. To achieve high conductivities, the polythiophene paradox must be overcome. Synthesis at reduced temperatures helps avoid overoxidation and can be used to increase the conductivity. The polymerization and conductivity of the resultant material are

influenced by the concentration of the monomer used during polymerization, since if this is too low the overoxidation reaction predominates (159, 160).

As substitution may change the chemical and physical properties of the polymers, soluble forms of various conjugated polymers including polyacetylene, polythiophene, polypyrrole, and polyaniline, have been prepared by grafting suitable side groups and/or side chains along their conjugated backbones (161, 162). Another approach towards circumventing the intractability of conjugated polymers is to synthesis copolymers of conjugated polymer segments with various soluble components. This can be achieved by random and alternating copolymerization (163 - 171). Block and graft copolymers differ from random and alternating copolymers in that relatively long conjugated polymer blocks are attached to a soluble polymer chain or vice versa. Therefore, the integrity of conjugated structures can largely be preserved in block or graft copolymers suggesting better electrical properties (172, 173).

Conducting polymers such as polypyrrole, polyaniline, and polythiophene are complex dynamic structures, making it possible to create conducting polymers with a diverse range of properties. For example, the chemical properties of these materials can be manipulated to produce materials capable of trapping simple anions (174), or to render them bioactive (175). Electrical properties can also be manipulated to produce materials with different conductivities and redox properties; the conductivity for polypyrrole, polyaniline, and polythiophene is 1 X 10^2-7.5 X 10^3, 30-400, and 10-10^3 S/cm respectively (176). After synthesis, the properties of these fascinating structures can be manipulated further via the redox process. The application of

electrical stimuli can result in drastic changes in the chemical, electrical, and mechanical properties of conducting polymers (177).

Conducting polymers have also had a tremendous impact on the development of new sensors. For example, sensing surfaces have been designed which are capable of interacting with simple anions (178), metal ions (179, 180), small organic molecules (181), or proteins (182).

Cyclic voltammetry is recognized as a standard method for the study of electrochemical behavior. It is a versatile electroanalytical technique for the study of electroactive species. The effectiveness of the cyclic voltammetry is due to the ability to rapidly observe the redox behavior of a species over a wide range of potentials. Cyclic voltammogrames (CVs) can be used to study the electrochemical behavior of species diffusing to an electrode surface, interfacial phenomena at an electrode surface, and bulk properties of materials in or on the electrode.

Cyclic voltammetry is recorded by cycling the potential of an electrode, which is immersed in solution and measuring the resulting current. The potential of the working electrode is controlled verses the reference electrode. The controlling potential that is applied across those two electrodes can be considered an excitation signal. An excitation signal for a CV is a linear potential scan with a triangular waveform. This triangular excitation signal sweeps the potential of the electrode between two values. A cyclic voltammetry is obtained by measuring the current at the working electrode during the potential scan. The current is considered the response signal, and the CV is displayed as the current verses the potential. The observed current behavior of a voltammogram is an increase to a peak current at which point the current decays due to depletion of electroactive species near the electrode. The

important measures of a CV is the anodic peak and anodic potential, and the cathodic peak and cathodic potential. In a truly reversible system, the number of electrons exchanged with the working electrode can be determined from the separation between these two potentials. In addition, it should be noted that the faradaic oxidation process is essentially represented by the anodic peak-shaped wave, while the adjoining broad anodic wave represents the double layer capacity of the system (183).

In an ideal case, reversible cyclic voltammetry of redox active films should show completely symmetrical cathodic and anodic waves with identical peak potential and current levels. This is valid for a monomolecular layer. However, in the case of films with greater thickness, account must be taken of the fact that charge transport is dependent on both electron exchange reactions between neighboring reduced and oxidized sites and the flux of counter ions in keeping with the principle of neutrality (183). The laws of diffusion can describe the mechanisms of these processes. All variants of the diffusive mass transport are possible depending on film thickness, values of the formal diffusion coefficient, and the experimental time scales. This implies that as the sweep rate increases there must be a shift from symmetrical to asymmetrical CVs. When the CV is asymmetrical this indicates electrochemical irreversibility, where the separation in potential between the anodic and cathodic peaks becomes larger and the peaks broader. Electrochemical irreversibility is caused by slow electron exchange of the redox species with the working electrode.

1.3- CARBON NANOTUBES AND CONDUCTING POLYMER COMPOSITES

A nanocomposite is defined as a material consisting of more than one solid phase, metal ceramic or polymer, compositionally or structurally, where at least one dimension falls in the nanometer range. There have been great efforts to fabricate nanocomposites (184, 185); to obtain unique physical properties since the properties become increasingly size dependent at low dimensions. The nanophase thus acts as a functional component in the composite to deliver new size sensitive properties (33). The combination of carbon nanotubes with polymers offers an attractive route not only to reinforce polymer films but also to introduce new electronic properties based on morphological modifications or electronic interactions between the two components.

Two distinct possibilities exist for creating carbon nanotubes based composites. First, the composite structures are made in the arc-discharge process itself by using a composite anode, metallic species are thereby introduced into the product, nanotubes encapsulating mostly metal carbides and sometimes pure metals can be made. Nanotubes with boron and nitrogen substituted in the hexagonal network have also been synthesized by this technique (176). Secondly, pure nanotubes are collected and then treated with other materials under different conditions to make composites (33).

Filled nanotubes: the idea here is to utilize the central hollow channels in the nanotubes and fill them with a second phase material to obtain encapsulated tubes. One way to do this is again by introducing metallic species into the plasma zone where growth occurs, during the arc-discharge process. Another way to fill the

carbon nanotubes channels is by using the capillarity technique. Strong capillarity forces exist in nanotubes so that simultaneous opening and filling of molten material is possible by oxidation and melting of a second phase near the tube's open ends (176). Based on the fact that the carbon nanotubes can be opened in solution, a general technique using capillarity has been developed recently by Sang *et al* (186), opening and filling of the tubes is done in solution under an oxidative environment. Deposits inside nanotubes are then obtained by calcining the tubes that have been wet by the solution with dissolved metal containing salts (33). The resulting structures are nearly one dimensional, retaining the dimensionality of nanotubes which are of nanometer sizes in two dimensions and micrometers in the length direction (33).

Capillarity of carbon nanotubes is directly related to the surface energies of interactions between the liquid and the solid surface of the nanotube and therefore, it is a problem of wetting (187). This is clear when considering the Young-Laplace equation which relates the pressure difference across the liquid-vapor interface to the surface tension of the liquid and the contact angle between the solid and the liquid θ. If θ is larger than 90°, the contact is said to be non-wetting, which means that pressure will always have to be applied to force a liquid into a capillary. If θ is smaller than 90°, the liquid will spontaneously be pulled into a capillary. Raw carbon nanotubes samples are composed of nanotubes in bundles and nanoparticles. When compacted, the space between these particles can act as capillaries also (188). A liquid will be drawn into the material only if it has a wetting contact angle with the surface. Therefore, if the liquid is pulled into capillaries between the nanotubes along the outside surfaces, it should also be drawn into the inside of the nanotubes. In other

words, the low surface tension liquids which wet the outside surface should fill open nanotubes by capillary (187). Lead oxide, Bismuth oxides, and Vanadium oxides have unusually low surface tension which allows them to be pulled into the inside of the nanotubes (188 – 190). Liquid metals have a relatively high surface tension, one approach to filling the nanotubes with metal is to force the liquid metal inside by the application of a positive pressure (θ is larger than 90°), the sample should then be cooled to solidify the metal before dropping the pressure.

Coated nanotubes: capillarity can also be used to coat the nanotubes uniformly with structures that form layered compounds such as Vanadium oxides, by annealing the carbon nanotubes and the oxide above the melting point of the oxide (33).

Successful fabrication of carbon nanotubes polymer composites depends crucially on maintaining a stable colloidal mixture of nanotubes and polymer. Composite film of nanotubes and Poly(vinyl alcohol) (PVA) were prepared by Shaffer *et al* (191). By dispersing the carbon nanotubes in PVA solution, followed by casting and then water evaporation. To form a stable mixture, each nanotube must be covered with an adsorbed layer of polymer before it is able to interact with a significant number of other nanotubes. In colloidal terms, the adsorbed polymer then stabilizes the nanotubes dispersion, and protects it against bridging flocculation and depletion aggregation caused by the free polymer (192). However, the layer of polymer will hinder the contact between the carbon nanotubes resulting in lower conductivity.

1.4- APPLICATIONS

Carbon nanotubes due to their high mechanical strength and outstanding electrical properties, have attracted considerable interest for applications such as field emitters (193), mechanically reinforced composite material (194), scanning probe microscopy tips (195), as well as molecular scale electronic devices such as field-effect transistors (196), or sensors (197). For most of these potential applications, defects in the carbon nanotubes play a critical role in performance, reliability, and stability. Moreover, defects are considered as reactive sites during chemical tube modifications. The defects in carbon nanotubes can be classified into several categories including topological defects, incomplete bonding defects, and chemical defects consisting of atoms/groups covalently attached to the carbon lattice of the tube (198). The use of carbon nanotubes with or without polymer for biosensors or artificial application would require the chemical modification of the surface characteristics to meet certain specific requirements. Therefore, research on carbon nanotubes have recently been extended to include chemical modification such as treatment with certain acids (functionalization), side-wall fluorination, derivatization with highly reactive chemicals such as dichlorobenzene, and radio-frequency glow discharge plasma treatment.

Because of their geometry nanotubes are sensitive to defects and impurities. This sensitivity gives rise to unusual properties. For example in three dimensions, we are accustomed to the fact that if one metal carrying current is put in contact with a second metal then the electrical current will flow across the junction from the first metal to the second. For two metallic carbon nanotubes, depending on the helicity,

the junction can stop the current because of the mismatch of wave function symmetry (50). Theoretical studies suggest that breaking the symmetry by bending the tubes will allow the current to flow. Another example which may lead to useful devices is the junction between a semiconducting and a metallic carbon nanotube, where the tubes are joined by a defect. The defect involves the rotation of bonds between two hexagons to form a five-fold ring and an adjacent seven-fold ring.

Lefebvre *et al* presented three different types of SWCNT based devices: the SWCNT diode, the tube-tube junction and an ultra short SWCNT contacted with electrodes whose separation is less than 30 nm (199). The SWCNT diode behavior is due to the presence of a local impurity. It was also shown that a nanotube bundle and a metal electrode lying on top of a SWCNT induce the formation of an isolated quantum dot bound by the barriers. They have also indicated that in the case of the SWCNT junction, the barrier can be tuned away, thus transforming a nanotube that consists of two quantum dots into a single quantum wire. These features can be used to create various devices using SWCNT.

CHAPTER TWO

PREPARATION AND CHARACTERIZATION OF DISPERSIONS AND MATS OF LASER PRODUCED RICE CARBON NANOTUBES/DISPERSANT COMPOSITES

2.1- INTRODUCTION

Production of stable Single-Walled Carbon-Nanotubes (SWCNT)/dispersant composites depends on the ability of the dispersant to wet the nanotubes, and to induce chemical properties that will stabilize the nanotubes in solution. This interaction is polymer or surfactant specific depending on the chemical nature of these compounds (200).

SWCNT/polymer composites have been prepared by a number of groups. Stephane *et al* and Koshio *et al* prepared SWCNT/Poly(methyl methacrylatye) (PMMA), which is a non-conjugated polymer (201, 202). SWCNT/Poly(m-phenylenevinylene-co-2,5-dioctyloxy-p-phenylenevinylene) (PmPV) which is a conjugated semi-conducting polymer was prepared by a number of research groups (200, 203, 204, 205). It was found that ropes of SWCNT are coated with a layer of this polymer about thirty times the diameter of the SWCNT ~ 1.2 – 1.4 nm, the thickness of the PmPV layer was 30-50 nm (200, 205). The diameter of the SWCNT/PmPV ropes is in the range of 60-120 nm, suggesting that these ropes consist of 20-80 SWCNT (200). It was also found that electron delocalization along the polymer chain in the composite is much less than in the pure PmPV as would be the case if the backbone conformation was

modified due to interaction with SWCNT. When a polymer capable of π-π stacking such as PmPV is wrapped around an individual tube the polymer rigidly adheres to the tube, while the presence of SWCNT reduces the polymer-polymer interactions (203).

In other studies, Poly(vinyl alcohol) (PVA) which is a non-conducting polymer and SWCNT composite mats, with a wide range of SWCNT loading were prepared (206, 207). It was found that the SWCNT in the SWCNT/PVA mat are completely isolated from each other by the presence of PVA, where the polymer covers the whole length of the rope (206).

SWCNT are usually randomly oriented into ropes with a diameter of only 5-20 nm. Through the use of ultrasonication and surfactants, the ropes self organize into bundles comprising around 100 ropes. Samples prepared as a "mat" typically consist of randomly oriented interconnecting ropes (208). In some cases, "superbundles" are formed where the SWCNT collapse into this configuration. The superbundle configuration arises from the minimized interactions between the SWCNT surfaces and the polymer or surfactant such that the van der Waals interactions along the axial length of the SWCNT are maximized leading to the formation of superbundles (209).

On the other hand, the introduction of the polymer increases the distance between the nanotubes and therefore, the interactions between the nanotubes decrease (201). In addition, adhesion of the polymer or the surfactant around SWCNT prevents them from reforming thick bundles (202).

When using low concentration of SWCNT the mats obtained are more uniform and homogenous than when using a higher concentration of SWCNT. In mats where low

concentration of SWCNT is used, the ropes and bundles of SWCNT have a similar number of tubes, and the thickness is consistent throughout the mat (203). When the concentration of SWCNT is less than 2.5%, the nanotubes are uniformly dispersed in the polymer or surfactant matrix.

In this chapter laser produced Rice Carbon nanotube (RCNT) dispersions and mats are prepared. Three different batches (**I**, **II, III**) of the RCNT were used to prepare three separate sets of dispersions and mats for comparison. In addition, using dispersions containing four times the concentration of the RCNT, thick mats were prepared in order to determine the effect of thickness on the properties of the different mats. A wide range of dispersants were tested and the dispersants chosen had the ability to disperse the RCNT, and a chemical function such as being cationic, anionic, neutral or a functional dispersant which are discussed separately. The characterization of the dispersions was carried out using a variety of techniques such as, cyclic voltammetry, particle-size, and Ultraviolet and Visible Absorption spectroscopy (UV-Vis). These dispersions were then filtered to produce RCNT/dispersant mats. The characterization of these mats was carried out using techniques such as, cyclic voltammetry, capacitance, and Atomic Force Microscopy (AFM). Conductivity, and Young's modulus for the different RCNT mats were also measured.

2.2- EXPERIMENTAL

Three different batches (**I**, **II**, and **III**) of RCNT were used to prepare RCNT dispersions and mats. Two sets were prepared using batch **I** and **II**, and also two sets were prepared using batch-**III** (**IIIA** and **IIIB**), in order to determine if these batches had similar or different properties. In addition, to examine the effect of mat thickness on the different properties of the mats, RCNT mats four times the thickness of the standard mats were prepared using batch-**III**.

2.2.1 Preparation of RCNT dispersions and mats

RCNTs were obtained from Tubes @ Rice (Rice University, Houston TX) as a suspension in toluene, with a tube diameter of 1.2-1.38 nm. 1 g of RCNT dispersion (5.9 mg/mL), and 0.1 g TritonX 100® (TX100) (<3% w/v polyethylene glycol, Aldrich) were added to 100 mL Milli-Q-Water, and sonicated for 30 min. This produced the standard RCNT/TX100 dispersion. As shown in Scheme –2.1, a 50 ml aliquot of the standard RCNT/TX100 dispersion was filtered using a stirred filtration cell (model 8050 purchased from Amicon/Millipore) under nitrogen pressure of 400 KPa. Polyvinylidene fluoride (PVDF) membranes with pore size of 0.22 μm were used as filters. The PVDF membranes were pre-soaked for 30 minutes in 50:50 v/v ethanol to Milli-Q-Water prior to use. After filtration the resultant RCNT mat, was washed with 150 mL Milli-Q-Water and 150 mL methanol to remove excess TX100. The RCNT mats were then peeled of the PVDF membrane and re-dispersed in 50 mL of the following solutions, 0.2% w/w Sodium dodecyl sulfate (SDS) (M.W. 288.37 Da, Aldrich), 0.2% w/w Polyvinyl alcohol (PVA) (97% hydrolyzed, M.W. 50,000 –

85,000 Da, Aldrich), 0.2% w/w Polyvinyl pyrrolidone (PVP) (M.W. 25,000 Da, Merck), 0.2% w/w Poly(methoxyaniline-5-sulfonic acid) (PMAS) (M.W. 8,000 – 12,000 Da, Nitto Chemical Industry), 0.2% w/w Allyl alcohol 1,2-butoxylate ethoxylate (AA12BE) (Aldrich), 0.2% w/w Benzalkonium chloride (BC) (M.W. 339.5 Da, Aldrich), 0.2% w/w Noxamium 0.15® (N0.15) (Aldrich), 0.2% w/w Didodecyldimethyl ammonium bromide (DDAB) (M.W. 462.64 Da, Aldrich), 0.2% w/w N-isopropylacrylamide 2-acrylamido-2-methyl-1-propanesulfonic acid (NIPPAm-AMPS) (90:10 NIPPAm:AMPS w/w, synthesized organically, University of Wollongong), 0.2% w/w Deoxyribose Nucleic Acid (DNA) (Salmon sperm, 300 – 600 base pairs), from Prof. N. Ogata (Sophia University, Japan). These mixtures were then sonicated for 2 hours. The resulting dispersions were filtered as described previously and RCNT/dispersant mats were obtained, Scheme-2.1.

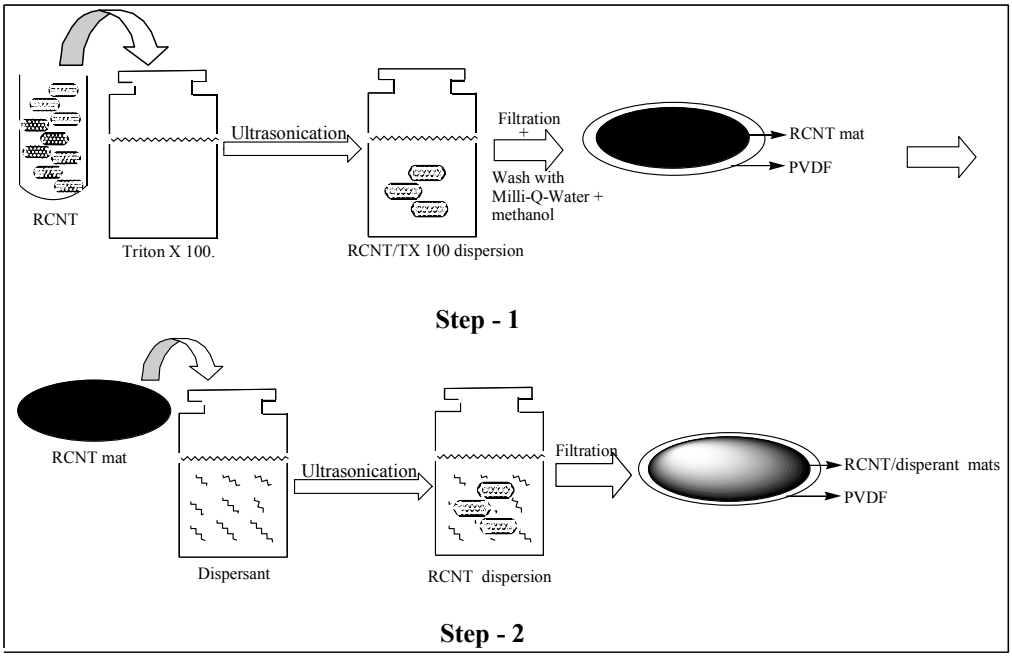

Scheme 2.1 Preparation of RCNT/dispersant mats.

2.2.1.1 Dispersant structures

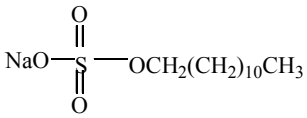

Sodium dodecyl sulfate (SDS)

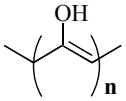

Polyvinyl alcohol (PVA)

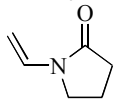

Polyvinyl pyrrolidone (PVP)

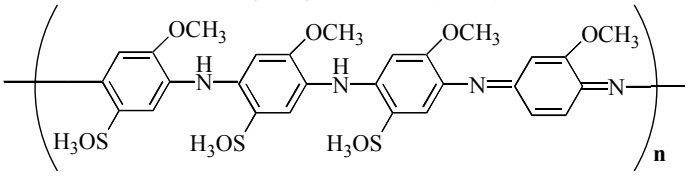

Poly(methoxyaniline-5-sulfonic acid) (PMAS)

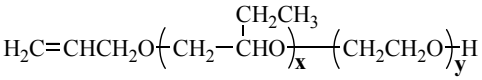

Allyl alcohol 1,2-butoxylate ethoxylate (AA12BE)

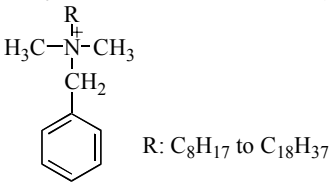

R: C_8H_{17} to $C_{18}H_{37}$

Benzalkonium chloride (BC)

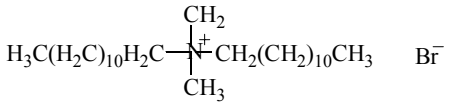

Didodecyldimethyl ammonium bromide (DDAB)

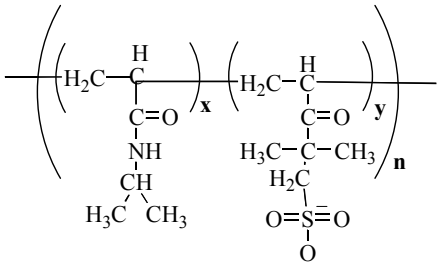

N-isopropylacrylamide 2-acrylamido-2-methyl-1-propanesulfonic acid (NIPPAm-AMPS)

*** m, n, x and y indicate the number of molecules**

2.2.2 Instrumentation

2.2.2.1 Characterization of RCNT dispersions

Cyclic voltammograms (CVs) were recorded for the different aqueous RCNT dispersions using MacLab/4e and a MacLab potentiostat. Silver/Silver-chloride (Ag/AgCl) electrode was used as the reference electrode and a Platinum (Pt)-mesh electrode as the auxiliary electrode. A Platinum (Pt), Glassy carbon (G.C.), or Gold (Au)-electrode were used separately as the working electrodes. The potential window for each CV recorded varied depending on the electrode used. In general, for the Pt-electrode the potential window applied was E = -0.8, +1.2 V, for glassy carbon electrode and Au-electrode E = -0.4, +1.2 V, the scan rate applied was 50 mV/s. CVs were recorded with and without the addition of 0.1 M $NaNO_3$.

A UV-1601, UV-Visible spectrophotometer (Shimadzu) was employed to record the UV-Vis spectra of the dispersions. The absorbance (Abs.) was recorded between 350 nm and 1100 nm for the different dispersions. In addition, a UV-Vis spectra was recorded for each of the different dispersions, using a constant wavelength of 600 nm, where the Abs was recorded every 15 min over a period of 48 hours.

A Malvern Zetasizer 3000 was used to measure the particle size and the zeta potential (surface charge) of the different dispersions.

2.2.2.2 Characterization of RCNT/dispersant mats

Four-point probe conductivity measurements were carried out using 2.5 X 0.5 cm strip of each mat. A digital micrometer was used to measure the thickness of the mats. A constant current of 1 mA was passed through the sample and the voltage was

recorded using a Hewlett Packard model 34401A multimeter and an EG & G Princeton Applied Research model 363 Potentiostat/Galvanostat.

CVs for the different RCNT/dispersant mats were recorded using a MacLabe/4e, in 0.01 M potassium ferrocyanide ($K_4Fe(CN)_6$) with a supporting electrolyte of 0.1 M sodium nitrate ($NaNO_3$), a potential window of E = -0.3, +0.6 V, and a scan rate of 50 mV/s, were applied. CVs were also recorded over a wide range of potentials in 0.1 M $NaNO_3$, E = -1, +1 V for the different RCNT/dispersant mats. The electrochemical cell consisted of RCNT/dispersant mats 2.5 X 0.5 cm strips (fully immersed) as the working electrode, Ag/AgCl as the reference electrode and Pt-mesh as the auxiliary electrode.

The capacitance for the different RCNT/dispersant mats was measured by recording CVs at different scan rates 50, 25, 10 and 5 mV/s. The potential window used was E = -0.1, +0.3 V, and current measurements were taken at E = +0.1 V. The electrochemical cell was as described above with the electrolyte used being 1 M $NaNO_3$.

The mechanical properties were measured for the thick RCNT/dispersant mats using Instron 4302. The samples were prepared for testing by cutting them into 2-3 mm wide strips with a razor blade. A load cell of 10 N was used and a crosshead speed of 1 mm/s was used to extend the samples.

AFM pictures of RCNT/dispersant mats were taken using a DI Joel 2000 Microscope Multimode. The pictures were taken using the tapping mode, and the channels outputs were height and friction.

Scanning electron microscopy (SEM) pictures were takes using a Hitachi S-900 FESEM.

2.3- RESULTS & DISCUSSION

2.3.1 RCNT dispersions characterization

Different concentrations of the dispersants were investigated, and the optimum concentration was determined to be 0.2% for all dispersants investigated. It was found that at concentrations higher than 0.2%, the CNT coagulated and were difficult to disperse even with ultrasonication.

2.3.1.1 Particle size and Zeta potential

The particle size distribution for the different dispersions was measured to determine which was a more effective dispersant for the RCNT. The photon-correlation spectroscopy, with the analysis algorithms was modified to compensate for the non-spherical nature of the carbon nanotube. Multi-exponential analysis mode was applied, where a number of size channels in this case 24 are used, and the correlation function is represented as a sum of discrete exponentials spaced logarithmically. The result of this analysis is a distribution of the 24 size classes on the X-axis, and the Y-axis gives the relative intensity of the light scattered by particles in each size class. However, carbon nanotubes *are* non-spherical in nature, therefore, the size measured is not absolute but indicative. The zeta potential (surface charge) for the dispersions was also measured. The zeta potential was measured for the dispersions at different pHs ranging from 1 to 9, the surface charge was negative in all cases which indicated that the pH had no effect on the zeta potential measurements in this case. Therefore, the following zeta potential measurements were carried out at a neutral p H ~ 7. Table -2.1 represents the results for dispersions prepared from two different batches

(**I** and **II**), and Table -2.2 represents the results for dispersions prepared using batch (**III**). We find that there are significant differences in particle sizes even when the same dispersant is used with RCNT from different batches (**I**, **II**, and **III**). However, when the same batch of RCNT is used the results are very similar. In addition, we notice that the particle size was very large in general; this could be due to the fact that RCNT tend to form aggregated ropes, which are much larger than a single RCNT. Size determination using light scattering techniques produces a scatter intensity that is directly proportional to the particle size ($I \alpha r^6$). Therefore, if a small percentage of the RCNT in the dispersion existed as large entangled ropes this would skew the observed particle size resulting in significantly higher values. Regarding the zeta potential, in all cases it was negative as expected, since the RCNT are negatively charged (209). In addition, when BC a cationic surfactant was used, the zeta potential was positive which also agrees with what was expected. However, BC was not used as a dispersant with Batch-**III** due to the fact that it did not disperse the RCNT sufficiently.

Table –2.1 Particle size and zeta potential for RCNT/dispersant mats prepared from batches **I** and **II**.

Dispersant	Batch-I		Batch-II	
	Particle size (nm ± 1)	Zeta potential (mV ± 0.1)	Particle size (nm ± 1)	Zeta potential (mV ± 0.1)
TX100	166	-31.1	148	-1.6
SDS	327	-47.5	328	-39.9
PVP	431	-2.7	197	-23.7
PVA	352	-4.5	112	-17.4
PMAS	860	-55.6	1352	-44.7
AA12BE	259	-33.1	617	-24.7
BC	421	22.2	---	---

Table –2.2 Particle size and zeta potential for RCNT/dispersant mats prepared from batch **III**.

Dispersant	Batch-IIIA		Batch-IIIB	
	Particle size (nm ± 1)	Zeta potential (mV ± 0.1)	Particle size (nm ± 1)	Zeta potential (mV ± 0.1)
TX100	257	-34.1	257	- 34.1
SDS	384	-39.2	325	-37.9
PVP	250	-22.0	270	-24.3
PVA	182	-14.4	147	-11.8
PMAS	157	-23.1	181	-27.4
AA12BE	173	-25.9	215	-21.6

2.3.1.2 Cyclic voltammetry

The CVs obtained for all the different RCNT dispersions investigated here exhibited similar characteristics. These CVs do not exhibit any oxidation/reduction peaks (Fig 2.1). When PMAS was used as a dispersant redox peaks were observed (Fig 2.2), and these correlate with the expected electrochemical behavior of PMAS (210 - 212). Indicating that the presence of the RCNT has no significant effect on the electrochemical behavior of PMAS. This is understandable since PMAS is in large excess.

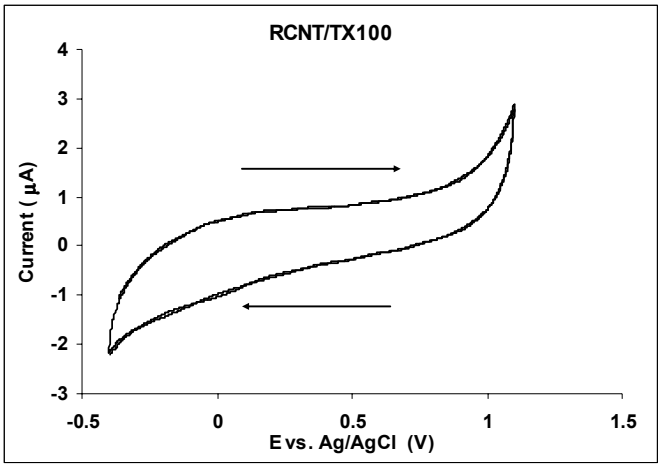

Fig 2.1 Cyclic voltammogram (2nd cycle) obtained using a glassy carbon electrode in RCNT/TX100 dispersion and 0.1 M $NaNO_3$ (supporting electrolyte) with a scan rate of 50 mV/s.

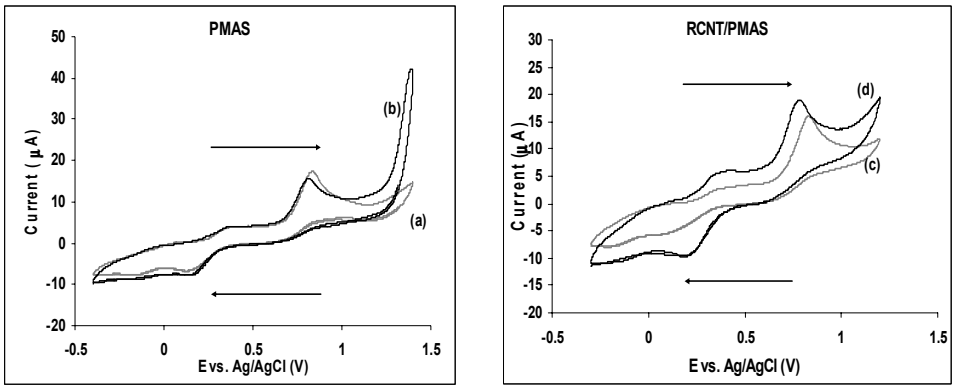

Fig 2.2 Cyclic voltammogram (2nd cycle) obtained using a glassy carbon electrode, and a scan rate of 50 mV/s. (a) PMAS, (b) PMAS with 0.1 M $NaNO_3$ added, (c) RCNT/PMAS dispersion, (d) RCNT/PMAS dispersion with 0.1 M $NaNO_3$ added.

2.3.1.3 Ultraviolet and Visible Absorption spectroscopy (UV-Vis spectra)

The Abs. for the different dispersions was recorded as a function of wavelength starting at 300 nm and finishing at 1100 nm. The absorption band for PMAS (pH 3.5 – 4) is expected to be between 330 and 425 nm, due to its yellow color (204). This band is broader in the UV-Vis spectra for RCNT/PMAS (Fig 2.3A), presumably as a result of π-π interactions between the RCNT and the fully conjugated PMAS backbone (204).

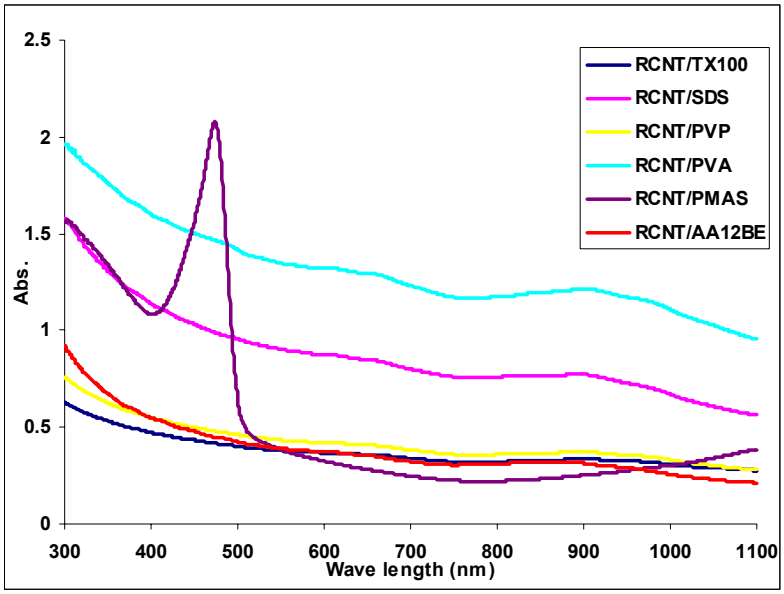

Fig 2.3A UV-Vis spectra of RCNT dispersions.

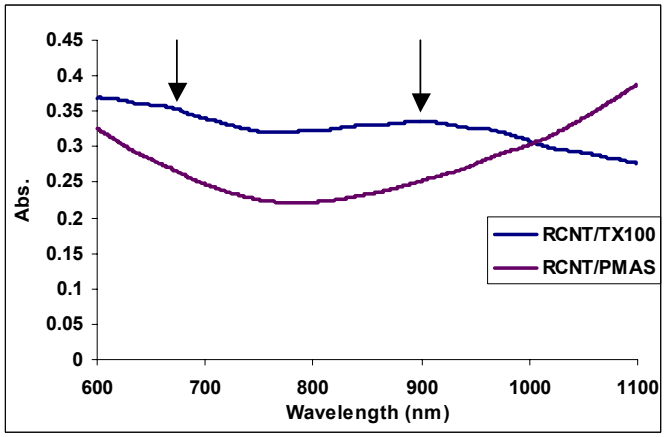

Fig 2.3B UV-Vis spectra of RCNT/TX100 and RCNT/PMAS between 600-1100nm.

Moreover, for RCNT dispersions with the exception of RCNT/PMAS dispersion, the broad peaks that are observed at ~ 650 and ~ 900 nm (Fig 2.3A) are characteristic of

the transition between the first pair of singularities in the density of state (DOS) of the metallic SWCNT (213, 214). The peak at 650 nm is assigned to the first Van Hove transition of metallic SWCNT, while the peak at 900 nm is due to the second Van Hove singularity. The Van Hove peaks are a sensitive function of RCNT diameters. Smaller diameter tubes exhibit Van Hove transitions at shorter wavelengths; the observed peaks are due to overlapping of Van Hove transition from all nanotubes sizes and chiral indices that are present (215, 216).

The spectra of RCNT/PMAS in this region is essentially featureless (Fig 2.3B), the loss of structure indicates that a significant electronic perturbation of the nanotubes and disruption of the extended π network has occurred due to the presence of the conducting polymer. This effect indicates covalent functionalization rather than simple adsorption to the nanotubes walls or ends (204).

In order to determine the stability of different RCNT dispersions, the light absorption characteristics were measured as a function of time, the Abs. for the different dispersions was recorded every 15 min over a period of 48-hours at λ = 600 nm (Fig 2.4). A wavelength of 600 nm was selected as it is directly related to the first Van Hove transition of carbon nanotubes and thus was clear of other interferences. RCNT/PMAS, RCNT/DDAB, and RCNT/DNA had a constant absorption throughout the 48-hours, which indicated that these dispersions are very stable over time. In general, the Abs. for all other dispersions started to decrease at 150 min, which indicated that the RCNT started to settle and/or coagulate. This was confirmed by the accompanying time lapse pictures (Fig 2.5 and 2.6).

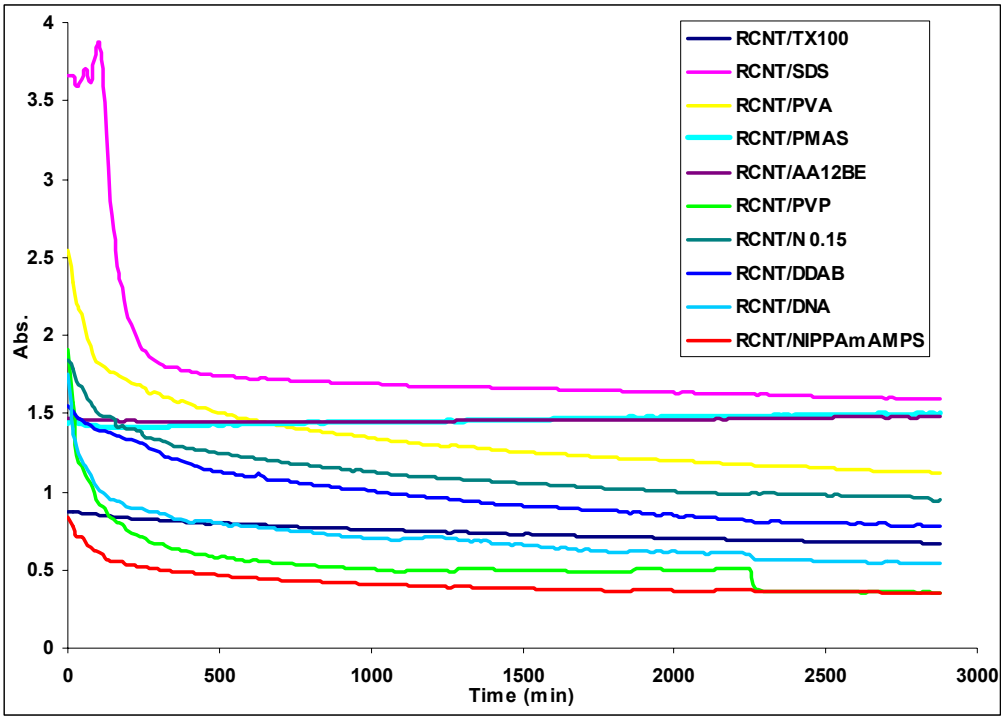

Fig 2.4 Abs. for different RCNT dispersions over a period of 48-hours at 600 nm.

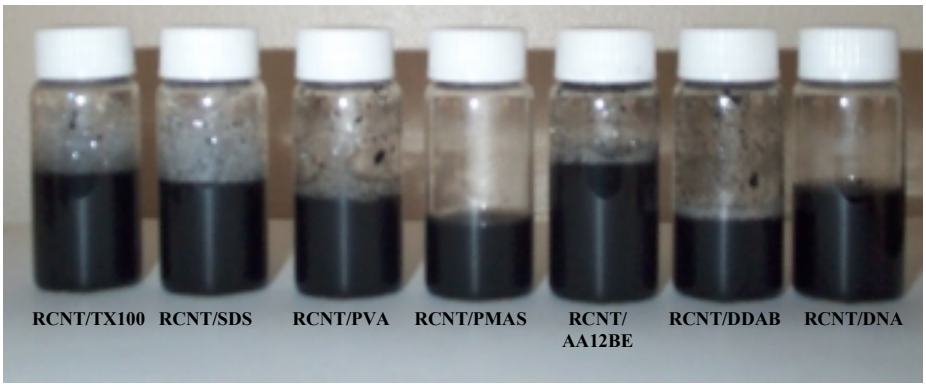

Fig 2.5 RCNT dispersions at t = 0.00 min.

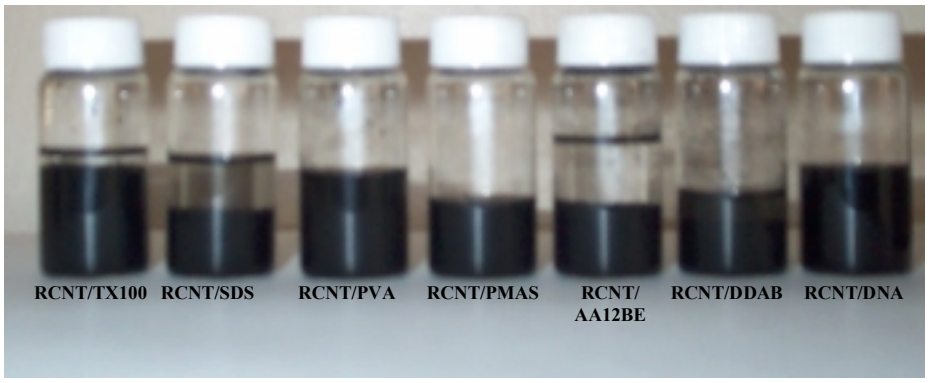

Fig 2.6 RCNT dispersions at t = 48 hours.

2.3.2 Characterization of RCNT/dispersant mats

PVDF membranes were weighed before and after the microfiltration of 50 mL of each of the different dispersions. The difference between the two weights is therefore the weight of the RCNT mat. In addition, the mats were prepared using 50 ml aliquot of the standard RCNT/TX100 dispersion; this aliquot contains 2.95 mg RCNT. The thick RCNT mats were prepared using four times the concentration. Where 200 ml aliquot of the standard RCNT/TX100 dispersion was used, this aliquot contains 11.8 mg RCNT. Therefore, the difference between the weight of the mat and the weight of the RCNT is the weight of the dispersant retained within the matrix of the RCNT mat, Tables 2.3 and 2.4.

Table –2.3 Weight of RCNT/dispersant mats prepared from batches **I** and **II**.

Dispersant	Batch-I		Batch-II	
	Weight of mat (mg ± 0.1)	Weight of dispersant (mg ± 0.01)	Weight of mat (mg ± 0.1)	Weight of dispersant (mg ± 0.01)
TX100	3.2	0.25	3.1	0.15
SDS	3.5	0.55	3.2	0.25
PVP	3.8	0.85	3.4	0.45
PVA	43.3	40.35	41.4	38.45
PMAS	15.2	12.25	14.1	11.15
AA12BE	31.2	28.25	29.8	26.85
N0.15	7.8	4.85	6.5	3.55

Table – 2.4 Weight of RCNT/dispersant mats prepared from batch **III**.

Dispersant	Batch-III					
	IIIA		IIB		III thick mats	
	Wight of IIIA mats (mg ± 0.1)	Wight of dispersant (mg ± 0.01)	Wight of IIB mats (mg ± 0.1)	Wight of dispersant (mg ± 0.01)	Wight of III thick mats (mg ± 0.1)	Wight of dispersant (mg ± 0.1)
TX100	5.6	2.65	5.6	2.65	15.2	3.4
SDS	4.7	1.75	4.9	1.95	17.9	6.1
PVP	4.5	1.55	5.1	2.15	22.9	11.1
PVA	17.4	14.45	19.6	16.65	62.1	50.3
PMAS	7.6	4.65	7.5	4.55	26.0	14.2
AA12BE	12.8	9.85	14.0	11.05	48.8	37.0
N0.15	9.4	6.45	11.2	8.25	31.3	19.5

Comparing the values in Table –2.3 and Table –2.4 we can see that the weight of the mats when using the same dispersant but different RCNT batches differs markedly, while when using RCNT from the same batch as in Table –2.4 the differences in the weight of the mats are much less significant. This shows that different batches of RCNT from the same manufacturer have different properties. In addition, there are significant differences between the weights of the different RCNT/dispersant mats prepared using the same RCNT batch. This is due to the fact that a certain amount of the dispersant used is retained in the mat. The chemical nature of the dispersant determines the types of chemical/physical interactions between the dispersant and the RCNT, ultimately affecting the RCNT uptake of the dispersant. The weight of the mat will also depend on the molecular weight of the dispersant, where a high molecular weight dispersant will result in high mat weight. Therefore, the weight of the mat will depend on the mass of the dispersant retained.

2.3.2.1 Conductivity

Theoretical calculations predict that some SWCNT are metallic while others are semi-conducting. Metallic materials usually have conductivities in the range of 100 S/cm. However, a metallic sample can have conductivity an order of magnitude or more less than a non-metallic sample. One reason for this is likely to be the existence of samples with good metallic conductivity only in a small fraction of their cross-sectional area, and so low overall conductivity, such as the case in SWCNT/dispersant mats (208). Mats are made of bundles of ropes of nanotube, electrical measurements indicate that SWCNT ropes are metallic, with a single rope resistivity lower than 10^{-4} Ωcm at room temperature (217), and 6 Ωcm for a mat

(218). However, we should also note that the effects of inter-tube interactions in a disordered rope are quite different from what is obtained for a crystalline rope (219). Therefore, it is difficult to determine the exact conductivity of SWCNT mats, but since the conductivity of an individual rope is approximate 10000 S/cm (208), the expected effective conductivity of the mats samples is expected to be more than an order of magnitude less than that for a rope.

The following equations were used to calculate the resistance and conductivity of the RCNT/dispersant mats; the results are presented in Tables –2.5, 2.6, and 2.7.

$R = \rho L / A$;

R = Resistance in Ω,

$R = V / I$

V= Voltage difference (mV), I = Current (mA).

L = Distance between the two inner electrodes in the four point probe measurement device = 0.2 cm.

A = Cross section area (cm^2)

A = T X W,

T = Thickness (cm), W = Width (cm) = 0.3 cm.

$\rho = 1 / \sigma$, σ = Conductivity ($1/\Omega$. cm) or (S/cm).

Table –2.5 Conductivity measurements for RCNT/dispersant mats prepared from batch **I** and **II.**

Dispersant	**Batch-I**		**Batch-II**	
	Thickness (μm ± 0.1)	**Conductivity (S/cm ± 0.1)**	**Thickness (μm ± 0.1)**	**Conductivity (S/cm ± 0.1)**
TX100	10.3	176.9	1.2	137.7
SDS	7.0	214.1	0.4	18.9
PVP	3.3	18.5	0.4	26.4
PVA	6.0	15.2	3.2	4.0×10^{-3}
PMAS	8.5	45.5	1.1	25.2
AA12BE	7.3	45.5	0.8	11.3
N0.15	8.2	61.2	4.2	45.3

Table –2.6 Conductivity measurements for RCNT/dispersant mats prepared from batch **III.**

Dispersant	**Batch-IIIA**		**Batch-IIIB**	
	Thickness (μm ± 0.1)	**Conductivity (S/cm ± 0.1)**	**Thickness (μm ± 0.1)**	**Conductivity (S/cm ± 0.1)**
TX100	19.0	97.0	19.0	97.0
SDS	14.0	109.8	6.3	100.3
PVP	8.0	108.1	9.7	105.6
PVA	11.0	3.3×10^{-3}	9.0	3×10^{-3}
PMAS	5.8	109.5	8.8	111.5
AA12BE	8.8	56.3	5.8	59.1
N0.15	10.9	80.3	9.7	77.3

Table –2.7 Conductivity measurements for thick RCNT/dispersant mats prepared from batch **III**.

Dispersant	**Batch-III Thick mats**	
	Thickness (μm ± 0.1)	**Conductivity (S/cm ± 0.1)**
TX100	41.5	159.1
SDS	33.5	176.0
PVP	26.5	181.0
PVA	22.7	1.5×10^{-5}
PMAS	19.8	307.0
AA12BE	26.0	65.7
N0.15	38.0	143.2

The SWCNT/dispersant mats consist of ropes of SWCNT, themselves containing strands of metallic and semi-conducting tubes loosely touching each other. This means that the conductivity of these mats is the result of a metallic on-tube conduction in series with an activated, hopping-like conduction of the contact regions (220, 221). If conduction requires either scattering or tunneling then the resistance can be very large (222). The value of the resistance maximum is related to the inter-tube coupling resistance between the involved tubes, the resistance was shown to be caused by direct tunneling between tubes (223).

The heterogeneous model, involving regions of antistrophic metallic conduction together with hopping or tunneling through small electrical barriers corresponding to defects of various types (224), seems appropriate for understanding conduction in the individual ropes separated by tangled regions, and also for mats of tangled ropes in

which inter-rope contact are likely to act as barriers (218, 225) this is applicable to the mats investigated in this study. The increase in the non-metallic terms in the mats relative to the single rope indicates that inter-rope contacts make a significant contribution to resistance in the mats, and the large hopping term for the rope within tangled regions suggests a large contribution from disordered semiconductor-like conduction in the tangled regions (221, 224).

Introduction of SWCNT to a semi-conjugated polymer (e.g. PMAS) to form a composite mat can result in increases of conductivity by up to ten orders of magnitude (206, 226, 227). The increase in conductivity as a result of CNT addition is characteristic of percolation; the first percolation threshold for these composites is approximately 8.5% mass fraction. This is mainly due to the introduction of conducting paths to the polymer. As the concentration of SWCNT increase the distance between the tubes becomes sufficiently small for the electrons to tunnel through the polymer or for physical contacts between the tubes to be formed (228 - 230). Therefore, the introduction of SWCNT to the polymer increases the conductivity, this has been observed in the current investigation with regard to RCNT/PMAS composite mat.

We find that there are significant and some large differences in terms of conductivity for mats prepared using the same dispersant but RCNT from different batches. On the other hand, mats prepared using the same dispersant and RCNT from the same batch (e.g. batch-**IIIA** and **IIIB**), have very similar conductivities. This indicated that dispersions or mats prepared from the same original material have similar properties. Which in turn is different to the properties of dispersions prepared from different starting material. We find that the average conductivity for the RCNT/TX100 is ~100

S/cm. In addition, we notice that RCNT/PMAS mat exhibits the highest conductivity due to the introduction of conducting paths to the polymer as discussed previously. The conductivity increased dramatically from ~ 0.01 S/cm for pure PMAS to ~307 S/cm for the RCNT/PMAS mat. In contrast RCNT/PVA mats where PVA is a non-conducting polymer always exhibited the lowest conductivity, in some cases the decrease in conductivity was four orders of magnitude less, compared to the conductivity of the other RCNT/dispersant mats. This indicated that the properties of the dispersant used affects the corresponding properties of the RCNT mat.

For the composite mats that were prepared using four times the concentration of the RCNT Table –2.7, we notice that the thickness of the mats in some cases (e.g. RCNT/TX100 mat) was only twice and not four times the thickness of the mats that were prepared using a quarter of the RCNT concentration Table –2.6. This could be due to the effect of the dispersant on the packing order of ropes with in the mats, and to the effect of the dispersant on the size of these ropes.

2.3.2.2 Cyclic voltammetry of RCNT/dispersant mats over a wide potential range in 0.01 M $K_4Fe(CN)_6$

Cyclic voltammetry is recognized as a standard method for the study of electrochemical behavior. It is a versatile electroanalytical technique for the study of electroactive species. The effectiveness of the cyclic voltammetry is due to the ability to rapidly observe the redox behavior of a species over a wide range of potentials. CVs can be used to study the electrochemical behavior of species diffusing to an electrode surface, interfacial phenomena at an electrode surface, and bulk properties of materials in or on the electrode.

All the CVs obtained for the different mats were similar to these observed for RCNT/TX100 (Fig 2.7). However, the CV for RCNT/PMAS exhibited very broad redox peaks (Fig 2.8). This indicates the large double layer capacity of the system (183). This could also indicate the slow electron exchange with the RCNT/PMAS mats. Previous studies of the cyclic voltammetry responses and capacitive behavior of SWCNT mats show broad redox responses in aqueous solutions that are probably due to the presence of oxygen-containing groups bound to the surface of the nanotubes or the impurities produced during nanotubes purification (231, 232). The CV for the RCNT/PVA mat exhibited significantly broad peaks due to the high resistivity of the composite (Fig 2.9). The CV for N0.15 (Fig 2.10), exhibited broad but more defined peaks, which could indicate a faster electron exchange of the redox species with the RCNT/N0.15 mat, this in turn could be due to the cationic nature of N0.15.

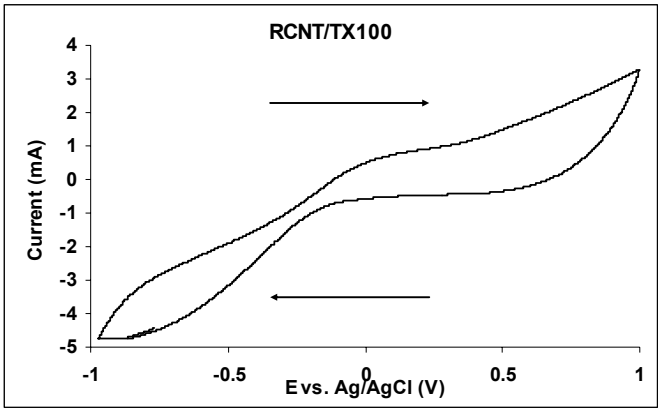

Fig 2.7 Cyclic voltammogram (2nd cycle) of RCNT/TX100 mat in 0.01 M $K_4Fe(CN)_6$ with 0.1 M $NaNO_3$ as a supporting electrolyte, E = -1, + 1 V, scan rate of 50 mV/s.

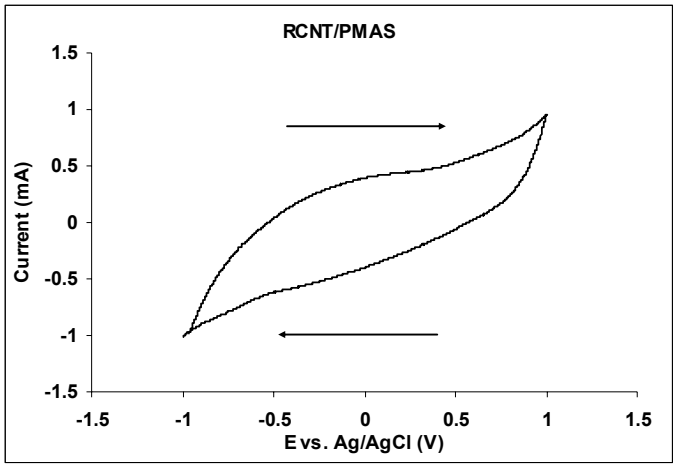

Fig 2.8 Cyclic voltammogram (2nd cycle) of RCNT/PMAS mat in 0.01 M $K_4Fe(CN)_6$ with 0.1 M $NaNO_3$ as a supporting electrolyte, E = -1, + 1 V, scan rate of 50 mV/s.

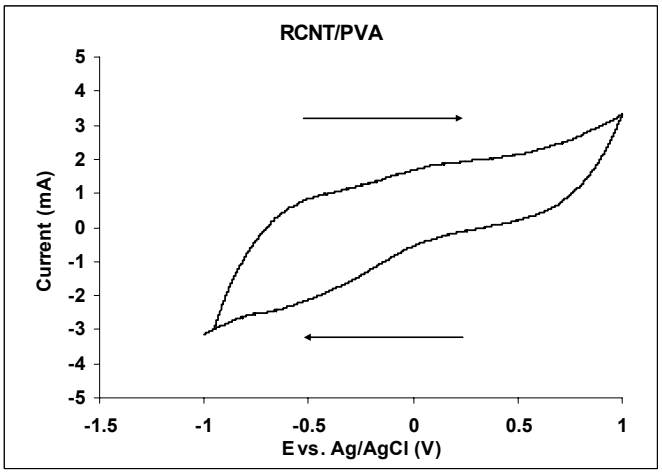

Fig 2.9 Cyclic voltammogram (2nd cycle) of RCNT/PVA mat in 0.01 M $K_4Fe(CN)_6$ with 0.1 M $NaNO_3$ as a supporting electrolyte, E = -1, + 1 V, scan rate of 50 mV/s.

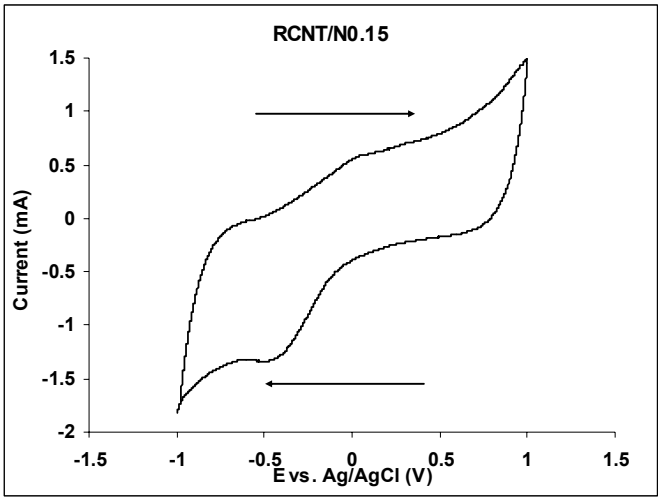

Fig 2.10 Cyclic voltammogram (2nd cycle) of RCNT/N0.15 mat in 0.01 M $K_4Fe(CN)_6$ with 0.1 M $NaNO_3$ as a supporting electrolyte, E = -1, + 1 V, scan rate of 50 mV/s.

2.3.2.3 Capacitance

CVs were recorded for the different mats using different scan rates. The difference between the oxidation and reduction current at E = 0.1 V (Fig 2.11), was plotted as a function of the scan rate (Fig 2.12), the best straight line was graphed and slope calculated. Capacitance = ½ slope (F), Specific Capacitance = Capacitance/weight (F/g). The results are presented in Tables 2.8, and 2.9.

Example calculation:

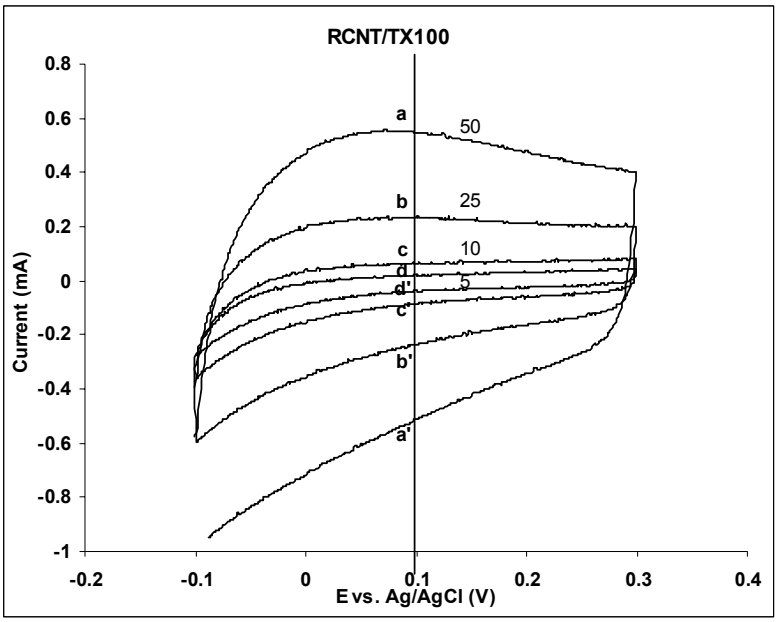

Fig 2.11 Cyclic voltammogram of RCNT/TX100 mat in 0.1 M $NaNO_3$, E = -0.1, + 0.3 V, scan rate of 50, 25, 10, and 5 mV/s.

Range = 1 mA, where 0.2 mA = 1.1 cm

The difference between the oxidation and reduction current at 0.1 V.

For scan rate of 50 mV/s → (a-a`) = 5.7 cm → 1.03 mA

For scan rate of 25 mV/s → (b-b`) = 2.6 cm → 0.472 mA

For scan rate of 10 mV/s → (c-c`) = 0.85 cm → 0.0154 mA

For scan rate of 5 mV/s → (d- d`) = 0.3 cm → 0.00545 mA

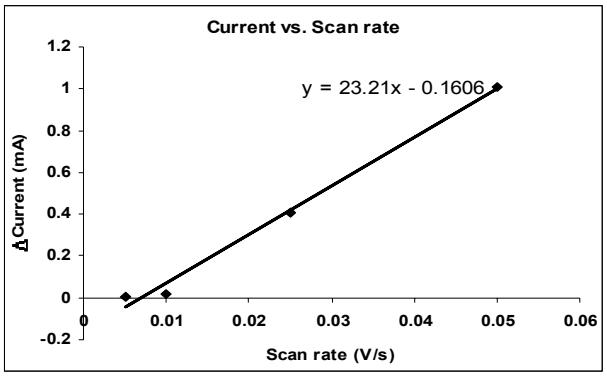

Fig 2.12 ΔCurrent vs. Scan rate.

Capacitance = slope / 2 = (23.2 / 2) = 11.6 F

The area of the mat that was submerged in the 1 M $NaNO_3$ = 0.7 cm^2

The weight of the mat = 5.6 mg. Therefore, the weight of 0.7 cm^2 = 0.29 mg

Specific capacitance = Capacitance / weight = (11.6 / 0.29) = 40.0 F/g

Table –2.8 Capacitance measurements for RCNT/dispersant mats prepared from batch **I** and **II**.

Dispersant	**Specific Capacitance (F/g ± 0.1)**	
	Batch-I	**Batch-II**
TX100	3.6	11.8
SDS	4.3	11.3
PVP	2.0	4.7
PVA	0.5	0.3
PMAS	22.7	23.2
AA12BE	5.0	13.2
N0.15	12.4	17.5

Table –2.9 Capacitance measurements for mat RCNT/dispersant prepared from batch **III**.

Dispersant	**Specific Capacitance (F/g ± 0.1)**		
	Batch-IIIA	**Batch-IIIB**	**Batch-III Thick mats**
TX100	40.0	40.0	37.0
SDS	37.1	35.4	32.8
PVP	13.4	12.9	24.0
PVA	2.0	2.9	0.02
PMAS	25.5	27.5	28.5
AA12BE	7.6	10.1	10.4
N0.15	16.2	14.3	14.5

There are big differences between the capacitance of the different RCNT/dispersant mats that were prepared from different starting material. However, when looking at RCNT/dispersant mats prepared using the same batch (e.g. batches-**IIIA** and **IIIB**), the capacitance measurements are very similar. This provides further evidence to the fact that the dispersions or mats prepared form the same original material have similar properties, which are at the same time different from the properties of the dispersions or mats that were prepared using different starting materials. In addition, regardless of the starting material RCNT/PVA exhibited the lowest capacitance value. This agrees with the CV and conductivity measurements obtained for this composite mat. The capacity for RCNT/TX100 mats ~39 F/g is lower than the reported values of 104 F/g (233). However, we should keep in mind that this value was measured for aligned SWCNT and that the electrolyte used was H_2SO_4.

2.3.2.4 Atomic Force Microscopy (AFM)

AFM pictures of the different RCNT/dispersant mats were taken to see if there were any differences in the RCNT alignments, lengths or bundles that might have resulted from the use of different dispersants (Fig 2.13).

a)

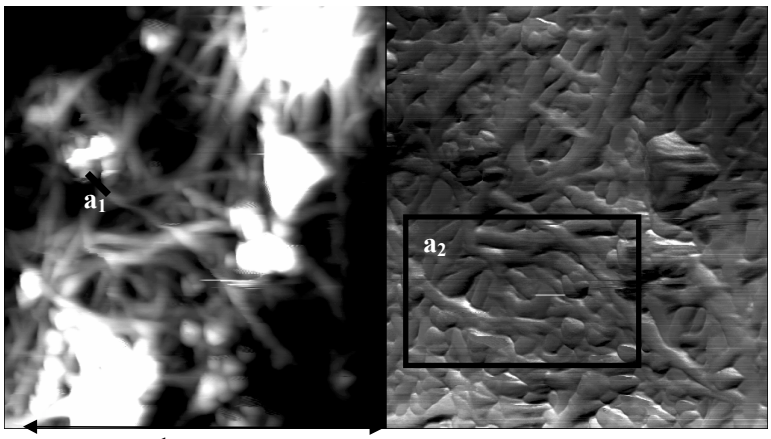

b)

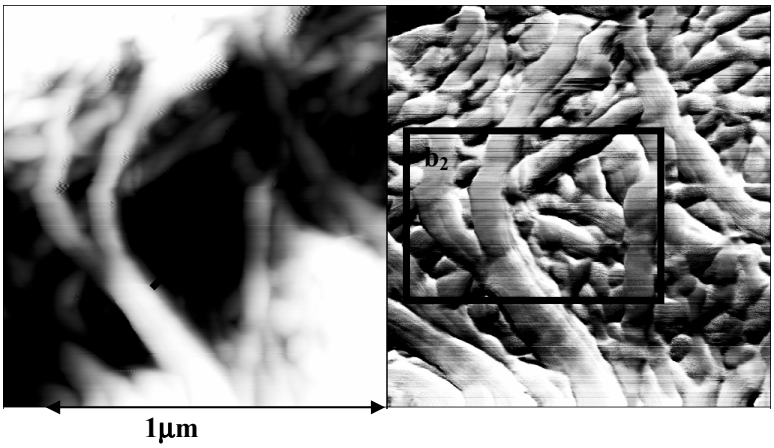

c)

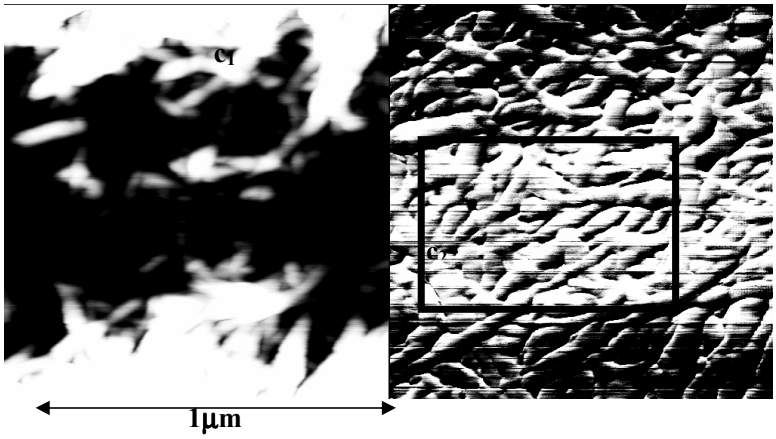

Fig 2.13 AFM pictures of a) RCNT/TX100, b) RCNT/PMAS, and c) RCNT/PVP mats. The images on the left are height data; the images on the right are friction data.

We can see that the ropes in RCNT/TX100 (a_1) are much smaller in diameter than that for RCNT/PMAS (b_1). In addition, in the RCNT/TX100 mat the ropes seem to be more entangled and entwined with each other (a_2). The presence of different dispersants seems to affect the packing order of ropes in the mats, in RCNT/PVP mat; the ropes seem to be more entwined and smaller (c_2). On the other hand, in the RCNT/PMAS mats, the ropes are more entangled, bulkier and longer (b_2). This means that different dispersants affect the packing order of the RCNT ropes within the matrix of the mats, which in turn will affect the mechanical properties of these mats. However, that does not affect the chemical and electrochemical properties of the different mats. It was not possible to obtain pictures of RCNT/PVA and RCNT/AA12BE mat due to the fact that these mats had a very adhesive surface that resulted in the AFM tip becoming stuck to the mat.

2.3.2.5 Mechanical properties

The mechanical properties were measured for batch-**III** Thick mats, a load cell of 10 N was used, and a crosshead speed of 1mm/s was used to extend the sample. From the recorded measurements Force (N) was plotted against Extension (m), and Stress (σ) (MPa) was plotted against strain (ε).

Stress (MPa) = F(N) / W(m) X T (m)

Strain = Extension(m)/Gauge length(m)

From the plot of Stress vs. Strain (Fig 2.14), we can obtain σ_{Break} (MPa), and ε_{Break}, where σ_{Break} is the stress value, and ε_{Break} is the corresponding strain at the breaking point. Also, from the slope of the curve we can calculate Young's modulus Y (GPa). As can be seen in the stress-strain curves (Fig 2.14), the samples exhibit brittle behavior with a slight dectility at high stress-strain values. This is presumably due to the creep/slippage of the ropes within the matrix of the mat near the break point.

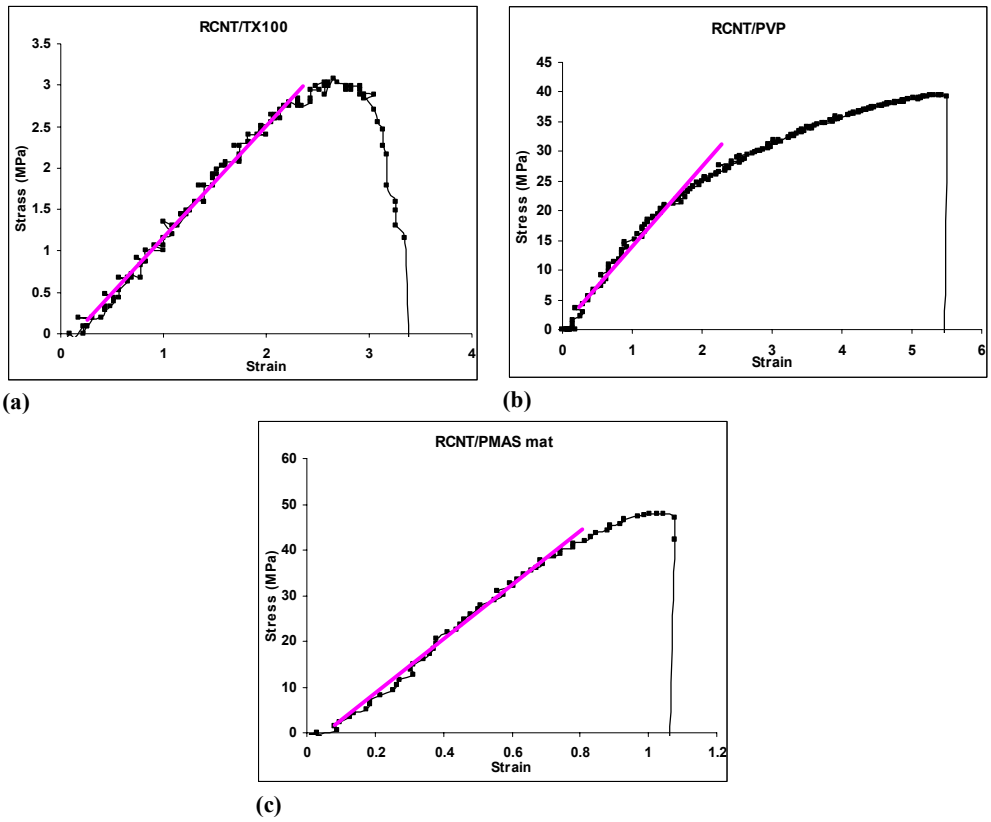

Fig 2.14 Stress-Strain curves of a) RCNT/TX100, b) RCNT/PVP, and c) RCNT/PMAS mats.

When looking at our results in Table –2.10, there are many factors to consider. First, the RCNT/dispersant mats that were used in these measurements were not annealed. Also, these mats consist of bundles of combined non-aligned ropes, which means that the Young's modulus value will be very small, as discussed in **Ch. 1**, section **1.1.5**. In addition, the value for the cross sectional area used when calculating the stress values is not the real area, since we are using a mesh of ropes and not a single rope. This also means that there are pockets of air within the mesh. Finally, the stress values obtained are more probably due to shear stress than to tension stress. Young's

modulus for the RCNT/PMAS mat was 6.4 GPa, this is a very high value especially where conducting polymers are concerned. Also, for RCNT/PVP mat, the Young's modulus was 2.1 GPa that is also higher than that for conducting polymers.

Table –2.10 Mechanical properties for thick RCNT/dispersant mats prepared from batch **III**.

Dispersant	**σ_{Break} (MPa ± 0.1)**	**ε_{Break} ± 0.1**	**Y (GPa ± 0.1)**
TX100	3.0	3.0	0.2
SDS	Weak	Weak	Weak
PVP	39.1	5.5	2.1
PVA	Weak	Weak	Weak
PMAS	47.0	1.0	6.4

2.3.3 RCNT/functional-dispersants mats characterization

Functional dispersants are discussed separately because each of these has a function other than dispersing the RCNT. The functional dispersants used were DNA a biological molecule, NIPPAm-AMPS a temperature sensitive polyelectrolyte, and DDAB an organic compound that can be polymerized in addition to being cationic. PVDF membranes were weighed before and after the microfiltration of 50 mL of each of the different dispersions. The difference between the two weights is therefore the weight of the RCNT/Functional-dispersant mat Table –2.11.

Table –2.11 Weight of RCNT/functional-dispersants mats.

Dispersant	Weight of mats (mg ± 0.1)
DNA	21.7
DDAB	8.9
NIPPAm-AMPS	4.2

There are differences between the weights of the different mats prepared. This is due to the fact that a certain amount of the dispersant used is retained in the mat. Therefore, the weight of the mat also depends on the mass of the dispersant retained, as discussed in section **2.3.2**.

2.3.3.1 Conductivity

The conductivity was calculated as described earlier section **2.3.2.1**, and the results are presented in Table –2.12.

Table –2.12 Conductivity for RCNT/functional-dispersants mats.

Dispersant	Thickness (μm ± 0.1)	Conductivity (S/cm ± 0.1)
DNA	17.0	2.4
DDAB	18.3	31.5
NIPPAm-AMPS	10.5	71.4

Following the discussion in section **2.3.2.1**, we find that in general the conductivity of the RCNT/functional-dispersant mats is lower than that for the other RCNT/dispersant mats (Table –5, 6, and 7). This could be due to the different

physical/chemical interaction between the functional-dispersants molecules and the RCNT.

2.3.3.2 Cyclic voltammetry for RCNT/functional-dispersant mats over a wide potential range in 0.01 M $K_4Fe(CN)_6$

The CV for RCNT/DDAB, and RCNT/NIPPAm-AMPS mats were similar (Fig 2.15, and Fig 2.16). The broad peaks are attributed to the high surface area of the mats. In addition, the CV for the RCNT/DNA mat exhibited broad but more defined peaks (Fig 2.17). This could indicate the slow electron exchange with the mats. Also, it could be due to the presence of oxygen-containing groups bound to the surface of the nanotubes (231, 232).

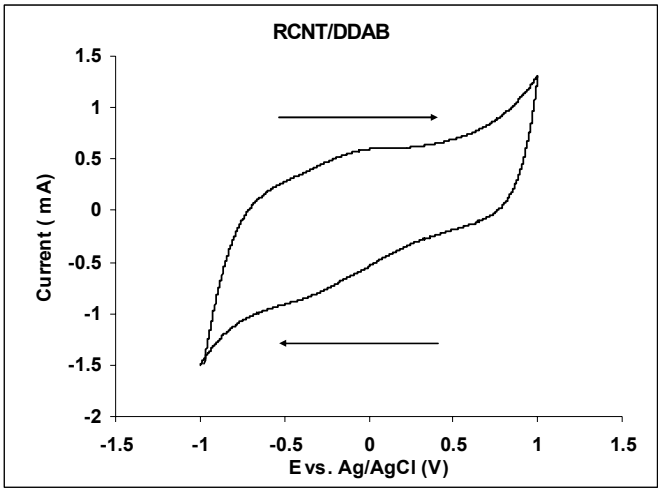

Fig 2.15 Cyclic voltammogram (2nd cycle) of RCNT/DDAB mat in 0.01 M $K_4Fe(CN)_6$ with 0.1 M $NaNO_3$ as a supporting electrolyte, E = -1, + 1 V, scan rate of 50 mV/s.

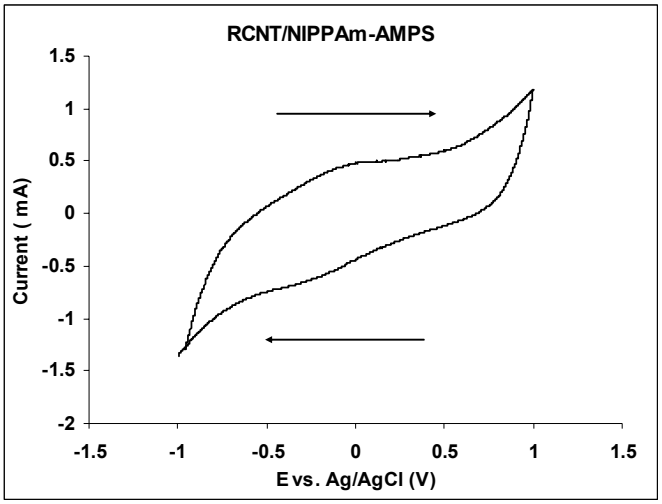

Fig 2.16 Cyclic voltammogram (2nd cycle) of RCNT/NIPPAm-AMPS mat in 0.01 M $K_4Fe(CN)_6$ with 0.1 M $NaNO_3$ as a supporting electrolyte, E = -1, + 1 V, scan rate of 50 mV/s.

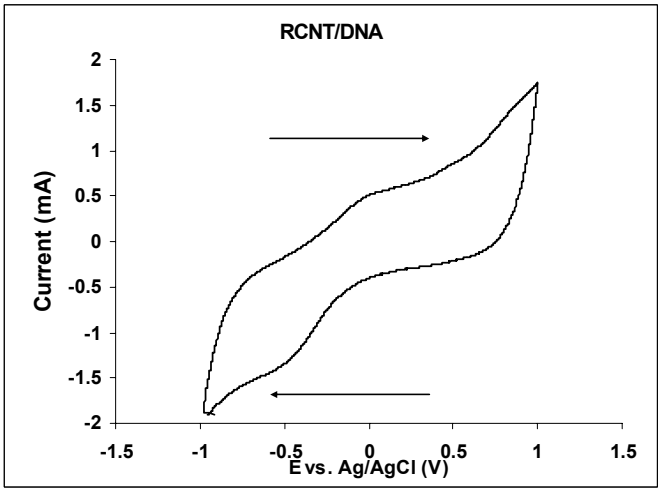

Fig 2.17 Cyclic voltammogram (2nd cycle) of RCNT/DNA mat in 0.01 M $K_4Fe(CN)_6$ with 0.1 M $NaNO_3$ as a supporting electrolyte, E = -1, + 1 V, scan rate of 50 mV/s.

2.3.3.3 Capacitance

Cyclic voltammograms were recorded for the different RCNT/functional-dispersant mats using different scan rates. The difference between the oxidation and reduction current at E = 0.1 V was plotted as a function of the scan rate, the best straight line was graphed and slope calculated. Capacitance = ½ slope (F), Specific Capacitance = Capacitance/weight (F/g). An example of the capacitance calculations is presented section **2.3.2.3**. The capacitance values determined are presented in Table –2.13.

Table –2.13 Capacitance for RCNT/functional-dispersant mats.

Dispersant	**Capacitance (F/g ± 0.1)**
DNA	4.9
DDAB	14.0
NIPPAm-AMPS	28.9

RCNT/DNA had the lowest capacitance; this is due to the fact that the DNA coverage of the RCNT is extensive (as can be seen in the AFM pictures), thus eliminating the capacitance attributed to the RCNT. On the other hand, the RCNT/NIPPAm-AMPS mat had the highest capacitance. This could be due to the fact that NIPPAm-AMPS is a polyelectrolyte, thus contributing significantly to the charge storage ability of the RCNT mat.

2.3.3.4 Atomic Force Microscopy (AFM)

AFM pictures of the RCNT/functional-dispersant mats were obtained to see if there were any differences in the RCNT alignments, lengths or bundles that might have resulted from the use of different dispersants (Fig 2.18).

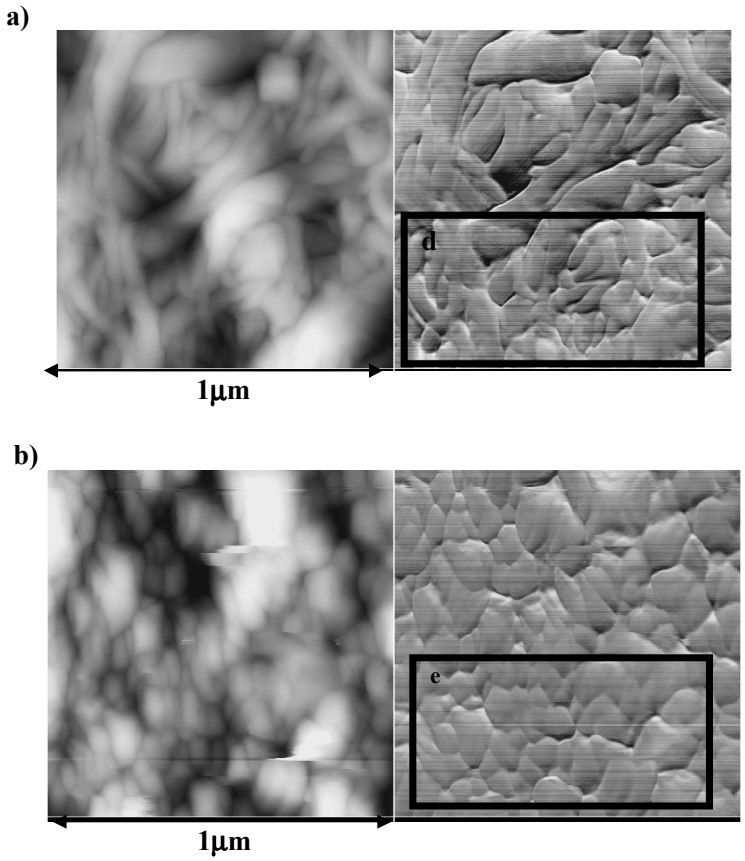

Fig 2.18 AFM pictures of a) RCNT/NIPPAm-AMPS mat, and b) RCNT/DDAB mat. The left image is height data and the right image is friction data.

We can see that the bundles of ropes in the RCNT/functional-dispersant mats seem to be bigger, bulkier, and more entwined (d) compared to RCNT/TX100 (Fig 2.18, a_2). This indicated that either the number of RCNT in the ropes or the extent of the coverage of these ropes in the RCNT/functional-dispersant mats is larger than that in the RCNT/dispersant mats. In addition, in the AFM picture of the RCNT/DDAB mat, we observe that the ropes of RCNT are barely visible where the coverage by the dispersant is comprehensive. One reason could be due to ability of this dispersant to

undergo polymerization, indicating that there could be π-interactions between the dispersant and the surface of the RCNT. Another reason could be the very adhesive nature of the polymer, since it is in the form of a highly viscous liquid.

2.3.3.5 Scanning Electron Microscopy (SEM)

It was not possible to obtain AFM pictures of the RCNT/DNA mat. This mat was very rough, due to the very high DNA uptake by the RCNT. Therefore, SEMs were obtained (Fig 2.19). We find that the RCNT are highly entangled into a complex network. In addition, since the uptake by the RCNT of the DNA is very high, and no DNA clusters can be seen in the picture, we assume that the RCNT are nearly 100% covered by the DNA.

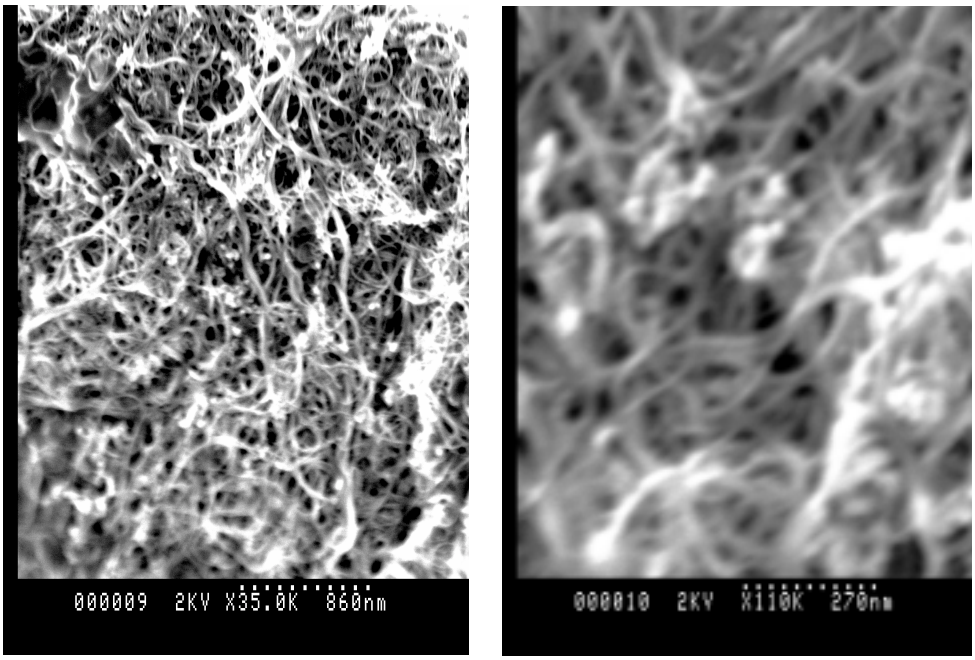

Fig 2.19 SEM of RCNT/DNA mat.

2.4- CONCLUSIONS

A range of RCNT/dispersant dispersions and mats, have been prepared. The electrochemistry of the RCNT dispersions was studied and was found to be similar regardless of the dispersant used. This indicates that the RCNT had the dominant effect while the dispersant had the minor effect with regard to electrochemistry.

Using particle size analysis, it was found that some dispersing solutions are more effective in dispersing the RCNT than others. TX100, SDS, AA12BE, and DDAB were better dispersants than PVP, PVA, PMAS, N0.15, DNA, and NIPPAm-AMPS, while BC was very poor in its ability to disperse the RCNT. However, a dispersing solution that provides a stable dispersion of RCNT is not necessarily an effective solution for dispersing the RCNT, and vice versa. For example, AA12BE is a very good dispersant for the RCNT but is not stable over long periods of time. Zeta potential measurements confirmed that the RCNT are negatively charged.

Using UV-Vis spectra, the absorption band due to the yellow color of PMAS was observed for the RCNT/PMAS dispersion between 329 and 410 nm. This band was broader than the traditional PMAS band presumably as a result of the π-π interactions between the RCNT and the fully conjugated PMAS backbone. In addition, all the RCNT dispersions with the exception of RCNT/PMAS dispersion, exhibited broad bands at 650 and 900 nm, these bands are characteristic of the transmission between the first pair of singularities in the density of state of the metallic RCNT. The absence of these bands in the RCNT/PMAS dispersion indicates that a significant electronic

perturbation of the nanotubes and disruption of the extended π-network has occurred due to the presence pf PMAS. This effect indicates covalent functionalization other than simple adsorption to the nanotubes walls and ends. Stability of the RCNT dispersions was also investigated using UV-Vis, and it was determined that some dispersions are more stable than others depending on the chemical nature of the dispersing solution.

The weight of the RCNT/dispersant mats was found to depend on the molecular weight and the chemical nature of the dispersant. The CVs of the RCNT/dispersant mats did not exhibit defined redox peaks, except when PMAS (an inherently conducting polymer was used as the dispersant. However, the RCNT/dispersant mats exhibited a highly capacitive behavior indicating that they are composites with high charge storage capabilities. The average conductivity for the RCNT/TX100 was determined to be ~100 S/cm. RCNT/PMAS mat exhibits the highest conductivity due to the introduction of conducting paths. The conductivity increased dramatically from ~ 0.01 S/cm for pure PMAS to ~307 S/cm for the RCNT/PMAS mat. In contrast RCNT/PVA mats, where PVA is a non-conducting polymer always exhibited the lowest conductivity, up to four orders of magnitude less compared to the conductivity of the other RCNT/dispersant mats. This indicates that the conductivity and capacitance of the RCNT mats are affected significantly by the nature of the dispersant used.

Using AFM we can see that the coverage of the RCNT by the dispersant varies in thickness. This is due to the chemical nature of the dispersants and the way they chemically/physically interact with the RCNT. This in turn is reflected in the mechanical properties of the RCNT/dispersant mats as can be seen in the results obtained for the Young's modulus. For example, the Young's modulus for the RCNT/PMAS mat was 6.4 GPa which is a very high value especially where conducting polymers are concerned. Also, for RCNT/PVP mat, the Young's modulus was 2.1 GPa which is also higher than that for conducting polymers.

For the RCNT/functional dispersant composites, we find that the RCNT/DNA has the highest mass, the RCNT/N0.15 has the highest conductivity, and the RCNT/NIPPAm-AMPS has the highest capacitance. From this we conclude that the effect of the different functional-dispersants on the RCNT is different depending on the chemistry of the dispersant.

CHAPTER THREE

PREPARATION AND CHARACTERIZATION OF DISPERSIONS AND MATS OF HIPCO CARBON NANOTUBES/DISPERSANT COMPOSITES

3.1- INTRODUCTION

A high pressure CO disproportionation (HiPco) process, has been shown recently to produce nanotubes of high purity, yielding > 90 % atomic percent SWCNT (234). In this process, $Fe(CO)_5$ is injected into a stream of CO gas at high temperature and pressure. The iron forms metal clusters that act as catalytic sites to promote the Boudard reaction: $CO + CO \rightarrow C_{(s)} + CO_{2(g)}$. When the metal clusters achieve a size close to C_{60} they nucleate and grow SWCNT. This occurs as the SWCNT is a more stable form of carbon than a near spherical carbon overcoat of a metal cluster when diameters are larger than 1 nm (234). The SWCNT will continue to grow until the metal cluster, which is also growing with the addition of residual free iron atoms, reaches a size that favors formation of a carbon shell around the cluster. This ends the growth of the SWCNT. The dominant impurity in HiPco nanotubes (HCNT) is the metal catalyst, which is encased in the thin carbon shells and distributed throughout the samples as 3-5 nm size particles. Four to five atomic percent of Fe is typical in current raw HiPco materials (234, 235).

Carbon nanotubes have been incorporated in conventional polymer films to improve the mechanical/electrical properties of the polymers (236). Bandyopadhyaya *et al*

have dispersed HCNT in an aqueous solution of Arabic gum. Due to the apparent physical adsorption of the polymer, a stable dispersion of full-length, well-separated, individual tubes was achieved in one step (237).

Different research groups have prepared a range of SWCNT/polymer composites such as SWCNT/Polyurethane acrylate (238, 239), SWCNT/Polypropylene (240), and SWCNT/Poly(3-octylthiophene) (241).

The spontaneous re-dispersion of the dried carbon nanotubes powder in aqueous solutions of polymers, and the stability of high concentration dispersions are signatures of steric stabilization (242). In this mechanism, entropic repulsion among polymeric chains is utilized for stabilization of colloids. In good solvent conditions polymer chains tend to avoid each other so as not to constrain the conformational space available to each of them. In addition, it was found that the polymer coated nanotubes experience a repulsive force that contributes to the stability of the dispersions. Therefore, the nanotubes are sufficiently isolated and unable to re-aggregate. The results also indicate that during the stirring period, the polymer preferentially interacts with nanotubes while residual amphorous carbon (impurities) precipitate to form sediments at the bottom of the solution (243).

SWCNT/polyethylene dioxythiophene was prepared by Woo *et al* (244). It was found that there was an electronic interaction between the SWCNT and the host polymeric material. This electronic interaction originated from the hole trapping nature of SWCNT in a hole-conducting polymer due to the structural or chemical defects in the conjugated polymer chain. The charge traps in a polymeric material are generated by organic dopants. Therefore, in the case of the SWCNT/conjugated polymer composites the injected holes are initially trapped by the SWCNT.

In this chapter the preparation of aqueous HiPco carbon nanotubes (HCNT) dispersions and mats have been investigated. The dispersions were characterized using Atomic Force Microscopy, HCNT/Poly(vinyl pyrrolidone) dispersion exhibited alignment of the HCNT and was further investigated using Raman spectroscopy. UV-Vis spectrophotometry was then recorded for the different dispersions to evaluate their stability over time. These dispersions were then filtered to produce HCNT/dispersant mats. The mats were characterized to determine their suitability for actuation or sensor applications. The characterization of these composites were carried out using a variety of techniques such as, cyclic voltammetry, capacitance, Atomic Force Microscopy (AFM), and Scanning Electron Microscopy (SEM). Conductivity, Young's modulus, and the actuation behavior for the different HCNT/dispersant mats were also measured.

3.2- EXPERIMENTAL

3.2.1 Preparation of HCNT dispersions and mats

The HiPco single-walled carbon nanotubes (average tube diameter of 1.1 nm) were purchased from Carbon Nanotechnologies Incorporated (CNI) as a solid powder.

25 mg of HCNT were added to 50 ml of the following solutions, 1% w/w Triton X 100® (TX100) (<3% w/v polyethylene glycol, Aldrich), 0.2% w/w Sodium dodecyl sulfate (SDS) (M.W. 288.37 Da, Aldrich), 0.2% w/w Polyvinyl pyrrolidone (PVP) (M.W. 25,000 Da, Merck), 0.2% w/w Poly(methoxyaniline-5-sulfonic acid) (PMAS) (M.W. 8,000 – 12,000 Da, Nitto Chemical Industry), 0.2% w/w Allyl alcohol 1,2-butoxylate ethoxylate (AA12BE) (Aldrich), 0.2% w/w Noxamium 0.15® (N0.15)

(Aldrich), 0.2% w/w Didodecyldimethyl ammonium bromide (DDAB) (M.W. 462.64 Da, Aldrich), 0.2% w/w N-isopropylacrylamide 2-acrylamido-2-methyl-1-propanesulfonic acid (NIPPAm-AMPS) (90:10 NIPPAm:AMPS w/w, synthesized organically, University of Wollongong), 0.2% w/w Deoxyribose Nucleic Acid (DNA) (Salmon sperm, 300 – 600 base pairs), from Prof. N. Ogata (Sophia University, Japan). When DNA was used, to disperse the HCNT the solution was heated to 91 °C in order to break the DNA into single strands. These mixtures where then sonicated for 1-hour, and the HCNT dispersions were obtained. The dispersions were then filtered using a stirred filtration cell (model 8050 purchased from Amicon/Millipore) under nitrogen pressure of 400 KPa. Polyvinylidene fluoride (PVDF) membranes with pore size of 0.22 μm were used as filters. The PVDF membranes were wetted for 30 min in 50:50 v/v ethanol to Milli-Q-Water prior to use. This resulted in HCNT/dispersant mats.

3.2.2 Instrumentation and procedures

3.2.2.1 Characterization of HCNT dispersions

Atomic Force Microscopy pictures of HCNT dispersions were taken at Trinity University, Dublin, Ireland. The samples were sonicated for 15 min, and then subsequently allowed to settle for 30 min. Using a pipette several drops were placed on a clean glass substrate, which was then allowed to dry in an oven at 30 °C.

Raman scattering was recorded using an FT Raman Brüker RSF 100, at 632 nm excitation in the backscattering configuration. The sample was rotated to change the orientation of the bundles relative to the excitation light polarization.

UV-1601 Shimadzu UV-Visible spectrophotometer was used to record the UV-Vis spectra of the dispersions, and to monitor the absorbance at constant wavelength of 600 nm. The absorbance (Abs.) was recorded every 15 min over a period of 48 hours.

3.2.2.2 Characterization of HCNT/dispersant mats

Four point probe conductivity measurements were carried out using a 2.5 X 0.5 cm strip of the HCNT mats. A digital micrometer was used to measure the thickness of the HCNT strips. A constant current of 1 mA was passed through the sample and the voltage was recorded using a Hewlett Packard model 34401A multimeter and EG & G Princeton Applied Research model 363 Potentiostat/Galvanostat.

Cyclic voltammograms were recorded using a MacLab/4e in a solution containing 0.01 M $K_4Fe(CN)_6$ and 0.1 M $NaNO_3$ as a supporting electrolyte, with E = -0.3, +0.6 V. In addition, cyclic voltammograms were also recorded over a wide potential range of E = -1, +1 V for the different HCNT mats in 0.1 M $NaNO_3$. The experimental cell consisted of a 2.5 X 0.5 cm strips (fully immersed) of the HCNT/dispersant mats as the working electrode, Ag/AgCl as the reference electrode and Pt-mesh as the auxiliary electrode.

The capacitance for the different HCNT/dispersant mats were measured by recording cyclic voltammograms at scan rates of 50, 25, 10 and 5 mV/s using 1 M $NaNO_3$. The potential window used was E = -0.1, +0.3 V, and current measurements were taken at E = +0.1 V. The electrochemical cell was as described above.

The mechanical properties for the HCNT/dispersant mats were measured using 2.5 X 0.5 cm strips of the HCNT mats. These strips were placed between two stainless steel

clamps; the clamps were then mounted in an Instron 4302. A load cell of 10 N was used and a crosshead speed of 1 mm/s was used to extend the samples.

The actuation behavior of the HCNT/dispersant mats was recorded using the following techniques and instruments. The samples were prepared for testing by cutting them into 0.25 X 1.2 cm wide strips with a razor blade. Actuation studies were carried out with a single platinum electrode connected to the top of the HCNT strip and isolated from the stainless steel clamps by plastic adhesive tape. The clamp and the sample layout are shown in (Fig 3.1), the sample was then suspended from the arm of the analytical balance, with the lower clamp held captive by a fixed frame so that with the removal of the adjustable weights, the sample was loaded in tension. A linear variable distance transducer (LVDT) probe, was mounted atop the arm of the analytical balance, and the expansion/contraction of the sample was detected by the LVDT. The electrochemical cell consisted of 1 M $NaNO_3$ as the electrolyte, the HCNT mat strips (through the clamps) as the working electrode, a Pt-mesh electrode as the auxiliary electrode and an Ag/AgCl as the reference electrode. The electrodes and the LVDT were connected to a CV27 Voltammograph and a MacLab/4e. The potential window applied was E = -1, +0.5 V and the loads were increased by 2 g starting from 2 g. The overall layout of the analytical balance is shown in (Fig 3.2).

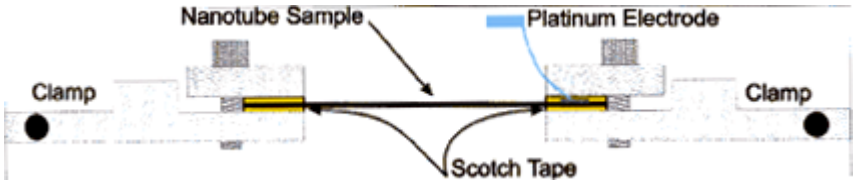

Fig 3.1 Clamp and sample layout (245).

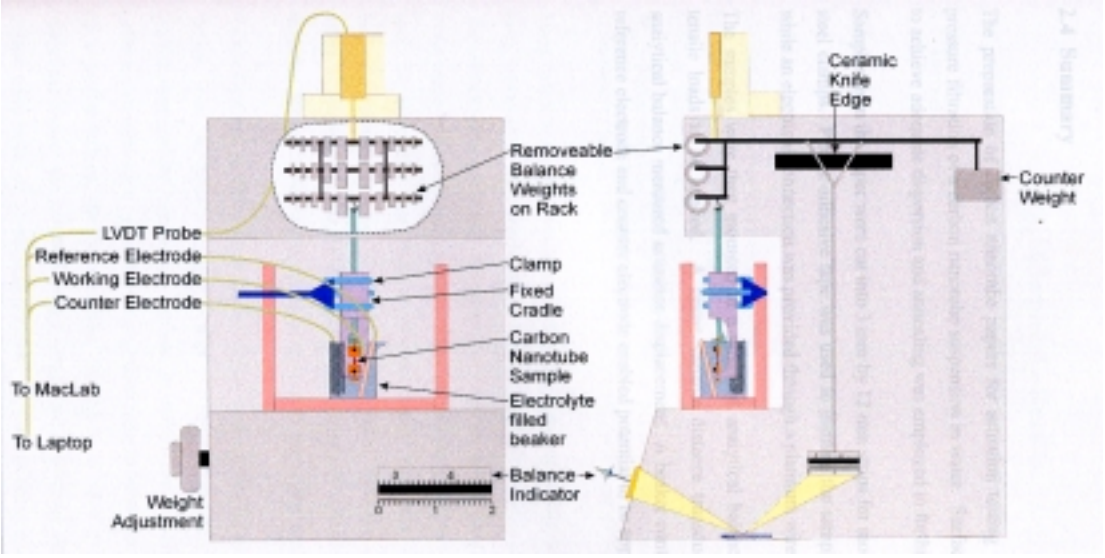

Fig 3.2 The analytical balance converted for actuation testing (245).

AFM pictures of HCNT/dispersant mats were taken using a DI Joel 2000 Microscope Multimode. The pictures were acquired using the tapping mode, and the channel outputs were height, amplitude, and friction.

Scanning electron microscopy (SEM) pictures were taken using a Hitachi S-900 FESEM.

3.3- RESULTS & DISCUSSION

3.3.1 Characterization of HCNT dispersions

3.3.1.1 Ultraviolet and visible Absorption spectroscopy (UV-Vis spectra)

In general, SWCNT exhibit long wavelength Van Hove features, the Van Hove features are discussed in **Ch. 2**, section **2.3.1.3**. SWCNT exhibit two broad peaks at 650 and 900 nm, these peaks are assigned to the transition between the first pair of singularities in the Density Of State (DOS) of the metallic SWCNT (246). The wavelengths for the Van Hove features decrease in an acidic environment and increase in a basic environment. This is attributed to the effect of protonation of SWCNT when exposed to acidic environment, where most of the available electrons (those responsible for the van Hove features) interact strongly with the adsorbed protons (234). In addition, other researchers observed peaks at 490 nm and 550 nm (247, 248).

UV-Vis spectra of the different dispersions was recorded between 350 nm and 1100 nm. However, the spectra for the dispersions displayed a very high level of noise such that no useful information could be obtained. In order to determine the stability of different HCNT dispersions, the absorption was measured as a function of time. A constant wavelength of 600 nm was selected as it is directly related to the first Van Hove transition of carbon nanotubes and thus was clear of other interferences. The Abs. was recorded every 15 min over a period of 48-hours (Fig 3.3).

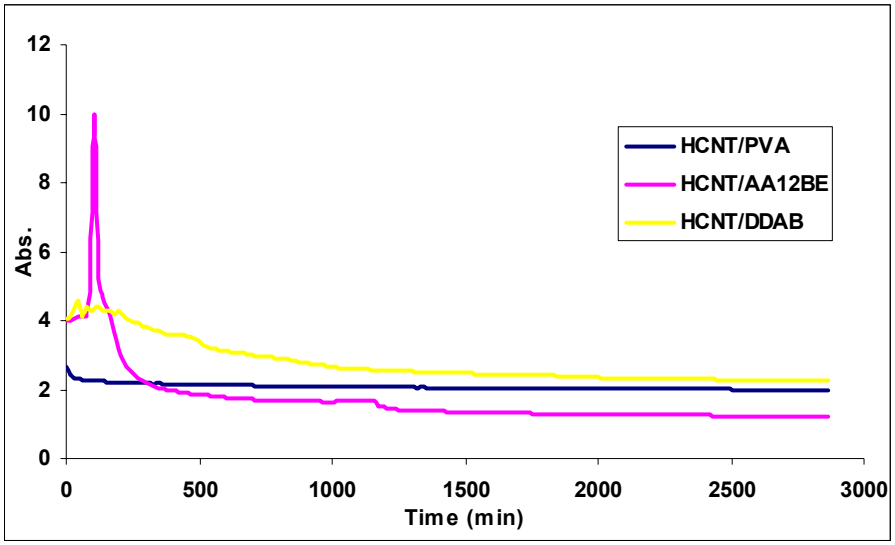

Fig 3.3 Abs. of HCNT dispersion over a 48-hour period at a constant wavelength of 600 nm.

Figure 3.3 displays the UV-Vis spectra of HCNT/PVA, HCNT/DDAB, and HCNT/AA12BE. In general, the Abs. for the different dispersions started to decrease at 250 min, which indicated that the HCNT started to settle and/or coagulate. The spectra for the other dispersion exhibited a high level of noise, and hence no useful information could be obtained from these spectra.

Photographs were taken over the period of one week in order to estimate the stability of the different dispersions over time. The first picture was taken at time t = 0 hour, and the second picture was taken at time t = 168 hours (one week) (Fig 3.4, and Fig 3.5). From these pictures we find that for HCNT/PVP, HCNT/SDS, and HCNT/DNA dispersions the HCNT nearly settled completely at the bottom of the vials. In the case of HCNT/TX100, and HCNT/DDAB dispersions, most of the HCNT settled at the bottom of the vial. However, a small amount of the HCNT remained suspended in the

solution. The HCNT in HCNT/AA12BE dispersion continued to be completely dispersed in the solution. This indicates that the latter solution is the most stable over time.

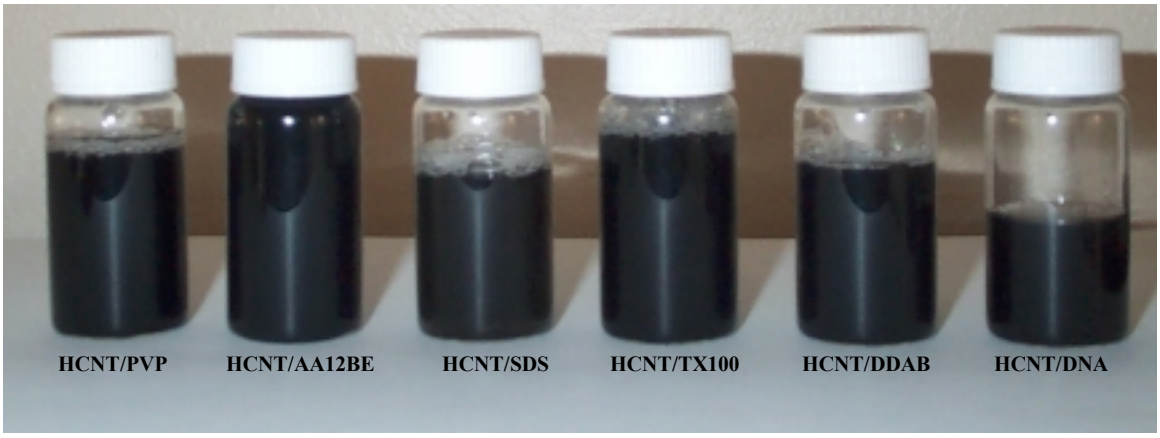

Fig 3.4 HCNT dispersions at t = 0 hour.

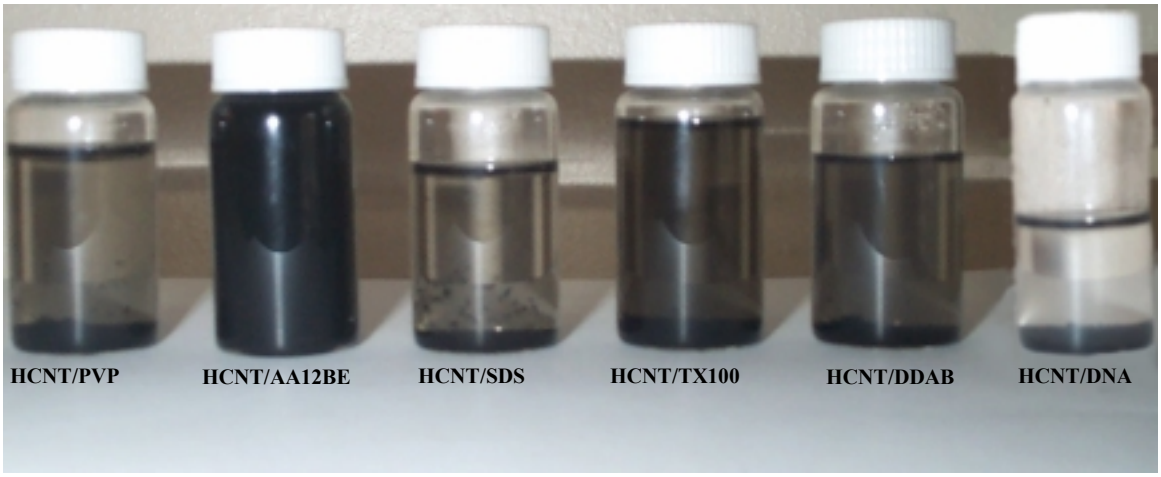

Fig 3.5 HCNT dispersions at t = 168 hours (one week).

3.3.1.2 Atomic Force Microscopy (AFM)*

AFM pictures of the different HCNT dispersions were obtained. The AFM pictures of HCNT/PVP dispersion clearly show super-alignment of bundles of the HCNT (Fig 3.6). Our investigation also showed that we find areas with a high concentration of

* Work carried in collaboration with M. in Het Panhuis at Trinity University, Dublin, Ireland.

the HCNT (land area) and areas with no HCNT (sea area) (Fig 3.7). What is observed in this AFM picture is a land area; the sea area does not contain any tubes at all. Investigations of the different factors involved indicate that the PVP polymer in the HCNT/PVP dispersion plays an important role in the alignment of the HCNT. Therefore, this seems to be a templated self-assembly, and it only occurs with the HCNT. This templated-self assembly is not observed in the RCNT, possibly due to the fact that HCNT are relatively short compared to the RCNT (249).

Fig 3.6 AFM picture of HCNT/PVP dispersion dried on glass slides, domain > 15 X 15 μm^2 (249).

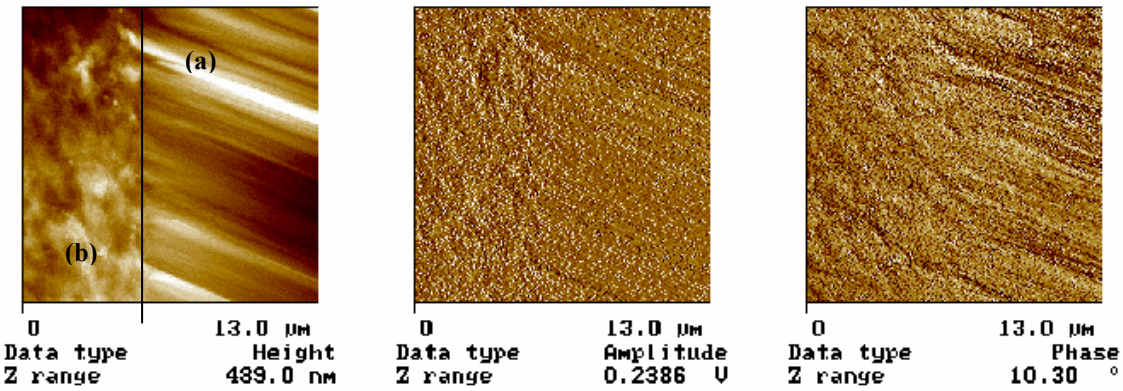

Fig 3.7 Cross-sectional AFM picture of HCNT/PVP dispersion dried on glass slide, domain > 15 X 15 μm^2. (a) Land area, aligned HCNT, (b) Sea area, no HCNT (249).

On the other hand, the AFM pictures of the other HCNT dispersions show spaghetti like tube arrangement of tubes, with no alignment. This can be seen in (Fig 3.8), which is an AFM picture of HCNT/DDAB dispersion.

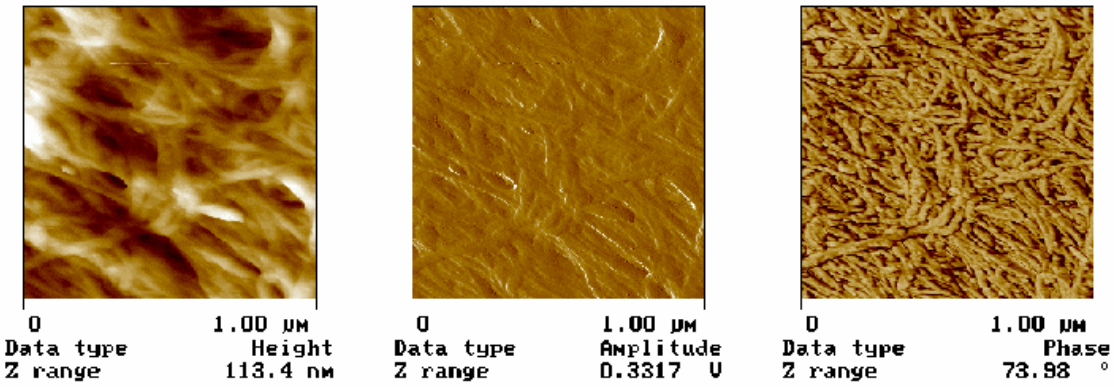

Fig 3.8 AFM picture of HCNT/DDAB dispersion dried on glass slide, domain > 15 X 15 μm^2. No alignment is observed (249).

3.3.1.3 Raman spectroscopy*

Yaudasaka *et al* investigated the change in diameter of HCNT due to heat treatment using Raman spectroscopy (250). Also, hybrid systems of semi-conjugated organic polymers and single-walled carbon nanotubes have been characterized using Raman spectroscopy by Dalton *et al* (251).

There are two frequency ranges in the Raman spectra, a low energy range between 150-200 cm^{-1}, and a high energy band between 1500-1650 cm^{-1}. The lower energy range contains the radial breathing mode (RBM), this mode is a purely radial vibration with all atoms moving perpendicularly to the length of the tube. The Radial breathing mode is used to determine the diameter of the tubes probed by a particular

* Work carried in collaboration with M. in Het Panhuis at Trinity University, Dublin, Ireland.

excitation frequency λ. The high-energy range contains the modes associated with the graphite like structure characteristic of SWCNT. This range is termed as the tangential displacement mode (TDM), and it is the range where the **G** (Graphite) and the **D** (Disorder) modes are identified. There are various combinations resulting from these modes, and the intensities of both modes depend upon the excitation frequency λ (252 - 254).

Satio *et al* calculated in a classical model the intensity of the Raman lines for a single nanotube in several configurations of polarization as a function of the angle between the nanotube axis and the laser light polarization α_l (255). Gomman *et al* and Hwang *et al* showed that the VV (vertical/vertical, same polarization for incident and scattered light) intensity of all Raman modes decrease continuously when the angle between nanotube axis and light polarization α_l increases (256, 257).

The optical absorption spectra of carbon nanotubes has been calculated by Ajiki *et al* (258), their calculations show that optical absorption exhibits strong resonance peaks when the light polarization is parallel to the tube's axis, while the resonance peaks are all depressed for light polarization perpendicular to the tube's axis (258). They argued that these resonance peaks disappear completely for perpendicular light polarization because of the strong depolarization effect. Yu *et al* obtained experimental results confirming these calculations (259).

Here we have examined the HCNT/PVP dispersion using Raman spectroscopy, to confirm the super-alignment of the HCNT observed in the AFM pictures. Taking the above discussion into consideration, we assumed that by using a $\alpha_l = 0°$, and then 90°, we should obtain a very high peak resulting when one angle is used due to

alignment, and a very low peak when the other angle is used. The Raman spectroscopy of the HCNT/PVP dispersion is shown in (Fig 3.9), from this figure we can see that the RBM interaction of the HCNT with the PVP matrix is obvious. The TDM of the Raman spectra for the two different angles of light polarization $\alpha_l = 0°$, and 90° are shown in (Fig 3.10). When comparing the height of the resonance peaks at $\alpha_l = 0°$ to the height of the resonance peak at $\alpha_l = 90°$, we find that the percentage is 96 : 4 respectively. This means that 96% of the HCNT are aligned, which would confirm the super alignment observed previously (249).

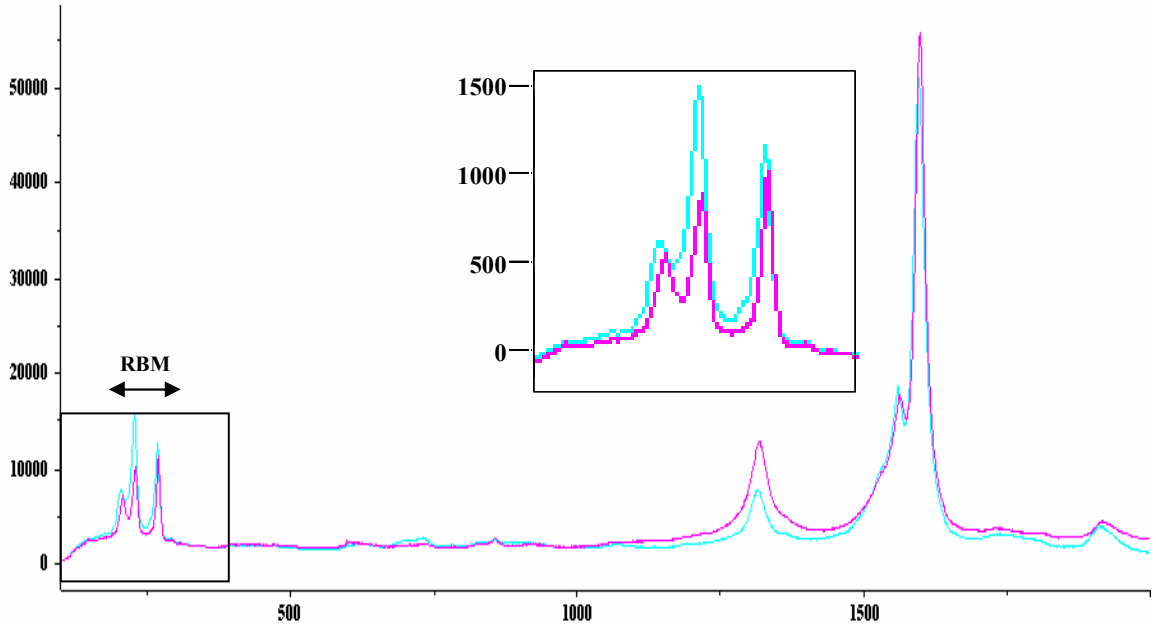

Fig 3.9 Raman spectroscopy of HCNT/PVP, at $\lambda = 633$ nm (249).

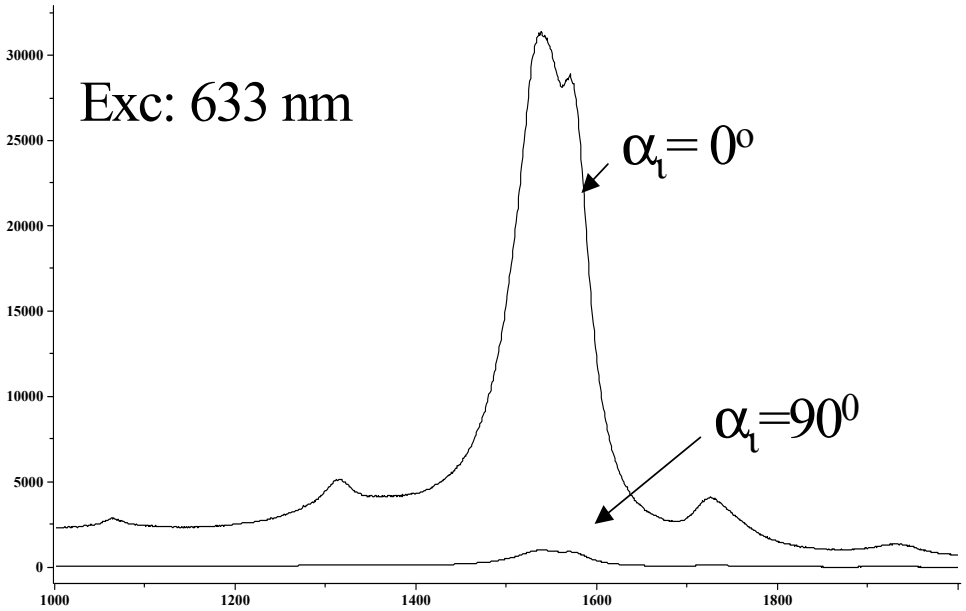

Fig 3.10 Raman spectroscopy of HCNT/PVP at λ = 633 nm (249).

3.3.2 Characterization of HCNT/dispersant mats

25 mg of HCNT were added to the different dispersant solutions to produce the dispersions, which were then filtered to produce the HCNT/dispersant mats. The HCNT mats were weighed after they were peeled off the PVDF membranes and dried Table –3.1. This weight is the weight of the dispersant that was incorporated into the mats in addition to the 25 mg of HCNT. Therefore, weight of dispersant incorporated into the HCNT = (weight of HCNT – 25 mg). From Table –3.1, we notice the HCNT uptake of the different dispersant is different, presumably depending on the chemical nature of the dispersant as discussed in **Ch. 2**, section **2.3.2**.

Table –3.1 Weight of the different HCNT/dispersant mats.

Dispersant	Weight of mat (mg ± 0.1)	Dispersant Weight (mg ± 0.1)
TX100	29.0	4.0
SDS	52.5	27.5
PVP	70.1	41.1
PMAS	46.4	21.4
DDAB	65.5	40.5
AA12BE	81.8	56.8
DNA	59.1	34.1

3.3.2.1 Conductivity

The equations used to calculate the resistance and conductivity are discussed in **Ch. 2**, section **2.3.2.1**. The results are presented in Table –3.2.

Table –3.2 Conductivity of HCNT/dispersant mats.

Dispersant	Thickness (μm ± 0.1)	Conductivity (S/cm ± 0.1)
TX100	40.9	11.7
SDS	35.3	137.5
PVP	70.0	44.2
PMAS	33.6	15.9
DDAB	61.0	8.2
AA12BE	70.0	7.4
DNA	69.6	24.4

The conductivity in SWCNT mats was described as the passage of electrons between nanotubes that are in contact with each other where there is no need to overcome the internal resistance (240). It was also found that conduction current is limited to the few nanotubes in the bundle that exist at the surface and which are in direct contact with the electrodes (260). In addition, investigations of the electrical transport properties of metallic SWCNT containing defects showed that the defects lead to an increase in resistance, inducing strong barriers for electron transport (85). One assumption is that by using a four-point probe method to measure the conductivity of the HCNT mats, we are creating defects in the HCNT that exist at the surface and which are in direct contact with the four electrodes. Changes in the transport properties of the SWCNT have been predicted in terms of change in the carbon-carbon bonds. However, to produce these changes mechanical stress has to be applied within the atomic structure of the HCNT, where the electronic properties of the nanotube change locally at the deformation point. Therefore, our conductivity measurements are not affected by any local deformation of the carbon bonds in the nanotubes (84).

The SWCNT/polymer or SWCNT/surfactant mats consists of bundles of ropes of SWCNT, themselves containing strands of metallic and semi-conducting nanotubes loosely touching each other. Consequently the conductivity is the result of a metallic on-tube conduction in series with an activated, hopping-like conduction of the contact regions (88, 89). Other factors that might affect the conductivity measurements are, scattering or tunneling (90). This conduction mechanism is described by the heterogeneous model (91). This model seems appropriate for understanding conduction in the individual ropes separated by tangled regions such as polymer or

surfactant materials, and also for mats of tangled ropes in which inter-rope contact are likely to act as barriers (92).

From the results in the table above, we find that the conductivity of the HCNT mats is within the range of the results reported previously in the literature. In general we find that the conductivity values of the HCNT mats are lower than those for RCNT mats. This may be due to the different impurities that result from the two different production methods (139, 140, 234, 235).

The HCNT/PMAS mat had a higher conductivity ~ 15.9 S/cm than that for HCNT/TX100 mat ~ 11.7 S/cm. This was expected since the combination of a conducting material such as PMAS with the HCNT will enhance the conductivity of both the PMAS and the HCNT (88, 89). However, the conductivity of the HCNT/PMAS mat was lower than that for HCNT/SDS mat, which exhibited the highest conductivity ~ 137.5 S/cm, and lower than the conductivity of HCNT/DNA mat ~ 24.4 S/cm. This indicated that the electrical properties of the HCNT are affected to a significant degree by the chemical nature of the dispersant used, and its ability to align the carbon nanotubes. The introduction of the dispersant increases the distance between the nanotubes and therefore, the interactions between the nanotubes decrease, which by the above reasoning will lead to a decrease in the conductivity of the mat. This can be observed for HCNT/DDAB and HCNT/AA12BE, where a significant amount of DDAB and AA12BE was incorporated within the mats (Table –3.1), we find that the conductivity decreased. On the other hand, a smaller amount of SDS was incorporated within the HCNT mat, and this resulted in an increased conductivity of the mat. However, it should be noted that the same concentration of

the different dispersants was used to disperse the HCNT. Indicating that the amount retained within the mat is dependent on the chemical nature of the dispersant.

3.3.2.2 Cyclic voltammograms of HCNT/dispersant mats over a wide potential range in 0.01 M $K_4Fe(CN)_6$

In general the HCNT CVs over a wide range of potentials in 0.01 M $K_4Fe(CN)_6$ exhibited broad redox peaks. The HCNT/TX100 CV (Fig 3.11), was significantly different from that of RCNT/TX100 (**Ch. 2**, Fig 2.7) under the same conditions. This is due to the presence of different impurities in the CNT materials, as a result of the two different production methods (139, 140, 234, 235). The CVs obtained using HCNT/TX100, HCNT/AA12BE, and HCNT/DDAB CVs (Figs 3.11, 3.12, and 3.13) were similar. In addition, we find that the electrochemical response of these mats is highly capacitive in nature, with HCNT/DDAB exhibiting the biggest difference between the oxidation and reduction currents. When considering the CV obtained using HCNT/SDS mat, more defined redox peaks were observed with an oxidation peak (a) at E ~ 0.65 V and a reduction peak (b) at E ~ 0.25 V (Fig 3.14). This response is consistent with the high conductivity values for the HCNT/SDS mat. On the other hand, the redox responses for the HCNT/DNA mat were very broad and undefined (Fig 3.15), indicating that the HCNT/DNA mat is resistive in nature. This indicated that the redox responses are attributed to the dispersant and not the HCNT.

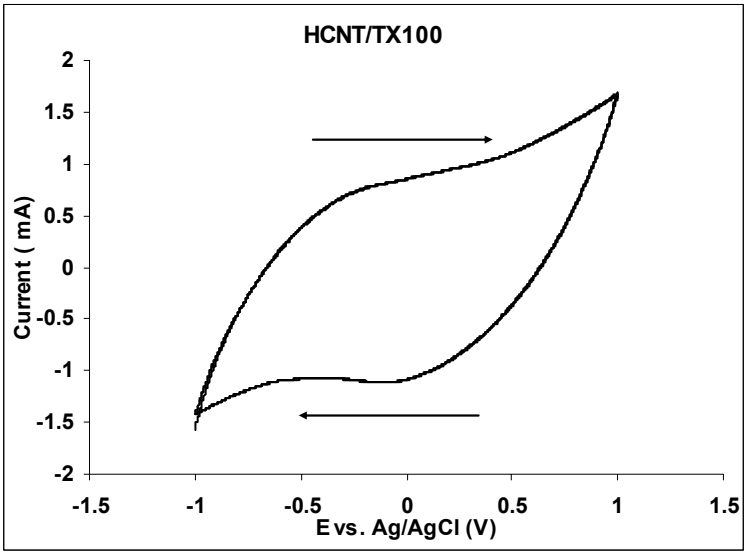

Fig 3.11 Cyclic voltammogram (2nd cycle) of HCNT/TX100 mat in 0.01 M $K_4Fe(CN)_6$ with 0.1 M $NaNO_3$ as a supporting electrolyte, E = -1, + 1 V, scan rate of 50 mV/s.

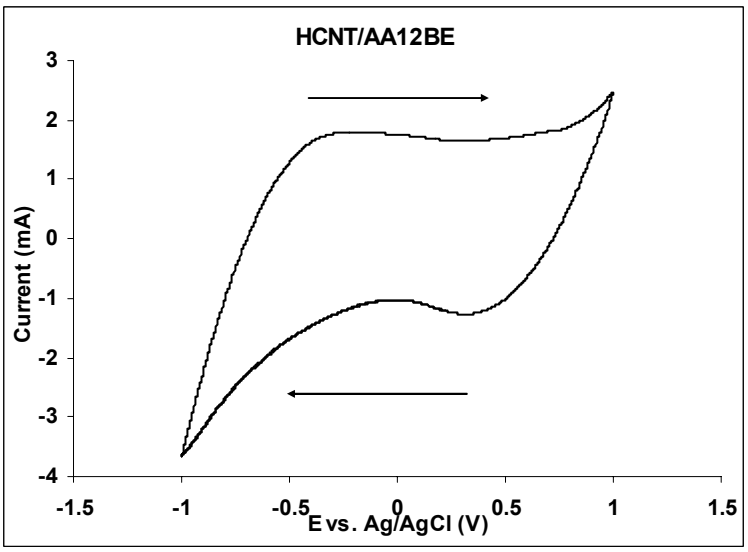

Fig 3.12 Cyclic voltammogram (2nd cycle) of HCNT/AA12BE mat in 0.01 M $K_4Fe(CN)_6$ with 0.1 M $NaNO_3$ as a supporting electrolyte, E = -1, + 1 V, scan rate of 50 mV/s.

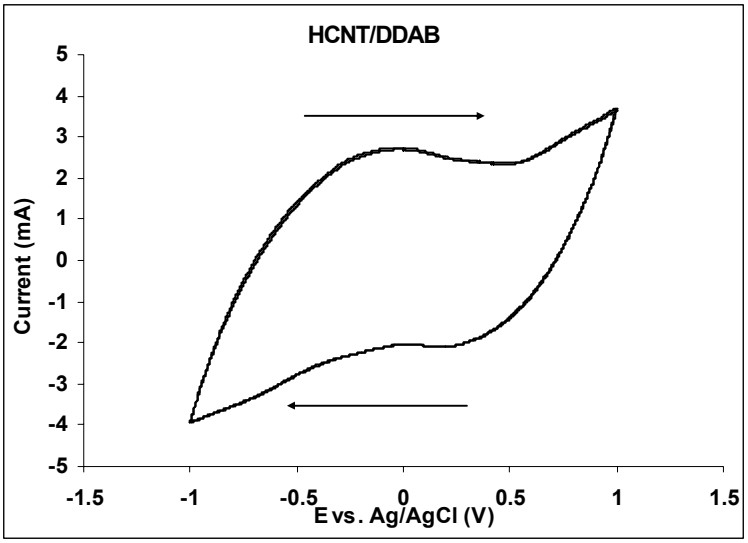

Fig 3.13 Cyclic voltammogram (2nd cycle) of HCNT/DDAB mat in 0.01 M $K_4Fe(CN)_6$ with 0.1 M $NaNO_3$ as a supporting electrolyte, E = -1, + 1 V, scan rate of 50 mV/s.

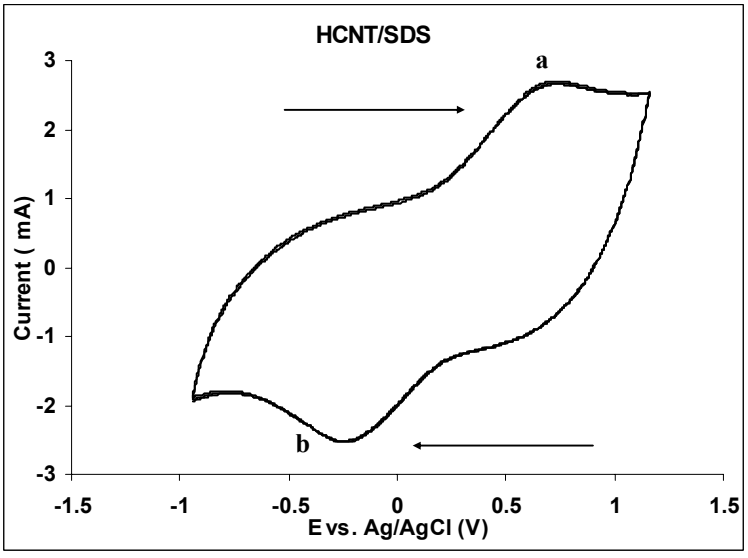

Fig 3.14 Cyclic voltammogram (2nd cycle) of HCNT/SDS mat at in 0.01 M $K_4Fe(CN)_6$ with 0.1 M $NaNO_3$ as a supporting electrolyte, E = -1, + 1 V, scan rate of 50 mV/s.

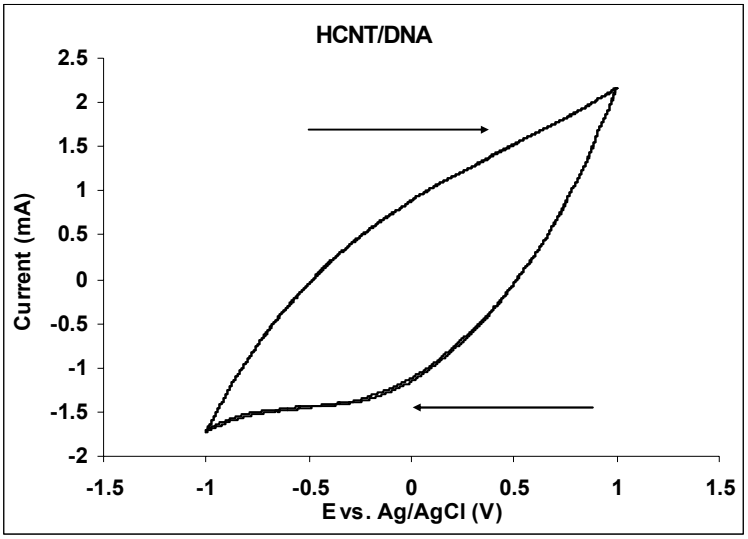

Fig 3.15 Cyclic voltammogram (2nd cycle) of HCNT/DNA mat in 0.01 M $K_4Fe(CN)_6$ with 0.1 M $NaNO_3$ as a supporting electrolyte, E = -1, + 1 V, scan rate of 50 mV/s.

3.3.2.3 Capacitance

Cyclic voltammograms were recorded for the different HCNT/dispersant mats using different scan rates. The difference between the oxidation and reduction current at E = 0.1 V was plotted as a function of the scan rate, the best straight line was graphed and slope calculated. Capacitance = ½ slope (F), Specific Capacitance = Capacitance/weight (F/g), the results obtained are presented in Table –3.3. An example of the calculations is presented in **Ch. 2**, section **2.3.2.3**.

Table –3.3 Capacitance for the different HCNT/dispersant mats.

Dispersant	**Specific capacitance (F/g ± 0.01)**
TX100	3.74
SDS	23.25
PVP	5.6
PMAS	13.2
DDAB	1.08
AA12BE	0.85
DNA	1.7

From the table above we find that the capacitance for the HCNT/dispersant mats is significantly lower than that for the RCNT/dispersant mats, **Ch. 2**, section **2.3.2.3**. It was reported that in the region between –0.5 V and 0.5 V SWCNT approach the behavior of an ideal double-layer capacitor (261). This was observed in all the HCNT/dispersant cyclic voltammograms, such as the case in the cyclic voltammogram of HCNT/TX100 (Fig 3.16).

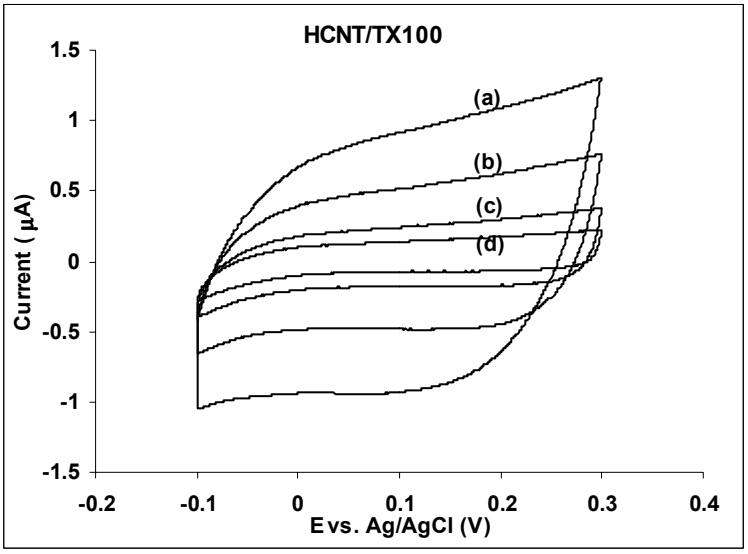

Fig 3.16 Cyclic voltammogram of HCNT/TX100 mat in 0.1 M $NaNO_3$, E = -0.1, + 0.3 V. (a) scan rate of 50 mV/s, (b) scan rate of 25 mV/s, (c) scan rate of 10 mV/s, and (d) scan rate of 5 mV/s.

3.3.2.4 Atomic Force Microscopy (AFM)

AFMs of the HCNT/dispersant mats were obtained and compared to those obtained for RCNT/dispersant mats (**Ch. 2**, Fig 2.13). We find that the HCNT aggregate into ropes and bundles as do the RCNT. However, the HCNT ropes and bundles seem to be smaller in diameter. This is due to the fact that a HCNT has a diameter of ~ 1 nm compared to the diameter of a RCNT ~1.38 nm, and they are also shorter in length as was previously reported (234, 235) (Fig 3.17). These differences result in a more even distribution of the HCNT throughout the mat. This was observed in all the AFM pictures for the different HCNT/dispersant mats, an example is the AFM picture of the HCNT/SDS mat (Fig 3.18). We were not able to obtain AFM pictures of the

HCNT/DNA mat. This mat was very rough, as the DNA uptake by the HCNT is very high. SEM pictures of the HCNT/DNA mat were obtained.

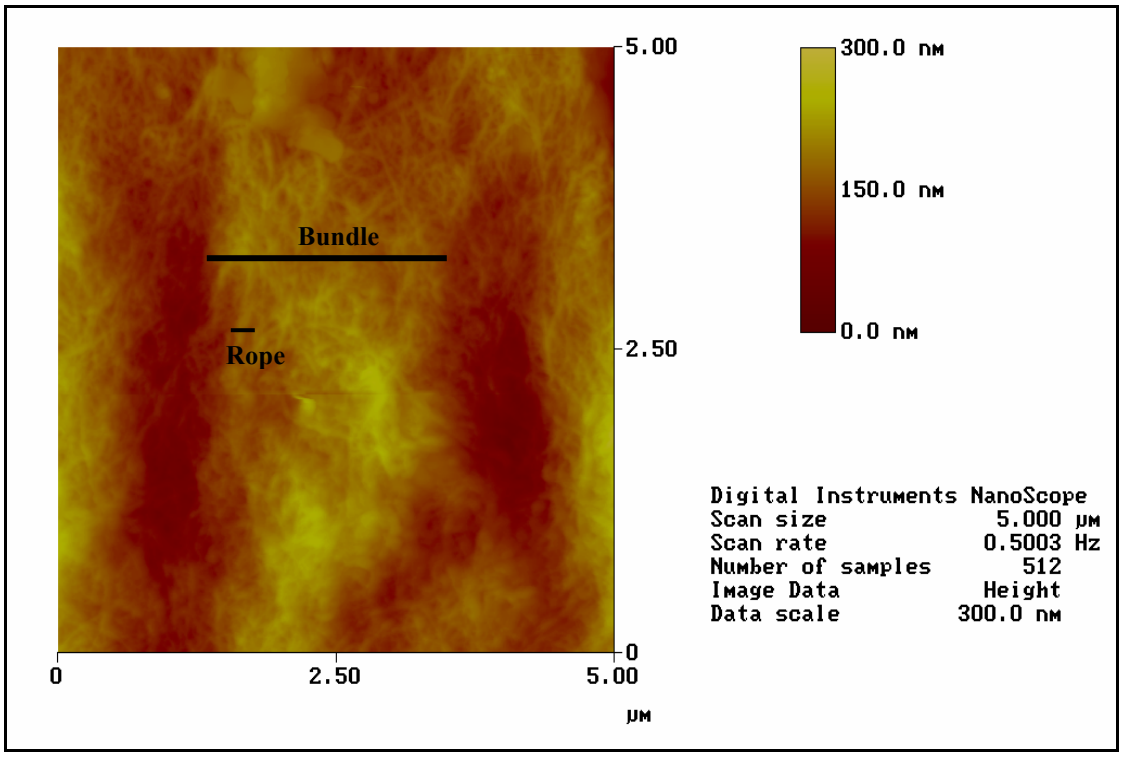

Fig 3.17 AFM picture of HCNT/TX100 mat.

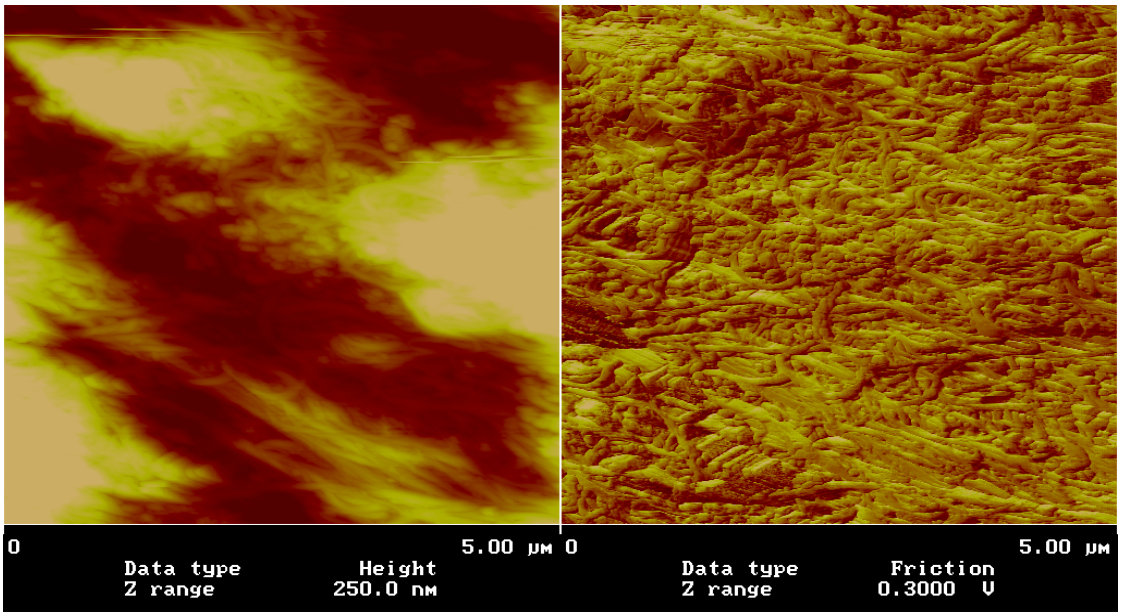

Fig 3.18 AFM picture of HCNT/SDS mat.

3.3.2.5 Scanning Electron Microscopy (SEM)

SEM pictures were obtained for the HCNT/DNA mat (Fig 3.19), as we can see from the picture, the HCNT are highly entangled into a complex network. In addition, since the uptake by the HCNT of the DNA is very high, and we cannot see DNA clusters in the picture, we assume that the HCNT are nearly 100% covered by the DNA. Comparing the HCNT/DNA mat with the RCNT/DNA mat (**Ch. 2**, Fig 2.17), we can see that the HCNT are more densely packed within the matrix of the mat.

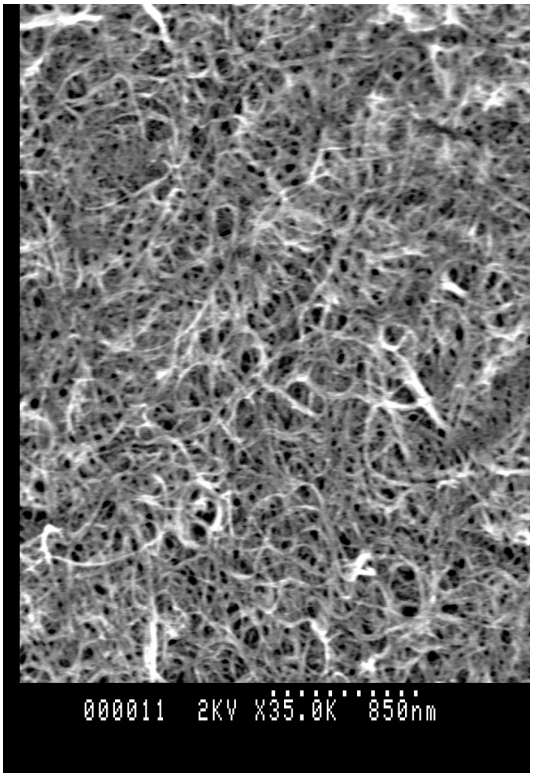

Fig 3.19 SEM picture of HCNT/DNA mat.

3.3.2.6 Mechanical properties

The mechanical properties were measured for the HCNT/dispersant mats using a 10 N load cell, and a crosshead speed of 1 mm/s was used to extend the samples. From the recorded measurements Force (N) was plotted against Extension (m), and Stress (σ) (MPa) was plotted against Strain (ε).

Stress (MPa) = F (N) / W(m) X T (m)

Strain = Extension (m)/Gauge length (m)

From the plot of Stress vs. Strain (Fig 3.20), we can obtain σ_{Break} (MPa), and ε_{Break}, where σ_{Break} is the stress value, and ε_{Break} is the corresponding strain at the breaking point. Also, from the slope of the curve we can calculate Young's modulus Y (GPa). Results are presented in Table –3.4.

Table –3.4 Mechanical properties for the different HCNT/dispersant mats.

Dispersant	**σ_{Break} (MPa ± 0.1)**	**ε_{Break} ± 0. 1**	**Y (GPa ± 0.01)**
TX100	2.3	2.1	0.19
SDS	28.2	3.1	1.32
PVP	17.2	2.3	0.95
PMAS	51.7	2.2	2.80
DDAB	4.7	5.9	0.16
AA12BE	2.0	8.0	0.04
DNA	17.8	2.1	1.30

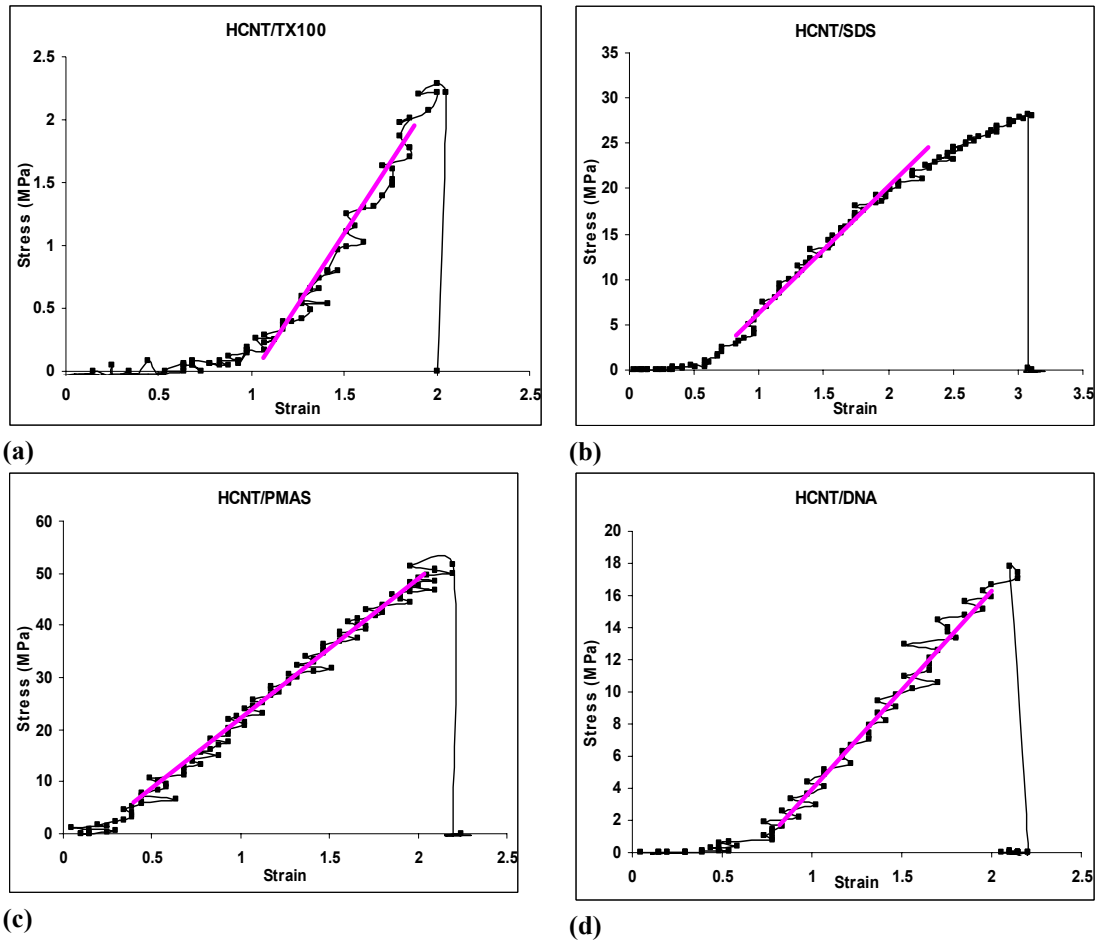

Fig 3.20 Stress-strain curves of a) HCNT/TX100, b) HCNT/SDS, c) HCNT/PMAS, and d) HCNT/DNA.

As can be seen in the stress-strain curves the different samples exhibit brittle behavior with a slight dectility at high stress-strain values. This behavior is very similar to that previously observed for the RCNT/dispersant mats (**Ch. 2**, Fig 2.14). This is presumably due to the creep/slippage of the ropes within the matrix of the mat near the break point.

The HCNT/dispersant mats were less brittle compared to the RCNT/dispersant mats, **Ch. 2**, section **2.3.2.5**. This is due to the HCNT/dispersant mats being more homogenous and uniform as observed by AFM pictures. HCNT/PMAS had the

highest Young's modulus, while HCNT/AA12BE had the lowest. HCNT/TX100 and HCNT/DDAB mats had a similar Young's modulus, as is the case with HCNT/SDS and HCNT/DNA mats.

There are three reasons why the Young's modulus for the HCNT mats is smaller than previously reported values in the literature as discussed in **Ch. 2**, section **2.3.2.5**. First, the HCNT are packed into ropes, and the ropes are packed into bundles which are covered by the dispersant. This will result in a very large increase in the overall diameter, compared to the diameter of a single-walled carbon nanotube. Secondly, the HCNT mats that we used in these measurements were not annealed. Finally, the value for the cross sectional area used when calculating the stress values is not the real area, since the mats are composed of a mesh of ropes and not a single rope, and the stress values obtained are probably due mainly to shear stress rather than tension stress. However, the values we obtained for the HCNT/SDS, HCNT/PMAS and HCNT/DNA are higher than the Young's modulus for conducting polymers.

2.3.2.7 Actuation

Carbon nanotubes have been shown to provide actuation with several key advantages over other actuator materials (262). The proposed actuation mechanism is based on charge injection that requires the carbon nanotubes to be immersed in electrolyte to allow a potential to be applied. Changing the applied voltage injects charge into the carbon nanotubes structure, which is compensated at the nanotube/electrolyte interface by electrolyte ions forming a double layer (262). This charge injection causes dimensional changes in the carbon-carbon covalent bond length that originates from quantum mechanical and double layer electrostatic effects. The result of this is a

change in the bulk dimension (262). As nanotubes exhibit actuation through this unique mechanism, and due to their natural atomic structure, they have been predicted to be able to generate extremely high stress. Gao *et al* predicted that for the achievable actuator strain of 1%, the individual nanotubes should generate stress up to 6 GPa since the measured elastic modulus is around 640 GPa for nanotubes ropes (263).

It was not until the work of Mazzoldi *et al* that nanotubes mats were tested in a linear actuation configuration (264). The investigation of carbon nanotube actuation in comparison to polypyrrole and carbon nanotube/polypyrrole composites indicated that the carbon nanotubes actuators exhibited lower actuation strains than polypyrrole, but that these were attainable at increasing loads (264). Under the same loads, the strain of polypyrrole actuators decreased to zero.

In this work we examined the actuation behavior of the HCNT/dispersant mats in 0.1 M $NaNO_3$, starting from 2 g load and increasing the load by 2 g until failure. The results are shown in Table –3.5 and (Fig 3.21 – 3.24). The Figures represent the creep of the different samples and the CV of each of these samples during the application of voltage, when a load of 2 g was used.

Table –3.5 %Strain for the HCNT/dispersant mats.

Dispersant	**Strain % ± 0.001**		
	Load of 2 g	**Load of 4 g**	**Load of 6 g**
TX100	0.047	0.031	0.014
SDS	0.034	0.017	---
PMAS	0.004	---	---
DDAB	0.036	0.013	---

From the table above we can see that the HCNT/TX100 mat exhibited the highest strain, the maximum load used was 6 g. HCNT/SDS and HCNT/DDAB mats exhibited lower strains with similar values, and a maximum load of 4 g was used before failure. HCNT/PMAS mat on the other hand exhibited a significantly lower strain value compared to the other samples, and the maximum load used was 2 g before failure. HCNT/AA12BE and HCNT/DNA did not exhibit any actuation behavior.

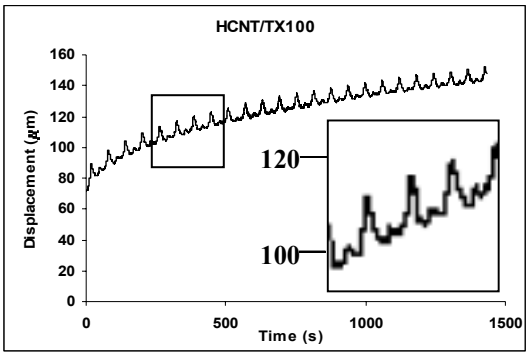

0.047%

Fig 3.21a Displacement as potential is applied for HCNT/TX100 mat in 1 M $NaNO_3$, with a 2 g load.

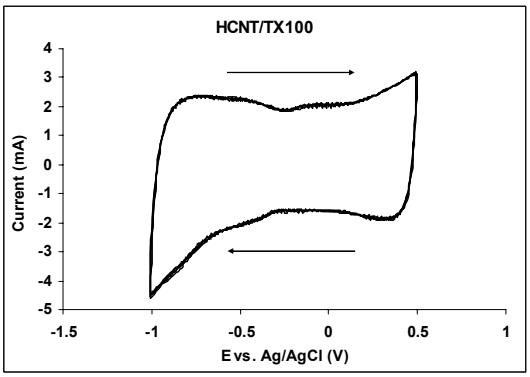

Fig 3.21b Cyclic voltammogram (2nd cycle) for HCNT/TX100 mat in 1 M $NaNO_3$ during the application of Voltage. E= -1, 0.5 V, scan rate of 50 mV/s.

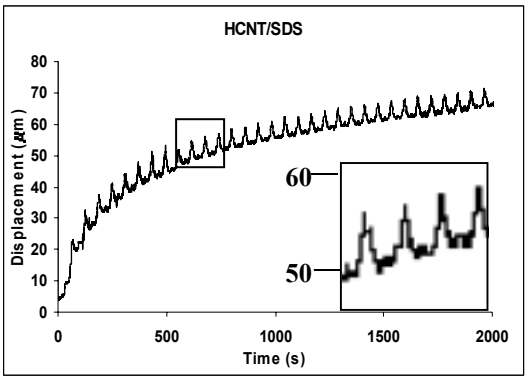

0.034%

Fig 3.22a Displacement as potential is applied for HCNT/SDS mat in 1 M $NaNO_3$, with a 2 g load.

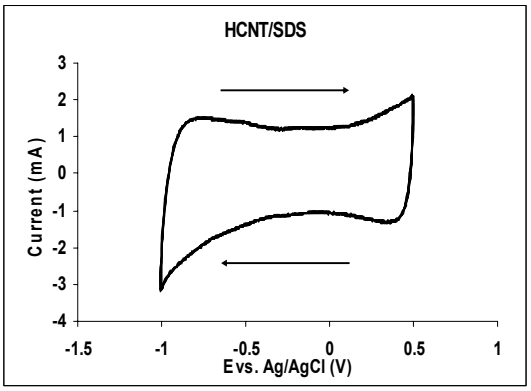

Fig 3.22b Cyclic voltammogram for HCNT/SDS mat in 1 M $NaNO_3$ during the application of Voltage. E= -1, 0.5 V, scan rate of 50 mV/s.

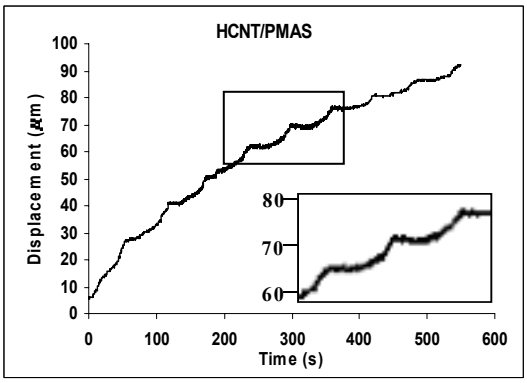

0.004%

Fig 3.23a Displacement as potential is applied for HCNT/PMAS mat in 1 M $NaNO_3$, with a 2 g load.

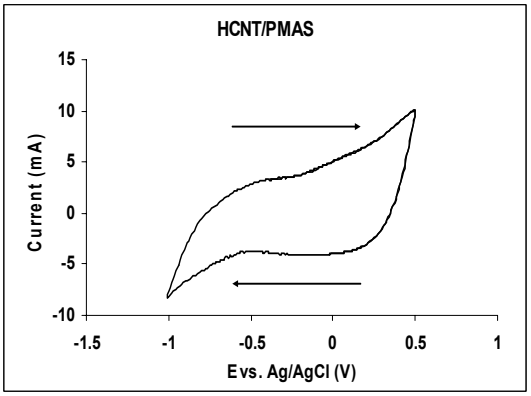

Fig 3.23b Cyclic voltammogram for HCNT/PMAS mat in 1 M $NaNO_3$ during the application of Voltage. E= -1, 0.5 V, scan rate of 50 mV/s.

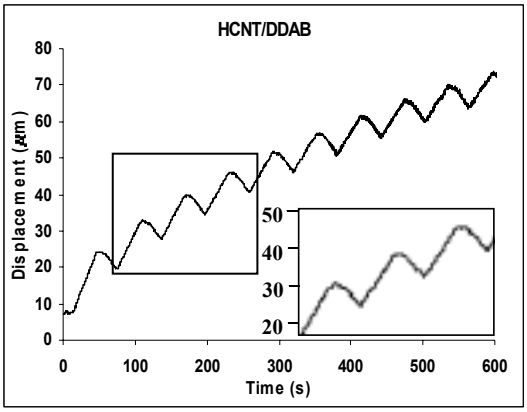

0.036%

Fig 3.24a Displacement as potential is applied for HCNT/DDAB mat in 1 M $NaNO_3$, with a 2 g load.

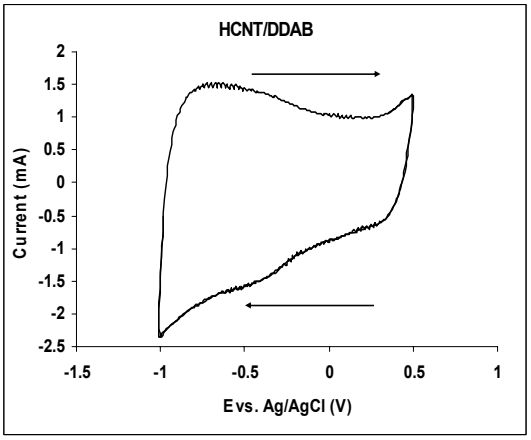

Fig 3.24b Cyclic voltammogram for HCNT/DDAB mat in 1 M $NaNO_3$ during the application of Voltage. E= -1, 0.5 V, scan rate of 50 mV/s.

From these figures we can see the creep in each sample. This is due to the fact that the HCNT/dispersant mats are composed of randomly packed ropes and bundles, which result in stretching, pulling and sliding within the mat during actuation, and hence the obvious creep. In addition, the insertion and expulsion of the ions into the dispersant depends to a significant degree on the chemical nature of the dispersant. This contributes to the differences in the actuation behavior for the different HCNT/dispersant mats.

3.4- CONCLUSION

HCNT dispersions and mats have been prepared and characterized using a variety of methods. Using AFM, it was found that the HCNT/PVP dispersion exhibited super-alignment of the HCNT. This was confirmed by Raman spectroscopy. This alignment seems to be a templated self-assembly. It was also determined that the alignment of the HCNT is a characteristic that depends on the dispersant used. The stability of the dispersion over time was examined by recording the UV-Vis spectra for the different dispersion over a 48-hour period. It was found that HCNT/PVA, HCNT/PMAS and HCNT/DNA were stable over long periods of time.

CVs were obtained using the HCNT/dispersant mats as working electrodes, and it was found that the CVs were significantly different than those observed for the RCNT/dispersant mats. This indicated that the electrochemistry of the HCNT is different from that for the RCNT. In addition, CVs of the HCNT/dispersant mats were recorded over a wide potential range. The results indicated that the electrochemical response of the HCNT mats depends on the chemical nature of the dispersant. Also, the CVs exhibited a highly capacitive behavior indicating that they are composites with high charge storage capabilities.

Conductivity and capacitance measurements were obtained for the different HCNT/dispersant mats. Both the conductivity and capacitance values were smaller than those for the RCNT/dispersant mats. In addition, some of the capacitance values obtained were negative. This could be due to the high porosity of the

HCNT/dispersant mats; it could also be due to the complexity of the samples, which result in different kinetic processes occurring at the same time, some slower than the others.

The mechanical properties of the HCNT/dispersant mats were much better than those for the RCNT/dispersant mats, this is due to the more uniform and homogenous morphology of the mats as can be seen in the AFM and SEM pictures. In addition, actuation studies on the HCNT/dispersant mats were carried out, and in general the HCNT/dispersant mats exhibited good actuation responses. In addition, a creep was observed in each sample. This is due to the fact that the HCNT/dispersant mats are composed of randomly packed ropes and bundles, which result in stretching, pulling and sliding within the mat during actuation, and hence the obvious creep.

CHAPTER FOUR

PREPARATION AND CHARACTERIZATION OF DISPERSIONS AND MATS OF MULTI-WALLED CARBON NANOTUBES/DISPERSANT COMPOSITES

4.1- INTRODUCTION

MWCNT were the first CNT to be discovered. They are similar to hollow graphite fibers, except that these have a much higher degree of structural perfection. They are composed of concentric cylinders, with a spacing between the layers close to that of the inter-layer distance in graphite ~34 nm. This interlayer spacing is larger than the single-crystal graphite value ~ 3.35 nm. This is due to the fact that in MWCNT there is a severe geometrical constraint when forming the concentric seamless cylinders while maintaining the graphite spacing between them. The three dimensional structural correlation that prevails in single-crystal graphite is lost in the MWCNT and the layers are rotationally disordered with respect to each other (93).

MWCNT dispersions have been prepared by a number of research groups. MWCNT have been dispersed in ethanol (265), isopropanol (266), and methylene chloride (267). In addition, MWCNT have been dispersed in 2-butanone using bath sonication. It was found that the MWCNT ribbons that were formed are highly flexible. It was also observed that the dispersing process could lead to the collapse of the MWCNT, where the inter-layer distance between the tubes decreases significantly. This in turn results in a decrease in the internal and external surface

area of the MWCNT due to the new interlayer van der Waals contact of the inner most MWCNT cylinder (268).

MWCNT/polymer composites have also been prepared by a number of research groups. For example, composites with polystyrene (269, 270), Poly(3-octylthiophene) (271), poly(methylmethacrylate) (PMMA) (272), poly(3-hexylthiophene) (P3HT) (273), and Poly(propionylethylenimine-*co*-ethylenimine) (PPEI-EI) in chloroform have been prepared (274 - 276).

MWCNT/epoxy was prepared by Lee *et al* (96), Ijjima *et al* (277) and Gong *et al* (278). Gong *et al* investigated the role of the dispersant as a processing aid in the preparation of MWCNT/polymer composites. The dispersant used as the wetting agent was Poly(vinyl alcohol) (PVA). It was found that using a dispersant as a processing aid improved the thermochemical properties of MWCNT/polymer composites. The elastic modulus also increased by ~30%. In contrast the addition of MWCNT to epoxy without the dispersant only has moderate effects on the mechanical properties (279). It was also found that the outer surface of the MWCNT is partially covered with the dispersant even after washing with water (280).

Composites with Poly(m-phenylene-co-2,5-dioctoxy-p-phenylenevinylene) (PmPV), a conjugated polymer, have been prepared and examined by a number of groups (93, 281, 282, 283, 284). The MWCNT appeared to be well dispersed, as the conjugated polymer is able to wet the MWCNT (281). This polymer chain tends to coil to form a helical structure; it is possible that the coiled polymer conformation allows it to surround the MWCNT. As the polymer structure possesses helicity, it is not surprising that it is able to wrap itself around the MWCNT and keep them suspended in solution indefinitely (282). It was also found that in some instances when the

MWCNT are open at the tip, the polymer was able to migrate inside (284). The nanotubes appear to be held in the polymer matrix through a weak interaction between the backbone of the polymer and the lattice of the nanotubes. The interaction probably arises from π-π stacking or from Van der Waals attraction between the oxygen atoms of the polymer side group and the lattice of the nanotube. In addition, the nanotubes act to prevent aggregation in the polymer system. However, as the concentration of the nanotubes in the solution increase, the polymer is unable to break down the aggregates of the MWCNT (283).

It was also concluded that semi-conjugated organic polymers are capable of suspending MWCNT indefinitely whilst the accompanying amorphous graphite settles out. In the case of a non-conjugated polymer such as polystyrene, this was not observed and all the carbonaceous material settled out (281).

When considering MWCNT/polymer composites in general, it was found that there was an increase in the electrical conductivity of the composite compared to the pristine polymer of nearly 8 orders of magnitude, the highest conductivity achieved was 10^{-2} S/cm (93, 282). The best description of this conduction process is provided by a percolation model, which fits the composites conductivity very well. The high aspect ratio and good dispersion help to achieve percolation at very low volume fraction of MWCNT, where connectivity is very low but conduction lengths are large, resulting in such dramatic changes in the conductivity (282). The nanotubes appear to act as nano-metric heat sinks, preventing the build up of large thermal effects, caused optically or electrically, which degrades these conjugated systems.

MWCNT/Poly(3-octylthiophene) composite was prepared (271). It was found that the electrical conductivity for the composite increased by up to five orders of magnitude from the 'undoped' polymer film, which suggested that there is some interaction between the MWCNT and the polymer chain.

In this chapter the preparation of aqueous Multi-walled Carbon Nanotubes (MWCNT) dispersions and mats is investigated. The dispersions were characterized by using particle size and zeta potential measurements. UV-Vis spectrophotometry was then recorded for the different dispersions to evaluate their stability over time. These dispersions were then filtered to produce MWCNT/dispersant mats. The characterization of these composites was carried out using a variety of different techniques such as, cyclic voltammetry, capacitance, and Scanning Electron Microscopy (SEM). Conductivity, for the different MWCNT mats was also measured.

4.2- EXPERIMENTAL

4.2.1 Preparation of MWCNT dispersions and mats

The multi-walled carbon nanotubes were purchased from MER as a solid powder, with an average tube diameter of 1.1 nm. For a comparison between SWCNT (RCNT) and MWCNT, a MWCNT solution with a concentration similar to that of the RCNT solution, **Ch. 2** section **2.2.1** was prepared. This was achieved as follows; 0.1 g TritonX 100® (TX100) (<3% w/v polyethylene glycol, Aldrich) was added to 43 ml Milli-Q-Water to produce a 0.23% TX100 solution, 0.5 g of the solid MWCNT were then added to this solution. 1 g aliquot of this mixture was added to 100 ml Milli-Q-Water and sonicated for 30 min, this produced the standard MWCNT/TX100 dispersion. From the standard MWCNT/TX100 dispersion, a 50 ml aliquot was filtered using a stirred filtration cell (model 8050 purchased from Amicon/Millipore) under nitrogen pressure of 400 KPa. Polyvinylidene fluoride (PVDF) membranes with pore size of 0.22 μm were used as filters. The PVDF membranes were wetted for 30 min in 50:50 v/v ethanol to Milli-Q-Water prior to use. The mat was then washed with 150 ml Milli-Q-Water, then 150 ml methanol to remove excess TX100. MWCNT mats were pealed off the PVDF membranes and re-dispersed in 50 ml of the following solutions, 0.2% w/w Noxamium 0.15® (N0.15) (Aldrich), 0.2% w/w Didodecyldimethyl ammonium bromide (DDAB) (M.W. 462.64 Da, Aldrich), 0.2% w/w N-isopropylacrylamide 2-acrylamido-2-methyl-1-propanesulfonic acid (NIPPAm-AMPS) (90:10 NIPPAm:AMPS w/w, synthesized organically, University of Wollongong), and 0.2% w/w Deoxyribose Nucleic Acid (DNA) (Salmon sperm, 300 – 600 base pairs), from Prof. N. Ogata (Sophia University, Japan). These

mixtures were then sonicated for 2 hours. The resulting dispersions were filtered as described previously and MWCNT mats were obtained, Scheme-4.1.

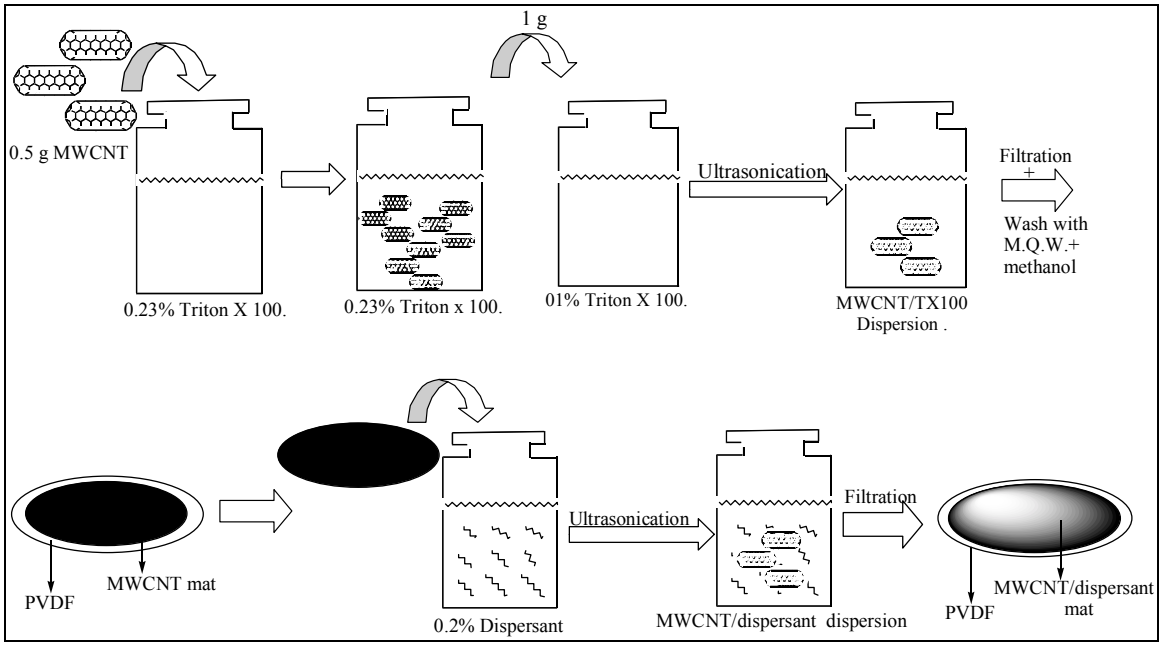

Scheme 4.1 Preparation of MWCNT dispersions and mats.

4.2.2 Instrumentation

4.2.2.1 Characterization of MWCNT dispersions

A UV-1601 UV-Visible spectrophotometer (Shimadzu) was used to record the UV-Vis spectra for the dispersions. The absorbance (Abs.) was recorded for each of the different dispersions, using a constant wavelength of 600 nm, where the Abs. was recorded every 15 min over a period of 48 hours.

Malvern Zetasizer 3000 was used to measure the particle size and the zeta potential (surface charge) of the different dispersions.

4.2.2.2 Characterization of MWCNT/dispersant mats

Four-point probe conductivity measurements were recorded for the MWCNT/dispersant mats using 2.5 X 0.5 cm strips of the mats. A digital micrometer was used to measure the thickness of the composites. A constant current of 1 mA was passed through the sample using an EG & G Princeton Applied Research model 363 Potentiostat/Galvanostat, and the voltage was recorded using a Hewlett Packard model 34401.

Cyclic voltammograms were recorded using a MacLab/4e over a wide potential range of E = -1, +1 V for the different MWCNT/dispersant mats in 0.01 M $K_4Fe(CN)_6$ with 0.1 M $NaNO_3$ as a supporting electrolyte. 2.5 X 0.5 cm strips (fully immersed) of the MWCNT mats were used as the working electrode. Ag/AgCl was used as the reference electrode and Pt-mesh as the auxiliary electrode. The scan rate applied was 50 mV/s. The capacitance for the different MWCNT/dispersant mats were measured by recording cyclic voltammograms for the different mats using different scan rates 50, 25, 10 and 5 mV/s. The potential window used was E = -0.1, +0.3 V, and current measurements were taken at E = +0.1 V. The electrochemical cell was as described above with the exception of the electrolyte used being 1 M $NaNO_3$. Scanning Electron Microscopy (SEM) pictures of the MWCNT/dispersant mats were obtained using a Hitachi S-900 FESEM.

4.3- RESULTS & DISCUSSION

4.3.1 Characterization of the MWCNT dispersions

4.3.1.1 Particle size and Zeta potential

The particle size distribution for the different dispersions was measured in order to determine the effectiveness of the different dispersants with respect to dispersing the MWCNT. The photon-correlation spectroscopy, with the analysis algorithms was modified to compensate for the non-spherical nature of the carbon nanotube as discussed in **Ch. 2** section **2.3.1.1**. The zeta potential (surface charge) for the dispersions was also measured to confirm that the MWCNT are negatively charged, Table –4.1. It was found that N0.15 was the most effective dispersant while DNA was the least effective. Zeta potential measurements of the MWCNT dispersed in TX100, DNA, and NIPAAm-AMPS determined that the surface charge was negative. For MWCNT dispersed in N0.15 and DDAB, the surface charge was positive. This is in agreement with what was expected since N0.15 and DDAB are cationic surfactants. In addition, it was observed that the particle size was very large in general. This is due to the fact that MWCNT tend to form aggregated ropes, which are much larger than a single MWCNT. Size determination using light scattering techniques produces a scatter intensity that is directly proportional to the particle size ($I \alpha r^6$). Therefore, if a small percentage of the MWCNT in the dispersion existed as large entangled rope aggregates this would skew the observed particle size resulting in significantly higher values.

Table –4.1 Particle size and zeta potential for MWCNT dispersion.

Dispersant	Particle size (nm ± 1)	Zeta Potential (mV ± 0.1)
TX100	629	-3.5
DNA	920	-56.4
N 0.15	228	19.9
NIPPAm-AMPS	259	-22.2
DDAB	462	6.5

4.3.1.2 Ultraviolet and Visible Absorption spectroscopy (UV-Vis)

The Abs. for the different MWCNT dispersions was recorded as a function of wavelength starting at 350 nm and finishing at 1100 nm. The UV-Vis spectra of MWCNT (Fig 4.1) were found to be similar to those observed for SWCNT (**Ch. 2**, Fig 2.6).

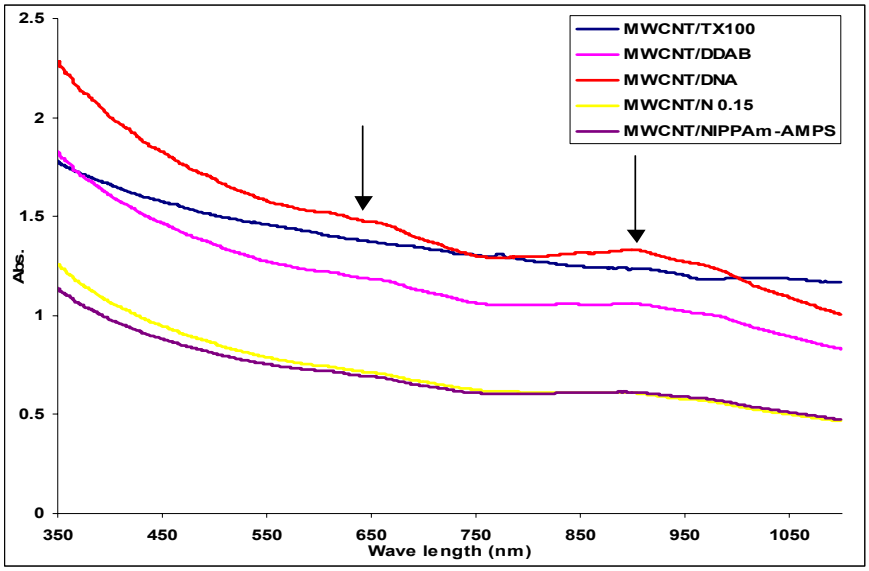

Fig 4.1 UV-Vis spectra of MWCNT dispersions over 300-1100nm.

The spectra for the MWCNT were featureless curves with broad bands, this was also observed by other workers (274, 276). The broad double peaks that are observed at 650 and 900 nm are characteristic of the transition between the first pair of singularities in the density of state (DOS) of the metallic MWCNT (285, 286). The peak at 650 nm is assigned to the first Van Hove transition of metallic MWCNT, while the peak at 900 nm is due to the second Van Hove singularity. In addition, the Van Hove peaks are sensitive to MWCNT diameters. Therefore, we expect MWCNT that contain less cylinders to have a smaller diameter and thus exhibit Van Hove transitions at shorter wavelengths and MWCNT that contain more cylinders to exhibit Van Hove transition at longer wavelengths. The peaks observed are due to the overlapping of Van Hove transitions from all nanotube sizes that are present in the sample (287, 288).

In order to determine the stability of the different MWCNT dispersions, the absorption was measured as a function of time. A constant wavelength of 600 nm was selected as it is directly related to the first Van Hove transition of carbon nanotubes and thus was clear of other interferences. The Abs. was recorded every 15 min over a period of 48-hours (Fig 4.2).

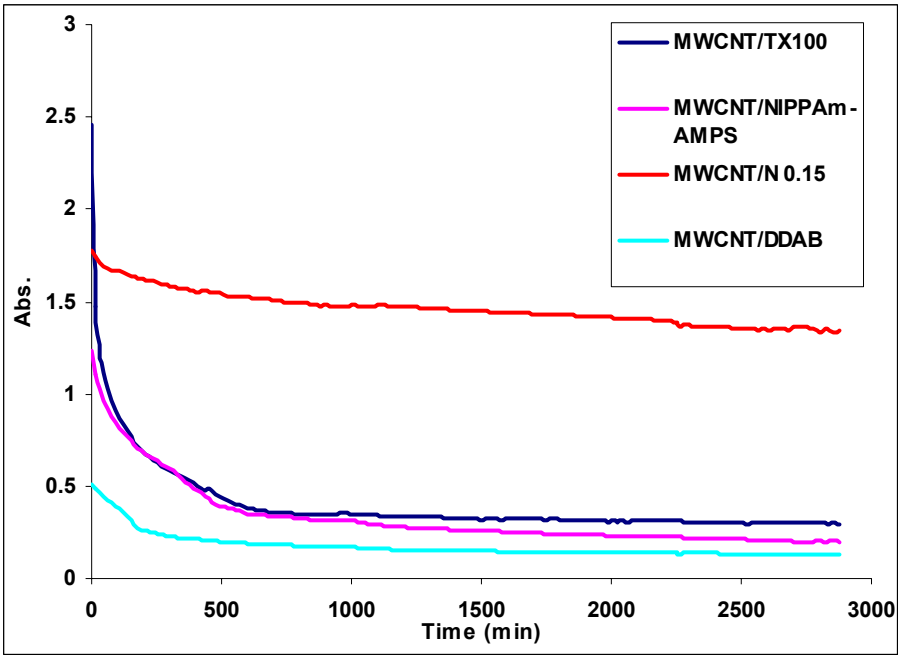

Fig 4.2 Abs. for different MWCNT dispersions over a period of 48-hours at 600 nm.

In general, the Abs. for all the dispersions were observed to decrease at 150 min, indicating that the MWCNT started to settle and/or coagulate. The Abs. for all the MWCNT dispersions was constant through the remainder of the 48-hours. From the accompanying time lapse pictures (Fig 4.3, and 4.4), it was verified that the MWCNT/DDAB dispersion was stable over the 48-hour period. For MWCNT/TX100 and MWCNT/N0.15 dispersions some tubes settled at the bottom of the vial. In the case of MWCNT/NIPPAm-AMPS and MWCNT/DNA dispersions we can see that all the MWCNT settled out of the aqueous phase after 48-hours.

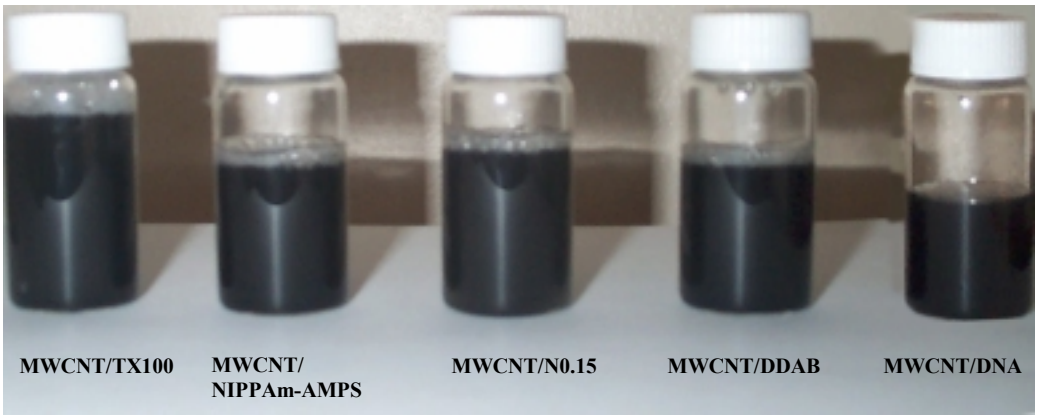

Fig 4.3 MWCNT dispersions at t = 0.00 min.

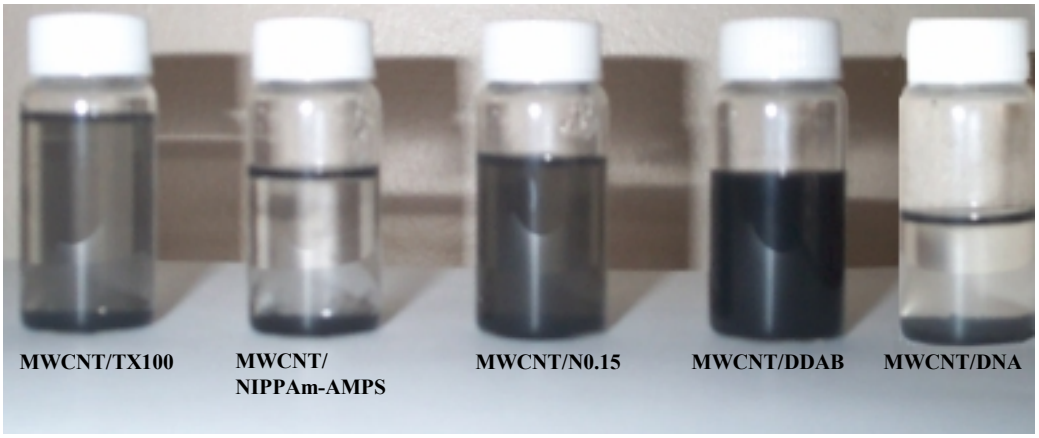

Fig 4.4 MWCNT dispersions at t = 48 hour.

4.3.2 Characterization of MWCNT/dispersant mats

The weight of the MWCNT dispersed in the different solutions was 5.6 mg. Therefore, the weight of the MWCNT/dispersant mats after drying includes the 5.6 mg of MWCNT, and the remaining weight is attributed to the dispersant that is incorporated within the MWCNT matrix.

Table –4.2 Weight of MWCNT/dispersant mats.

Dispersant	**Weight (mg ± 0.1)**	**Dispersant weight retained in the mat (mg ± 0.1)**
TX100	16.2	10.6
DNA	115.6	110.0
N 0.15	6.3	0.7
NIPPAm-AMPS	16.5	10.9
DDAB	27.3	21.7

There are significant differences between the weights of the different mats, due to the fact that a certain amount of the dispersant used is retained within the mat, where the chemical nature of the dispersant ultimately affects its uptake by the MWCNT as discussed in **Ch. 2**, section **2.3.2**. In addition, the weight of the mat will also depend on the molecular weight of the dispersant, where a high molecular weight resulted in a higher mat weight, as is the case in the MWCNT/DNA mat.

4.3.2.1 Conductivity

The equations used to calculate the resistance and conductivity were discussed in **Ch. 2**, section **2.3.2.1**. The results are presented in Table –4.3.

Table –4.3 Conductivity of MWCNT/dispersant mats.

Dispersant	**Thickness (μm ± 0.1)**	**Conductivity (S/cm ± 5%)**
TX100	32.8	2.3
DNA	119.0	4.2×10^{-4}
N 0.15	9.0	7.9×10^{-4}
NIPPAm-AMPS	30.3	1.6×10^{-3}
DDAB	36.5	7.6×10^{-4}

From the results in the table above, we can see that the MWCNT/TX100 mat exhibited the highest conductivity compared to the other MWCNT/dispersant mats. In general, we find that the conductivity of the MWCNT/dispersant mats is lower by nearly four orders of magnitude compared to the conductivity of the corresponding RCNT/dispersant mats (**Ch. 2**, section **2.3.2.1**) and HCNT/dispersant mats (**Ch. 3**, section **3.3.2.1**). One possible explanation is that when relating the static conductivity of SWCNT to the static in plane conductivity of a graphite sheet it is concluded that SWCNT are excellent conductors. In contrast, MWCNT are composed of different cylinders, where the electronic properties of bulk graphite are strongly affected by the outer sheet electron hopping, thus MWCNT may posses conductivities substantially below that of the sum of the constituent tubes.

4.3.2.2 Cyclic voltammetry of MWCNT/dispersant mats over a wide potential range in 0.01 M $K_4Fe(CN)_6$

CVs for the different MWCNT mats were recorded over a wide range of potentials in 0.01 M $K_4Fe(CN)_6$ with 0.1 M $NaNO_3$ as a supporting electrolyte (Fig 4.5 – 4.8), oxidation of water and reduction of hydrogen at the solvent limits were observed. MWCNT/TX100 mat (Fig 4.5) generally exhibited ohmic behavior, and a capacitive behavior was observed between E ~ -0.00 to +0.8 V. In addition, there were no similarities between the CV obtained using this mat and of that of RCNT/TX100 mat (**Ch. 2**, Fig 2.7) or HCNT/TX100 (**Ch. 3**, Fig 3.11), demonstrating the different electrochemistry of RCNT, HCNT, and MWCNT. The CV for MWCNT/N0.15 mat (Fig 4.6) was different from that of RCNT/N0.15 mat (**Ch. 2**, Fig 2.10), where the MWCNT/N0.15 exhibited no redox peaks, while the RCNT/N0.15 exhibited broad redox peaks. However, CVs for both MWCNT/N01.5 and RCNT/N0.15 mats exhibited a capacitive behavior between E ~ -0.2, +0.6 V.

There were no significant differences between the CV for MWCNT/DDAB (Fig 4.7) and RCNT/DDAB (**Ch. 2**, Fig 2.14). In addition, the CV for the HCNT/DDAB (**Ch. 3**, Fig 3.13), exhibited very broad redox peaks that are absent in the CV of the MWCNT/DDAB. The CV for MWCNT/NIPPAm-AMPS (Fig 4.8), exhibited more defined redox peaks than that of RCNT/NIPPAm-AMPS (**Ch. 2**, Fig 2.15). CVs for the MWCNT/DNA mat are not presented due to the fact that the mat was very thick and brittle which lead to irregular effects within the CV.

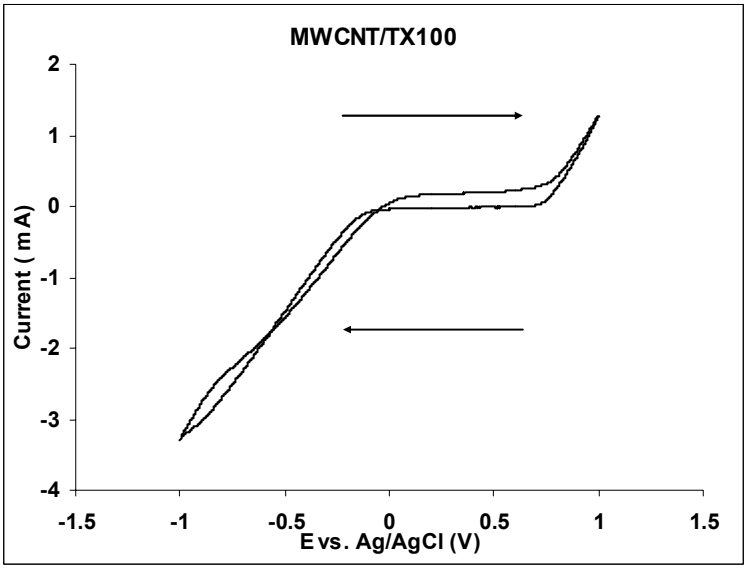

Fig 4.5 Cyclic voltammogram (2nd cycle) of MWCNT/TX100 mat in 0.01 M $K_4Fe(CN)_6$ with 0.1 M $NaNO_3$ as a supporting electrolyte, E = -1, + 1 V, scan rate of 50 mV/s.

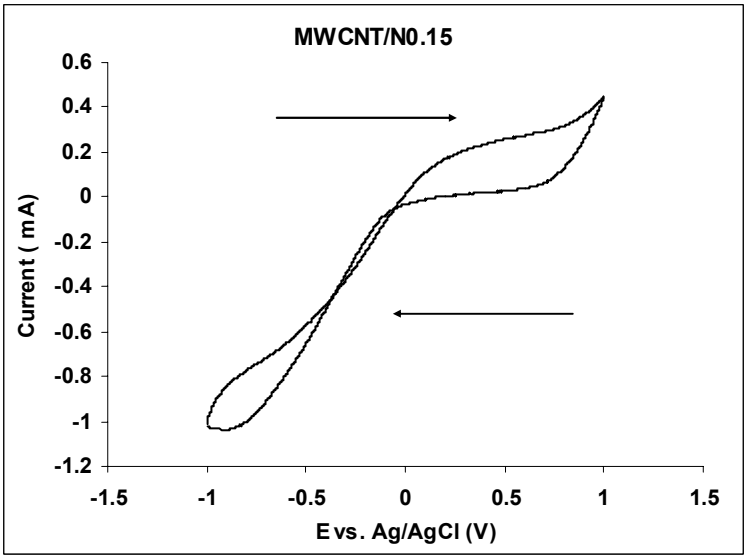

Fig 4.6 Cyclic voltammogram (2nd cycle) of MWCNT/N0.15 mat in 0.01 M $K_4Fe(CN)_6$ with 0.1 M $NaNO_3$ as a supporting electrolyte, E = -1, + 1 V, scan rate of 50 mV/s.

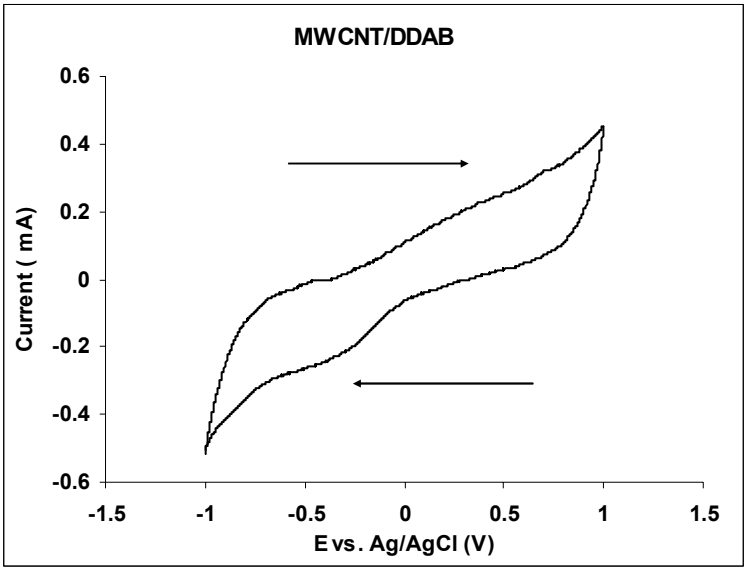

Fig 4.7 Cyclic voltammogram (2nd cycle) of MWCNT/DDAB mat in 0.01 M $K_4Fe(CN)_6$ with 0.1 M $NaNO_3$ as a supporting electrolyte, E = -1, + 1 V, scan rate of 50 mV/s.

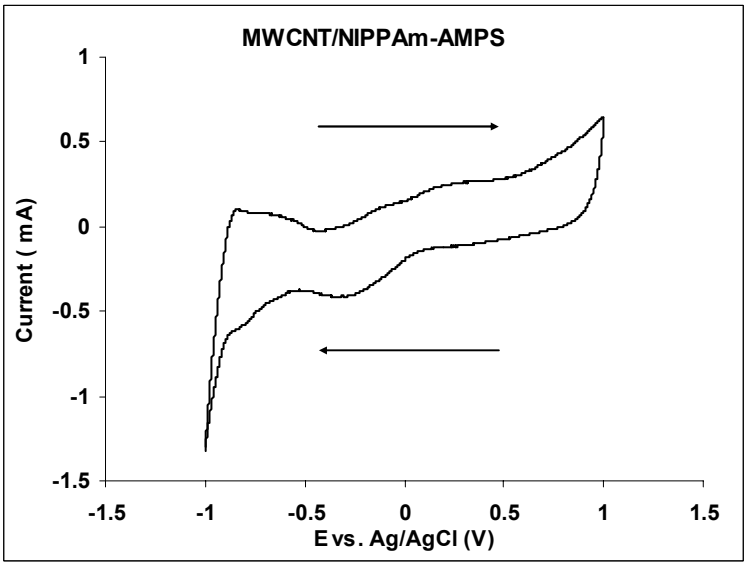

Fig 4.8 Cyclic voltammogram (2nd cycle) of MWCNT/NIPPAm-AMPS mat in 0.01 M $K_4Fe(CN)_6$ with 0.1 M $NaNO_3$ as a supporting electrolyte, E = -1, + 1 V, scan rate of 50 mV/s.

4.3.2.3 Capacitance

CVs were recorded for the different MWCNT/dispersant mats using different scan rates. The difference between the oxidation and reduction current at E = 0.1 V was plotted as a function of the scan rate, the best straight line was graphed and slope calculated. Capacitance = ½ slope (F), Specific Capacitance = Capacitance/weight (F/g), the results obtained are presented in Table –4.4. An example of the calculations is presented in **Ch. 2**, section **2.3.2.3**.

Table –4.4 Capacitance for the different MWCNT/dispersant mats.

Dispersant	**Specific Capacitance (F/g ± 0.01)**
TX100	0.48
DNA*	---
N 0.15	1.31
NIPPAm-AMPS	1.60
DDAB	1.06

* The MWCNT/DNA was very brittle, and very hard to handle. No CVs could be obtained for this mat.

The specific capacitance of an individual MWCNT was reported to be in the range of 4 to 135 F/g, depending on the different individual MWCNT tested (289). From this we can assume that the specific capacitance for bundles of ropes of non-aligned MWCNT that make up a mat would be much smaller. In general, we find that the capacitance for the MWCNT/dispersant mats is significantly lower than that measured for the corresponding RCNT/dispersant mats. This was expected following the reasoning for the low conductivity of the MWCNT/dispersant mats.

4.3.2.4 Scanning Electron Microscopy (SEM)

SEM pictures were obtained for the different MWCNT/dispersant mats (Fig 4.9). In general, the MWCNT/dispersant mats had similar morphologies to that of MWCNT/TX100 (Fig 4.9a). However, when looking at the MWCNT/NIPPAm-AMPS mat (Fig 4.9b) we notice that the MWCNT are not completely covered by the dispersant, and the mat formed is very fragile. In contrast, in the MWCNT/N0.15 mat (Fig 4.9c) we can see that the MWCNT have an extensive dispersant coverage and that the matrix formed is significantly packed. In the case of MWCNT/DDAB mat (Fig 4.9d), the MWCNT have a very thin dispersant cover, but the matrix of the mat is highly packed. The MWCNT/DNA mat had a significantly different morphology. We can see that the MWCNT are highly entangled into a complex network. In addition, since the uptake by the MWCNT of the DNA is very high and no DNA clusters can be seen in the picture, we assume that the DNA coverage of the MWCNT is evenly distributed over the entangled ropes of the MWCNT.

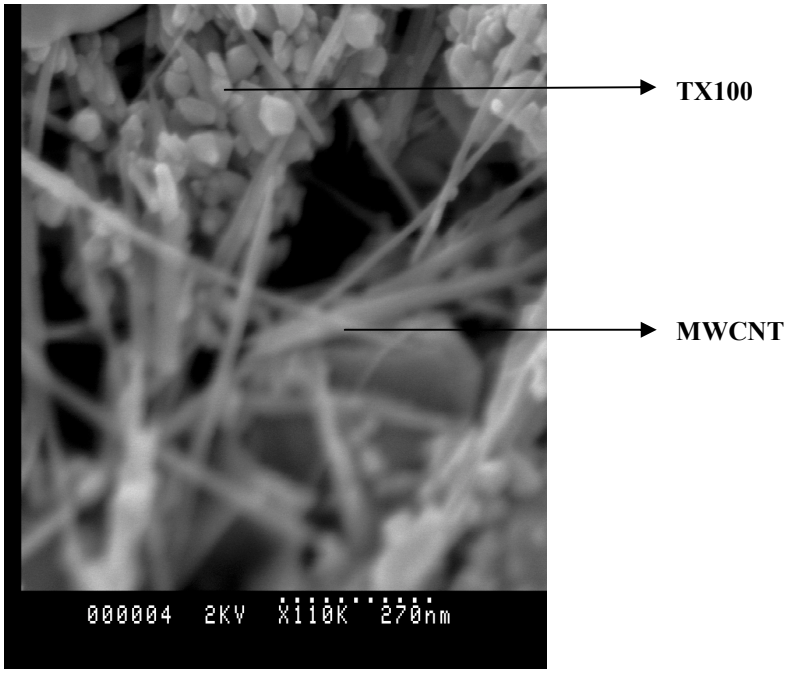

Fig 4.9 SEM picture of MWCNT/TX100

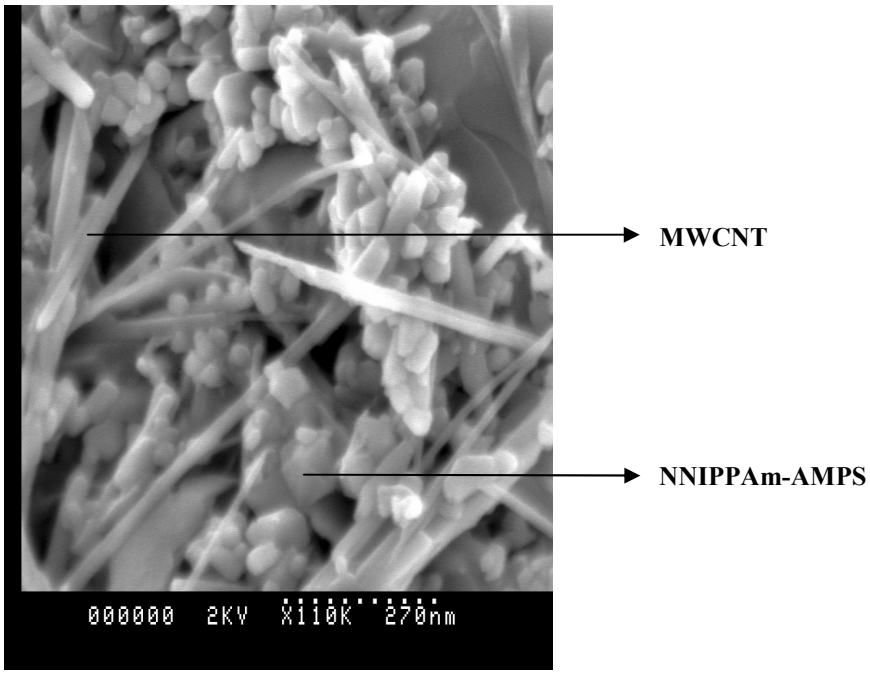

Fig 4.10 SEM picture MWCNT/NIPPAm-AMPS

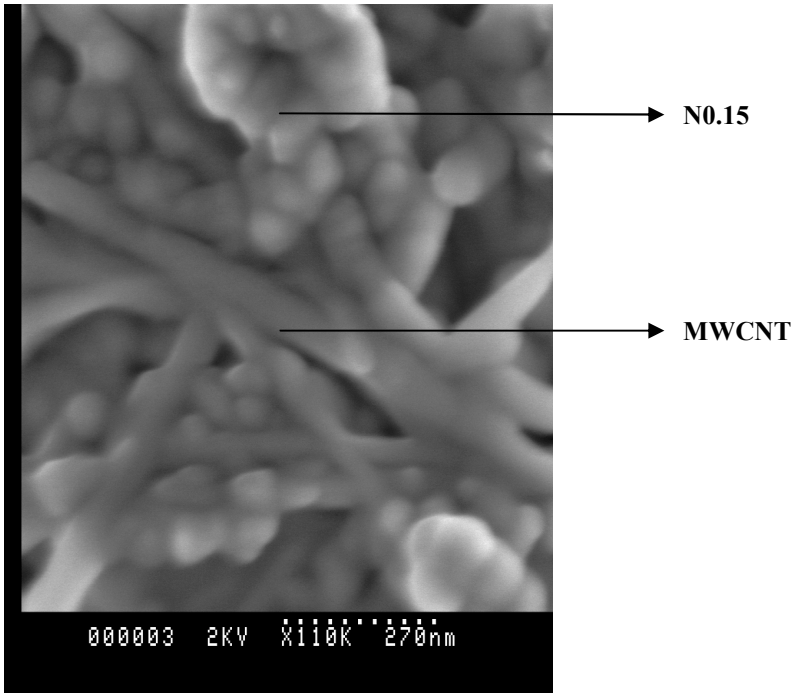

Fig 4.11 SEM picture MWCNT/N0.15

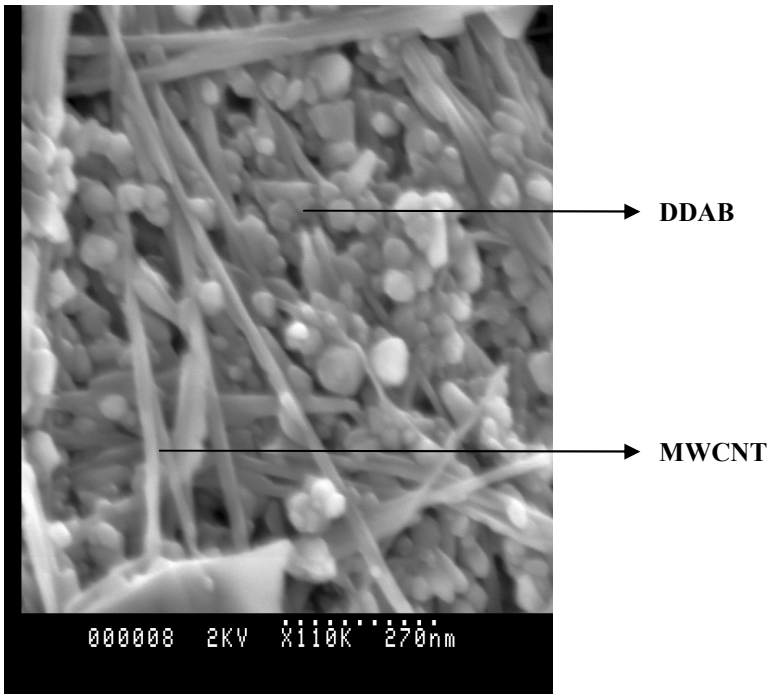

Fig 4.12 SEM picture MWCNT/DDAB

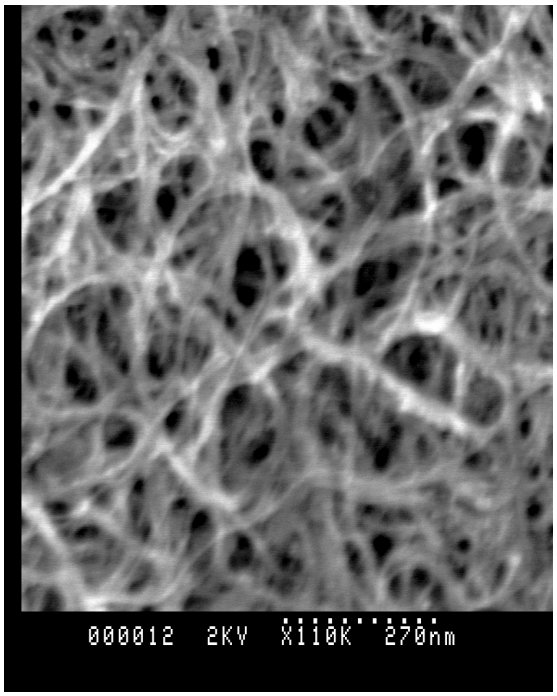

Fig 4.13 SEM picture MWCNT/DNA.

4.4- CONCLUSION

Five different MWCNT composites have been prepared. The zeta potential for MWCNT/N0.15 and MWCNT/DDAB dispersions was positive. This was expected since both of these dispersant are cationic. The other MWCNT dispersions exhibited a negative surface charge, which indicates that the MWCNT are negatively charged. Using particle size and zeta potential analysis, it was found that some dispersant solutions are more effective than others. It was determined that N0.15 and NIPPAm-AMPS are the better dispersing solutions for the MWCNT.

The UV-Vis spectra for the different dispersions were essentially featureless. The UV-Vis spectra of the different dispersions as a function of time was recorded in order to determine the stability of the different dispersions over time. It was found that MWCNT dispersed in TX100 and N0.15 were stable over long periods of time. Real time pictures also confirm this. In this study, of the five different dispersants investigated, N0.15 was found to provide the best MWCNT dispersion, where the MWCNT are well dispersed and also stable over time.

The conductivity and capacitance of MWCNT/dispersant mats were lower in magnitude than those observed for the corresponding RCNT/dispersant and HCNT/dispersant mats. It was found that the conductivity of the MWCNT/dispersant mats is lower than that for the corresponding RCNT and the HCNT mats by four orders of magnitude. Since all mats were prepared using the same dispersant

concentration, and under the same conditions. The low conductivity and capacitance values obtained must be mainly due to the MWCNT.

The electrochemical responses of the MWCNT/dispersant mats were also significantly different from that for the corresponding RCNT/dispersant and HCNT/dispersant mats. This is due to the different properties of the MWCNT compared to the SWCNT.

SEM pictures for the different MWCNT/dispersant mats had similar morphologies. However, the dispersant cover varied in thickness and distribution depending on the dispersant.

CHAPTER FIVE

PREPARATION AND CHARACTERIZATION OF CONDUCTING POLYMER-CARBON NANOTUBES COMPOSITES

5.1- INTRODUCTION

In this chapter we investigate the preparation and characterization of three different types of carbon nanotubes/polymer composites. The combination of the electrical properties of polymers with the mechanical properties of carbon nanotubes, results in novel composites with new electrical and mechanical properties. These composites can be used in a variety of applications such as actuators, sensors, or mechanically reinforced conducting polymers.

5.1.1 Rice carbon nanotubes and conducting polymer composites

Chen *et al* prepared CNT/polymer composites following a similar electrochemical route to the one used in this study (290). However, in this study no additional supporting electrolyte was used in order to avoid the involvement of competitive doping other than the CNT. High-resolution electron Microscopy revealed that the CNT were uniformly covered with PPy, which formed bridges between the tubes.

In addition, a number of approaches involving the development of CNT/conducting polymers composites have been investigated by different researchers. For example,

composite structures of single walled carbon nanotubes (SWCNT) and Poly(3-octylthiophene) polymer were prepared by Alexandrou *et al* (291), conducting polymers and SWCNT have been deposited by evaporating the solvent on different substrates such as gold, silver, and copper, after being dispersed in liquid solvents such as ethanol (292). SWCNT/PPy composites have also been prepared using *in situ* PPy polymerization (293). Characterization of these composites using elemental analysis, X-ray photoelectron spectroscopy, Raman spectra, and X-ray diffraction indicated that there were no significant chemical interactions between the PPy and the SWCNT, the latter simply acting as a template for the polymerization of the conducting PPy. However, it was found that the thermal properties of the SWCNT were modified by the conducting polymer. In addition, it was found that the conductivity of the PPy ~ 3 S/cm and the SWCNT ~50 S/cm were modified by the coating of PPy onto the SWCNT, resulting in a conductivity of 16 S/cm for the composite (304).

Fan *et al*, also polymerized PPy on SWCNT using *in situ* polymerization, the resulting SWCNT/PPy composites exhibited a uniform morphology (294). It was clear that the PPy was coated on the surface of the SWCNT, where the diameter of SWCNT/PPy 80-100 nm was much larger than that for the SWCNT 20-30 nm. However, it was found that the diameter of the SWCNT/PPy could be changed by varying the synthesis conditions.

In this study, first we investigated the preparation of Rice carbon nanotubes (RCNT) and Polypyrrole (PPy) composites. PPy/dopant, PPy/dopant/dispersant, and PPy/dopant/RCNT/dispersant composites were prepared. In the last composite the RCNT were used as dopants Scheme –5.1. Pyrrole (Py) was chosen as it can be

polymerized in a neutral aqueous solution, compatible with the RCNT dispersions. These composites were characterized using a variety of different techniques such as cyclic voltammetry, capacitance, and Scanning Electron Microscopy (SEM).

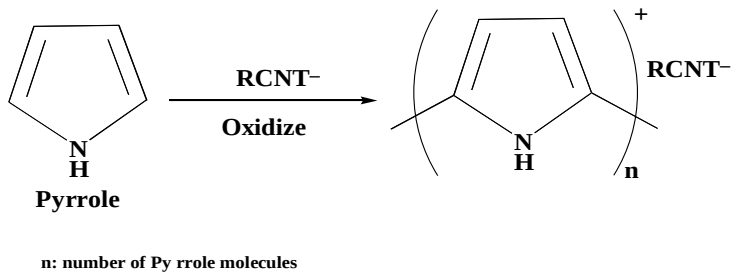

Scheme 5.1 Electropolymerization of PPy with RCNT.

5.1.2 Functionalized Multi-walled carbon nanotubes and conducting polymer composites

Functionalization of SWCNT and MWCNT leads to a high level of solubility in organic and aqueous solutions such as ethanol, methanol, and water (295, 296). However, MWCNT are more suitable for functionalization than SWCNT, as the inner graphene layers can remain unreacted and the essential electronic structure can be retained (297). Suitable oxidative treatment of MWCNT introduces oxygen containing surface groups. These groups stabilize dispersions of MWCNT at much higher concentrations than are possible with the raw material. Once oxidized, the MWCNT will spontaneously disperse in water, due to the fact that oxidation of the MWCNT induces a negatively charged surface particularly through the ionization of the acidic surface groups (298).

Functionalized SWCNT and MWCNT were mixed with poly(propionylethylenimmine-*co*-ethylenimine) (PPEI-EI), the resulting composites were soluble in organic and aqueous solvents (297, 299). The reaction between the nanotubes and the PPEI-EI was through the nanotubes surface-bound carboxylic acid moieties. These acidic groups were found to be associated with the surface defects on the tips and on the side-walls (300).

MWCNT and Poly(*p*-phenylene vinylene) (PPV) composite has been prepared by Ago *et al* (295). It was found that the PPV covers the surface of the MWCNT and forms a well-mixed composite, indicating a very high contact area between the components. Composites with randomly dispersed MWCNT embedded in thermoplastic poly(hydroxyaminoether) were fabricated by solution casting (300). Examination of the surface showed contact and adherence of the polymer to most of the MWCNT and in some cases, the entire surface of the MWCNT was covered with a layer of polymer. Therefore, it is clear that the MWCNT can form intimate contact with the polymer matrix.

MWCNT/poly(phenylacetylene) (PPA) composites were prepared by *in-situ* polymerization (301). It was observed that the presence of the MWCNT in the polymerization matrix decreases the polymer yield. It was also found that the MWCNT were encased by the helical PPA chains. SEM images of these composites suggest that the MWCNT are compounded with PPA *in situ* during the polymerization reaction. Since the nanotubes are full of π-electrons, the phenylacetylene monomers are likely to “wet” the surface of the tubes through the

≡C—H---π hydrogen bonds, and polymerization of such absorbed monomers would produce PPA chains wrapped around the tubes (302).

Jia *et al* synthesized MWCNT and poly(methyl methacrylate) (PMMA) (303). MWCNT/PMMA was also produced by *in situ* polymerization by Hwang *et al* (304). In this case, the MWCNT have been initiated by 2,2`-azobisisobutyronitrile (AIBN) to open their π-bonds, which imply that the MWCNT may participate in methyl methaacrylate (MMA) polymerization and in this case form strong combining interface between the MWCNT and the PMMA. In addition, the MWCNT can link covalently with PMMA, which results in obstructing the growth of PMMA, with this bond a strong interface between the MWCNT and the PMMA will be produced. Finally, the MWCNT can react with AIBN and link to each other (303).

Other workers have used electro-deposition to coat PPy onto aligned MWCNT where the MWCNT were electrochemically coated with PPy in a three-electrode cell (305, 306). PPy formed a continuous layer over the length and tips of the MWCNT in the aligned array. It was also found that it is possible for PPy to encapsulate more than one MWCNT in each of the distinct composite tubes.

In this section we have prepared functionalized multi-walled carbon nanotubes (FMWCNT) and PPy composites. The MWCNT were functionalized using sulfonic acid ($–SO_3H$) in three different ratios. The PPy/FMWCNT composites were grown using constant current and constant potential. The resulting composites were characterized using different techniques such as cyclic voltammetry, capacitance, and Scanning Electron Microscopy (SEM).

5.1.3 HiPco-Carbon nanotubes and Polyaniline composites

Polyaniline films (PAn) were electrodeposited on MWCNT by Downes *et al* (307). The combination of carbon nanotubes with polymers offers an attractive route not only to reinforce the polymer films but also to introduce new electronic properties due to morphological modification or electronic interactions between the two components.

In this section we describe the preparation of HCNT/PAn composites. These composites are prepared by either casting films of HCNT/PAn mixtures, or by casting PAn(acid) films onto HCNT mats. Characterization of these composites was carried out using cyclic voltammetry. In addition, conductivity measurements and the actuation behavior for the different composites were recorded.

5.2- EXPERIMENTAL

5.2.1 Materials

Sodium nitrate (M.W. 84.99 Da, Aldrich), dextran sulfate (Dex) (M.W. 500,000 Da, Aldrich), ammonium hexafluorophosphate (AHFP) (M.W. 163.0 Da, Aldrich), sodium dodecyl sulfate (SDS) (M.W. 288.37 Da, Aldrich), Poly(vinyl alcohol) (PVA) (97% hydrolyzed, M.W. 50,000 – 85,000 Da, Aldrich), Polyvinyl pyrrolidone (PVP) (M.W. 25,000 Da, Merck). Pyrrole and Aniline were purchased from Sigma-Aldrich, and were both distilled prior to use.

RCNT were obtained from Tubes @ Rice (Rice University, Houston TX) as a suspension in toluene, with a tube diameter of 1.2-1.38 nm. The FMWCNT were obtained from CSIRO (Australia). The MWCNT were functionalized using sulfonic

acid ($–SO_3H$) as supplied by CSIRO, and the $–SO_3H$ content in the MWCNT was varied according to Table –5.1.

Table –5.1 Sulfonic acid ($–SO_3H$) contents in MWCNT.

Number	**W_{MWCNT}**	**pH**	**$[SO_3H]$ mmol/ml**	**SO_3H w/w**	**SO_3H mol/mol**
Sulf-MWCNT # I	5.9	2.54	2.88×10^{-3}	19.7	2.58
Sulf-MWCNT # II	4.4	2.48	3.31×10^{-3}	30.5	4.51
Sulf-MWCNT # III	4.7	2.34	4.57×10^{-3}	39.3	5.83

The HiPco carbon nanotubes were purchased from Carbon Nanotechnologies Incorporated (CNI) as a solid powder. These carbon nanotubes are produced by the HiPco process (**Ch. 3** section **3.1)**, with an average tube diameter of 1.1 nm.

5.2.2 Instrumentation

Four-point probe conductivity measurements were recorded for the HCNT/PAn composites. A digital micrometer was used to measure the thickness of the composites. A constant current of 1 mA was passed through the sample using an EG & G Princeton Applied Research model 363 Potentiostat/Galvanostat, and the resistance was recorded using a Hewlett Packard model 34401.

After growth cyclic voltammograms were recorded using a MacLab/4e and a Mac lab potentiostat. The electrochemical cell consisted of a silver/silver-chloride (Ag/AgCl) electrode as the reference electrode, a Platinum (Pt)-mesh electrode as the auxiliary electrode. The working electrode was gold-coated Mylar in the case of RCNT/polymer composites, gold-coated Mylar or Indium Tin Oxide coated glass

(ITO-glass) in the case of FMWCNT/polymer composites, and 2.5 X 0.5 cm strips (fully immersed) of the different composites in the case of HCNT/PAn composites. The potential window applied for the RCNT/polymer composites varied with the different composites. For the FMWCNT/polymer and HCNT/PAn composites the potential applied was from E = –1, +1 V. 0.1 M $NaNO_3$ was used as the supporting electrolyte for the RCNT/polymer and FMWCNT/polymer composites. In the case of HCNT/PAn composites 0.1 M $NaNO_3$, 0.1 M HNO_3, and 1 M HNO_3 were used separately as the electrolyte solution. Scan rate of 50 mV/s was applied in all cases.

The capacitance for the RCNT/polymer and FMWCNT/polymer composites were measured by recording CVs at different scan rates 50, 25, 10 and 5 mV/s. The capacitance measured was in mF/cm^2, due to the fact that the weight of the deposited thin films could not be measured. The potential window used was E = -0.1, +0.3 V, and current measurements were taken at E = +0.1 V. The electrochemical cell was as described above with the electrolyte used being 1 M $NaNO_3$.

The actuation behavior of the HCNT/PAn composites was recorded using the following techniques and instruments. The samples were prepared for testing by cutting them into 0.25 X 1.2 cm wide strips with a razor blade. Actuation studies were carried out with a single platinum electrode connected to the top of the HCNT/PAn composite strip and isolated from the stainless steel clamps by plastic adhesive tape. The sample was then suspended from the arm of the analytical balance, with the lower clamp held captive by a fixed frame so that with the removal of the adjustable weights, the sample was loaded in tension. A linear variable distance transducer (LVDT) probe, that was calibrated by hand, was mounted atop the arm of the analytical balance, and the expansion/contraction of the sample was detected by

the LVDT. The electrochemical cell consisted of 1 M $NaNO_3$, 1 M HCl, 1 M NaCl and 3 M NaCl as the electrolyte testing solutions, the HCNT/PAn strips (through the clamps) as the working electrode, a Pt-mesh electrode as the auxiliary electrode and an Ag/AgCl as the reference electrode. The electrodes and the LVDT were connected to a CV27 Voltammograph and a MacLab/4e. The potential window applied was E = -1, +1 V for PAn(acid) and E = -1, +0.5 V for HCNT/PAn composites. A HCNT/PAn sample was used to investigate the effect of load attached to the sample on the actuation behavior. The load was increased in the tensile mode from 2 to 30 g (equivalent to stresses of 0.08 to 1.23 MPa). The overall layout of the analytical balance is shown in (**Ch. 3**, Fig 3.1, and 3.2).

Scanning Electron Microscopy (SEM) Pictures were obtained using a Hitachi S-900 FESEM.

5.2.3 Composite preparation

5.2.3.1 RCNT/polymer composites

5.2.3.1.1 Polymer preparation

PPy/NO_3, PPy/Dex, PPy/AHFP and PPy/SDS were electrodeposited on gold-coated Mylar. 0.1 M Py was added to 5 mL of each of the following solutions, 0.1 M $NaNO_3$, 0.1 M Dex, 0.1 M AHFP, and 0.2% SDS. The electrochemical polymerization cell consisted of a silver/silver-chloride (Ag/AgCl) electrode as the reference electrode, a Platinum (Pt)-mesh electrode as the auxiliary electrode, and a gold-coated Mylar as the working electrode. The gold-coated Mylar electrodes were washed with Milli-Q-Water, then ethanol and left to dry prior to use. A Galvanostat

was then used to apply a constant current of 1 mA (j= 1.3 mA/cm^2) for 5 min, and a MacLab/4e was used to record the output.

5.2.3.1.2 Polymer/dispersant with no RCNT incorporated

PPy/NO_3/PVP, PPy/Dex/PVP, and PPy/AHFP/PVP were prepared as follows:

- 0.1 M Py and 0.1 M $NaNO_3$ were added to 5 mL of 0.2% PVP solution.
- 0.1 M Py and 0.1 M Dex were added to 5 mL of 0.2% PVP solution.
- 0.1 M Py and 0.1 M AHFP were added to 5 mL of 0.2% PVP solution.

PPy/NO_3/PVA, PPy/Dex/PVA, and PPy/AHFP/PVA were prepared as follows:

- 0.1 M Py and 0.1 M $NaNO_3$ were added to 5 mL of 0.2% PVA solution.
- 0.1 M Py and 0.1 M Dex were added to 5 mL of 0.2% PVA solution.
- 0.1 M Py and 0.1 M AHFP were added to 5 mL of 0.2% PVA solution.

A Galvanostat was used to apply a current of 1 mA (j= 1.3 mA/cm^2) for 5 min to electrodeposit the polymers.

5.2.3.1.3 Polymer/dispersant with RCNT incorporated

RCNT were dispersed using 0.2% SDS, or 0.2% PVP, or 0.2% PVA as described in **Ch. 2**, section **2.2.1**.

RCNT/PPy/NO_3/PVP, RCNT/PPy/Dex/PVP, and RCNT/PPy/AHFP/PVP were prepared as follows:

- 0.1 M Py and 0.1 M $NaNO_3$ were added to 5 mL of 0.2% RCNT/PVP dispersion.
- 0.1 M Py and 0.1 M Dex were added to 5 mL of 0.2% RCNT/PVP dispersion.

- 0.1 M Py and 0.1 M AHFP were added to 5 mL of 0.2% RCNT/PVP dispersion.

RCNT/PPy/NO_3/PVA, RCNT/PPy/Dex/PVA, and RCNT/PPy/AHFP/RCNT/PVA were prepared as follows:

- 0.1 M Py and 0.1 M $NaNO_3$ were added to 5 mL of 0.2% RCNT/PVA dispersion.
- 0.1 M Py and 0.1 M Dex were added to 5 mL of 0.2% RCNT/PVA dispersion.
- 0.1 M Py and 0.1 M AHFP were added to 5 mL of 0.2% RCNT/PVA dispersion.

RCNT/PPy/SDS was also prepared by adding 0.1 M Py to 5 ml of RCNT/SDS dispersion, where SDS acted as both the dopant to PPy and the dispersant to RCNT.

All the mixtures were then sonicated for 15 min. A Galvanostat was used to apply a current of 1 mA (j= 1.3 mA/cm^2) for 5 min to electrodeposit the composites, and a MacLab/4e was used to record the output.

5.2.3.2 FMWCNT/polymer preparation

The electrochemical cell was a two-electrode cell, with a Pt-mesh electrode acting as the counter electrode (auxiliary and reference electrodes combined), and a working electrode. The working electrode was a gold-coated Mylar electrode in some experiments and ITO-glass in other experiments.

10.5 mg FMWCNT (0.176 w%) were added to 6 mL Milli-Q-Water and sonicated for 15 min, 0.15 mL Py (0.25 M) was added and the mixture was then sonicated for an additional 15 min.

The composites were prepared by electrodeposition from a solution containing the FMWCNT and Py by applying a constant current of *i*=1 mA (j=3.55 mA/cm^2) for 1-hour using a Galvanostat. The composites were also deposited by applying a constant potential of E = +1 V for 1-hour using CV27 Potentiostat. In this case the charge passed (Q) was measured using a MacLab/4e, where the charge (Q) was constant in all experiments.

5.2.3.3 Preparation of HCNT/PAn composites

5.2.3.3.1 Preparation of Polyaniline films

85 g of ± Camphor sulfonic acid (1 M) and 3.4 g of distilled Aniline (0.1 M) were added to 325 mL of Milli-Q-Water, and placed in an ice bath. To this 41 mL ammonium potassium sulfate (0.1 M) was added drop wise, and the solution was left overnight for the reaction to take place in order for PAn (salt) to be formed.

The product was vacuum filtered, and then dispersed in Milli-Q-Water. An excess of sodium hydroxide (NaOH) pellets were added to produce PAn(base), the mixture was then filtered and dried in an oven at 60 °C overnight.

The PAn(base) was added to N-methyl pyrrolidone (NMP) to make up a 4% w/w solution. This translates to 400 mg PAn(base) in 10 ml NMP. 1 mL 8% v/v ammonium hydroxide (NH_4OH) was added to prevent the mixture from gelling.

The mixture was cast on glass slides and placed on a heating plate to dry. The resulting film was then peeled off and placed in 1 M HCl to convert it into the PAn(acid) form, which is electrically conductive.

5.2.3.3.2 Preparation of PAn(acid) on HCNT mats

HCNT mats were prepared as described previously in **Ch. 3**. The PAn(base) was cast on the HCNT mat and left to dry. The mat was then placed in 1 M HCl to convert the PAn(base) into the PAn(acid).

5.2.3.3.3 Preparation of HCNT/PAn(acid) composites

8 mg HCNT were added to 5 mL 1,2-Dichlorobenzene (1,2-DCB) 4% w/w loading, and sonicated for 30 min. This dispersion was then added to 5 mL of the previously prepared PAn(base) in N-methoxypyrrolidone (NMP), and sonicated for 15 min. Films from the final mixture were cast on a glass slide, and placed on a heating plate to dry. The films where then peeled off, and placed in 1 M HCl to convert the PAn(base) into the PAn(acid).

5.3- RESULTS & DISCUSSION

5.3.1 RCNT/polymer composites

5.3.1.1 Cyclic voltammetry

Cyclic voltammetry as a technique for the characterization of conducting compounds was discussed previously in **Ch. 1**, section **1.2**. In general, for PPy/dopant compounds a cathodic peak due to reduction is usually observed between E = -0.3, -0.1 V. Also, a broad anodic tail is observed during the oxidation process (308). However, we must note that the oxidation/reduction peaks for PPy/dopant compounds shift in either direction depending on the dopant and electrolyte used (309). For example, for PPy/SO_4 in $NaNO_3$, the oxidation peak occurs at E ~ -0.35 V, and the reduction peak is very sharp and occurs at E ~ -0.42 V. PPy/ClO_4 in $NaNO_3$, has reduction and oxidation peaks at E ~ -0.3 V (309).

CVs were obtained for the different conducting polymers prepared with and without RCNT present. The CVs for PPy/SDS and RCNT/PPy/SDS, and the CVs for PPy/NO_3, PPy/NO_3/PVP, and RCNT/PPy/NO_3/PVP were similar (Fig 5.1, 5.2), indicating that the presence of the RCNT did not have a significant effect on the electrochemistry of the polymer. In addition, a highly capacitive behavior was observed. Also, in the case of PPy/AHFP the addition of the dispersant and the incorporation of the RCNT did not have any effect, and all the CVs exhibited a capacitive behavior (Fig 5.4). In the case of PPy/Dex the polymer exhibited very broad redox peaks, while PPy/Dex/PVP had no redox peaks (Fig 5.3a, 5.3b). However, the addition of RCNT resulted in the emergence of a broad oxidation peak at E ~ -0.05 V (Fig 5.3c).

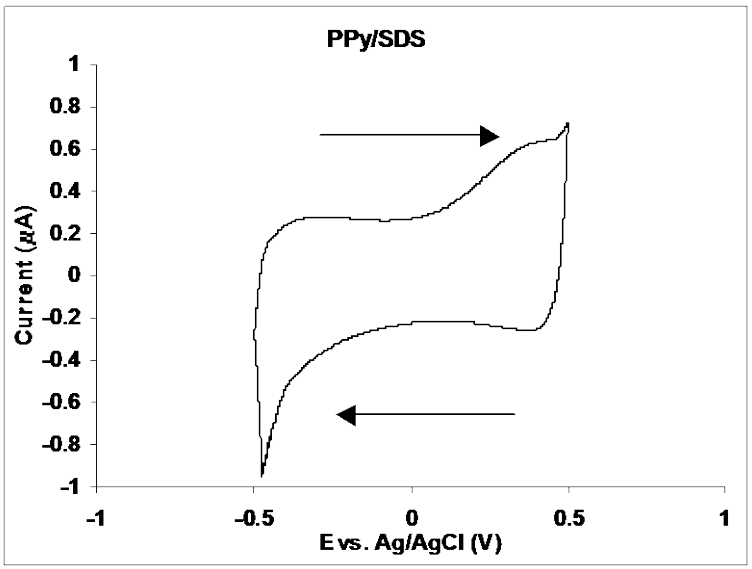

(a)

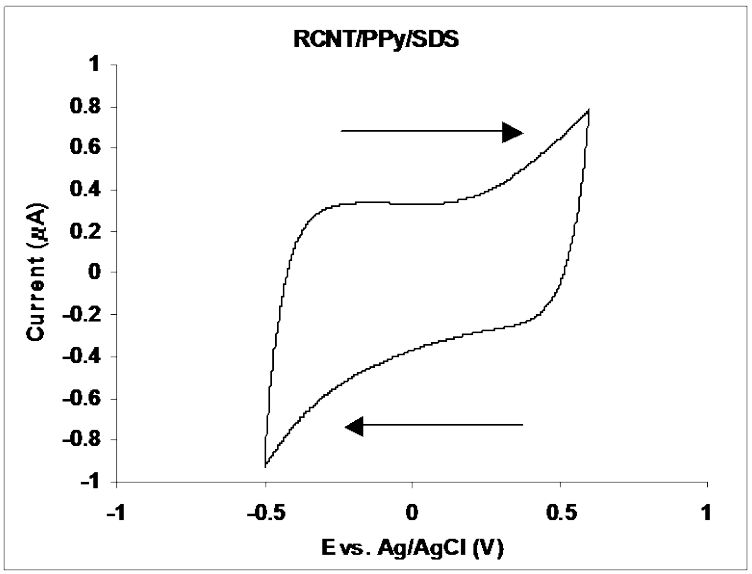

(b)

Fig 5.1 Cyclic voltammograms (2nd cycle) of (a) PPy/SDS, (b) RCNT/PPy/SDS with 0.1 M $NaNO_3$ as a supporting electrolyte, E = -0.5, + 0.5 V, scan rate of 50 mV/s.

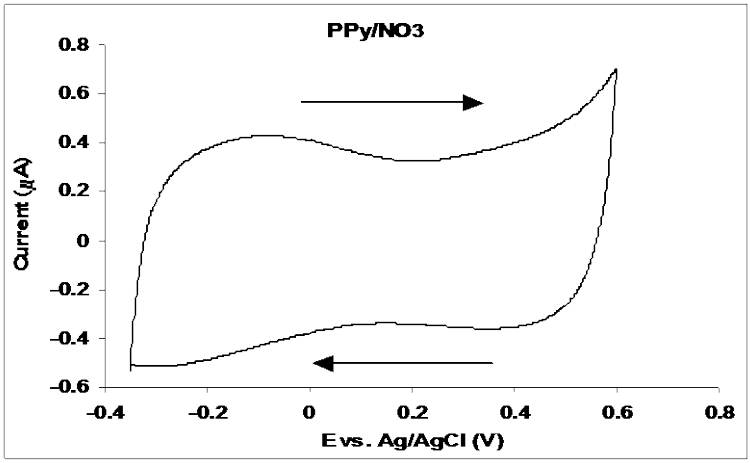

(a)

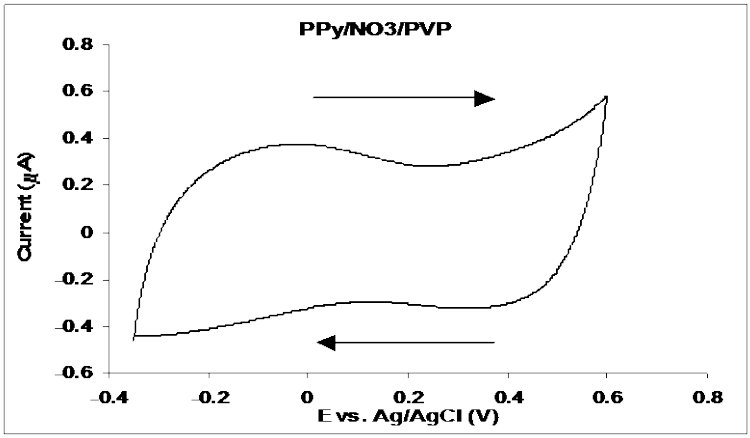

(b)

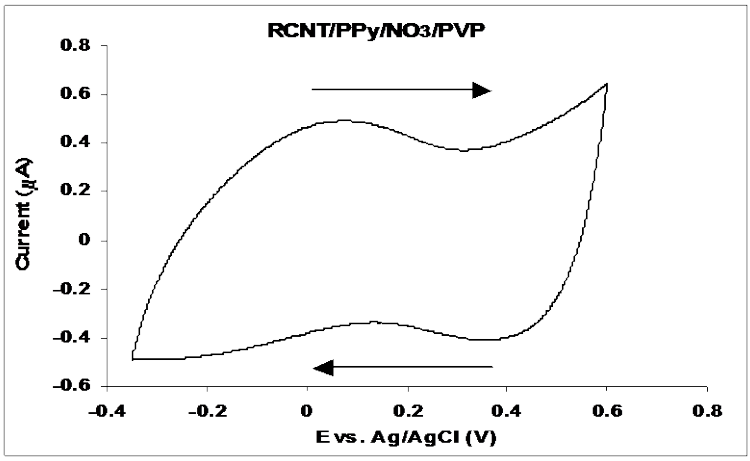

(c)

Fig 5.2 Cyclic voltammograms (2nd cycle) of (a) PPy/NO_3, (b) PPy/NO_3/PVP, and (c) RCNT/PPy/NO_3/PVP with 0.1 M $NaNO_3$ as a supporting electrolyte, E = -0.3, + 0.6 V, scan rate of 50 mV/s.

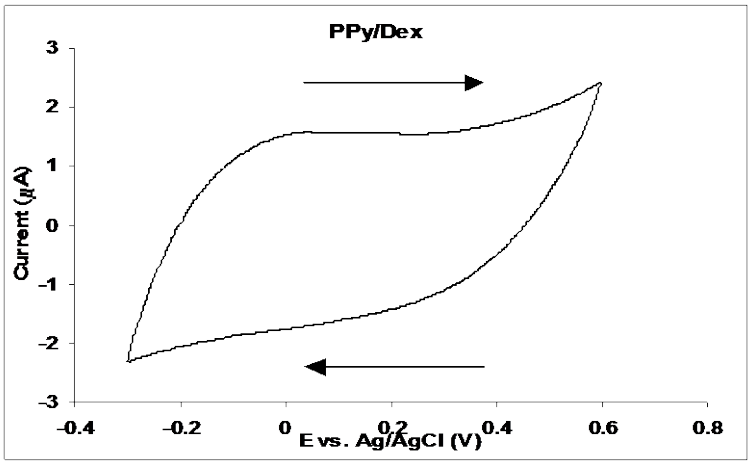

(a)

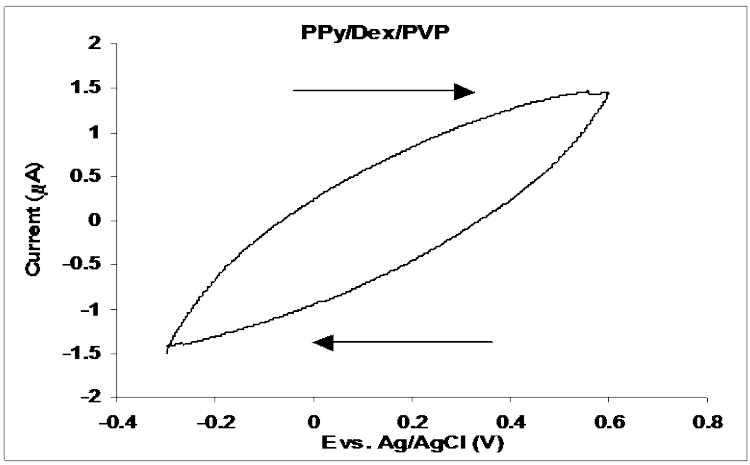

(b)

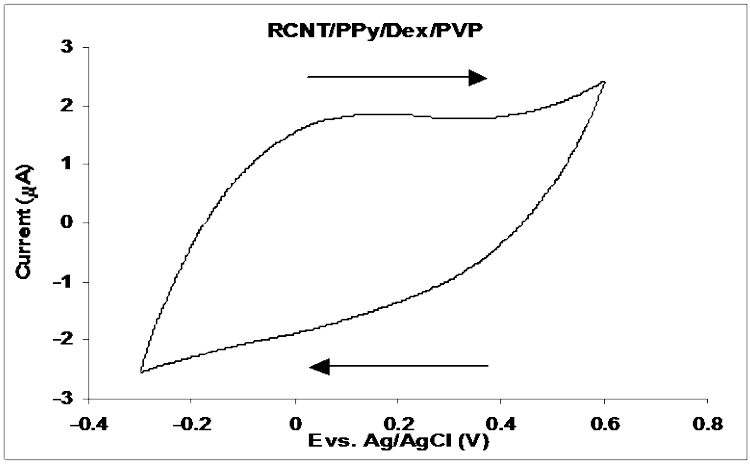

(c)

Fig 5.3 Cyclic voltammograms (2nd cycle) of (a) PPy/Dex, (b) PPy/Dex/PVP, and (c) RCNT/PPy/Dex/PVP with 0.1 M $NaNO_3$ as a supporting electrolyte, E = -0.3, + 0.6 V, scan rate of 50 mV/s.

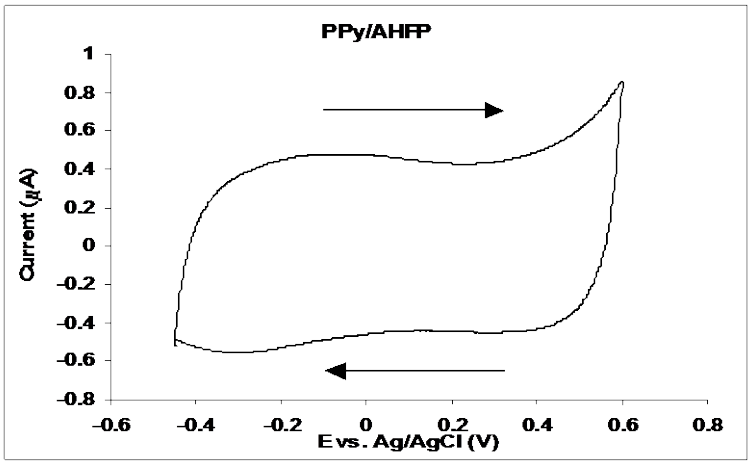

(a)

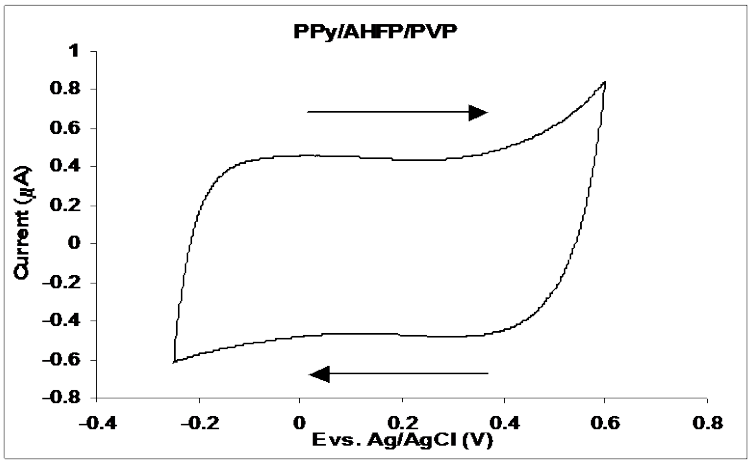

(b)

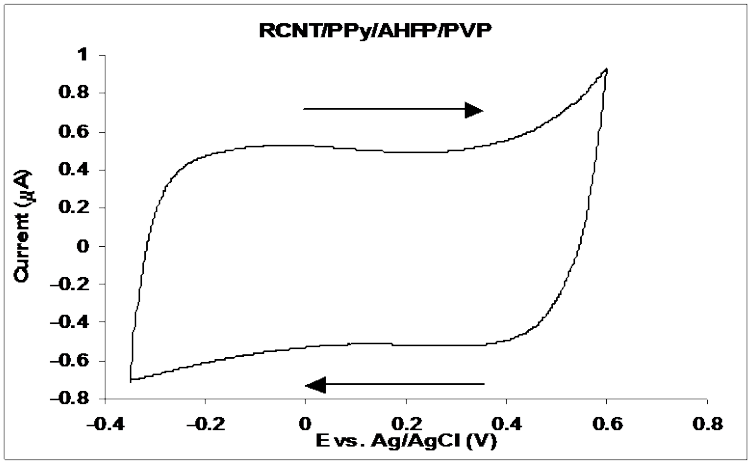

(c)

Fig 5.4 Cyclic voltammograms (2nd cycle) of (a) PPy/AHFP, (b) PPy/AHFP/PVP, and (c) RCNT/PPy/AHFP/PVP with 0.1 M $NaNO_3$ as a supporting electrolyte, E = -0.3, + 0.6 V, scan rate of 50 mV/s.

5.3.1.2 Capacitance

CVs were recorded for the different composites using different scan rates. The difference between the oxidation and reduction current at E = 0.1 V was plotted as a function of the scan rate, the best straight line was graphed and slope calculated. Capacitance = ½ slope (mF), Capacitance = Capacitance/area (mF/cm^2). In this case the capacitance was measured as mF/cm^2 instead of F/g, because the weight of the thin polymer layer could not be measured, Table –5.2. An example of the calculations is presented in **Ch. 2**, section **2.3.2.3**.

Table –5.2 Capacitance for the different composites.

Composite	**Capacitance (mF/cm^2 ± 0.1)**
PPy/SDS	1.3
RCNT/PPy/SDS	3.8
PPy/$NaNO_3$	6.0
PPy/NO_3/PVP	4.4
RCNT/PPy/NO_3/PVP	4.2
PPy/NO_3/PVA	4.8
RCNT/PPy/NO_3/PVA	4.6
PPy/Dex	26.2
PPy/Dex/PVP	5.9
RCNT/PPy/Dex/PVP	13.4
PPy/Dex/PVA	4.2
RCNT/PPy/Dex/PVA	6.5
PPy/AHFP	9.0
PPy/AHFP/PVP	9.0
RCNT/PPy/AHFP/PVP	7.6
PPy/AHFP/PVA	8.7
RCNT/PPy/AHFP/PVA	8.7

From the table above we notice that when RCNT were added to PPy/SDS there was an increase in the capacitance values. PPy/NO_3 had a higher capacitance value compared to the capacitance values when the dispersants or the RCNT/dispersant were added. In general, the addition of RCNT and/or dispersant to PPy/Dex resulted in a significant decrease in capacitance. However, RCNT/PPy/Dex/PVP had a higher capacitance value compared to PPy/DS/PVP. The addition of the RCNT and/or dispersant to PPy/AHFP did not have any significant effect on capacitance.

5.3.1.3 Scanning Electron Microscopy (SEM)

The SEM pictures show the differences in morphology for the composites that have no RCNT incorporated into them and the composites that contain RCNT (Fig 5.5). As can be seen in the polymer pictures, the typical cauliflower morphology of PPy is observed. However, in the picture of the polymers that incorporate RCNT, the morphology is completely different. The RCNT are assumed to be covered with the polymer or/and the polymer and the dispersant.

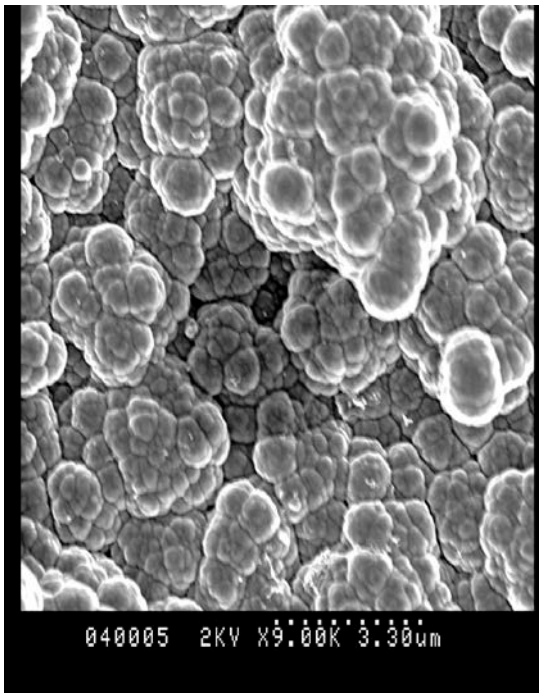

(a) PPy/SDS

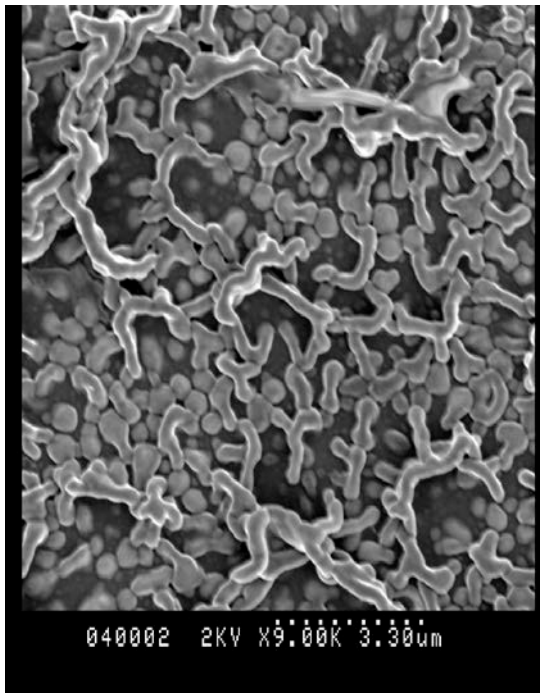

(b) RCNT/PPy/SDS

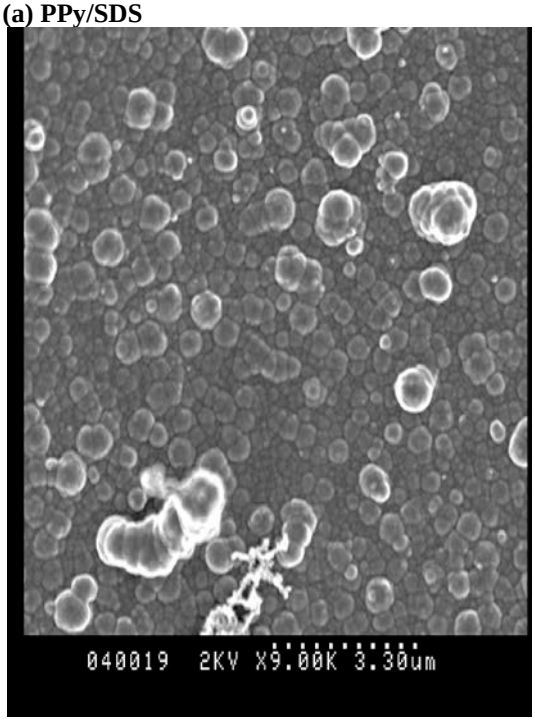

(c) PPy/$NaNO_3$

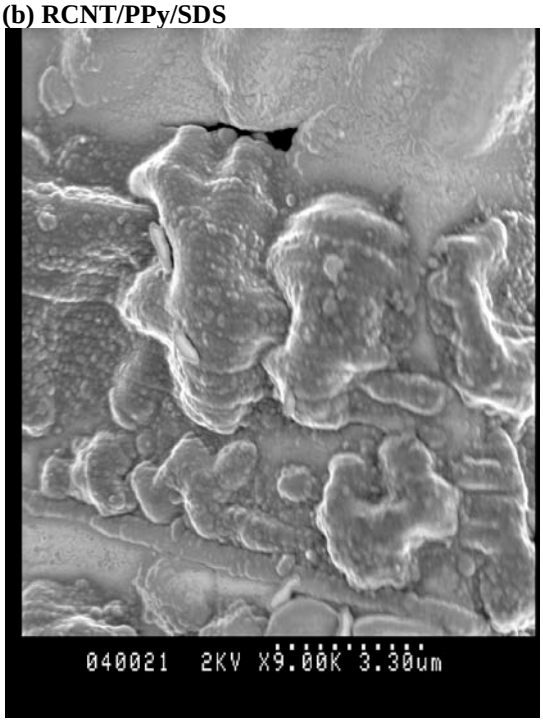

(d) RCNT/PPy/$NaNO_3$/PVP

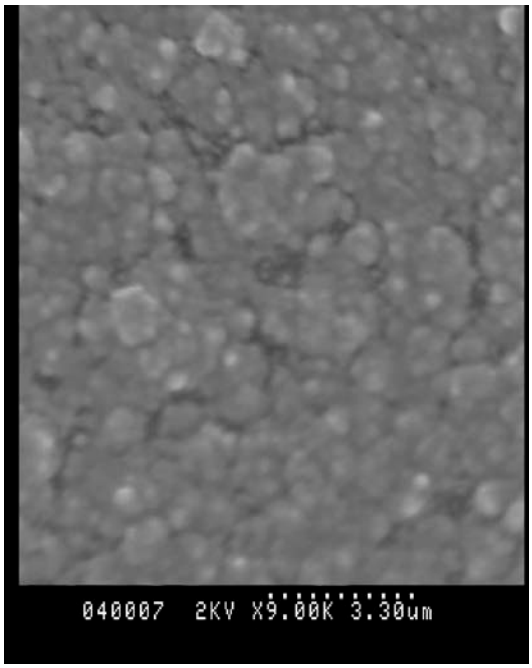

(e) PPy/Dex

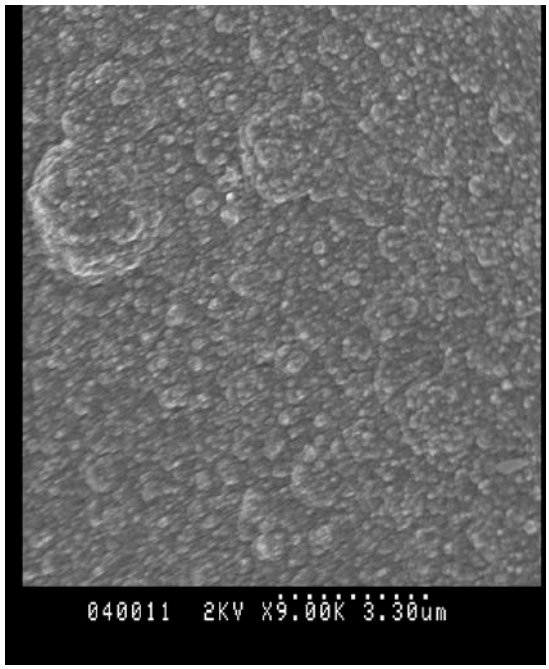

(f) RCNT/PPy/Dex/PVP

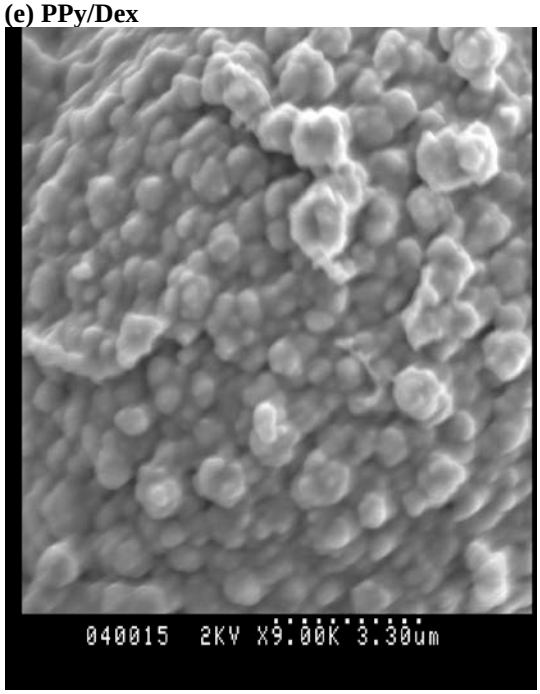

(g) PPy/AHFP

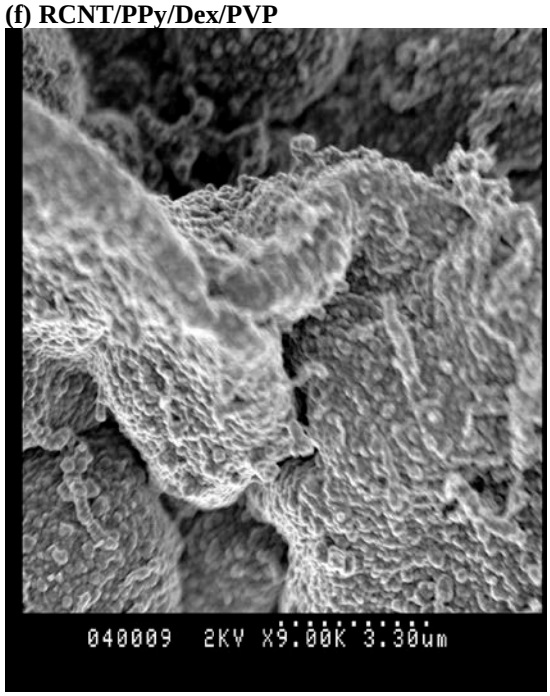

(h) RCNT/PPy/AHFP/PVP

Fig 5.5 SEM pictures of (a) PPy/SDS, (b) RCNT/PPy/SDS/PVP, (c) PPy/$NaNO_3$, (d) RCNT/PPy/$NaNO_3$/PVP, (e) PPy/Dex, (f) RCNT/PPy/Dex/PVP, (g) PPy/AHFP, and (h) RCNT/PPy/AHFP/PVP.

5.3.2 FMWCNT/polymer composites

FMWCNT can be dispersed in water. Therefore, there was no need for a dispersant to be used, leaving the FMWCNT acting as dopant to PPy. In addition, no other supporting electrolyte was added, insuring that the FMWCNT will act as the sole dopant to PPy. Electrodeposition was carried out as described in the experimental section.

In general, it was found that the samples electrodeposited on both gold-coated Mylar or ITO-glass, using constant current were thicker than the samples grown using constant potential to the same charge (Q). One explanation could be that a higher percentage of the FMWCNT was incorporated into the matrix of the composite when electrodeposited using constant current.

5.3.2.1 Cyclic voltammetry

5.3.2.1.1 FMWCNT/PPy composites grown on gold-coated Mylar

A CV for the gold-coated Mylar electrode was recorded to be used as a reference when comparing the composites grown on gold-coated electrodes (Fig 5.6). The CV for the PPy/FMWCNT **I**, **II**, and **III**, grown by constant current and constant potential to the same charge (Q) are shown in (Fig 5.7).

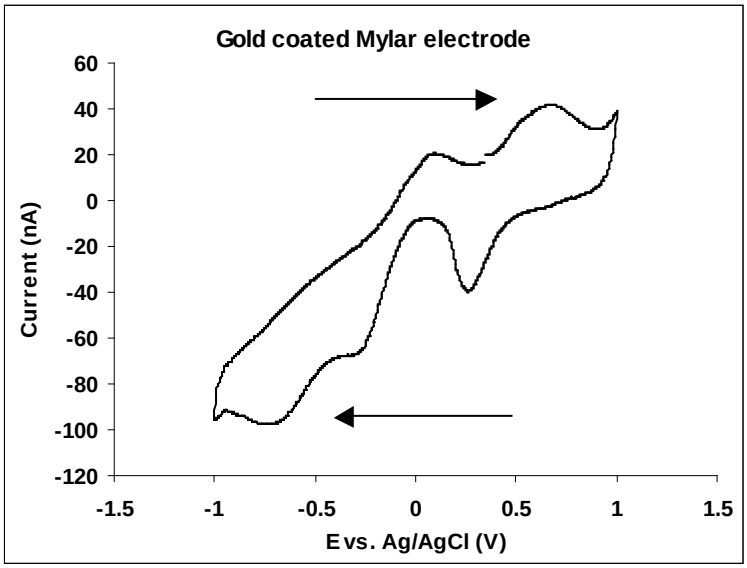

Fig 5.6 Cyclic voltammogram (2nd cycle) of gold-coated Mylar with 0.1 M $NaNO_3$ as a supporting electrolyte, E = -1, +1 V, with a scan rate of 50 mV/s.

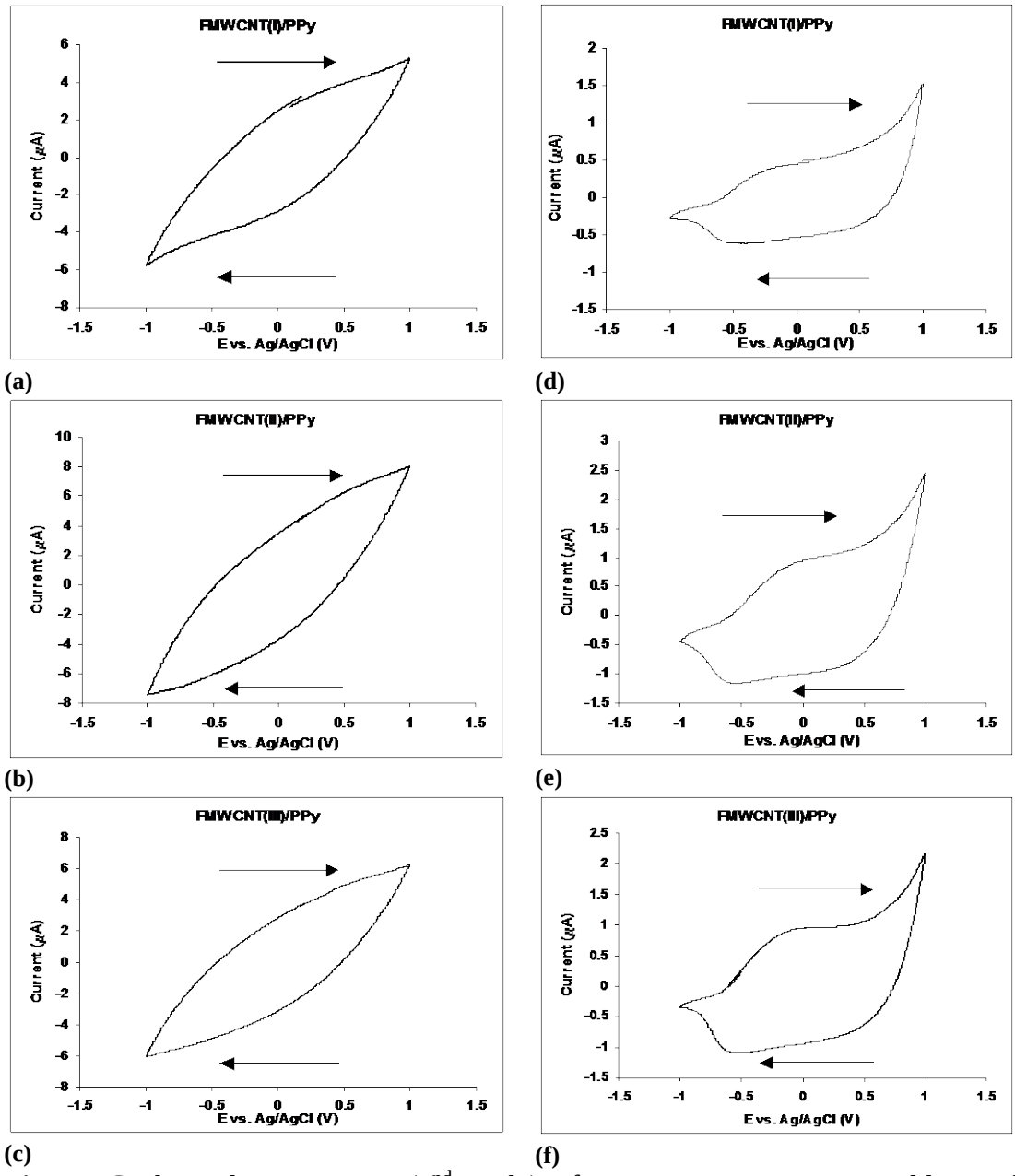

Fig 5.7 Cyclic voltammograms (2nd cycle) of composites grown on gold-coated Mylar using constant current (a) FMWCNT(**I**)/PPy, (b) FMWCNT(**II**)/PPy, (c) FMWCNT(**III**)/PPy, and composites grown using constant potential (d) FMWCNT(**I**)/PPy, (e) FMWCNT(**II**)/PPy, and (f) FMWCNT(**III**)/PPy. 0.1 M $NaNO_3$ was used as a supporting electrolyte, E = -1, +1 V, scan rate of 50 mV/s.

As we can see from the figures above, the PPy/FMWCNT grown using constant current do not exhibit any redox peaks. However, PPy/FMWCNT grown using constant potential exhibited the behavior of a conducting substance. An oxidation peak at E ~ -0.25 V, and a reduction peak at E ~ -0.5 V were observed. In addition, we can see that the CVs for the PPy/FMWCNT composites on the gold-coated Mylar show no similarities to the CV of the gold-coated Mylar itself. Indicating that the Mylar surface is covered by the composites.

5.3.2.1.2 FMWCNT/PPy composites grown on Indium Tin Oxide coated glass (ITO-glass)

A CV for the ITO glass was recorded to be used as a reference when comparing the composites grown on ITO glass (Fig 5.8). The CV for the FMWCNT (**I**, **II**, and **III**)/PPy grown by constant current and constant potential to the same charge (Q) are shown in (Fig 5.9).

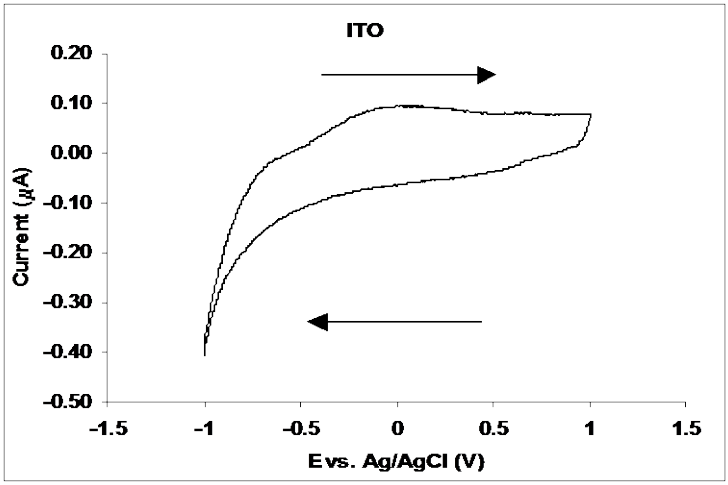

Fig 5.8 Cyclic voltammogram (2nd cycle) of ITO glass with 0.1 M $NaNO_3$ as a supporting electrolyte, E = -1, +1 V, with a scan rate of 50 mV/s.

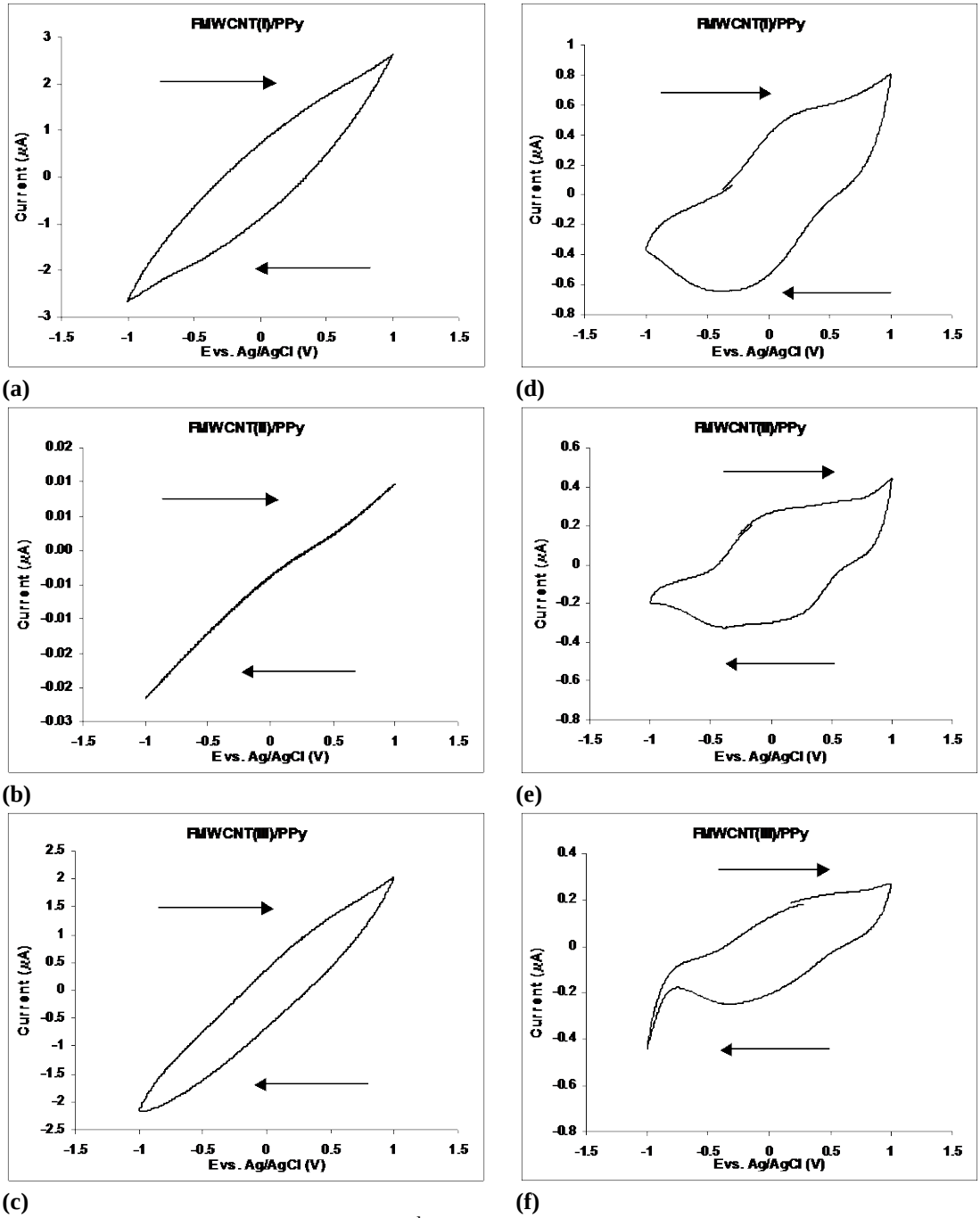

Fig 5.9 Cyclic voltammograms (2nd cycle) of composites grown on ITO glass using constant current (a) FMWCNT(**I**)/PPy, (b) FMWCNT(**II**)/PPy, (c) FMWCNT(**III**)/PPy, and composites grown using constant potential (d) FMWCNT(**I**)/PPy, (e) FMWCNT(**II**)/PPy, and (f) FMWCNT(**III**)/PPy. 0.1 M $NaNO_3$ was used as a supporting electrolyte, E = -1, +1 V, scan rate of 50 mV/s.

As we can see from the figures above, the FMWCNT/PPy composites grown by constant current do not exhibit any redox responses, while the FMWCNT/PPy composites grown by constant potential exhibit redox peaks. An oxidation peak is observed at E ~ 0.00 V, and a reduction peak at E ~ -0.4 V. This is the same behavior observed for the composites grown on gold-coated Mylar, which indicates that the redox behavior of these composites is not related to the underlying electrode, but rather to the method of growth.

5.3.2.2 Capacitance

Cyclic voltammograms were recorded for the different composites using different scan rates. The difference between the oxidation and reduction current at E = 0.1 V was plotted as a function of the scan rate, the best straight line was graphed and slope calculated. Capacitance = ½ slope (mF), Capacitance = Capacitance/area (mF/cm^2). In this case the capacitance was measured as mF/cm^2 instead of F/g, because the weight of the thin polymer layer could not be measured. An example of the calculations is presented in **Ch. 2**, section **2.3.2.3**. The results are presented in Table –5.3. From the results we find that the capacitance increases as the $–SO_3H$ contents in the MWCNT increases, regardless of the method of growth or the underlying electrode.

Table –5.3 Capacitance of FMWCNT/PPy composites.

Composite	**Capacitance ($mF/cm^2 \pm 0.01$)**
On Gold-coated Mylar by Constant current	
FMWCNT (I)/PPy	0.05
FMWCNT (II)/PPy	0.21
FMWCNT (III)/PPy	0.46
On Gold-coated Mylar by Constant potential	
FMWCNT (I)/PPy	0.02
FMWCNT (II)/PPy	0.03
FMWCNT (III)/PPy	0.42
On ITO glass by Constant current	
FMWCNT (I)/PPy	$2.4 X10^{-4}$
FMWCNT (II)/PPy	$1.78X10^{-3}$
FMWCNT (III)/PPy	1.74
On ITO glass by Constant potential	
FMWCNT (I)/PPy	$4X10^{-4}$
FMWCNT (II)/PPy	1.36
FMWCNT (III)/PPy	1.08

5.3.2.3 Scanning Electron Microscopy (SEM)

SEM pictures were obtained for the FMWCNT (**I**, **II**, and **III**)/PPy composites that were electrodeposited on gold-coated Mylar using constant current and constant potential (Fig 5.10 – 5.12). In general, we find that regardless of the electrodeposition

method the FMWCNT are coated with the cauliflower morphology typical of PPy. In addition, for the FMWCNT (**I**, and **III**) which contain the lowest and highest concentration of $–SO_3H$ respectively, the PPy does not cover the FMWCNT completely. On the other hand, when FMWCNT (**II**) are used the PPy coverage is comprehensive to the degree where the FMWCNT cannot bee seen in the SEM pictures. FMWCNT(**II**) contain an intermediate concentration of $–SO_3H$, which could represent an optimum condition for the polymerization of PPy, and thus the extensive PPy growth in this case.

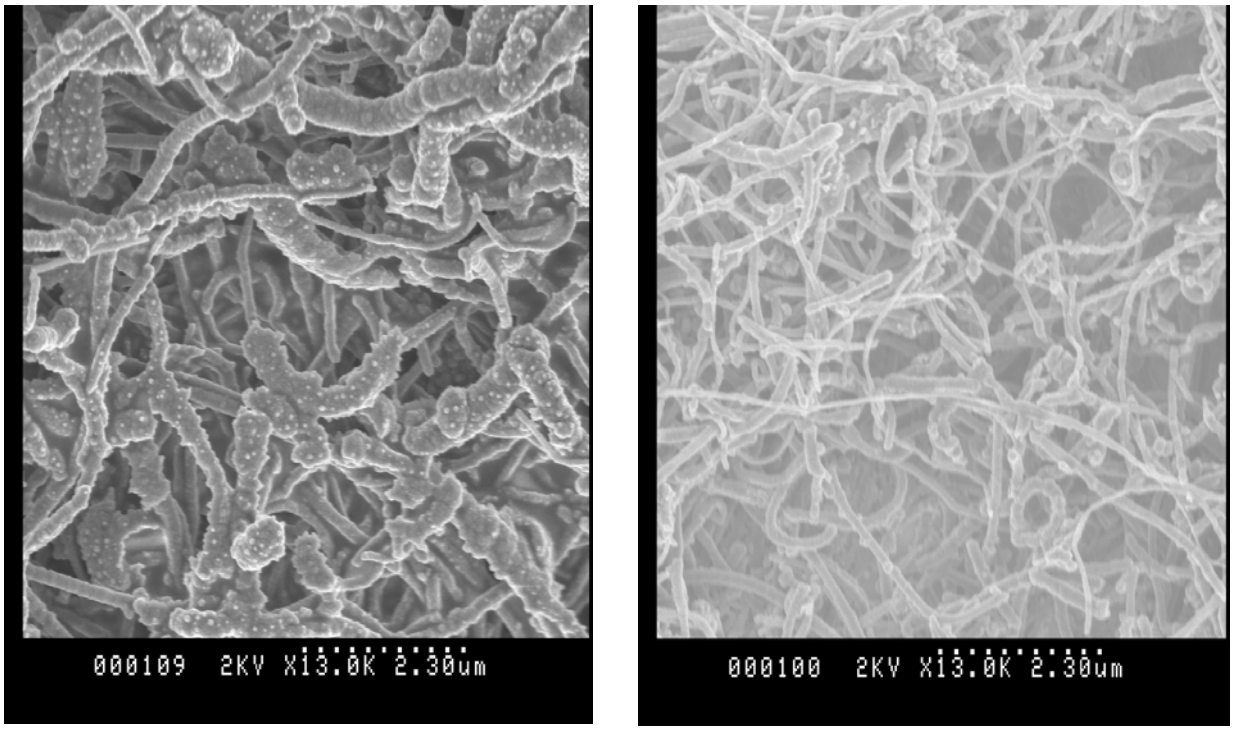

a) **b)**

Fig 5.10 SEM pictures of FMWCNT(**I**)/PPy composite a) grown using constant current and b) grown using constant potential.

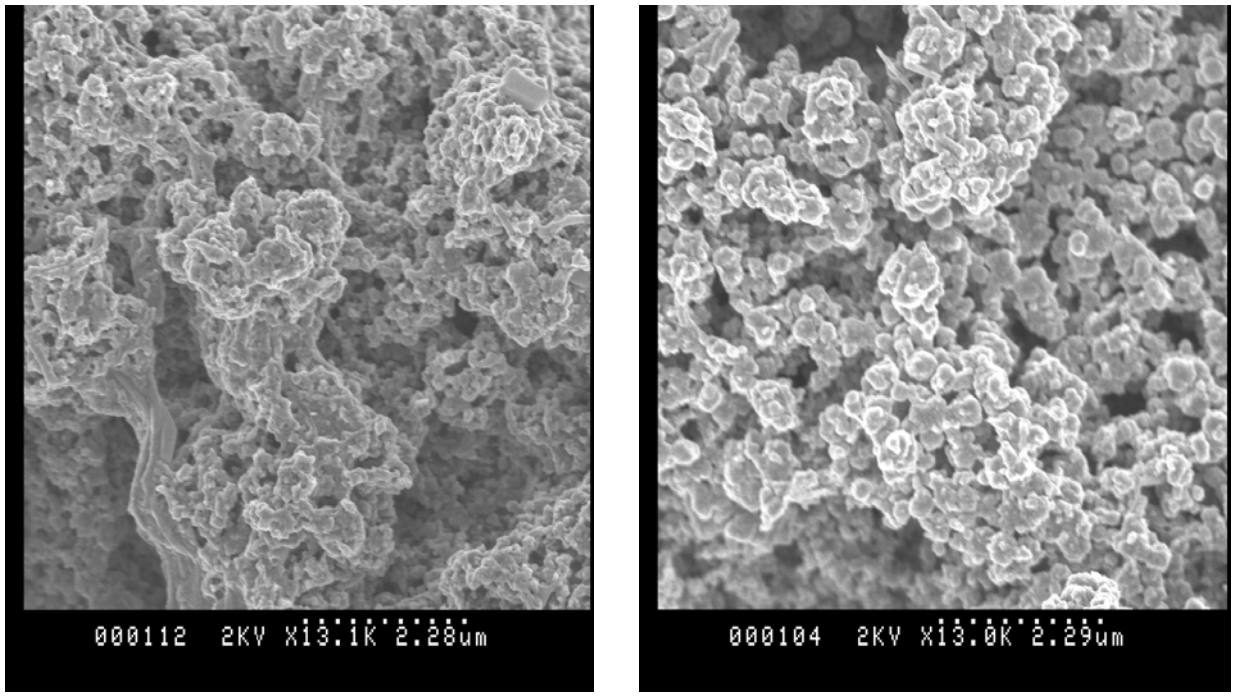

a) **b)**

Fig 5.11 SEM pictures of FMWCNT(**II**)/PPy composite a) grown using constant current and b) grown using constant potential.

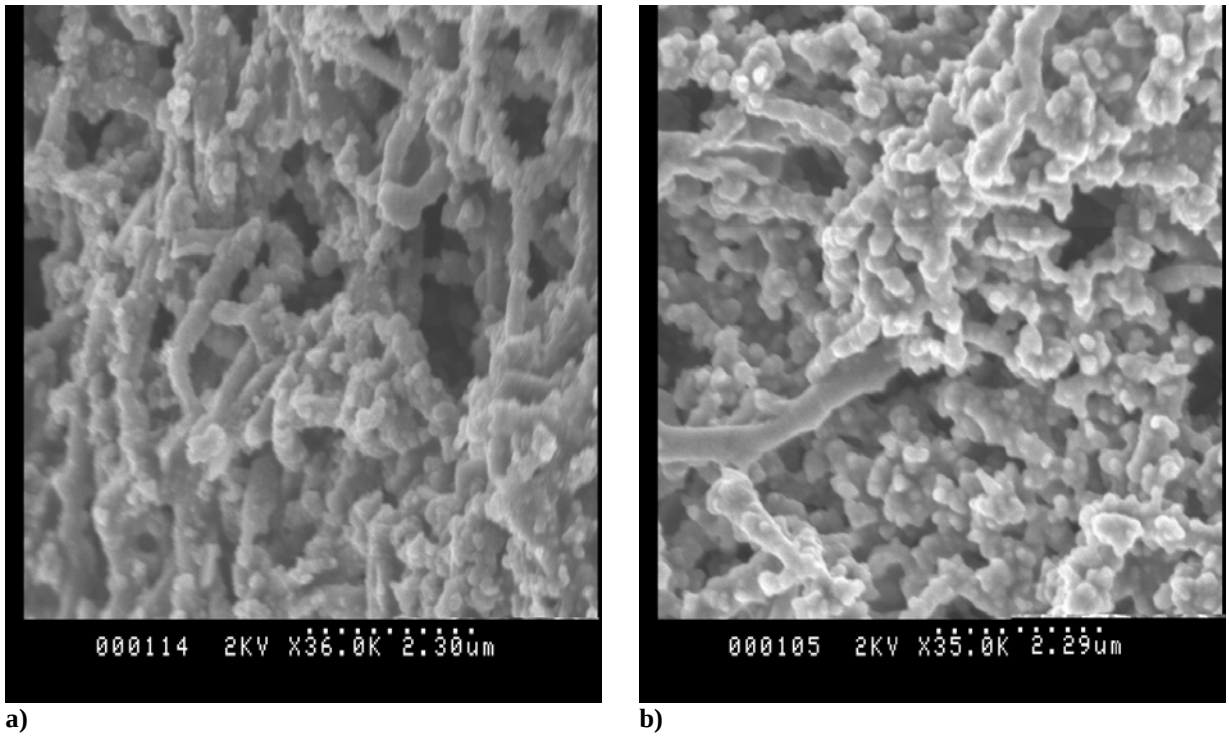

a) **b)**

Fig 5.12 SEM pictures of FMWCNT(**III**)/PPy composite a) grown using constant current and b) grown using constant potential.

5.3.3 HCNT/PAn composites

Different volume ratios of 1,2-DCB to NMP were experimented with and 1:1 ratio was determined to be the optimal volume ratio with respect to resulting in a true solution. Other ratios resulted in thin films that broke when peeled off the glass slide due to the high volume of 1,2-DCB.

5.3.3.1 Conductivity

The equations used to calculate the resistance and conductivity are discussed in **Ch. 2**, section **2.3.2.1**. The results are presented in Table –5.4.

Table –5.4 Thickness and conductivity measurement for HCNT/PAn(acid) composites.

Sample	Thickness (nm ± 0.1)	Conductivity (S/cm ± 0.1)
PAn(acid)	40.0	10.0
HCNT mat	110.0	14.1
PAn(acid) on HCNT mat	170.0	53.0
HCNT/PAn(acid)	50.0	11.7

The conductivity of the composite prepared by casting a PAn(acid) film on the HCNT mat ~ 53 S/cm was significantly higher than the conductivity of the PAn(acid) film ~ 10 S/cm, and the HCNT mat ~ 14 S/cm, separately. The conductivity for this composite was also significantly higher than the conductivity of the HCNT/PAn(acid) composite that was prepared by casting a film of HCNT/PAn(acid) solution ~ 11.7 S/cm. This could be due to the presence of NMP and 1,2-DCB within the HCNT/PAn(acid) solution, resulting in a lower overall conductivity. Also, the

physical/chemical interactions between the HCNT and the PAn(acid) when present as a mixture in solution could be completely different to those when a film of PAn(acid) is cast over the HCNT mat.

5.3.3.2 Cyclic voltammetry

CVs were recorded for the different HCNT/PAn composites in 0.1 M $NaNO_3$, 0.1 M HNO_3, and 1 M HNO_3. The samples were free standing films, and therefore good electrical contact was not achieved along the length of the film when clamped at one end. This resulted in very poor redox switching, where the samples acted as a resistor and exhibited a classic ohmic behavior with the *IR* drop being the overriding feature (Fig 5.13 – 5.15). This behavior was significant for the PAn(acid) film, and for the PAn(acid)/HCNT film that was cast from PAn(acid) and HCNT solution, indicating that the electrochemistry of PAn(acid) was dominant over that of the HCNT in these cases. However, the CV for the sample prepared by casting a PAn(acid) film on HCNT mat, exhibited a slightly more conductive behavior, indicating that both components contribute to the electrochemistry of this composite.

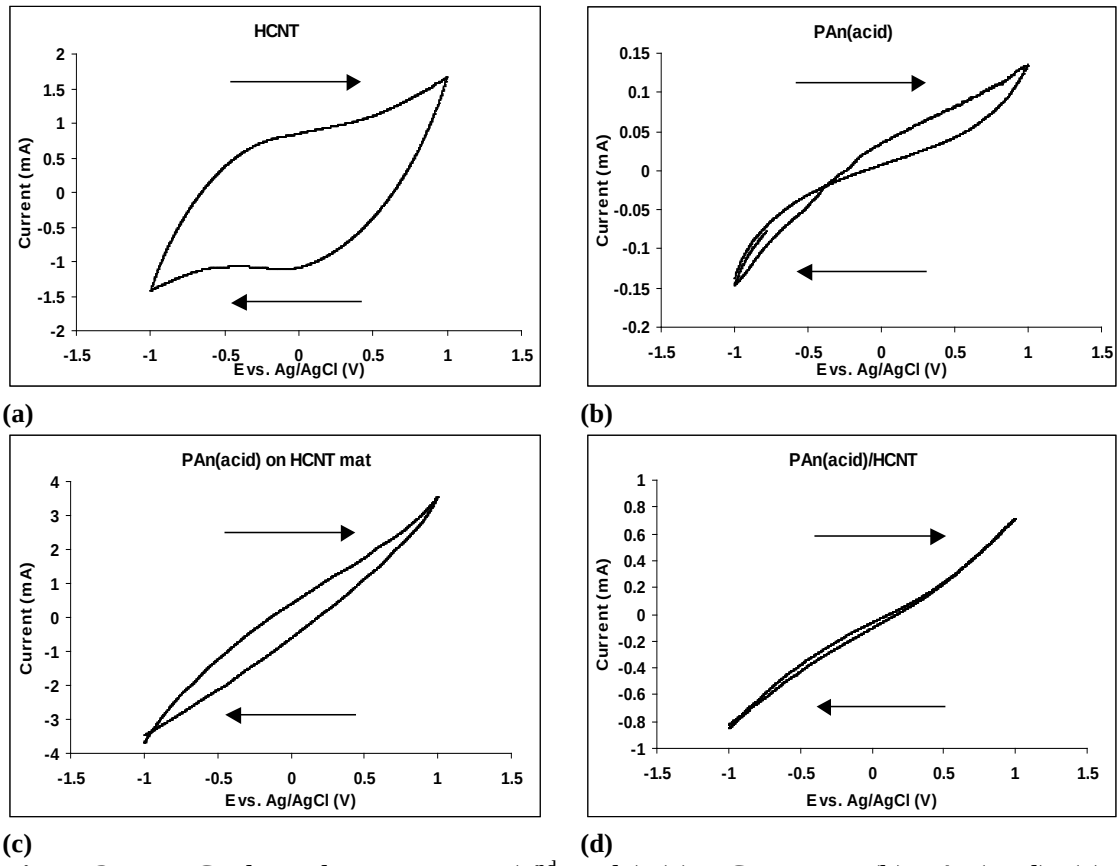

Fig 5.13 Cyclic voltammograms (2nd cycle) (a) HCNT mat, (b) PAn(acid), (c) PAn(acid) on HCNT mat, and (d) PAn(acid)/HCNT in 0.1 M $NaNO_3$, E = -1, +1 V, scan rate of 50 mV/s.

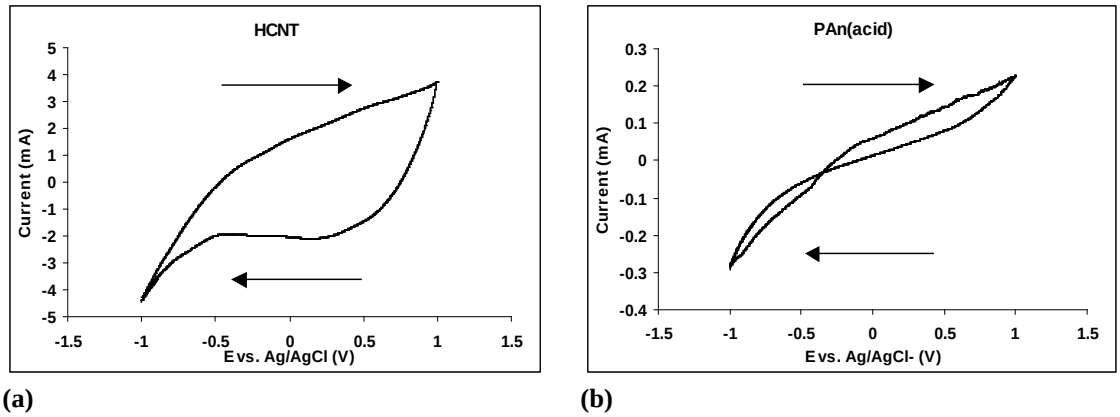

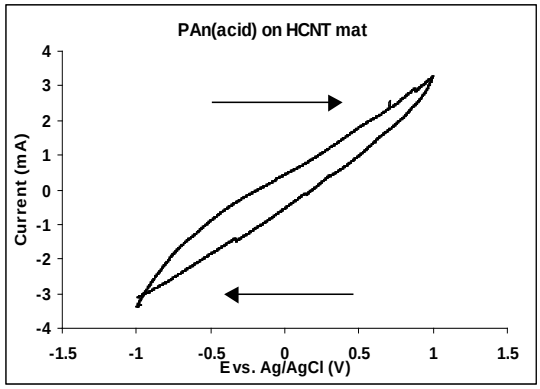

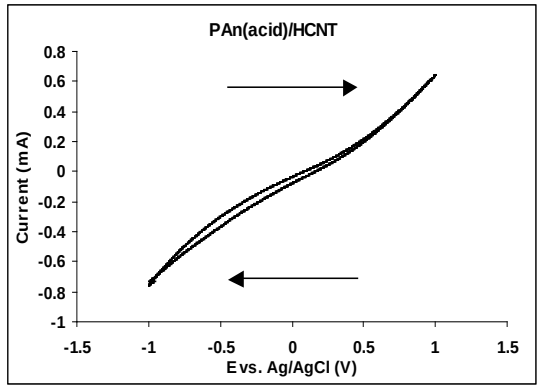

(c) **(d)**

Fig 5.14 Cyclic voltammograms (2nd cycle) (a) HCNT mat, (b) PAn(acid), (c) PAn(acid) on HCNT mat, and (d) PAn(acid)/HCNT in 0.1 M HNO_3, E = -1, +1 V, scan rate of 50 mV/s.

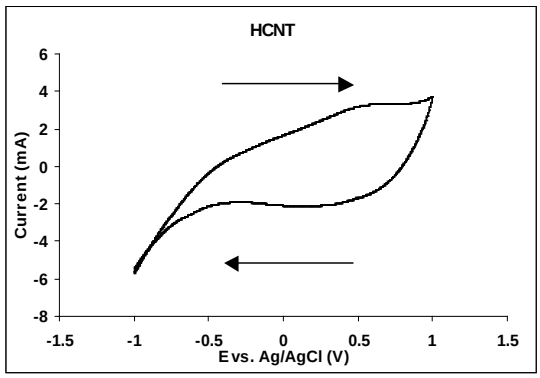

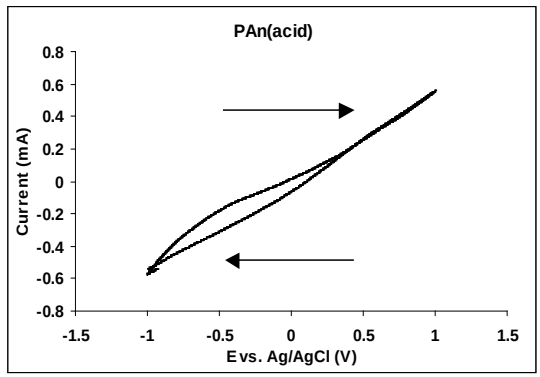

(a) **(b)**

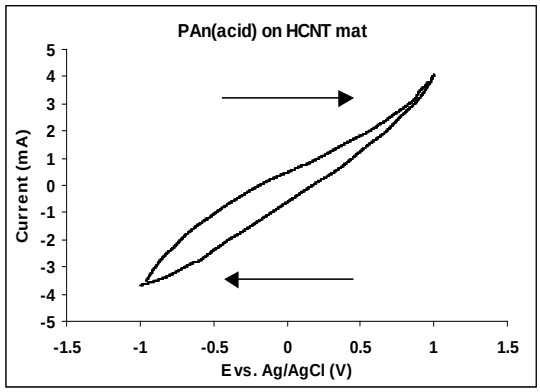

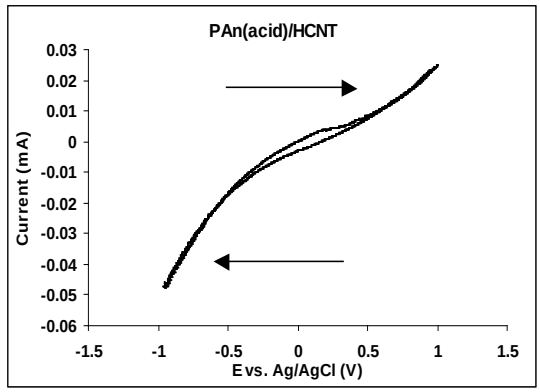

(c) **(d)**

Fig 5.15 Cyclic voltammograms (2nd cycle) (a) HCNT mat, (b) PAn(acid), (c) PAn(acid) on HCNT mat, and (d) PAn(acid)/HCNT in 1 M HNO_3, E = -1, +1 V, scan rate of 50 mV/s.

5.3.3.3 Actuation

Electrochemical actuation of PAn and CNT each proceeds according to different mechanisms. Baughman *et al* indicated that non-Faradaic electrochemical charging of the CNT is the main factor behind the expansion of CNT bundles (310). The charged species can be positive or negative depending on the sign of applied voltage. Therefore, the CNT mat expands at the maximum and minimum voltage and shrinks to the original length at voltage close to the point of 0.00 charge. On the other hand, the expansion/contraction of conducting polymers is dependent on the redox reactions of the polymers. One of the attractive features of the conducting polymer actuators is the low driving voltage that typically does not exceed 5 V. Even at low voltage, in suitable conditions such devices can achieve an actuation strain as high as 7% generating stresses that are comparable to or exceed those of biological muscles (311). CNT actuators have shown actuation strains in the order of 0.2 % with driving voltage of a few volts (312). Since the Young's modulus of individual CNT bundle has been found to be approximately 640 GPa (313), a strain of 0.2 % gives available stress of 1280 MPa from the bundles. Thus, a conducting CNT/polymer composite may result in an actuator where the conducting polymer component will contribute to a high actuation strain and the CNT component to a high modulus. Some preliminary results of CNT and polypyrrole hybrid actuators have been reported (314). However, the PPy component did not contribute any effect to the composite and the actuation performance of the hybrid was similar to that of CNT alone actuators.

The actuation of HCNT/PAn(acid) composites was investigated in 1 M $NaNO_3$, 1 M HCl, 1 M NaCl, and 3 M NaCl solutions. The actuation responses for the composite prepared by casting a film from PAn(acid) and HCNT solution could not be recorded

due to the fact that the sample was very fragile and broke before adding any weights. Also, the HCNT mat in 1 M HCl and 1 M NaCl did not exhibit any decipherable actuation data, and thus are not presented. The actuation responses of the remaining samples as well as the related CV for each of these samples during the application of voltage in the different solutions are presented in (Fig 5.16 – 5.25).

1 M HCl

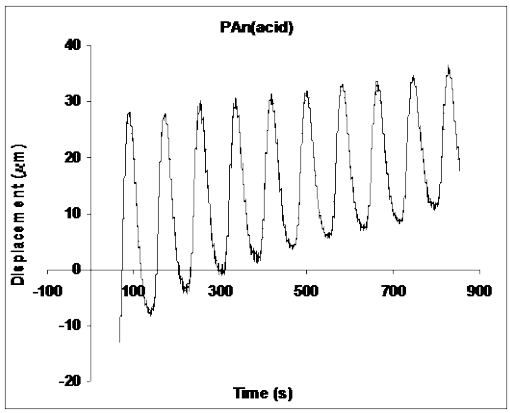

0.325%

Fig 5.16a Displacement as potential is applied for PAn(acid) film in 1 M HCl, with 2 g load.

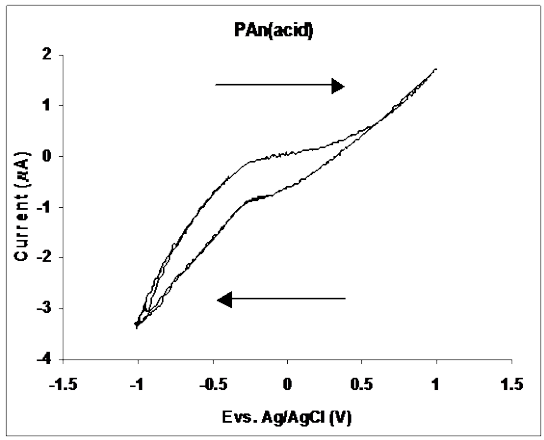

Fig 5.16b Cyclic voltammogram (2nd cycle) for PAn(acid) film in 1 M HCl during the application of Voltage. E= -1, +1 V, scan rate of 50 mV/s.

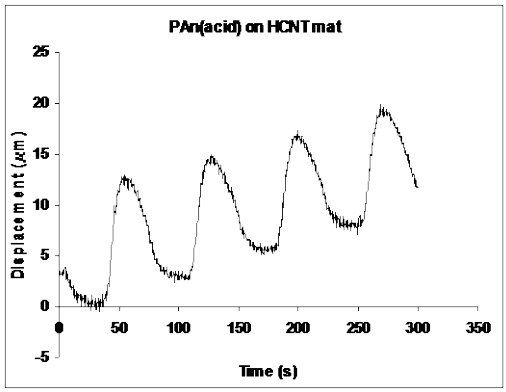

0.305%

Fig 5.17a Displacement as potential is applied for PAn(acid) on HCNT mat in 1 M HCl, with 2 g load.

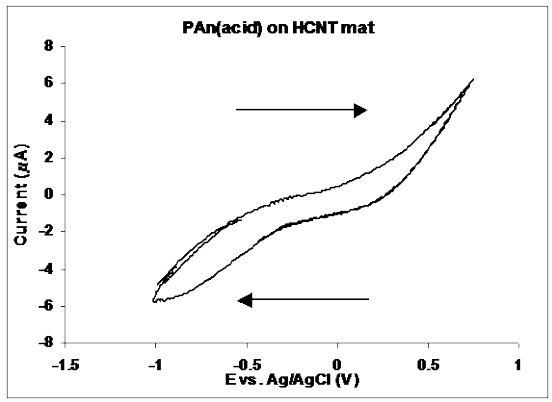

Fig 5.17b Cyclic voltammogram (2nd cycle) for PAn(acid) on HCNT mat in 1 M HCL during the application of Voltage. E= -1, +0.7 V, scan rate of 50 mV/s.

1 M $NaNO_3$

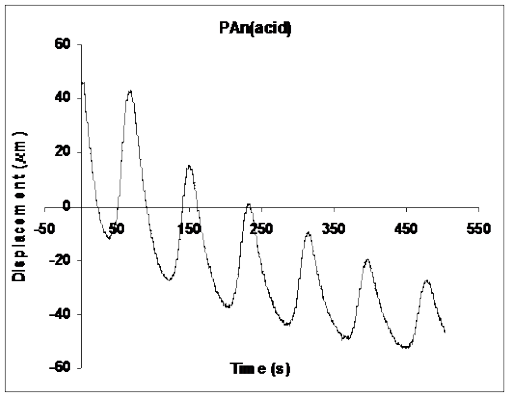

0.83%

Fig 5.18a Displacement as potential is applied for PAn(acid) film in 1 M $NaNO_3$, with 2 g load.

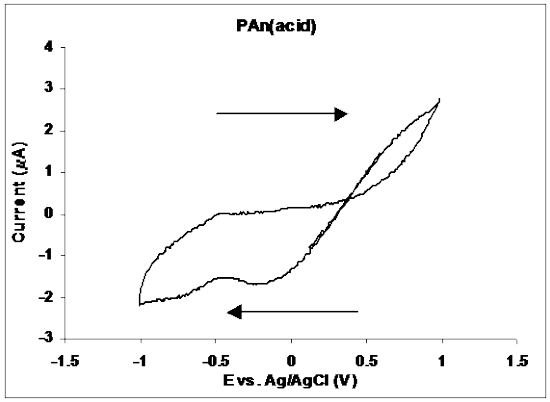

Fig 5.18b Cyclic voltammogram (2nd cycle) for PAn(acid) film in 1 M $NaNO_3$ during the application of Voltage. E= -1, +1 V, scan rate of 50 mV/s.

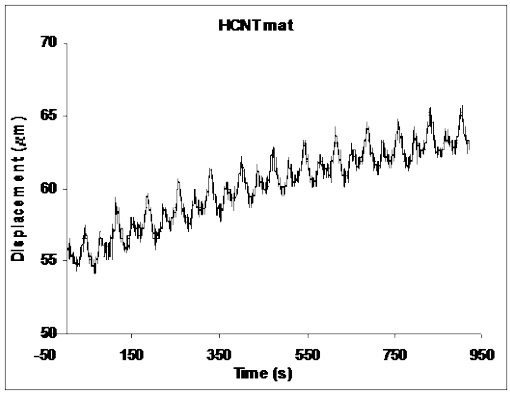

0.05%, 0.024%

Fig 5.19a Displacement as potential is applied for HCNT mat in 1 M $NaNO_3$, with a 2 g load.

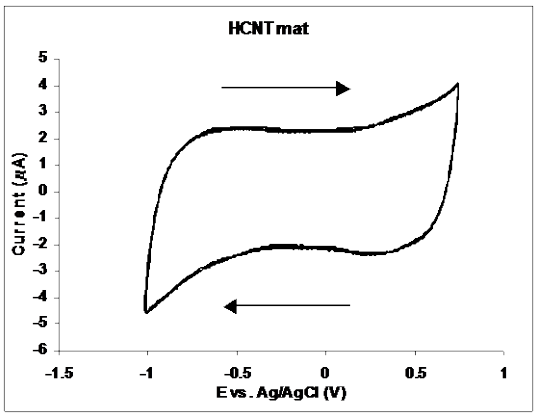

Fig 5.19b Cyclic voltammogram (2nd cycle) for HCNT mat in 1 M $NaNO_3$ during the application of Voltage. E= -1, +0.7 V, scan rate of 50 mV/s.

1 M $NaNO_3$ Cont.

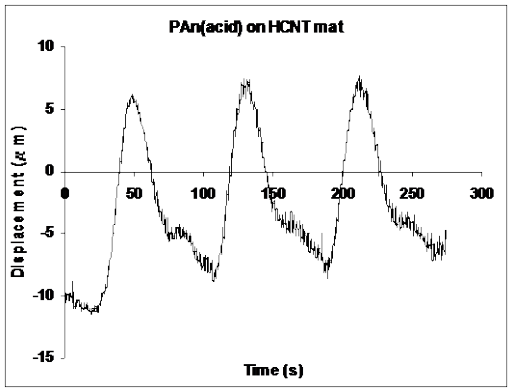

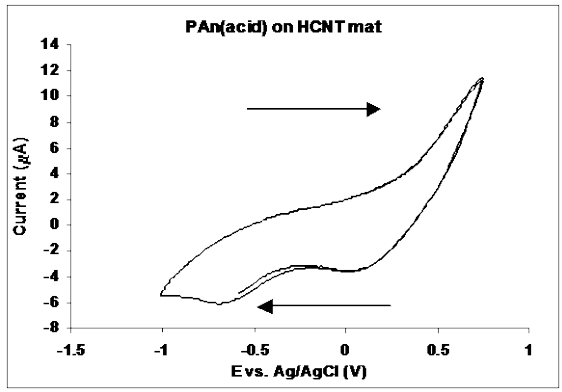

0.23%

Fig 5.20a Displacement as potential is applied for PAn(acid) on HCNT mat in 1 M $NaNO_3$, with 2 g load.

Fig 5.20b Cyclic voltammogram (2nd cycle) for PAn(acid) on HCNT mat in 1 M $NaNO_3$ during the application of Voltage. E= -1, +0.7 V, scan rate of 50 mV/s.

1 M NaCl

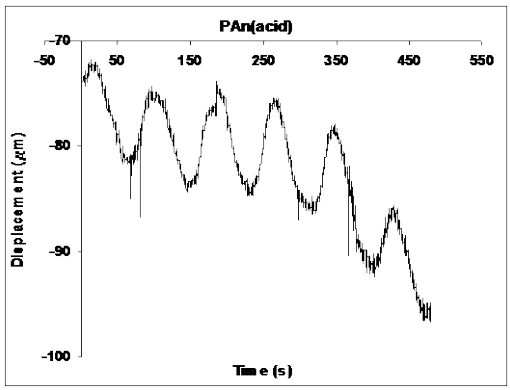

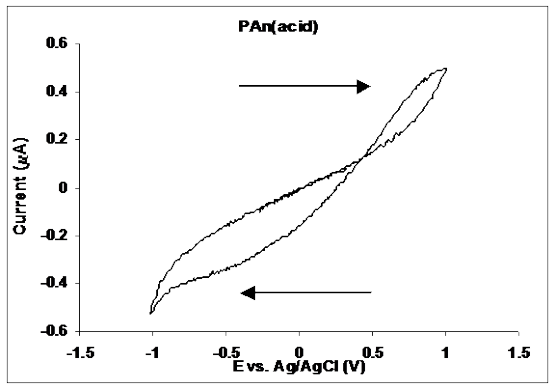

0.07%

Fig 5.21a Displacement as potential is applied for PAn(acid) film in 1 M NaCl, with 2 g load.

Fig 5.21b Cyclic voltammogram (2nd cycle) for PAn(acid) film in 1 M NaCl during the application of Voltage. E= -1, +1 V, scan rate of 50 mV/s.

1 M NaCl Cont.

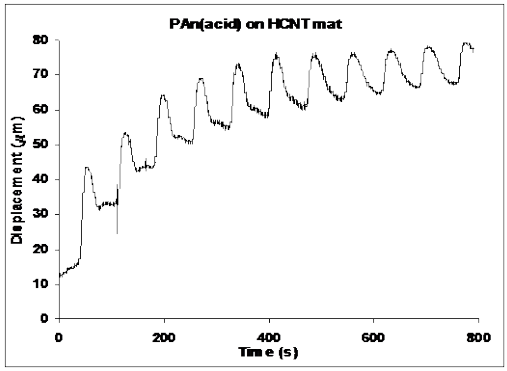

0.35%

Fig 5.22a Displacement as potential is applied for PAn(acid) on HCNT mat in 1 M NaCl, with 2 g load.

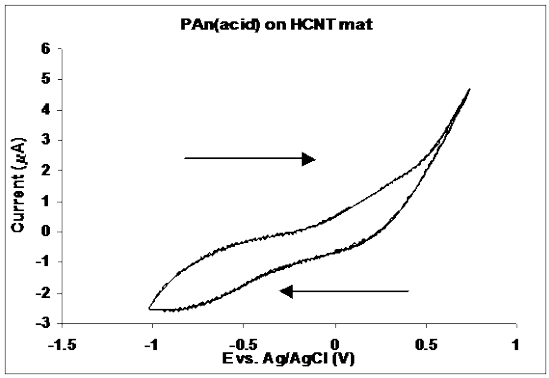

Fig 5.22b Cyclic voltammogram (2nd cycle) for PAn(acid) on HCNT mat in 1 M NaCl during the application of Voltage. E= -1, +0.7 V, scan rate of 50 mV/s.

3 M NaCl

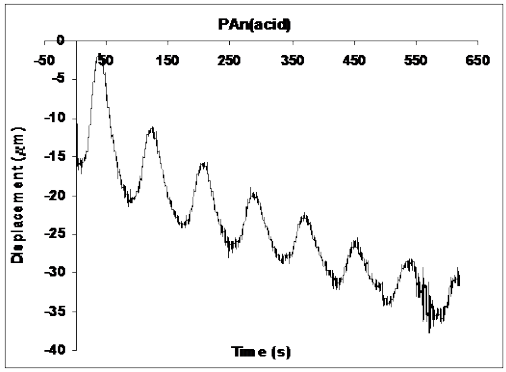

0.1%

Fig 5.23a Displacement as potential is applied for PAn(acid) film in 3 M NaCl, with 2 g load.

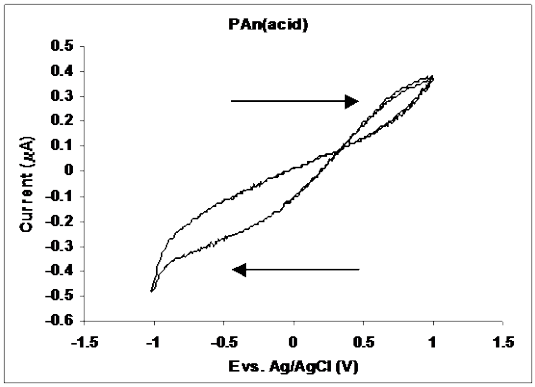

Fig 5.23b Cyclic voltammogram (2nd cycle) for PAn(acid) film in 3 M NaCl during the application of Voltage. E= -1, +1 V, scan rate of 50 mV/s.

3 M NaCl Cont.

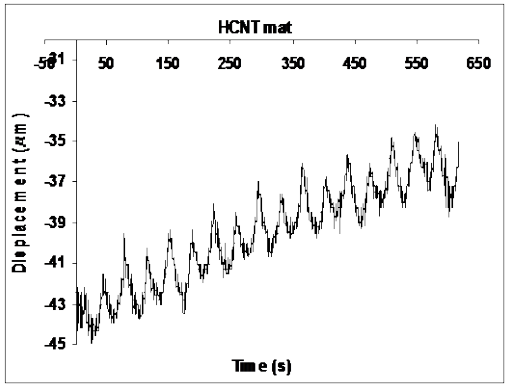

0.06%, 0.03%

Fig 5.24a Displacement as potential is applied for HCNT mat in 3 M NaCl, with 2 g load.

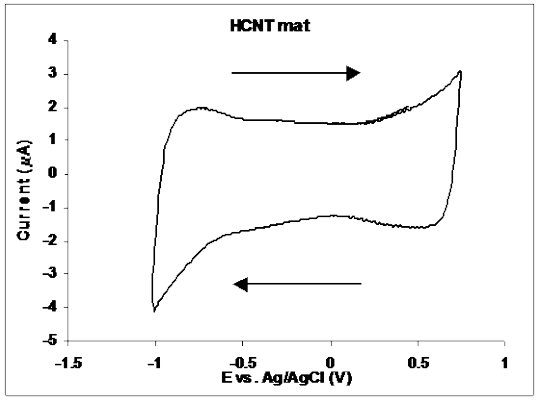

Fig 5.24b Cyclic voltammogram (2nd cycle) for HCNT mat in 3 M NaCl during the application of Voltage. E= -1, +0.7 V, scan rate of 50 mV/s.

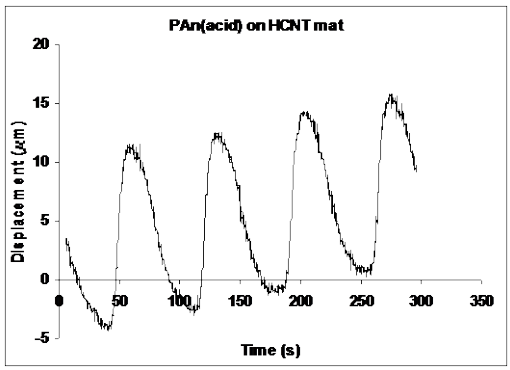

0.42%

Fig 5.25a Displacement as potential is applied for PAn(Acid) on HCNT mat in 3 M NaCl, with 2 g load.

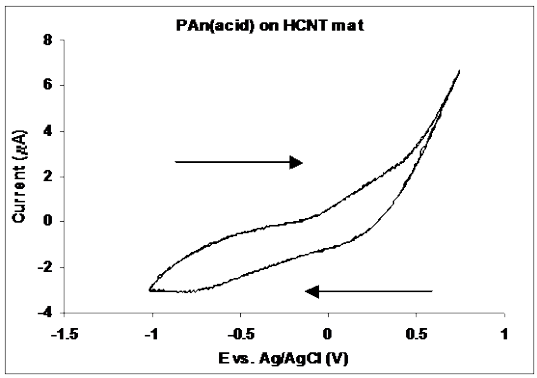

Fig 5.25b Cyclic voltammogram (2nd cycle) for PAn(acid) on HCNT mat in 3 M NaCl during the application of Voltage. E= -1, +0.7 V, scan rate of 50 mV/s.

In 1 M $NaNO_3$, the HCNT (Fig 5.19a) and PAn(acid) film (Fig 5.18) showed a strain of 0.05 and 0.83 %, respectively. The annealed HCNT can reach a strain of 0.2 % (313). We have reported the strain values ranging from 0.05 to 0.08 % for annealed

HCNT mats (315)*. For the unannealed HCNT of this study, the actuation strain of 0.05 % is reasonable given that impurities embedded in the HCNT mat could inhibit the movement of the HCNT strands. The actuation strain of 0.83 % in the PAn(acid) sample is comparable to the PAn(acid) sample in sulfuric acid (H_2SO_4) (0.5 M) solution with a strain of about 1 % (316). The actuation strain of the PAn(acid) on HCNT mat composite was 0.23 % (Fig 5.20a). The coating of PAn(acid) on the HCNT mat increased the actuation strain of pure HCNT from 0.05 % to 0.23 % (315).

The expansion/contraction patterns of the PAn(acid) and PAn(acid) on HCNT composites in HCl and NaCl solutions are similar to those in the $NaNO_3$ solution. The actuation strains was calculated as follows:

Actuation strain, ε, due to expansion/contraction of the sample is calculated by

$$\varepsilon = (\Delta l \times 100)/l_o \quad (\%)$$

where l_o is the original length and Δl is the movement between expansion and contraction. The actuation strains for each electrolyte are shown in Table –5.5.

Table –5.5 Strain% for the different samples.

Sample	**Strain% ± 0.001**			
	I M $NaNO_3$	**I M HCl**	**1 M NaCl**	**3 M NaCl**
HCNT mat	0.05, 0.024	---	---	0.065, 0.035
PAn(acid)	0.830	0.325	0.070	0.110
PAn(acid) on HCNT mat	0.235	0.305	0.350	0.425

* **Appendix A: Carbon nanotubes and polyaniline composite actuators.**

From the table above we can see that the Strain% for the HCNT mat has two values. This is due to the following, at a maximum V, the PAn(acid) component was oxidized and the volume simultaneously increases with the HCNT component. However, the increase in volume of the two composite components was not additive. This implied that the transport of ions to the composite might not be sufficient to meet the ion requirements of both composite components. A prolonged maximum V may lead to a synergism to obtain a full volume expansion in both components. At a minimum V, the PAn(acid) component is reduced and the volume consequently decreases while the volume of the HCNT component increases. This opposite effect results in a kink with a small expansion peak of the HCNT component as can be observed in the displacement curves (315).

The displacement pattern of the PAn(acid) on HCNT or HCNT/PAn(acid) composites are dominated by the PAn(acid) component, with a reduced expansion/contraction movement compared with PAn(acid) actuators. This also illustrates the fact that most of the ions transported in and out of the sample were mostly involved in redox reactions in PAn.

PAn coating substantially enhances the actuation strain (Table –5.5). This result indicates an important fact that the addition of PAn(acid) to HCNT mat can increase the strain while the Young's modulus of the composite could be maintained. In other words, the PAn component contributes to a high actuation strain value while the HCNT component to the Young's modulus. The combination of these two factors would result in high stresses produced by PAn(acid) on HCNT mat composite actuators. It should be noted that there is an experimental error in measuring the

actuation strain due to equipment arrangement and differences in sample batches. However, the casting of PAn(acid) onto the HCNT showed a general tendency in which the actuation strain of the composite was substantially enhanced from a low value of the HCNT sample for all solutions tested. Optimization of the HCNT/PAn(acid) composites with different fabrication methods and selecting a suitable input voltage pattern to reduce the opposite movement of the HCNT component and PAn(acid) component at negative voltage may help achieve the highest actuation strain.

5.3.3.4 Scanning Electron Microscopy (SEM)

SEM pictures were obtained for PAn(acid) film, HCNT/PAn(acid) film, and PAn(acid) on HCNT mat (Fig 5.26 – 5.28), respectively. The SEM for PAn(acid) film shows a smooth surface in contrast to the coarse surface observed for the HCNT/ PAn(acid) film due to the presence of HCNT. The SEM for the PAn(acid) cast on the HCNT mat, showed the HCNT covered with PAn(acid) distinctively (Fig 5.28).

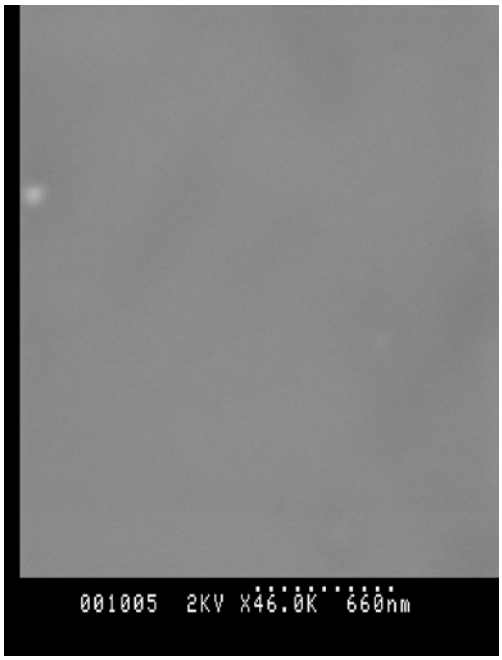

Fig 5.26 SEM of PAn(acid) film.

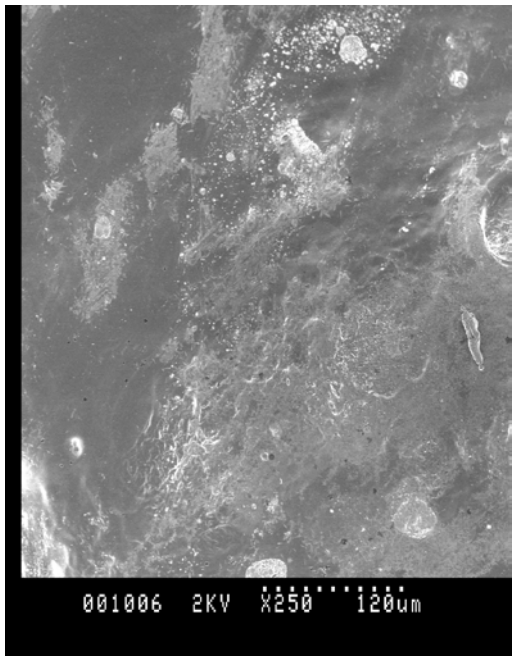

Fig 5.27 SEM of HCNT/PAn(acid) film.

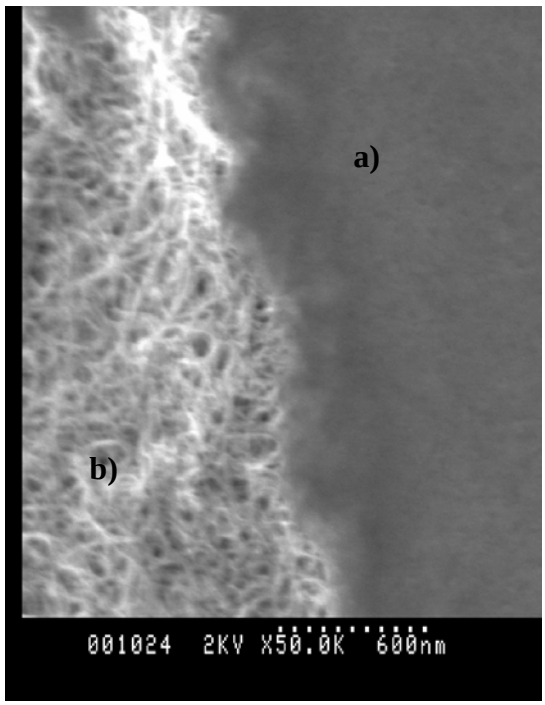

Fig 5.28 SEM picture (top view) of PAn(acid) cast on HCNT mat, a) PAn(acid), b) HCNT mat.

5.4- CONCLUSION

In the case of RCNT/PPy/dopant/dispersant composites, the addition of the RCNT resulted in significant changes in the after growth CVs, in terms of peak shifts and peaks sharpness. In general, the addition of the RCNT also resulted in an increase in capacitance values. The SEM pictures, show the differences in morphology between the polymer and the polymer with RCNT.

For FMWCT/PPy composites, the CVs for the composites grown on gold-coated Mylar or ITO glass using constant current exhibited no redox peaks. However, the composites grown using constant potential, exhibited well-defined oxidation and reduction peaks. The capacitance increased as the $–SO_3H$ contents in the MWCNT increased. In addition, the capacitance value for FMWCNT(**II**)/PPy either grown on gold-coated electrodes or ITO glass by either constant potential or constant current is significantly higher than all the other composites. SEM pictures of these composites showed that the PPy does cover the FMWCNT, and that the extent of the coverage depends on the $–SO_3H$ content in the FMWCNT.

In the case of PAn(acid) and HCNT composites, we find that the conductivity of the PAn(acid) on the HCNT mat composite is higher than that for PAn(acid) or HCNT mat individually.

CVs were recorded for the different HCNT/PAn composites in 0.1 M $NaNO_3$, 0.1 M HNO_3, and 1 M HNO_3. Due to weak electrical contact the samples acted as resistors and exhibited a classic ohmic behavior. This was significant for PAn(acid) film, and

PAn(acid)/HCNT film that was cast from PAn(acid) and HCNT solution, indicating that the electrochemistry of PAn(acid) is dominate over that for the HCNT in these cases. However, the CV for the sample prepared by casting a PAn(acid) film on HCNT mat, exhibited a slightly more conductive behavior, indicating that both components contribute to the electrochemistry of this composite. In addition, actuation resulting from the redox cycling of PAn was evident in the actuation studies. Most importantly we find that the strain increases to a significant degree when PAn(acid) is cast over the HCNT mat, where the PAn component contributes to a high actuation strain value while the HCNT component to the Young's modulus. The combination of these two factors would result in high stresses produced by PAn(acid) on HCNT mat composite actuators.

Finally, the combination of carbon nanotubes with polymers offers an attractive route not only to reinforce the polymer films but also to introduce new electronic properties based on morphological modification or electronic interaction between the two components. The resulting new materials can be used in a variety of different applications.

CHAPTER SIX

THE ELCTROPOLYMERIZATION OF CONDUCTING POLYMERS ONTO CARBON NANOTUBES ELECTRODES

6.1- INTRODUCTION

Conducting polymers have been deposited onto carbon nanotubes materials by different research groups. For example, Poly(3-methylthiophene) was deposited on a carbon nanotubes microelectrode by Arnantia *et al* (316). A layer of conducting polyaniline was uniformly deposited onto the surface of aligned carbon nanotubes by Gao *et al* (317); they also observed that PPy coating layers could form bridges between the nanotubes to give dense composite films (318). Polypyrrole films were uniformly electropolymerized over well-aligned carbon nanotubes array by Chen *et al* (319). The synthesis and redox performance of these films were carried out using cyclic voltammetry. It was observed that the electrodeposition of PPy films on the surface of the carbon nanotubes was much faster than on conventional electrodes such as platinum (Pt). It was also observed that the redox performance of PPy-coated carbon nanotubes electrode was significantly improved due to the high accessible surface area in the aligned carbon nanotubes array.

Kazaoui *et al* proposed that electrochemical doping of SWCNT mats can occur by placing these mats into a solution containing a counterion at E = 1 V and E = -1 V (320). Changes in the electronic state of the SWCNT induced by chemical and

electrochemical doping by bulky organic molecules was also investigated (321). Chiu *et al* deposited PPy onto carbon nanotube fibers by continuous electrochemical polymerization. They noted a significant improvement in the shear strength of the coated carbon nanotube fibers; it was found that this depended on the doping species used during the electrochemical polymerization (322, 323).

PPy coatings have been polymerized onto carbon nanotube fibers by Wood *et al* (324). The type of electrolyte, electrolyte concentration, monomer concentration, applied voltage, and electropolymerization time were found to have a significant effect on the morphology of the composite coatings. They also reported that the morphology of the PPy coating formed on the carbon nanotubes depended on the type of supporting electrolyte used. Four different morphologies were identified: smooth, microspheroidal, leafoidal, and porous. It was also found that the bigger the size of the counter-ion in the PPy complex the harder it is to effectively pack the chains, resulting in a rough morphology (324, 325).

This chapter investigates the electropolymerization of different polymers onto the surface of RCNT mats. Composites were characterized using a variety of different techniques such as cyclic voltammetry, and Scanning Electron Microscopy (SEM). Cyclic voltammetry exhibited unexpected results, namely that the resulting composites are non-conductive. This has been further investigated by the electrodeposition of PPy/SDS and PPy/AHPF onto different carbon surfaces using constant current, constant potential, and cyclic potential. PPy/SDS and PPy/AHFP were grown on glassy carbon, carbon foil, RCNT mat (unannealed) electrode, and RCNT mat (annealed) electrode. After growth cyclic voltammograms for the

resulting polymers and RCNT composites were recorded for comparison reasons, and the conductivity was measured.

6.2- EXPERIMENTAL

6.2.1 Materials

Sodium nitrate (M.W. 84.99 Da), dextran sulfate (Dex) (M.W. 500,000 Da), ammonium hexafluorophosphate (AHFP) (M.W. 163.0 Da), Sodium dodecyl sulfate (SDS) (M.W. 288.37 Da), and Pyrrole were purchased from Sigma-Aldrich. Pyrrole was distilled prior to use. RCNT were obtained from Tubes @ Rice (Rice University, Houston TX) as a suspension in toluene, with a tube diameter of 1.2-1.38 nm as reported by supplier.

6.2.2 Instrumentation

Four-point probe conductivity measurements were carried out using 2.5 X 0.5 cm strips of RCNT mats both annealed and unannealed, and carbon foil. A digital micrometer was used to measure the thickness of the strips. A constant current of 1 mA was passed through the sample using an EG & G Princeton Applied Research model 363 Potentiostat/Galvanostat, and the resistance was recorded using a Hewlett Packard model 34401.

Cyclic voltammetry was recorded using a MacLab/4e for glassy carbon electrode, RCNT mats both annealed and unannealed, and carbon foil electrode prior to the electrodeposition of the polymer. The electrochemical cell consisted of the above electrodes as the working electrode, a Pt-mesh electrode as the auxiliary electrode,

and an Ag/AgCl as the reference electrode. 0.01 M $K_4Fe(CN)_6$ was used as an electrolyte with 0.1 M $NaNO_3$ acting as a supporting electrolyte. The potential window applied was E = -0.3, +0.6 V. The scan rate applied was 50 mV/s, and a MacLab/4e was used to record the output.

After growth CVs of the polymers and RCNT composites electrodeposited on the different electrodes were recorded in 0.1 M $NaNO_3$, with a scan rate of 50 mV/s. The electrochemical cell configuration was as described above.

The capacitance for the different polymers and RCNT composites was measured by recording CVs at different scan rates 50, 25, 10 and 5 mV/s. The potential window applied was E = -0.1, +0.3 V, and current measurements were taken at E = +0.1 V. The electrochemical cell was as described above with the electrolyte used being 1 M $NaNO_3$.

Scanning electron microscopy (SEM) pictures were taken using a Hitachi S-900 FESEM.

6.2.3 Electrode preparation

The RCNT mats (unannealed) were prepared as described previously in **Ch. 2**, section **2.2.1** with one difference, the PVDF membrane was sputter-coated with Pt prior to the RCNT microfiltation. The reason for the Pt-sputter coating was that the RCNT are adhesive to the Pt-coat on the PVDF membrane. Strips of the RCNT mat with the sputter coated PVDF membrane of 2.5 X 0.5 cm were cut, and then attached to gold-coated Mylar by a double-sided adhesive tape (Fig 6.1). The RCNT mat (annealed) electrodes were prepared in the same manner except that the RCNT mat

was placed in an oven at 1000 °C for 2 hours prior to attachment to gold-coated Mylar.

Fig 6.1 RCNT mat electrode.

6.2.4 Composite preparation

6.2.4.1 Polymer electrodeposition on RCNT (unannealed) mat

Pyrrole 0.4 M was added to 10 mL of 0.1 M sodium nitrate, 0.1 M dextran sulfate (Dex), or 0.1 M ammonium hexafluorophosphate (AHFP). The electrochemical cell consisted of the previously prepared RCNT mat (unannealed) electrode as the working electrode (the surface area was constant), a Pt-mesh electrode as the auxiliary electrode and an Ag/AgCl was used as the reference electrode. PPy/NO_3, PPy/Dex, and PPy/AHFP were electropolymerized onto the surface of the RCNT mats (unannealed) using three different methods. A Galvanostat was used to apply constant current of 1 mA (j= 1 mA/cm^2) for 5 min, a potentiostat was used to apply constant potential of E =1 V for 15 min, and a MacLab potentiostat was used to apply cyclic potential with a potential window of E = +0.5, +0.9 V for 20 cycles to electrodeposit the polymers. In all three cases a MacLab/4e was used to record the output.

6.2.4.2 Polymer electrodeposition on different carbon electrodes

Pyrrole 0.4 M was added to 10 mL of the following solutions 0.1 M SDS and 0.1 M AHFP. Glassy carbon electrode, carbon foil, RCNT mat (unannealed) electrode, and RCNT mat (annealed) electrode were used separately as the working electrode, a Pt-mesh electrode as the auxiliary electrode and an Ag/AgCl was used as the reference electrode.

PPy/AHFP was electrodeposited on the different electrodes by applying a constant potential of E = +1 V for 15 min, using a potentiostat CV27.

PPy/SDS was grown on the different electrodes using three different methods. First, a Galvanostat was used to apply a constant current of 1 mA (j= 0.07 mA/cm^2) for 5 min. Second, a Potentiostat CV27 was used to apply a constant potential of E = +1 V for 15 min. Finally, a Mac lab potentiostat was used to apply cyclic potential with a potential window of E = +0.2, +0.9 V for 10 cycles to electrodeposit the polymer. In all three cases a MacLab/4e was used to record the output.

6.3- RESULTS & DISCUSSION

When PPy was electrochemically deposited on conventional electrodes using cyclic potential, the growth current in the first cycle was small and increased for subsequent cycles. It was reported by Tamm *et al*, that during the growth of PPy on aligned carbon nanotubes no significant increase in the current in the later cycles was observed (319). However, the observed current was still larger than conventional electrodes such as Pt-electrode. This was believed to be due to the high surface area of the aligned carbon nanotubes. The surface of the carbon nanotubes have also been

noted to be more active than that of conventional electrodes, so that lower nucleation energy is required at the beginning of the pyrrole polymerization (319).

6.3.1 Conductivity

The equations used to calculate the resistance and conductivity are discussed in **Ch. 2**, section **2.3.2.1**. The results are presented in Table –6.1.

Table –6.1 Conductivity measurements for the different electrodes.

Sample	**Thickness (μm ± 0.001)**	**Conductivity (S/cm ± 0.1)**
RCNT mat (unannealed)	0.006	25.1
RCNT mat (annealed)	0.033	44.4
Carbon foil	0.290	75.5

From the table above we can see that the carbon foil has the highest conductivity while the RCNT mat (unannealed) has the lowest. We also note that RCNT mat (annealed) had nearly twice the conductivity of the RCNT mat (unannealed).

6.3.2 Cyclic voltammetry for the different electrodes in 0.01 M $K_4Fe(CN)_6$

Cyclic voltammetry of glassy carbon electrode, RCNT mats annealed and unannealed, and carbon foil electrodes are presented in (Fig 6.2 – 6.5). In general, the CVs for the different electrodes were similar under the same conditions. An oxidation peak was observed at E ~ 0.35 V for all the different electrodes. A reduction peak at E ~ 0.1 V was observed for glassy carbon electrode and RCNT mat (unannealed), this

peak shifted to E ~ 0.00 V for RCNT mat (annealed) electrode and carbon foil electrode.

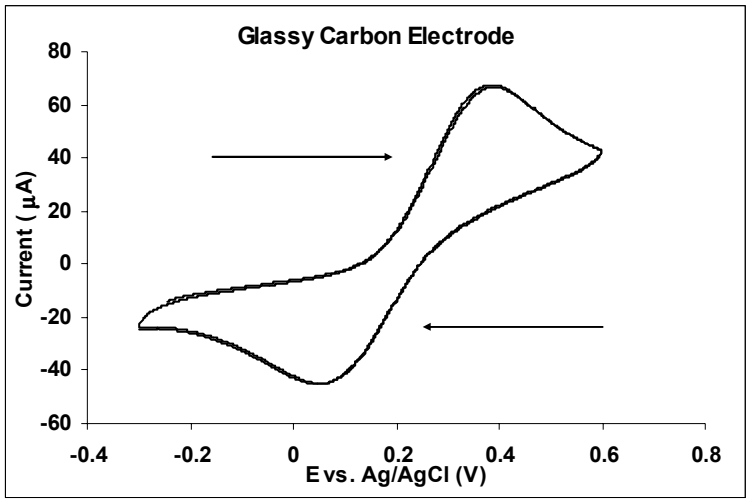

Fig 6.2 Cyclic voltammogram (2nd cycle) for glassy carbon electrode in 0.01 M $K_4Fe(CN)_6$ with 0.1 M $NaNO_3$ as a supporting electrolyte, E = -0.3, + 0.6 V, scan rate of 50 mV/s.

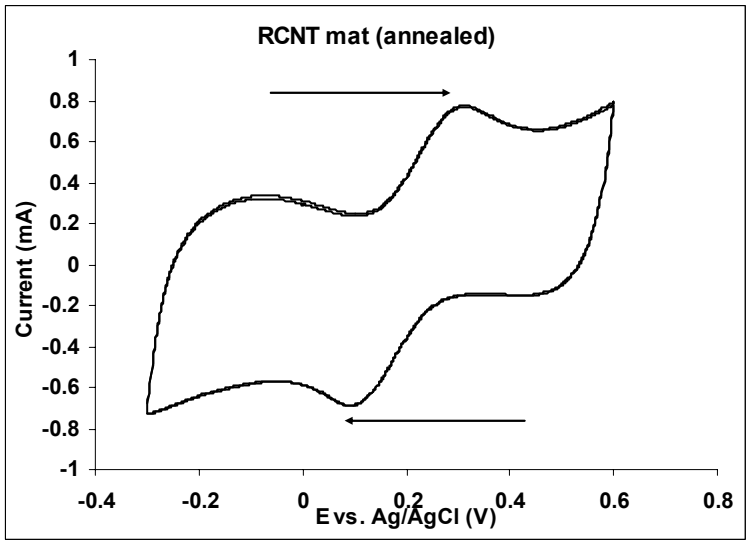

Fig 6.3 Cyclic voltammogram (2nd cycle) for RCNT mat (annealed) in 0.01 M $K_4Fe(CN)_6$ with 0.1 M $NaNO_3$ as a supporting electrolyte, E = -0.3, + 0.6 V, scan rate of 50 mV/s.

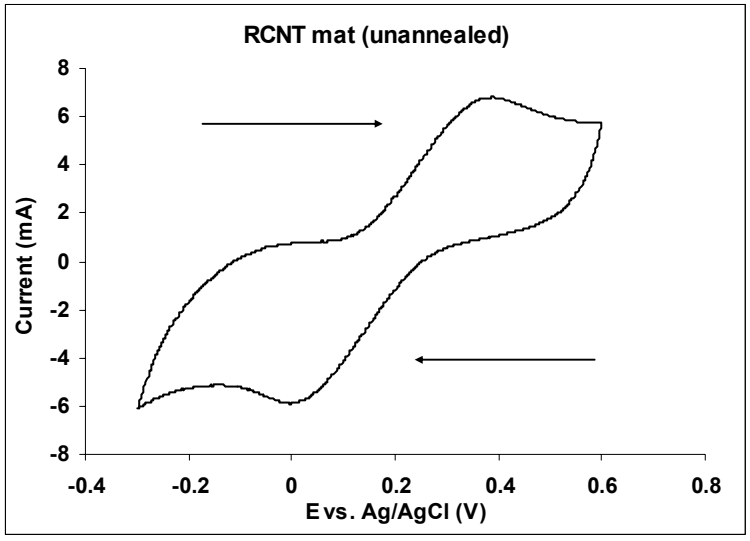

Fig 6.4 Cyclic voltammogram (2nd cycle) for RCNT mat (unannealed) in 0.01 M $K_4Fe(CN)_6$ with 0.1 M $NaNO_3$ as a supporting electrolyte, E = -0.3, + 0.6 V, scan rate of 50 mV/s.

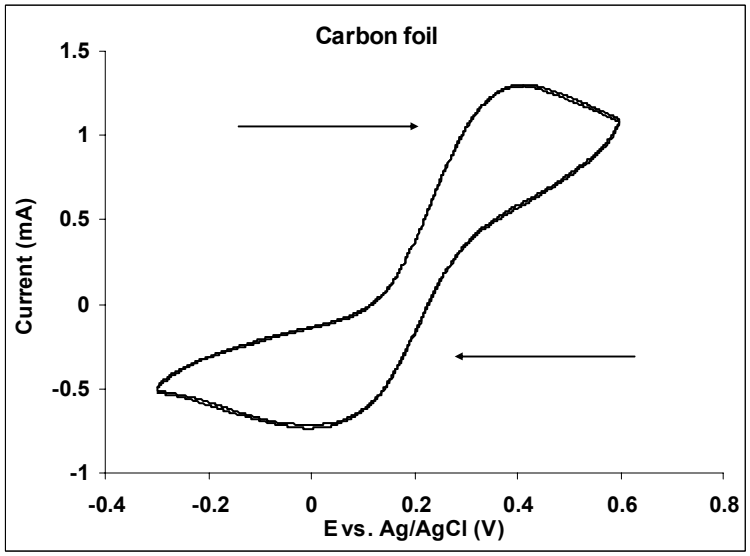

Fig 6.5 Cyclic voltammogram (2nd cycle) for carbon foil in 0.01 M $K_4Fe(CN)_6$ with 0.1 M $NaNO_3$ as a supporting electrolyte, E = -0.3, + 0.6 V, scan rate of 50 mV/s.

6.3.3 Polymers electrodeposition and after growth cyclic voltammetry

It has been reported that the CV of PPy in 0.1 M $LiClO_4$ exhibited a redox response superimposed on a capacitive background (326, 327). For uncoated carbon nanotubes electrode generally there are no redox peaks under the same conditions (328). However, for PPy-coated carbon nanotubes the following difference were observed. The CV characteristics of the PPy-coated carbon nanotubes were not influenced by the film formation charge but the charge capacity was observed to increase at negative potentials. This is in contrast to the behavior of conventional PPy film. In addition, it was noted that the specific charge capacity of the PPy coated carbon nanotubes is higher that that of PPy films (319).

PPy/NO_3, PPy/Dex, and PPy/AHFP were electrodeposited on RCNT mat (unannealed) to the same charge using constant current, constant potential, and cyclic potential. There was no polymer deposition on the RCNT mat (unannealed) when constant current was the electrodeposition method. When cyclic potential or constant potential were used as the electrodeposition method, the polymer did grow on the surface of the RCNT mat (unannealed) electrode. Although there was polymer deposition when cyclic potential was applied, the current decreased on each cycle compared to the previous cycle indicating an increased iR drop and/or a decrease in surface area due to the electrodeposition of the polymer, as can be seen in (Fig 6.6).

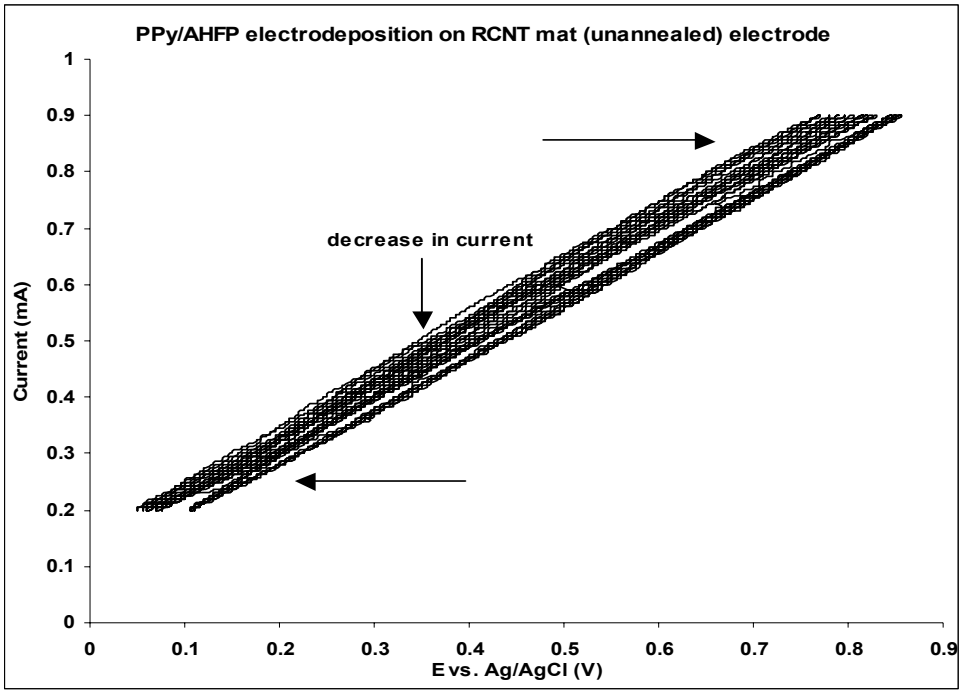

Fig 6.8 PPy/AHFP electrodeposition on RCNT mat (unannealed) using cyclic potential with a potential window of E = +0.5, +0.9 V and scan rate of 50 mV/s for 20 cycles.

Therefore, it was determined that constant potential was the preferred method of growth. Below are the after growth CVs for the polymers electrodeposited on the RCNT mat (unannealed) electrodes using constant potential (Fig 6.7 – 6.9).

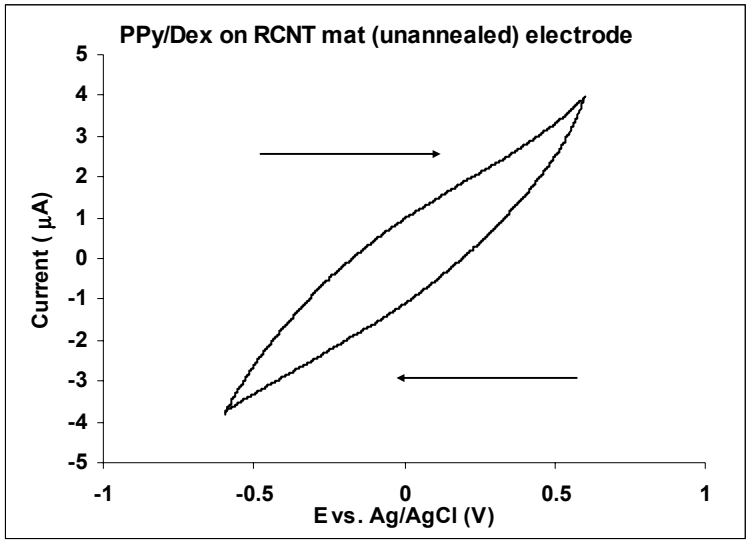

Fig 6.7 Cyclic voltammogram (2nd cycle) of PPy/Dex deposited on RCNT mat (unannealed) electrode in 0.1 M $NaNO_3$, E = -0.6, + 0.6, scan rate of 50 mV/s.

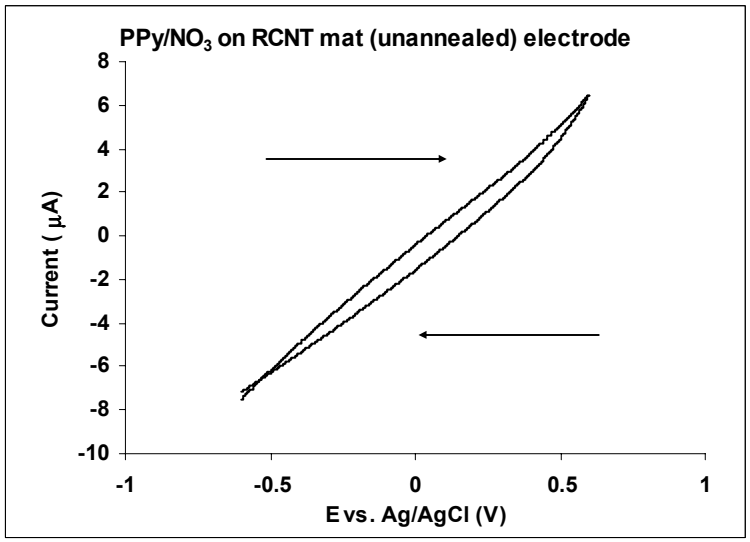

Fig 6.8 Cyclic voltammogram (2nd cycle) of PPy/NO_3 deposited on RCNT mat (unannealed) electrode in 0.1 M $NaNO_3$, E = -0.6, + 0.6, scan rate of 50 mV/s.

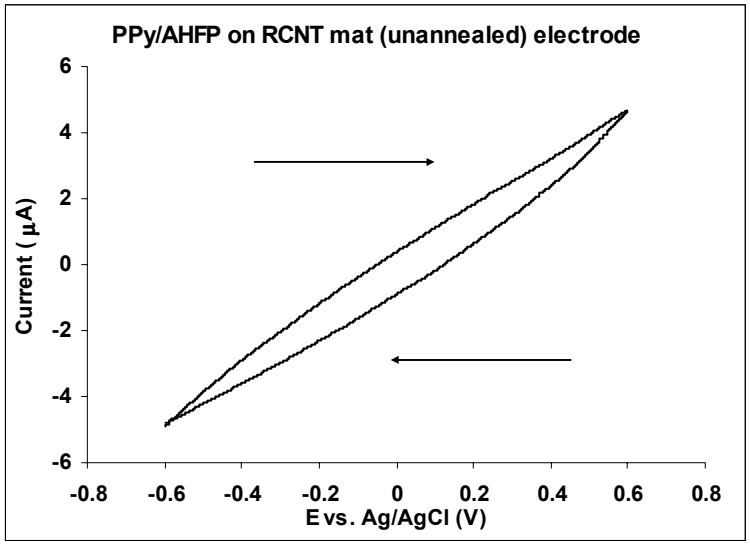

Fig 6.9 Cyclic voltammogram (2nd cycle) of PPy/AHFP deposited on RCNT mat (unannealed) electrode in 0.1 M $NaNO_3$, E = -0.6, + 0.6, scan rate of 50 mV/s.

The after growth CVs for the polymers deposited on RCNT mat (unannealed) electrodes using constant potential (above figures), constant current, or cyclic potential did not exhibit any redox peaks. This could be due to the nature of the underlying electrode, in this case the RCNT mat (unannealed) where physical and/or chemical interactions resulted in the absence of redox behavior. This was investigated by the electrodeposition of PPy/AHFP on RCNT mat (unannealed), RCNT mat (annealed) and glassy carbon electrodes using constant potential to the same charge. The after growth CVs of PPy/AHFP on these electrodes are presented below (Fig 6.10 – 6.12)

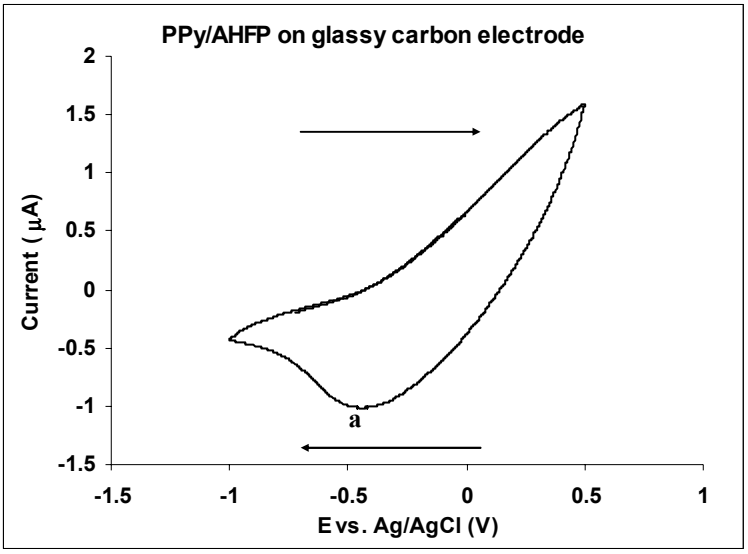

Fig 6.10 Cyclic voltammogram (2nd cycle) of PPy/AHFP deposited on glassy carbon electrode in 0.1 M $NaNO_3$, E = -1, +0.5 V with a scan rate of 50 mV/s.

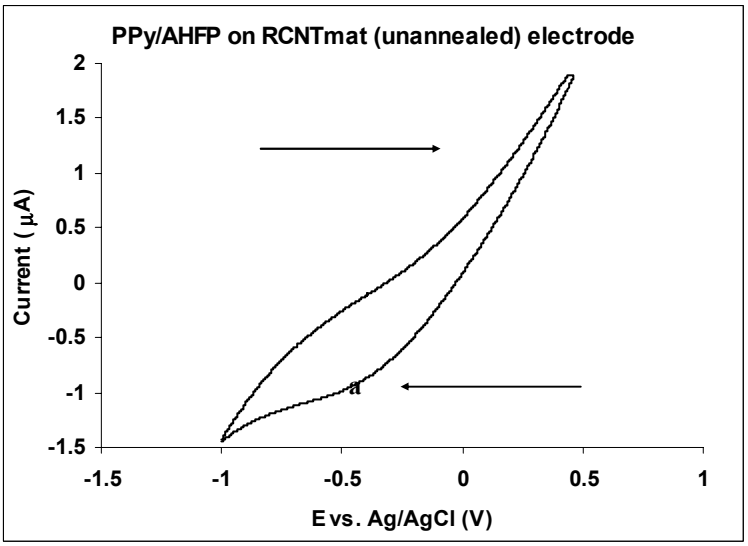

Fig 6.11 Cyclic voltammogram (2nd cycle) of PPy/AHFP deposited on RCNT mat (unannealed) electrode in 0.1 M $NaNO_3$, E = -1, +0.5 V with a scan rate of 50 mV/s.

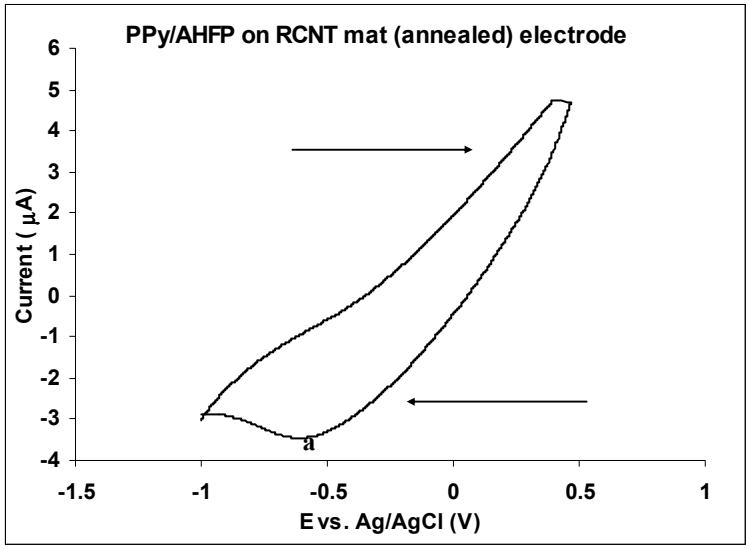

Fig 6.12 Cyclic voltammogram (2nd cycle) of PPy/AHFP deposited on RCNT mat (annealed) electrode in 0.1 M $NaNO_3$, E = -1, +0.5 V with a scan rate of 50 mV/s.

From these figures we can see a reduction peak (**a**) but no oxidation peak. This reduction peak is more defined when the polymer is deposited onto the glassy carbon, and RCNT mat (annealed) electrodes, indicating that these electrodes facilitate the redox process. In addition, it is observed that the current range for the PPy/AHFP on the RCNT mat (annealed) electrode is twice that of the polymer on the other two electrodes. This indicated that the rate of growth of the polymer onto the RCNT mat (annealed) electrode surface is higher than on the other electrodes, which means that the RCNT mat (annealed) electrode facilitates the growth of conducting polymers. On the other hand, RCNT mat (unannealed) electrode seems to inhibit the conductivity of the deposited polymers, where these polymers did not exhibit redox peaks.

Another factor that might have contributed to the non-conductive response of the polymers deposited on the RCNT mat (unannealed) electrodes as noted previously, could be the nature of the dopant used, where the dopant could interact with the RCNT mat (unannealed) resulting in a compound that does not exhibit any redox responses. This was investigated by the electrodeposition of PPy/SDS on four different electrodes: RCNT mat (unannealed), RCNT mat (annealed), carbon foil, and glassy carbon electrodes to the same charge. The electrodeposition was carried out using constant current, constant potential, and cyclic potential (Fig 6.13 – 6.15). The results were used for comparison with PPy/AHFP to determine whether the dopant used is a factor in the conductivity of the polymer deposited on the RCNT mats.

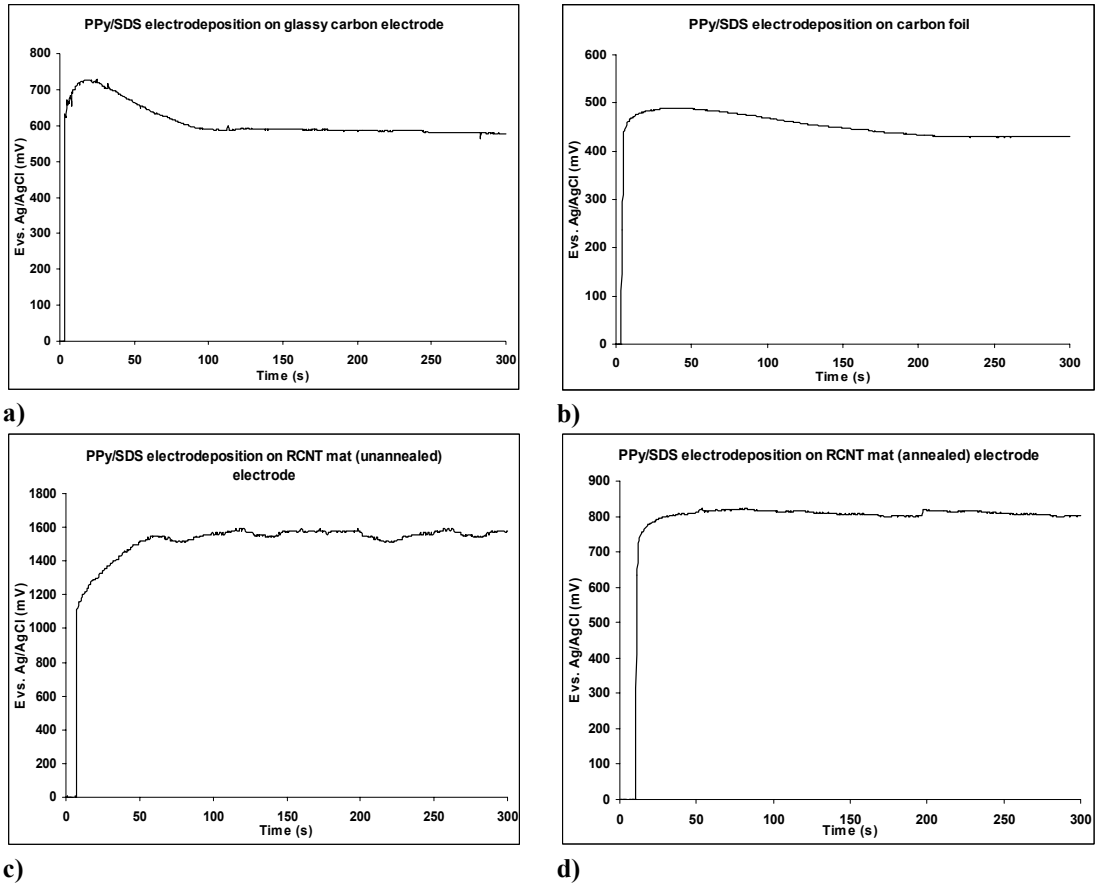

Fig 6.13 PPy/SDS electrodeposition on a) glassy carbon, b) carbon foil, c) RCNT mat (unannealed), and d) RCNT mat (annealed) using a constant current of 1 mA (j=1 mA/cm^2) for 5 min.

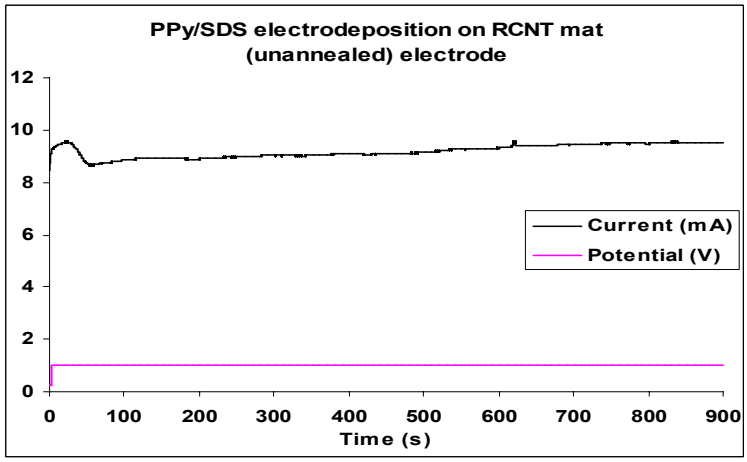

Fig 6.14 PPy/SDS electrodeposition on RCNT mat (unannealed) using constant potential of E =1 V for 15 min.

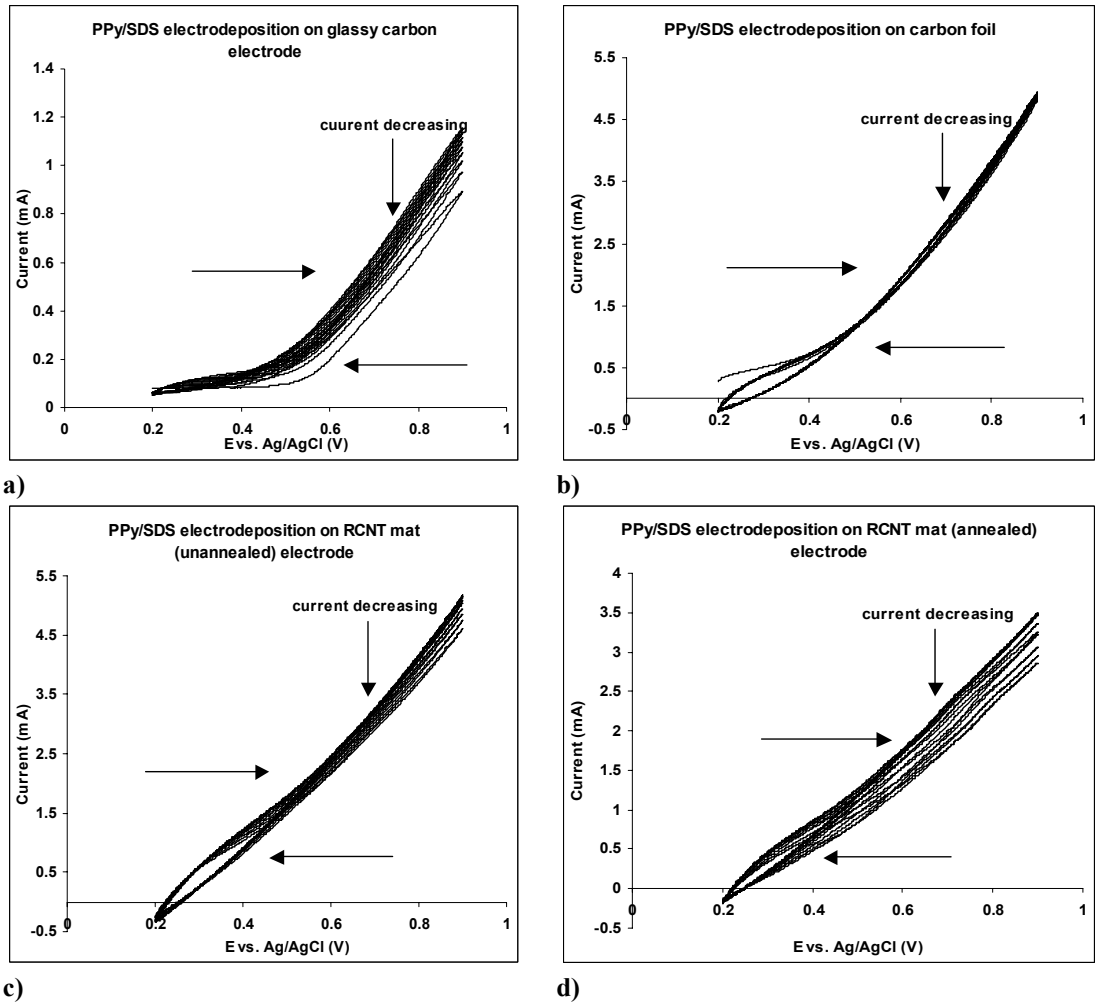

Fig 6.15 PPy/SDS electrodeposition on a) glassy carbon, b) carbon foil, c) RCNT mat (unannealed), and d) RCNT mat (annealed) using cyclic potential with a potential window of E = +0.2, +0.9 V and scan rate of 50 mV/s for 20 cycles.

As can be seen in the figures above, the polymer electrodeposition is dependent on the nature of the electrode. When PPy/SDS was electrodeposited using constant current, the current ranged from 1.6 mA maximum for RCNT mat (unannealed) to 8.5 mA maximum for RCNT mat (annealed) (Fig 6.13). In addition, when cyclic potential was the method used for polymer electrodeposition, the current decreased on each cycle compared to the previous cycle indicating an increased *iR* drop and/or

a decrease in surface area due to the electrodeposition of the polymer (Fig 6.15), this is consistent with previous observation in (Fig 6.6). The after growth CVs for PPy/SDS are presented below (Fig 6.16 – 6.18).

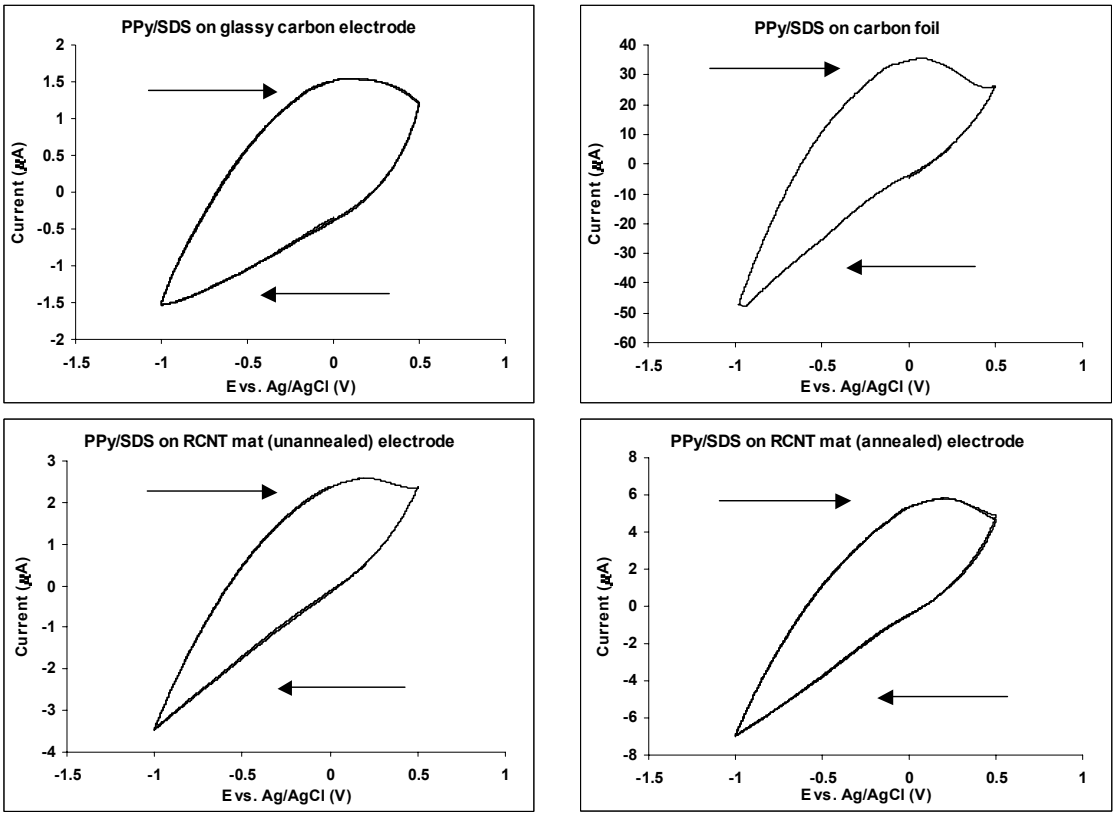

Fig 6.16 Cyclic voltammograms (2nd cycle) of PPy/SDS deposited on different carbon electrodes using constant current of 1 mA (j= 0.07 mA/cm^2) for 5 min. in 0.1 M $NaNO_3$, E = -1, +0.5 V with a scan rate of 50 mV/s.

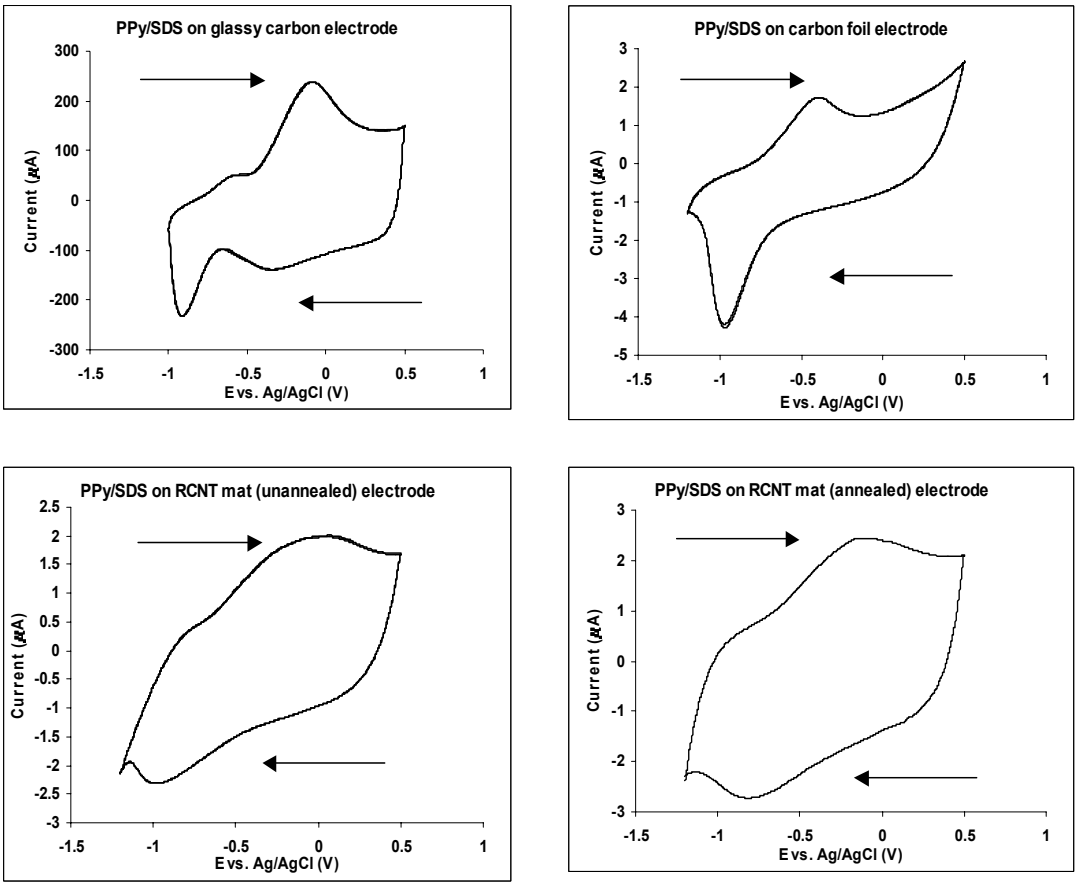

Fig 6.17 Cyclic voltammograms (2^{nd} cycle) of PPy/SDS deposited on different carbon electrodes using constant potential of E = +1 V for 15 min. in 0.1 M $NaNO_3$, E = -1, +0.5 V with a scan rate of 50 mV/s.

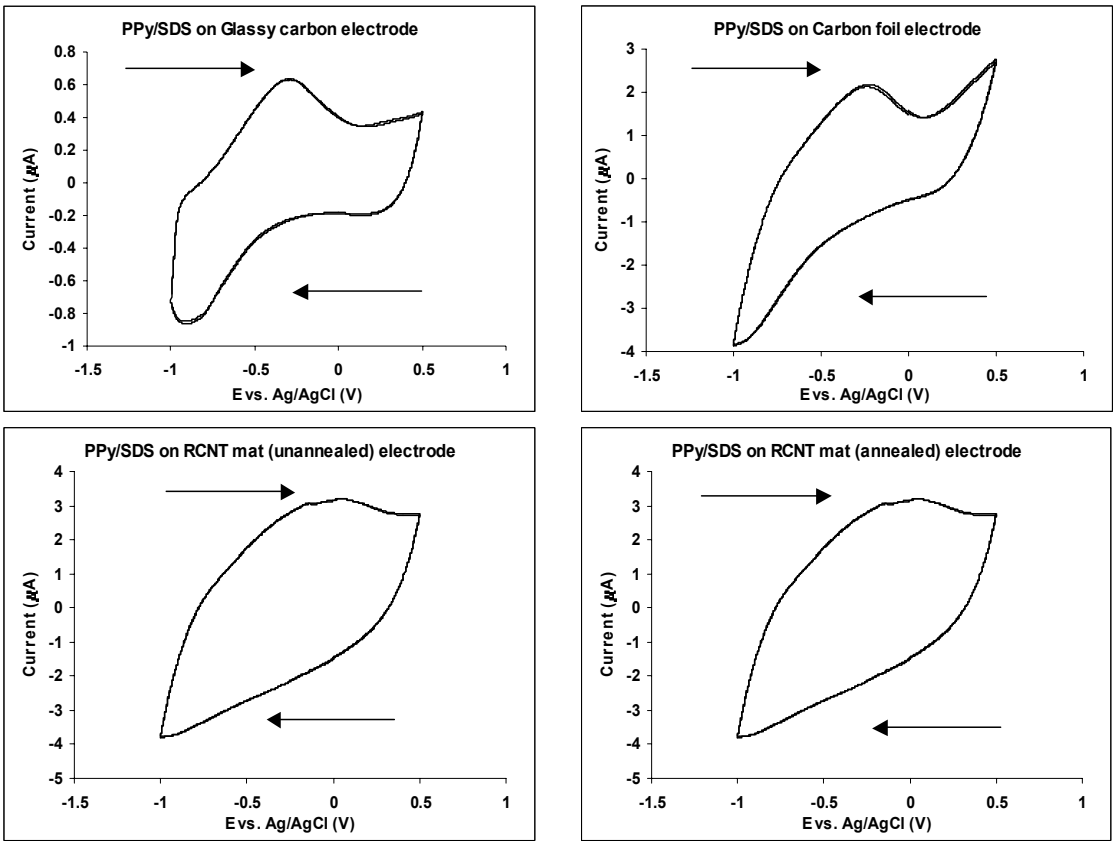

Fig 6.18 Cyclic voltammograms (2nd cycle) of PPy/SDS deposited on different carbon electrodes using cyclic potential with a potential window of E = +0.2, +0.9 V for 10 cycles in 0.1 M $NaNO_3$, E = -1, +0.5 V with a scan rate of 50 mV/s.

The after growth CVs of PPy/SDS electrodeposited using constant current on different carbon electrodes are presented in (Fig 6.16). The after growth CVs were similar regardless of the electrode used. In each, a broad oxidation peak was observed. However, the current range varied depending on the underlying electrode, carbon foil had a maximum current of ~ 40 μA which is nearly 10-times larger than that of the other electrodes.

The after growth cyclic voltammograms for PPy/SDS electrodeposited using constant potential on the different electrodes are presented in (Fig 6.17). We can see that the background current for the PPy/SDS on glassy carbon electrode ~ 300 μA is significantly higher than the background current for the polymer on the other electrodes ~ 4 μA. In addition, the PPy/SDS grown on glassy carbon electrode and carbon foil exhibit sharp well-defined oxidation and reduction peaks. However, the redox peaks for the PPy/SDS grown on RCNT mat (unannealed) and RCNT mat (annealed) are broad and less defined. Also, the after growth CV for the PPy/SDS on the RCNT mat (annealed) electrode exhibited a capacitive behavior. The same observations can be made for the after growth CVs for PPy/SDS grown using cyclic potential on the different electrodes (Fig 6.18). However, the current for the PPy/SDS grown on glassy carbon electrode was within the same range as for the other electrodes.

We find that the conductivity of the polymer deposited is affected by the method of deposition. When comparing the CVs of PPy/SDS deposited on carbon foil and glassy carbon electrode, we find that when the polymer was deposited using constant current a broad oxidation peak was observed only. On the other hand, when constant potential or cyclic potential were used as the electrodeposition method, distinct redox peaks were observed. However, we have to keep in mind that during electrodeposition using cyclic potential the current decreased with each cycle compared to the previous one. This means that electrodeposition using constant potential is preferred to the other methods.

In addition, we find that the PPy/SDS deposited on RCNT mat (unannealed) and RCNT mat (annealed) using constant potential exhibited redox peaks, in contrast to PPy/NO_3, PPy/DS, and PPy/AHFP electrodeposited on the same electrodes under the same conditions. This indicated that the dopant used has an affect on the electroactivity of the polymer when electrodeposited on RCNT mats.

6.3.4 Scanning Electron Microscopy (SEM)

SEM pictures were obtained for PPy/NO_3, PPy/Dex, PPy/AHFP, and PPy/SDS electrodeposited on RCNT mat (unannealed) (Fig 6.19 – 6.22), respectively. From the SEM pictures we can see that the different polymers have been electrodeposited on the RCNT mat (unannealed). This indicated that the non-conductive behavior observed for PPy/NO_3, PPy/Dex, and PPy/AHFP is not due to the absence of a polymer film but is a result of the nature of the underlying electrode, the nature of the polymer electrodeposited and its chemical/physical interaction with the underlying electrode, and finally the electrodeposition method.

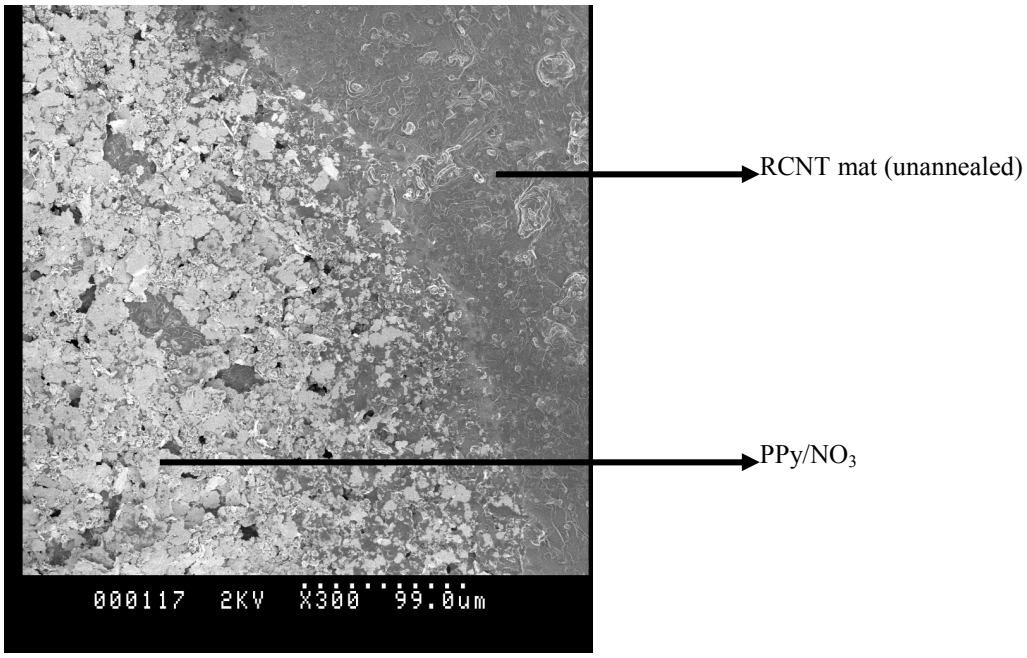

Fig 6.19 SEM picture of PPy/NO_3 electrodeposited using constant current on RCNT mat (unannealed).

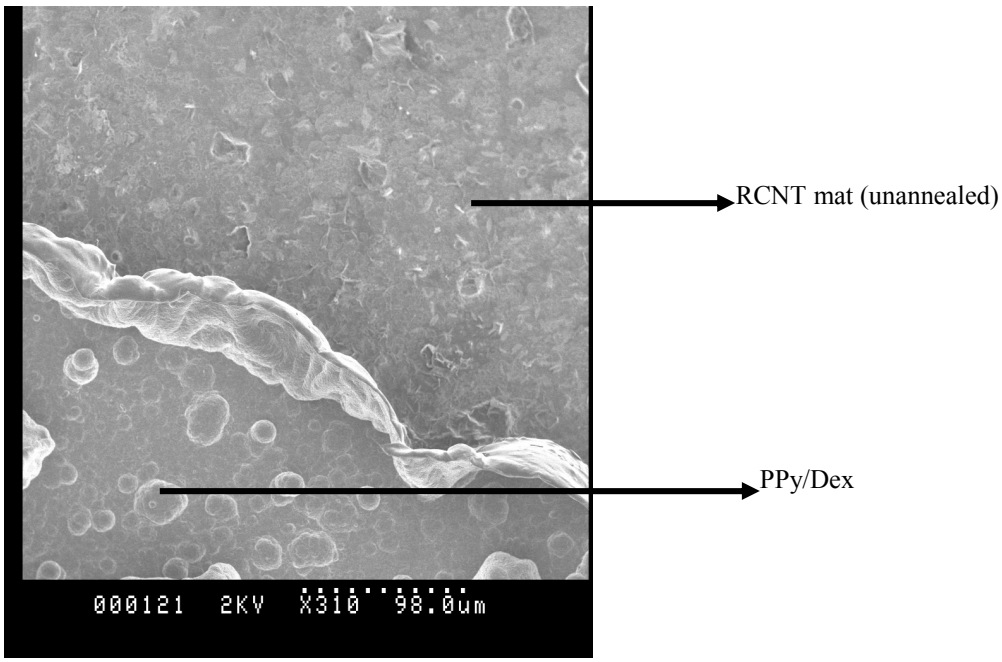

Fig 6.20 SEM picture of PPy/Dex electrodeposited using constant current on RCNT mat (unannealed).

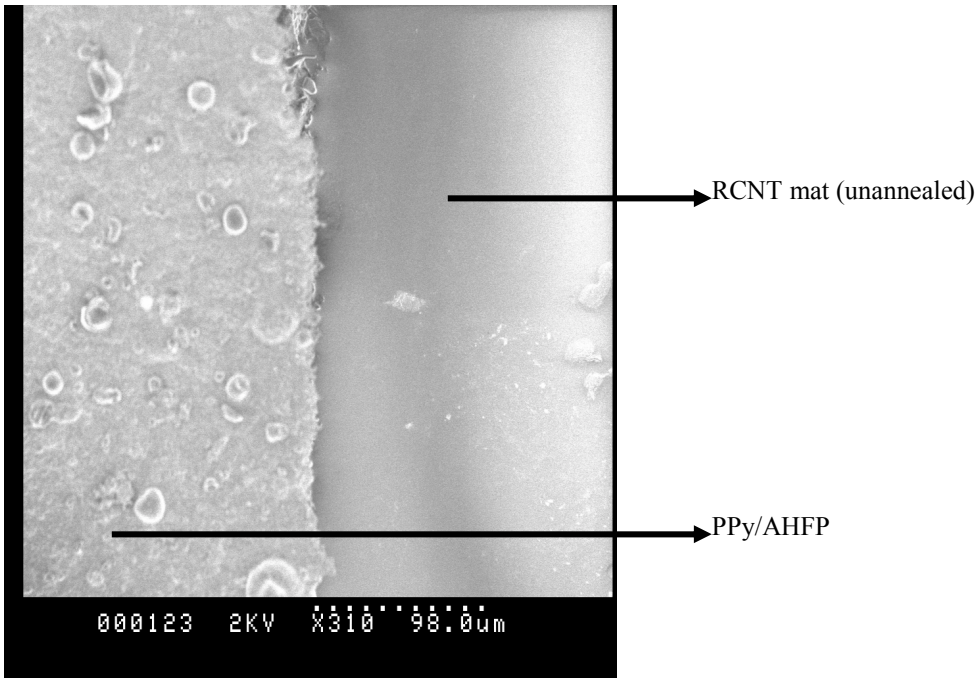

Fig 6.21 SEM picture of PPy/AHFP electrodeposited using constant current on RCNT mat (unannealed).

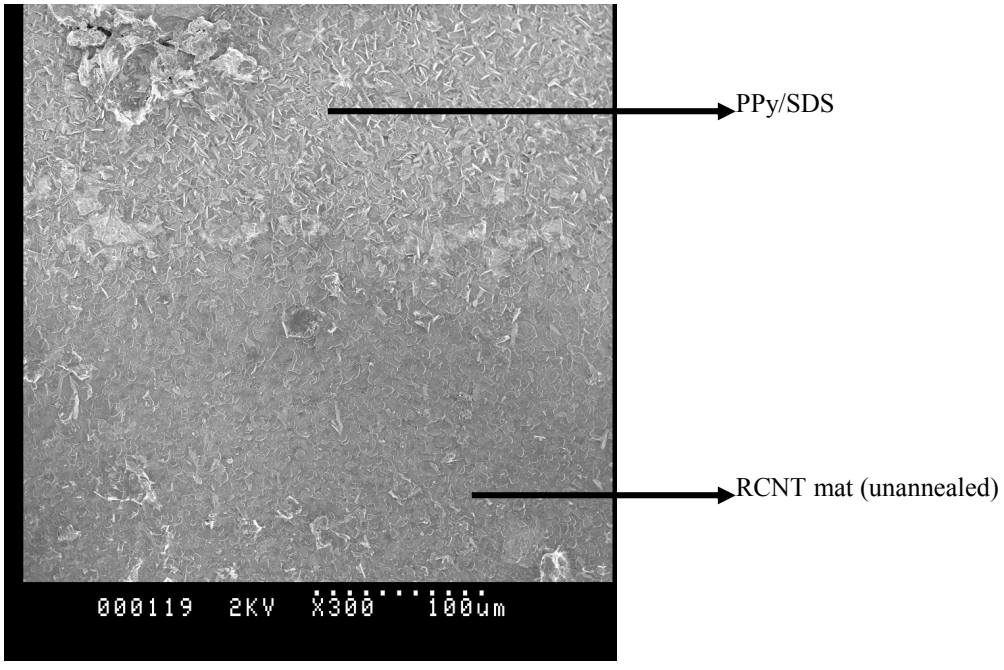

Fig 6.22 SEM picture of PPy/SDS electrodeposited using constant current on RCNT mat (unannealed).

6.4- CONCLUSION

Conducting polymers were electrodeposited on the surface of RCNT mat (unannealed) electrode. The polymers were electrodeposited using constant current, constant potential and cyclic potential. No polymer growth was observed when constant current deposition was employed. When cyclic potential was used as the method of growth there was polymer deposition. However, the current decreased in sequential cycles instead of increasing, indicating that the polymer deposited was very resistive. Therefore, constant potential was chosen as the preferred method for deposition of the polymer onto the RCNT mat (unannealed) electrode. The after growth CV of these composites did not exhibit any redox behavior. As a result, PPy/AHFP was electrodeposited using constant potential on RCNT mat (unannealed), RCNT mat (annealed), and glassy carbon electrode to determine if the reason for the absence of the redox behavior was the nature of the RCNT mat (unannealed). The results indicated that this could be a factor in the non-conductive behavior of the polymers deposited on the RCNT mat (unannealed), suggesting that the impurities present in the unannealed mat inhibit the conductivity of the polymer deposited. Also, we found that the polymer deposited on the RCNT mat (annealed) electrode had better growth rate and redox responses, indicating that polymer electrodeposition on RCNT mat (annealed) electrode is preferable compared to RCNT mat (unannealed) electrode. Finally, PPy/SDS was electrodeposited onto the surface of different carbon electrodes to investigate the role of dopant. PPy/SDS was electrodeposited onto glassy carbon electrode, carbon foil, RCNT mat (unannealed) electrode, and RCNT mat (annealed) electrode. The electrodeposition was carried out

using constant current, constant potential, and cyclic potential. The growth was dependent on the nature of the electrode, and consistent with previous observation when using cyclic potential as the electrodeposition method the current decreased in each cycle compared to the previous one. It was established that PPy/SDS deposited on RCNT mat (unannealed) and RCNT mat (annealed) using constant potential does exhibit electroactivity; in contrast to PPy/NO_3, PPy/Dex, and PPy/AHFP electrodeposited under the same conditions on RCNT mat (unannealed). This indicated that the dopant used does have an effect on the conductivity of the polymer when electrodeposited on RCNT mats. In addition, PPy/SDS deposited on carbon foil and glassy carbon electrode using constant potential or cyclic potential exhibited distinct redox peaks, while only a broad oxidation peak was observed when constant current was used as the electrodeposition method. Therefore, the conductivity of the polymer deposited is also affected by the method of deposition.

We conclude that constant current as the method of electrodeposition of a polymer onto RCNT mat (unannealed) results in polymers that are non-conductive, and that the dopant and the method of electrodeposition used seem to have a significant effect on the electrochemical behavior of the polymer especially when deposited on the RCNT mat electrode.

Finally, we can electrodeposit a conducting polymer on RCNT mats if the right conditions are applied. For example, PPy/SDS electrodeposited on RCNT using constant potential results in a conducting polymer.

CHAPTER SEVEN

DEOXYRIBOSE NUCLIEC ACID (DNA) AND POLY(METHOXYANILINE-5-SULFONIC ACID) COATED CARBON NANOTUBES RIBBONS AND FIBRES

7.1- INTRODUCTION

The interaction of biomolecules with carbon nanotubes have been of interest with a view to rendering them biocompatible (329), or useful as bioelectronic sensors (330), or even as platforms to support the growth of nerve cells (331). DNA has been shown to strongly interact with CNT's, forming uniform coatings (332). The interactions are strong enough to influence the electronic properties of the DNA (333). Synthetic strategies that enable the oligonucleotides to be covalently linked to carbon nanotubes have also been developed (334).

Fibres of polypropylene/carbon nanotubes have been previously spun using conventional melt spinning equipment (335). It was found that 5% w/w loading of carbon nanotubes increased the modulus and strength of the propylene by 50 and 100%, respectively.

In another study, SWCNT were dispersed in isotropic petroleum pitch to form carbon nanotubes composite fibres with enhanced mechanical and electrical properties (336). It was found that the tensile strength, Young's modulus and electrical conductivity increased by 90, 150, and 340% respectively, when a loading of 5% w/w SWCNT was used.

Single-walled carbon nanotubes ribbons and fibres have been prepared previously by particle coagulation spinning (PCS) (337 - 339). This process consists of dispersing the carbon nanotubes in a dispersant solution and then re-condensing the nanotubes in a stream of a polymer solution. The dispersant that was used in those studies was sodium dodecyl sulfate (SDS) and the polymer solution was Poly(vinyl alcohol) (PVA).

In this chapter, we investigate the preparation of HiPco carbon nanotubes (HCNT) ribbons (wet) and fibres (dry) using the PCS method, with deoxyribbonucleic acid (DNA) or Poly(methoxy aniline-5-sulfonic acid) (PMAS) as dispersants, with PVA as the coagulating polymer. The ribbons and fibres conductivity, and mechanical properties were determined, and Scanning Electron Microscopy (SEM) was used to probe the microstructures.

In contrast to composite fibers, where the carbon nanotubes are embedded in polymeric matrix, the fibers produced by the PCS method consist of an interconnected network of polymer chains and carbon nanotubes. These fibers exhibit attractive features such as, the possibility of making continuous and macroscopic structures of aligned nanotubes (340), mechanical flexibility (337), toughness (341), high porosity, and capabilities for adsorbing gases and liquids (342).

7.2- EXPERIMENTAL

7.2.1 Materials

The HiPco single-walled carbon nanotubes (average tube diameter of 1.1 nm) were purchased from Carbon Nanotechnologies Incorporated (CNI) as a solid powder. The dispersant solutions were prepared using sodium dodecyl sulfate (SDS) (M.W. 288.37 Da, Aldrich), Poly(methoxyaniline-5-sulfonic acid) (PMAS) (M.W. 8,000 – 12,000 Da, Nitto Chemical Industry), and Deoxyribose Nucleic Acid (DNA) (Salmon sperm, 300 – 600 base pairs), from Prof. N. Ogata (Sophia University, Japan). The coagulating polymer Poly(vinyl alcohol) (PVA) (M. W. ~ 100,000 Da, Fluka).

7.2.2 Instrumentation

The diameter of the fibres was measured using a Leica DMLP microscope. Four-point probe conductivity measurements were carried out using a Keithley Instruments SARL 2000 multimeter. Mechanical properties were measured using Zwick/Z 2.5 from Zwick materials testing; the sample length was 3 cm.

7.2.3 Fiber preparation

A phase diagram for HCNT w/w dispersed in SDS solution was prepared prior to this work by Vigolo *et al* (337). The optimum concentration for HCNT dispersed in SDS was determined to be 0.25% w/w. In this work values above and below this concentration ranging from 0.1% to 0.5% w/w of HCNT dispersed in poly(methoxy aniline-5-sulfonic acid) (PMAS) and in Deoxyribose nucleic acid (DNA) were

examined. It was determined that the optimum concentration of HCNT in PMAS is 0.3% w/w, and 0.4% w/w in DNA. The following mixtures were prepared:

Dispersion I: 0.4% HCNT in 1% SDS

Dispersion II: 0.3% HCNT in 0.2% PMAS

Dispersion III: 0.3% HCNT, 0.4% SDS, in 0.2% PMAS

Dispersion IV:0.4% HCNT in 0.2% DNA

Dispersion V: 0.4% HCNT, 0.4% SDS, in 0.2% DNA.

Mixtures were sonicated for 1-hour using a hand held sonicator, Vibra-cell 72405 from BioBlock Scientific with a 6 sec pulse and an amplitude of 80%.

The dispersion was injected by a KD Scientific syringe pump at 100 ml/h into a stream of 3% PVA solution. The PVA solution was rotated at 50 turns per min. Injection was performed tangentially to the polymer stream through a syringe needle (0.5 mm in diameter) located 2 cm from the rotation axis of the bath. During this process the PVA adsorbs onto the HCNT and thus they stick to each other in the PVA stream. Under these conditions, as for solutions of rigid polymers flow, induced-alignment of the nanotubes is expected in the direction of the fluid velocity Scheme – 7.1.

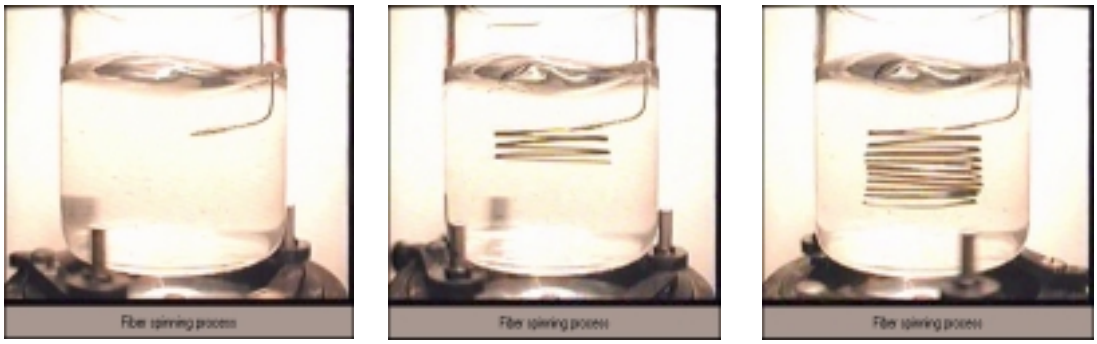

Scheme –7.1 Fiber spinning process.

The nanotubes are thus collected in the form of a ribbon, with preferential orientation along their axis (337, 338). The ribbons are washed with Milli-Q-Water and rinsed several times to remove PVA and dispersant molecules as much as possible. Rinsed ribbons are vertically suspended in air so that capillary and gravitational forces cause the water to be expelled. The ribbons collapse and ultimately form denser fibres when dry. Some fibres have been subsequently annealed at 1000 °C under reduced pressure and 500 sccm hydrogen flow (hydrogen was used to avoid nanotube damage due to oxidation).

From dispersion I (0.4% HCNT in 1% SDS) six fibres were produced, the first fiber (A) did not undergo any kind of treatment, the second fiber (B) was annealed, the third (C) was placed in 5% PMAS and 1% PVA solution for 35 min, the fourth fiber (D) was annealed first then placed in 5% PMAS and 1% PVA solution for 35 min, the fifth fiber (E) was placed in 5% PMAS and 1% PVA solution then placed in an oven at 120 °C for 4-hours, the sixth fiber (F) was annealed and placed in 5% PMAS and 1% PVA solution then in an oven at 120 °C for 4-hours. This was done in an attempt to cross link PMAS with PVA while coating the HCNT fiber.

Two fibres from each of the dispersions II, III, IV, and V were obtained, where one of these fibres was annealed.

7.3- RESULTS & DISCUSSION

Guo *et al* found that double-stranded DNA tends to cover the surface of nanotubes evenly, suggesting a strong interaction with the carbon surface (343). It was determined that double-stranded DNA did not disperse HCNT. However, a solution of single-stranded DNA that was obtained by heating to 91 °C, did result in an effective dispersion of the HCNT (344)*.

Single stranded DNA, in contrast to double-stranded DNA, exhibits amphiphilic character and adsorbed onto carbon nanotubes (345). In addition, single-stranded DNA allows for a more flexible formulation than classical dispersant. Studies of partially unwrapped double helix DNA molecules with carbon nanotubes have been conducted by Buzaneva *et al* and Matyshevska *et al* (346, 347). They found that the regular system of hydrogen bonds in the DNA has to be destroyed to promote the interaction of DNA with the carbon nanotubes. It was determined that the bonds between guanine-adenine and thymine-cytosine in the DNA molecules broke, which meant that the distance between electron levels in the molecule changed, and the hydrogen bonds between the bases of the DNA molecules broke as well. The results confirmed that the electronic structure of the DNA/SWCNT layer is determined by changes in the electronic level in the nucleotide bases of DNA molecules upon DNA/SWCNT interaction (347). In addition, they found that the DNA structure is modified after interacting with the carbon nanotubes, while the structure of the carbon nanotubes did not change in the DNA/SWCNT composite.

* **Appendix A: Properties of carbon nanotubes fibers spun from DNA- stabilized dispersions.**

7.3.1 Fiber diameter

The diameter of the HCNT fibres can be controlled by varying parameters such as injection rate, flow conditions, and dimensions of the capillary injection tube employed. These parameters impose the initial thickness of the ribbons. Qualitatively, the ribbons become thicker and wider by lowering the speed of the co-flowing polymer solution and increasing the injection rate. This behavior strongly suggested an important contribution of the hydrodynamic conditions. The parameters under which the fibers were prepared were constant. Therefore, the fibre diameter along its length is homogenous.

Table –7.1 shows the diameter for the fibres prepared from dispersion I, and Table – 7.2 shows the diameter of the fibres prepared from the remaining dispersions. In general, it is obvious from the results presented in the tables below that the diameter of the annealed fibres is smaller than that for the unannealed fibres. This indicated that the annealing process eliminates a significant amount of the remaining dispersant and the PVA molecules (343). Previous studies indicated that PVA is thermally degraded during the annealing process (344).

Table –7.1 Diameter for fibres prepared from dispersion I (0.4% HCNT, 1% SDS).

Fiber	**Diameter (μm ± 0.1)**
A (unannealed)	32.1
B (annealed)	20.2
C (unannealed placed in 5%PMAS and 1% PVA mixture for 35 min)	32.0
D (annealed placed in 5%PMAS and 1% PVA mixture for 35 min)	20.5
E (unannealed placed in 5% PMAS and 1% PVA mixture for 35 min, then placed in an oven at 120 °C for 4-hours)	36.3
F (annealed placed in 5% PMAS and 1% PVA mixture for 35 min, then placed in an oven at 120 °C for 4-hours)	20.6

Table –7.2 Diameter for fibres prepared from dispersion II, III, IV, and V.

Fiber composition	**Diameter (μm ± 0.1)**
0.4% HCNT / 0.3% PMAS (unannealed)	72.1
0.4% HCNT / 0.3% PMAS (annealed)	64.3
0.4% HCNT / 0.3% PMAS / 0.4% SDS (unannealed)	88.2
0.4% HCNT / 0.3% PMAS / 0.4% SDS (annealed)	84.4
0.4% HCNT / 0.4% DNA (unannealed)	48.7
0.4% HCNT / 0.4% DNA (annealed)	43.2
0.4% HCNT/ 0.4% DNA / 0.4% SDS (unannealed)	48.1
0.4% HCNT / 0.4% DNA / 0.4% SDS (annealed)	44.3

From Table –7.1 we notice that placing the fibers in 5% PMAS and 1% PVA solution whether followed by placement in an oven at 120 °C or not, did not result in any significant change in the diameter of the fibers. On the other hand, the diameter of the annealed fibers was only two thirds of the corresponding unannealed fibers. This indicated that the annealing process results in the thermal degradation of PVA, and the removal of amorphous carbon. In Table –7.2, we notice that the diameter of the HCNT/PMAS fibers is approximately twice that of HCNT/DNA fibers, indicating that the HCNT uptake of PMAS is nearly twice that of DNA. In addition, the diameter of the HCNT/PMAS/SDS fiber was larger than that for the HCNT/PMAS fiber, while the diameter of the HCNT/DNA and HCNT/DNA/SDS fibers were very similar (344). This indicated that either the SDS was also incorporated into the fiber matrix of the HCNT/PMAS/SDS fiber, or that SDS facilitated an even larger intake of the PMAS molecules by the HCNT. Moreover, we also notice that the diameter of the annealed fibers is smaller than that for the corresponding unannealed fibers. However, the difference in diameter is not as significant as that for the HCNT/SDS fibers (Table –7.1). This indicated that when the fibers are produced using SDS as the dispersant, the amount of PVA (coagulating polymer) incorporated within the fiber is significantly larger than that when PMAS or DNA are used as dispersants, resulting in a more significant decrease in diameter through the annealing process, due to the thermal degradation of the PVA.

7.3.2 Conductivity

The conductivity data for the different fibres are presented in Tables 7.3 and 7.4.

Table –7.3 Conductivity for the fibres prepared from dispersion I (0.4% HCNT, 1% SDS).

Fiber	**Conductivity (S/cm ± 0.1)**
A (unannealed)	0.2
B (annealed)	110.8
C (unannealed placed in 5%PMAS and 1% PVA mixture for 35 min)	0.1
D (annealed placed in 5%PMAS and 1% PVA mixture for 35 min)	108.8
E (unannealed placed in 5% PMAS and 1% PVA mixture for 35 min, then placed in an oven at 120 °C for 4-hours)	0.03
F (annealed placed in 5% PMAS and 1% PVA mixture for 35 min, then placed in an oven at 120 °C for 4-hours)	78.7

Table –7.4 Conductivity for fibres prepared from dispersion II, III, IV, and V.

Fiber	**Conductivity (S/cm ± 0.01)**
0.4% HCNT / 0.3% PMAS (unannealed)	0.32
0.4% HCNT / 0.3% PMAS (annealed)	7.71
0.4% HCNT / 0.3% PMAS / 0.4% SDS (unannealed)	0.05
0.4% HCNT / 0.3% PMAS / 0.4% SDS (annealed)	7.23
0.4% HCNT / 0.4% DNA (unannealed)	6.36
0.4% HCNT / 0.4% DNA (annealed)	100.07
0.4% HCNT/ 0.4% DNA / 0.4% SDS (unannealed)	7.73
0.4% HCNT / 0.4% DNA / 0.4% SDS (annealed)	100.05

One of the most important observations from Table –7.3 is the significant increase in the conductivity of the HCNT/SDS fibres when annealed. The increase in conductivity for the annealed fibers B, D, and F is ~ 500, 1000, and 2600 times respectively. Also, we notice that placing the fibers in 5% PMAS and 1% PVA solution for 35 min, had no effect on conductivity. However, for the fibres that were placed in 5% PMAS and 1% PVA and then in an oven at 120 °C for 4-hours, the conductivity values decreased with respect to the other fibers. However, the increase in conductivity due to the annealing process was the largest ~2600 times.

From Table –7.4 we can see that the fibres prepared using DNA as the dispersant had significantly higher conductivities than the fibres obtained using PMAS. The conductivity of the HCNT/DNA fibers was similar to that of HCNT/SDS fibers (Table – 7.3), while the conductivity of the HCNT/PMAS fibers was ~90% lower. This was not an expected result since PMAS is an inherently conducting polymer, and it was expected to increase the conductivity of HCNT fibres (before the annealing process, at least). We also notice, that HCNT/PMAS/SDS (unannealed) fibers have lower conductivities than HCNT/PMAS (unannealed) fibers. In addition, there was a significant increase in conductivity due to the annealing process, the increase in conductivity for the annealed HCNT/PMAS fiber compared to the unannealed HCNT/PMAS fiber was ~ 25 times. Also, the increase in conductivity for the HCNT/PMAS/SDS annealed fiber compared to the unannealed HCNT/PMAS/SDS fiber was ~ 150 times. This indicated that the annealing process resulted in the removal of not only PVA and amorphous carbon, but also the SDS. On the other hand, for the HCNT/DNA fibers the increase in conductivity due to the

annealing process was ~ 15 times, regardless of presence or absence of SDS. This indicated that the chemical/physical interaction between PMAS-SDS and DNA-SDS are significantly different.

7.3.3 Mechanical properties

In contrast to most ordinary carbon fibres, SWCNT fibres are ten times stronger than high quality SWCNT mats (336). In addition, the SWCNT fibres exhibit an elastic behavior before they break, that presumably arises from the possible displacement of the nanotubes within the bundles that make up the fibres (337).

The tables below present the Young's modulus values for the different fibres. For some of the annealed fibres the Young's modulus could not be measured due to the fact that they were very brittle (VB), and broke before mounting the sample. The Young's modulus values for the HCNT/SDS fibres were similar (Table –7.5). The Young's modulus for the HCNT/PMAS fibers and the HCNT/DNA (Table – 7.6) were higher than that for the HCNT/SDS fibers (Table – 7.5). An interesting result was the fact that the annealed HCNT/PMAS and HCNT/PMAS/SDS fibers had lower Young's modulus than the corresponding unannealed fibers. This indicated that the annealing process, which results in the removal of PVA and amorphous carbon, affects charge mobility along the fiber (e.g. conductivity) but plays no appreciable role in keeping the carbon nanotubes ropes together. Therefore, improving the electrical properties of the fibers and not the mechanical properties. This also suggests that the mechanical properties of the fibers are not affected by the different dispersants, and that they are mainly dependent on the mechanical properties of the HCNT themselves.

Table –7.5 Young's modulus for fibres prepared from dispersion I (0.4% HCNT, 1% SDS).

Fiber	**Y (GPa ± 0.01)**
A (unannealed)	9.16
B (annealed)	VB
C (unannealed placed in 5%PMAS and 1% PVA mixture for 35 min)	10.15
D (annealed placed in 5%PMAS and 1% PVA mixture for 35 min)	VB
E (unannealed placed in 5% PMAS and 1% PVA mixture for 35 min, then placed in an oven at 120 °C for 4-hours)	9.77
F (annealed placed in 5% PMAS and 1% PVA mixture for 35 min, then placed in an oven at 120 °C for 4-hours)	VB

***VB: very Brittle**

Table –7.6 Young's modulus for fibres prepared from dispersion II, III, IV, and V.

Fiber composition	**Y (GPa ± 0.01)**
0.4% HCNT / 0.3% PMAS (unannealed)	9.37
0.4% HCNT / 0.3% PMAS (annealed)	7.41
0.4% HCNT / 0.3% PMAS / 0.4% SDS (unannealed)	18.08
0.4% HCNT / 0.3% PMAS / 0.4% SDS (annealed)	12.72
0.4% HCNT / 0.4% DNA (unannealed)	15.26
0.4% HCNT / 0.4% DNA (annealed)	VB
0.4% HCNT/ 0.4% DNA / 0.4% SDS (unannealed)	12.72
0.4% HCNT / 0.4% DNA / 0.4% SDS (annealed)	VB

***VB: very Brittle**

7.3.4 Scanning Electron Microscopy (SEM)

It was determined previously that flow induced alignment leads to a preferential orientation of the nanotubes in the ribbons. The shape of the fiber is almost cylindrical and diameters typically range from 10 to 100 micrometer (339). It was also determined that the annealing process effects are limited to the diameter of the fiber (335, 347, 348), and does not modify the alignment (339).

SEM pictures were taken for the different fibres (Fig 7.1, and 7.2). From the figures below the alignment of the HCNT is obvious. Since the pictures were taken for the annealed fibres this also confirms that the annealing process does not affect the alignment of the HCNT in the fiber.

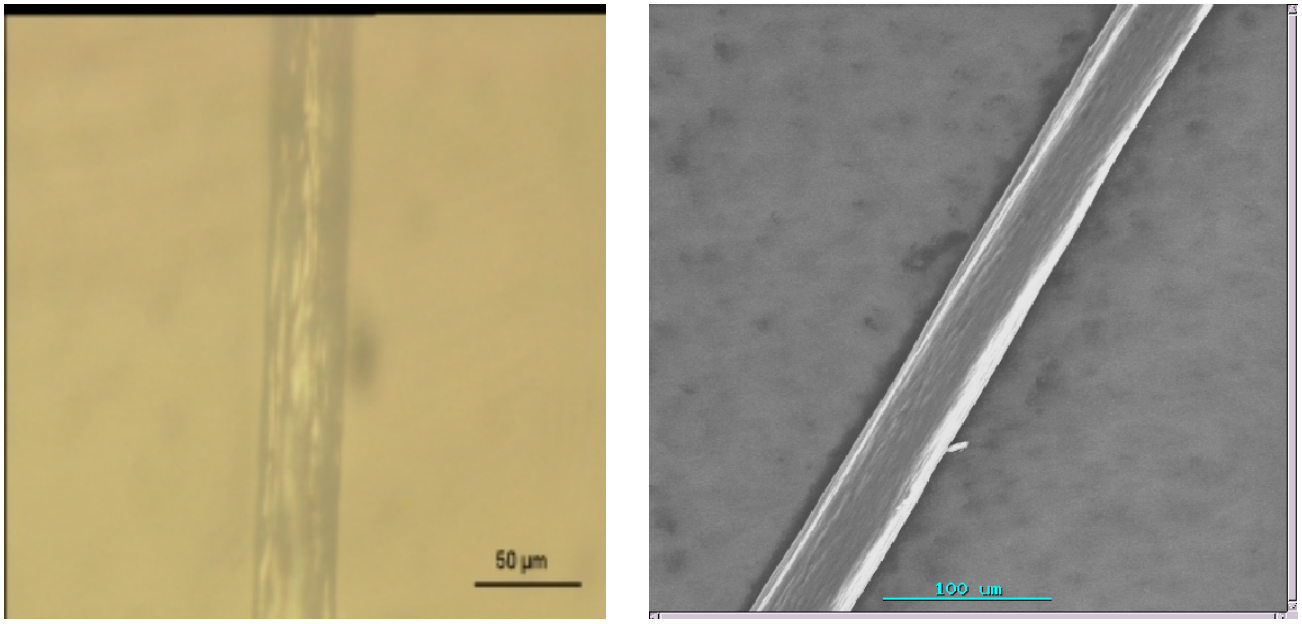

a) **b)**

Fig 7.1 SEM pictures of a) HCNT/SDS-fiber B (annealed), and b) HCNT/PMAS fiber (annealed).

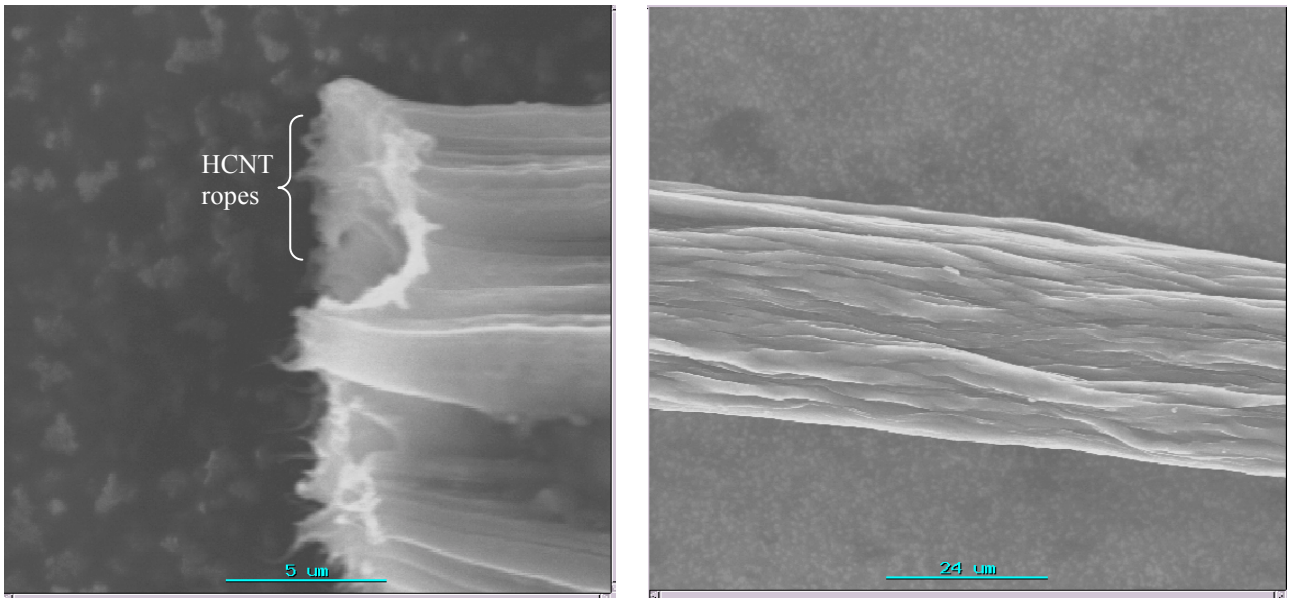

a) **b)**

Fig 7.2 SEM pictures of HCNT/DNA fiber (annealed) at different magnifications.

7.4- CONCLUSION

We have prepared HCNT/SDS, HCNT/PMAS and HCNT/DNA fibres by the particle coagulation spinning method. This process consists of dispersing the carbon nanotubes solution and then re-coagulating the nanotubes in a stream of a 3% w/w PVA solution. Some of these fibres were annealed, and some were placed in 5% w/w PMAS and 1% w/w PVA solution for cross-linking purposes.

The diameter of the annealed HCNT/SDS fibers was only two thirds of the corresponding unannealed fibers. This is due to the fact that the annealing process eliminates significant amounts of the remaining dispersant, PVA molecules, and amorphous carbon. Also, the diameter of the HCNT/PMAS fibers was approximately twice that of HCNT/DNA fibers, indicating that the HCNT uptake of PMAS is nearly twice that of DNA.

The conductivity of the annealed fibers compared to the corresponding unannealed fibers was dramatically higher, ranging from 15 to 2600 times higher. Indicating that the annealing process increases the conductivity of the fibers. Also, the fibres prepared using DNA as the dispersant had significantly higher conductivities than the fibres obtained using PMAS. The conductivity of the HCNT/PMAS fibers was ~90% lower than that for the HCNT/SDS fibers. This was not an expected result since PMAS is an inherently conducting polymer, and it was expected to increase the conductivity of HCNT fibres (before the annealing process, at least).

An interesting result was the fact that the annealed HCNT/PMAS and HCNT/PMAS/SDS fibers had lower Young's modulus than the corresponding unannealed fibers. It was also observed that most of the annealed fibers broke during mounting for Young's modulus measurements. This indicated that the annealing process, which resulted in the removal of PVA and amorphous carbon, affects charge mobility along the fiber but plays no appreciable role in keeping the carbon nanotubes ropes together. Therefore, the annealing process improves the electrical properties of the fibers and not the mechanical properties. This also suggests that the mechanical properties of the fibers are not affected by the different dispersants, and that they are mainly dependent on the mechanical properties of the HCNT themselves From the SEM pictures of the different fibers, the alignment of the HCNT was observed. Since the pictures were taken for the annealed fibres this also indicated that the annealing process does not affect the alignment of the HCNT in the fiber.

CHAPTER EIGHT

CONCLUSION

8.1- CONCLUSION

In this study we have investigated the preparation and characterization of carbon nanotubes (CNT) and conducting polymer composites. CNT dispersions and CNT/dispersant mats were prepared, using different types of carbon nanotubes; lazer produced single-walled carbon nanotubes (RCNT), HiPco carbon nanotubes (HCNT), and multi-walled carbon nanotubes (MWCNT). A variety of compounds were investigated as potential dispersants for the CNT, some of which were conducting polymers while others had an additional functionality such as DNA (biological molecule), NIPPAm-AMPS (polyelectrolyte), and DDAB (polymerizable compound).

Different concentrations of the dispersants were investigated, and the optimum concentration was determined to be 0.2% for all dispersants investigated. It was found that at concentrations higher than 0.2%, the CNT coagulated and were difficult to disperse even with ultrasonication.

The particle size distribution for the different dispersions was measured in order to determine their effectiveness by photon-correlation spectroscopy, with the analysis algorithms modified to compensate for the non-spherical nature of the carbon nanotube. In addition, the particle size was very large in general; this is due to the

fact that CNT tend to form aggregated ropes, which are much larger than a single CNT. Size determination using light scattering techniques produces a scatter intensity that is directly proportional to the particle size ($I \alpha r^6$). Therefore, if a small percentage of the CNT in the dispersion existed as large entangled ropes this would skew the observed particle size resulting in significantly higher values. The zeta potential (surface charge) for the dispersions was also measured, and it was determined that the CNT are negatively charged, where the charge ranged from –1.6 to -56.4 mV. The surface charge for CNT/N0.15 and CNT/BC dispersions was positive, this was expected since both of these dispersants are cationic.

UV-Vis for the different dispersions was recorded, where the Absorbance was plotted as a function of wavelength from 300 nm to 1100 nm. Broad peaks were observed at ~ 650 and ~ 900 nm, these peaks were assigned to the Van Hove singularities of metallic CNT. In addition, the spectra of RCNT/PMAS in the region between 650 nm and 900 nm was essentially featureless, the loss of structure indicated that a significant electronic perturbation of the nanotubes and disruption of the extended π network had occurred due to the presence of the conducting polymer.

In order to determine the stability of the different CNT dispersions, the light absorption characteristics were measured as a function of time. A wavelength of 600 nm was selected as it is directly related to the first Van Hove transition of CNT and thus was clear of other interferences. RCNT/PMAS, RCNT/DDAB, and RCNT/DNA dispersions were the most stable for this type of CNT, while

HCNT/AA12BE dispersion was the most stable for the HCNT. For MWCNT, MWCNT/DDAB dispersion was the most stable.

AFM pictures of the HCNT/PVP dispersion clearly showed super-alignment of bundles of the HCNT. This alignment was also confirmed by Raman spectroscopy, where light polarization responses for the HCNT/PVP dispersion were recorded at $\alpha_l = 0°$ and $\alpha_l = 90°$. Comparison of the height of the resonance peaks indicated that 96% of the HCNT were aligned. Investigations of the different factors involved indicated that the PVP polymer in the HCNT/PVP dispersion plays an important role in the alignment of the HCNT. It was concluded that this was a templated self-assembly, which was only observed for the HCNT. This templated-self assembly was not observed in the RCNT, possibly due to the fact that HCNT are relatively short compared to the RCNT.

The conductivity for the CNT/dispersant mats varied depending on the dispersant used which indicated that the electrical properties of the CNT were influenced to a significant degree by the chemical nature of the dispersant. In addition, the electrical conductivity increased with the introduction of a conducting polymer (e.g. PMAS) and decreased with the introduction of an insulating polymer (e.g. PVA). The conductivity values for the HCNT mats were lower than those for the corresponding RCNT, and the conductivity for MWCNT mats was lower by nearly four orders of magnitude compared to both RCNT and HCNT.

The electrochemistry of the different RCNT/dispersant mats and HCNT/dispersant mats were similar where the CVs exhibited very broad redox peaks. This is indicative of the large double layer capacity within each CNT electrode system and the slow electron exchange with the mats. For the MWCNT/dispersant mats, oxidation of water and reduction of hydrogen at the solvent limits were observed. In addition, these mats exhibited an ohmic behavior and a capacitive behavior was observed between E ~ -0.00 to +0.8 V. This demonstrated the different electrochemistry of SWCNT compared to MWCNT. It was also found that the capacitance values for the RCNT/dispersant mats were significantly higher than the capacitance values for both HCNT/dispersant mats and MWCNT/dispersant mats. This demonstrated that the different characteristics observed were due to the different production methods of SWCNT.

The AFM and SEM pictures of the CNT/dispersant mats exhibited the affect of the different dispersants on the packing order of the CNT ropes within the matrix of the mat. It was determined that the extent of coverage of the CNT by the dispersant was highly dependent on the chemical nature of the dispersant, where the dispersant coverage is mainly due to the chemical/physical interactions between the dispersant and the CNT. In addition, the HCNT were noted to aggregate into ropes and bundles as did the RCNT. However, the HCNT ropes and bundles were noted to be smaller in diameter as can be observed in the AFM and SEM pictures. This is attributed to the fact that a HCNT has a diameter of ~ 1 nm compared to the diameter of a RCNT ~1.38 nm, and they are also shorter in length. These differences resulted in a more even distribution of the HCNT throughout the mat.

The Young's modulus for the CNT/dispersant mats was as expected lower than reported values due to a variety of factors such as non-annealing of the CNT/dispersant mats, and the fact that the CNT existed as bundles of combined non-aligned ropes that are covered by the dispersant which resulted in a very large increase in the overall diameter compared to the diameter of a single-walled carbon nanotube. However, the Young's modulus values were higher than the values reported for conducting polymer.

Actuation studies of HCNT/dispersant mats exhibited creep in each sample. This was again due to the fact that the HCNT/dispersant mats are composed of randomly packed ropes and bundles resulting in stretching, pulling and sliding within the mat during actuation, and hence the observed creep. In addition, the insertion and expulsion of the ions into the dispersant depended to a significant degree on the chemical nature of the dispersant. This contributed to the differences in the actuation behavior for the different HCNT/dispersant mats.

CNT/conducting polymer composites were prepared by the electropolymerization of pyrrole with different dopants in different RCNT dispersions. It was found that the RCNT were completely covered by the polymer, which resulted in the RCNT having no significant effect on the electrochemistry of the composite; where it was dominated by the electrochemistry of the polymer and a highly capacitive behavior was observed for all the composites. However, the incorporation of the RCNT resulted in lower capacitance values compared to that of the pristine polymer.

Pyrrole was also electropolymerized using functionalized multi-walled carbon nanotubes (FMWCNT) as dopant. The electropolymerization was carried out using galvanostatic and potentiostatic techniques on both ITO-glass and gold-coated Mylar. It was determined that PPy/FMWCNT electrodeposited on either electrode using potentiostatic deposition exhibited redox peaks. This redox behavior was not observed when galvanostatic deposition was employed. This indicated that the electrodeposition method had a significant effect on the electroactivity of the resulting composite. It was also found that the capacitance increased as the degree of functionalization increased regardless of the electrodeposition method employed or the underlying electrode. In addition, it was determined that an intermediate functionalization resulted in optimum conditions for the polymerization of Pyrrole.

HCNT/PAn composites were prepared by either casting a film from a solution of HCNT and PAn in 1,2-DCB, or by casting a film of PAn onto a HCNT mat, the latter exhibited a significantly higher conductivity. This could be due to the presence of NMP and 1,2-DCB within the HCNT-PAn(acid) solution, resulting in a lower overall conductivity. Also, the physical/chemical interactions between the HCNT and the PAn(acid) when present in solution could be completely different to those when a film of PAn(acid) is cast over the HCNT mat. It was also determined that the electrochemistry of PAn(acid) was dominant over that of the HCNT in both cases. In addition, actuation studies showed that the Strain% for the HCNT mat has two values. This is due to the PAn(acid) component being oxidized at a maximum V with the volume simultaneously increasing with the HCNT component. However, the increase in volume of the two composite components was not additive. This implied

that the transport of ions to the composite might not be sufficient to meet the ion requirements of both composite components. A prolonged maximum V leads to a synergism to obtain a full volume expansion in both components. At a minimum V, the PAn(acid) component was reduced and the volume consequently decreases while the volume of the HCNT component increases. This opposite effect resulted in a kink with a small expansion peak for the HCNT component as was observed in the displacement curves.

The displacement pattern of the HCNT/PAn(acid) or PAn(acid) on HCNT mat composites are dominated by the PAn(acid) component, with a reduced expansion/contraction movement compared with PAn(acid) actuators. This also illustrated the fact that most of the ions transported in and out of the sample were mostly involved in redox reactions in PAn. Also, the PAn coating substantially enhanced the actuation strain. This result indicated the PAn component contributes to a high actuation strain value while the HCNT component to the Young's modulus.

There was no polymer deposition on the RCNT mat (unannealed) when constant current was the electrodeposition method. When cyclic potential or constant potential were used as the electrodeposition method the polymer did grow on the surface of the RCNT mat (unannealed) electrode. Although there was polymer deposition when cyclic potential was applied, the current decreased on each subsequent cycle, which indicated an increase in *iR* drop and/or a decrease in surface area due to the electrodeposition of the polymer. However, the after growth CVs for the polymers deposited on RCNT mat (unannealed) using constant potential did not exhibit any

redox peaks. Therefore, electrodeposition on different carbon electrodes using different dopants was investigated and it was determined that the method of electrodeposition, the dopant, and the nature of the underlying electrode especially in the case of RCNT mats play a significant role in the electroactivity of the deposited polymer.

HCNT/SDS, HCNT/PMAS, and HCNT/DNA fibers were prepared using the Particle Coagulating Spinning method (PCS). There was a significant decrease in the diameter of the fibers after the annealing process. However, this effect was more pronounced for the HCNT/SDS fibers compared to HCNT/PMAS and HCNTR/DNA fibers, this indicated that the annealing process resulted in the thermal degradation of PVA and the removal of amorphous carbon; and that when the fibers are produced using SDS as the dispersant, the amount of PVA (coagulating polymer) incorporated within the fiber was significantly larger than that when PMAS or DNA are used as dispersants. In addition, it was found that the diameter of the HCNT/PMAS fibers was approximately twice that of HCNT/DNA fibers, indicating that the HCNT uptake of PMAS was nearly twice that of DNA. Also, there was a significant increase in the conductivity of the HCNT/SDS fibres due to the annealing process of up to ~2600 times higher. The fibres prepared using DNA as the dispersant had significantly higher conductivities than the fibres obtained using PMAS. The conductivity of the HCNT/DNA fibers was similar to that of HCNT/SDS fibers, while the conductivity of the HCNT/PMAS fibers was ~90% lower.

It was determined that the annealing process affects charge mobility along the fiber but plays no appreciable role in keeping the carbon nanotubes ropes together. Therefore, improving the electrical properties of the fibers and not the mechanical properties. This also suggests that the mechanical properties of the fibers were not affected by the different dispersants, and that they were mainly dependent on the mechanical properties of the HCNT themselves. In addition, the annealing process does not affect the alignment of the HCNT in the fiber.

8.2- NOVELTY

Having an all carbon structure, carbon nanotubes posses characteristics similar to conducting polymers. Just as conducting polymers have widely been regarded as quasi-one dimensional semiconductors carbon nanotubes can be considered as quantum wires.

The novelty of our research lies in the different methodology applied in producing carbon nanotubes/conducting polymer composites. This novelty is also demonstrated in the wide variety of the composites produced, each with its specific characteristics. We have combined carbon nanotubes with conducting polymers through solid–state mixing by either dispersing the carbon nanotubes in conducting polymer solutions to produce mat composites, or by casting conducting polymers onto the surface of a pre-prepared carbon nanotubes mat. In addition, carbon nanotubes have been successfully used as dopants (A^-) during the polymerization process. Finally, we prepared carbon nanotubes/conducing polymer fibers for novel artificial muscle systems.

In this research we also addressed the issues of carbon nanotubes dispersion, alignment, and mechanical reinforcement via composite structures. We also demonstrated that the combination of carbon nanotubes and conducting polymers lead to synergistic composite materials possessing the properties of each of the constituent components.

8.3- LOOKING BEYOND CONVENTIONAL COMPOSITES

The investigation of materials with nanotubular structure is of great importance from both scientific and technological points of view due to their unique properties and promising potential applications in nanodevices. Recent developments in the design and synthesis of conducting one-dimensional (1-D) nanostructured materials, including carbon nanotubes, metal and/or oxide based nanowires, and polymer nanowires, have attracted much attention across scientific and engineering disciplines. These (1-D) materials have become prime candidates for replacing conventional bulk materials in micro- and nanoelectronic devices, and in chemical and biological sensors.

For example, electrochemical actuators often called “artificial muscles”, are of great importance for switches, valves to adjusting links, as well as for biomedical applications like microsurgical devices, artificial limps, or even in the future, implants like artificial ocular muscles, or hearts. The main requirements are low weight, low maintenance, and long cycle life. Also, growing demand in digital communication, electric vehicles, and other devices that require electrical energy at high power levels in relatively short pulses have promoted considerable interest in such materials and especially supercapacitors.

In recent years, conducting polymer based nanostructured materials in the shape of thin films and nanowires have been utilized extensively in resistive sensors because of their promising properties, which include high surface area, chemical specification,

tunable conductivities, and materials flexibility. Biological molecules, even whole living cells have been incorporated into conducting polymers (as the dopant A^-) during synthesis.

Carbon nanotubes are novel one-dimensional structures with promising applications perspectives. Along with their remarkable electronic properties that are entirely determined by their geometry, carbon nanotubes combine large surface area, excellent chemical stability, and significant elastic properties, thus appearing as appropriate candidate for novel supercapacitors, batteries, and actuators.

Such properties suggest that the use of carbon nanotubes as platforms to build new sensing technologies is an area worth of investigation. Work is under way to develop electrostatic dissipative (ESD) materials and electromagnetic interference (EMI) materials. SWCNT, when isolated from each other and not in ropes, are expected to be the preferred configuration. However, the majority of the systems produced are processed with ropes of SWCNT, since isolated SWCNT are not readily available. Consequently, the rope form which is though to be up to two orders magnitude longer than the isolated SWCNT, maybe the preferred nanotubes configuration for conducting polymer applications since high-aspect ratio materials are sought for lower percolation conditions.

Continued research in this multidisciplinary field should be very fruitful.

References

1. M. L. Cohen, *Mater. Sci. eng.,* **35:** 1, 2001.
2. S. Iijima, *Nature,* **354:** 56, 1991.
3. T. W. Ebbesen, and P. M. Ajayan, *Nature,* **358:** 220, 1992.
4. S. Motojima, M. Kawaguchi, K. Nozaki, and H. Iwanaga, *Appl. Phys. Lett.,* **56:** 321, 1990.
5. S. Motojima, Y. Itoh, and S. Asakura, *J. Mater. Sci.,* **30:** 5045, 1995.
6. S. Huang, L. Dai, and A. W. H. Mau, *J. Mater. Chem.,* **9:** 1221, 1999.
7. S. Ihara, and S. Itoh, *Carbon,* **33:** 931, 1995.
8. L. Chico, V. H. Crespi, S. G. Louie, and M. L. Cohen, *Phys. Rev. Lett.,* **76:** 971, 1996.
9. D. B. Romero, M. Carrard, W. D. Heer, and L. Zuppiroli, *Adv. Mater.,* **8:** 899, 1996.
10. M. Terrones, N. Grobert, J. Olivares, J. P. Zhang, H. Terrones, K. Kordatos, W. K. Hsu, J. P. Hare, P. D. Toensend, K. Prassides, A. K. Cheetham, H. W. Kroto, and D. R. M. Walton, *Nature,* **388:** 52, 1997.
11. P. G. Collins, A. Zettl, H. Bando, A. Thess, and R. E. Smalley, *Science,* **278:** 100, 1997.
12. G. E. Gadd, M. Blackford, S. Moricco, V. Webb, P. J. Evans, A. M. Smith, G. Jacobsen, S. Leung, A. Day, and Q. Hu, *Science,* **277:** 933, 1997.
13. W. A. DeHeer, J. M. Bonrad, K. Fauth, A. Chateain, L. Forro, and D. Ugarte, *Adv. Mater.,* **9:** 87, 1997.

14. H. Dai, E. W. Wong, and C. M. Lieber, *Science,* **272:** 523, 1996.

15. D. Ugatre, A. Chatelain, and W. A. DeHeer, *Science,* **274:** 1897, 1996.

16. K. B. Jirage, J. C. Hulteen, and C. R. Martin, *Science,* **278:** 655, 1997.

17. P. M. Ajayan, *Adv. Mater.,* **7:** 489, 1995.

18. R. Tenne, *Adv. Mater.,* **7:** 965, 1995.

19. M. Terrones, and W. K. Hsu, *Chem. Soc. Rev.,* **24:** 341, 1995.

20. N. Hamada, S. Sawada, and A. Oshiyama, *Phys. Rev. Lett.,* **68:** 1579, 1992.

21. M. Dewaawlhaus, G. Dresselhaus, P. Eklund, and R. Saito, *Phys. World,* **January:** 33, 1998.

22. P. M. Ajayan, and T. W. Ebbesen, *Rep. Prog. Phys.,* **60:** 1025, 1997.

23. J. Hu, T. W. Odom, and C. M. Lieber, *Acc. Chem. Res.,* **32:** 435, 1999.

24. L. C. Venema, V. Meunier, P. Lambin, and C. Deker, *Chem. Phys. Soc.,* **61:** 2991, 2000.

25. J. W. Mintmier, and C. T. White, *Carbon,* **33:** 893, 1995.

26. E. Dujardin, T. W. Ebbesen, A. Krishnan, and M. M. J. Treacy, *Adv. Mater.,* **10:** 1742, 1998.

27. T. W. Odom, J. L. Huang, P. Kim, and C. M. Lieber, *J. Phys. Chem. B.,* **104:** 2794, 2000.

28. P. Avouris, T. Hertel, R. Martel, T. Schmidt, H. R. Shea, and R. E. Walkup, *Appl. Surf. Sci.,* **141:** 201, 1999.

29. T. Pichler, M. Knupfer, M. S. Golden, J. Fink, A. Rinzler, and R. E. Smalley, *Phys. Rev. Lett.,* **80:** 4729, 1998.

30. M. S. Dresselhaus, G. Dresselhaus, and P. C. Eklund, *Science of Fullerenes and Carbon Nanotubes,* San Diego, Academic Press, 1996.
31. E. T. Thstenson, Z. Ren, and T. W. Chou, *Comp. Sci. Tech.,* **61:** 1899, 2001.
32. D. Bernaerts, A. Zettl, N. G. Chopra, A. Thess, and R. E. Smalley, *Solid State Communications,* **105:** 145, 1998.
33. P. M. Ajayan, P. Redlich, and M. Ruhle, *Journal of Microscopy,* **185:** 275, 1997.
34. M. Endo, K. Takeuchi, S. Igarashi, K. Kobori, M. Shiraishi, and H. W. Kroto, *J. Phys. Chem. Solids,* **54:** 1841, 1993.
35. Z. Y. Kosakovskaya, L. A. Chernozatonskii, and E. A. Fedorov, *JETP Lett.,* **56:** 26, 1992.
36. K. Yamamoto, Y. Koga, S. Fujiwara, and M. Kubota, *Appl. Phys. Lett.,* **69:** 4174, 1996.
37. W. K. Hsu, J. P. Hare, M. Terrones, H. W. Kroto, D. R. M. Walton, and P. J. F. Harris, *Nature,* **377:** 687, 1995.
38. W. K. Hsu, M. Terrones, J. P. Hare, H. Terrones, H. W. Kroto, and D. R. M. Walton, *Chem. Phys. Lett.,* **262:** 161, 1996.
39. R. Parthasarathy, K. L. N. Phani, and C. R. Martin, *Adv. Mater.,* **7:** 896, 1995.
40. T. Kyotani, T. Nagai, S. Inoue, and A. Tomita, *Chem. Mater.,* **9:** 609, 1997.
41. G. Che, B. B. Lakshmi, C. R. Martin, E. R. Fisher, and R. S. Ruoff, *Chem. Mater.,* **10:** 260, 1998.

42. S. Iijima, and T. Ichihashi, *Nature,* **363:** 603, 1993.

43. C. H. Kiang, W. A. Goddard III, R. Beyers, J. R. Salem, and D. S. Bethune, *J. Phys. Chem.,* **98:** 6621, 1994.

44. A. Thess, R. Lee, P. Nikolaev, H. Dai, P. Petit, J. Robert, C. Xu, Y. H. Lee, S. G. Kim, A. G. Rinzler, D. T. Colbert, G. E. Scuseria, D. Tomanek, J. E. Fischer, and R. E. Smalley, *Nature,* **273:** 483, 1996.

45. M. Yudasaka, T. Komatsu, T. Ichihashi, and S. Iijima, *Chem. Phys. Lett.,* **278:** 102, 1997.

46. C. C. Han, J. T. Lee, and H. Chang, *Chem. Mater.,* **13:** 4180, 2001.

47. K. Kageyama, J. L. Tamazawa, and T. Aida, *Science,* **285:** 2113, 1999.

48. V. H. Crespi, M. I. Cohen, and A. Rubio, *Phys. Rev. Lett.,* **79:** 2093, 1997.

49. J. H. Hwang, W. K. Hsu, and C. Y. Mou, *Adv. Mater.,* **5:** 643, 1993.

50. L. Chico, V. H. Crespi, L. X. Benedict, S. G. Louie, and M. L. Cohen, *Phys. Rev. Lett.,* **76:** 971, 1996.

51. Y. Miyamoto, A. Rubio, M. L. Cohen, and S. G. Louie, *Phys. Rev. Lett.,* **74:** 2993, 1995.

52. N. G. Chopra, R. J. Luyken, K. Cherrey, V. H. Crespi, M. L. Cohen, S. G. Louie, and A. Zettl, *Science,* **269:** 966, 1995.

53. Y. Miyamoto, G. S. Louie, and M. L. Cohen, *Phys. Rev. Lett.,* **76:** 2121, 1996.

54. P. G. Collins, A. Zettl, H. Bando, A. Thess, and R. E. Smalley, *Science,* **278:** 100, 1997.

55. P. L. McEuen, *Nature,* **393:** 15, 1998.

56. M. Bockrath, D. H. Cobden, P. L. McEuen, N. G. Choprs, A. Zettl, A. Thess, and R. E. Smalley, *Science,* **275:** 1922, 1997.

57. S. J. Tans, M. H. Devoret, R. J. A. Groeneveld, and C. Dekker, *Nature,* **394:** 761, 1998.

58. G. S. Duesberg, J. Muster, H. J. Byrne, S. Roth, and M. Burghard, *Appl. Phys. A.,* **69:** 269, 1999.

59. J. M. Moon, K. H. An, Y. H. Lee, Y. S. Park, D. J. Bae, and G. S. Park, *J. Phys. Chem. B.,* **105:** 5677, 2001.

60. K. Tohji, H. Takahashi, Y. Shinoda, N. Shimizu, B. Jeyadevan, I. Matsouka, Y. Saito, A. Kasuya, S. Ito, and Y. Nishina, *J. Phys. Chem. B.,* **101:** 1974, 1997.

61. J. F. Colomer, P. Piedigrosso, A. Fonseca, and J. B. Nagy, *Synth. Met.,* **103:** 2484, 1999.

62. F. Li, H. M. Cheng, Y. T. Xing, P. H. Tan, and G. Su, *Carbon,* **38:** 2041, 2000.

63. S. Bandow, A. M. Rao, K. A. Williams, A. Thess, R. E. Smalley, and P. C. Eklund, *J. Phys. Chem. B.,* **102:** 8839, 1997.

64. E. Dujardin, T. W. Ebbesen, A. Krishnan, and M. M. J. Treacy, *Adv. Mater.,* **10:** 611, 1998.

65. I. W. Chiang, B. E. Brinson, A. Y. Huang, P. A. Willis, M. J. Bronikowski, J. L. Margrave, R. E. Smalley, and R. H. Hauge, *J. Phys. Chem. B.,* **105:** 8297, 2001.

66. L. S. K. Pang, J. D. Saxby, and S. P. Chatfield, *J. Phys. Chem.,* **97:** 6941, 1993.

67. S. C. Tsang, P. J. F. Harrris, and M. L. H. Green, *Nature,* **362:** 520, 1993.

68. S. C. Tsang, Y. K. Chen, P. J. F. Harris, and M. L. H. Green, *Nature,* **372:** 159, 1994.

69. B. C. Satishkumar, A. Govindaraj, J. Mofokeng, G. N. Subbanna, and C. N. R. Rao, *J. Phys. B.,* **29:** 4925, 1996.

70. J. Liu, A. G. Rinzler, H. Dai, J. H. Hafner, R. K. Bradley, P. J. Boul, A. Lu, T. Iverson, K. Shelimov, C. B. Huffman, F. Rodrigues-Macias, Y. S. Shon, T. R. Lee, D. T. Collbert, and R. E. Smalley, *Science,* **280:** 1253, 1998.

71. G. S. Duesberg, W. Blau, H. J. Byrne, J. Muster, M. Burghard, and S. Roth, *Synth. Met.,* **103:** 2484, 1999.

72. T. W. Ebbesen, P. M. Ajayan, H. Hiura, and K. Tanigaki, *Nature,* **367:** 519, 1994.

73. J. M. Bonrad, T. Sora, J. P. Salvetal, F. Maier, T. Stockli, C. Duschl, L. Ferro, W. A. DeHeer, and A. Chatelain, *Adv. Mater.,* **9:** 827, 1997.

74. A. W. Admson, *Physical Chemistry of Surfaces,* Wiley Interscience, New York, 1990.

75. M. S. P. Shaffer, X. Fan, and A. H. Windle, *Carbon,* **36:** 1603, 1998.

76. Z. P. Tang, A. Kleinhammes, H. Shimoda, L. Fleming, K. Y. Bennoune, S. Sinha, C. Bower, O. Zhou, and Y. Wu, *Science,* **288:** 492, 1998.

77. T. Hertel, and G. Moos, *Chem. Phys. Lett.,* **320:** 359, 2000.

78. M. Bockrath, D. V. Cobden, P. L. McEuen, N. G. Chopra, A. Zettl, A. Thess, and R. E. Smalley, *Science,* **275:** 1922, 1997.

79. S. J. Tans, M. H. Devoret, H. Dai A. Thess, R. E. Smalley, L. J. Greeligs, and C. Dekker, *Nature,* **386:** 474, 1997.

80. H. Ago, T. Kugler, F. Cacialli, W. K. Salaneck, M. S. P. Shaffer, A. H. Windle, and R. H. Friend, *J. Phys. Chem. B.,* **103:** 8116, 1999.

81. R. Martel, T. Shmidt, H. R. Shea, T. Hertel, and P. Avouris, *Appl. Phys. Lett.,* **73:** 2447, 1998.

82. R. S. Lee, H. J. Kim, J. E. Fisher, J. Lafebvre, M. Radosavlijevic, J. Hone, and A. T. Johnson, *Phys. Rev. B.,* **61:** 4526, 2000.

83. Y. Zhang, T. Ichihashi, E. Landree, F. Nihey, and S. Iijima, *Science,* **285:** 1719, 1999.

84. P. J. Pablo, C. Gomez-Navarro, M. T. Martinez, A. M. Benito, W. K. Maser, J. Colchero, J. Gomez-Herrero, and A. M. Baro, *Appl. Phys. Lett.,* **80:** 1462, 2002.

85. J. W. Park, J. Kim, J. O. Lee, K. C. Kang, J. J. Kim, and K. H. Yoo, *Appl. Phys. Lett.,* **80:** 133, 2002.

86. A. B. Kaiser, *Adv. Mater.,* **13:** 927, 2001.

87. J. Gonzalez, *Phys. Rev. Lett.,* **88:** 4031, 2002.

88. R. Gaal, J. P. Salvetat, and L. Forro, *Phys. Rev. B.,* **61:** 7320, 2000.

89. M. Burghard, V. Krstic, G. S. Duesberg, G. Philip, J. Muster, and S. Roth, *Synth. Met.,* **103:** 2540, 1999.

90. J. Tersoff, *Appl. Phys. Lett.,* **74:** 2122, 1999.

91. A. B. Kaiser, Y. W. Park, G. T. Kim, E. S. Choi, G. Dusberg, and S. Roth, *Synth. Met.,* **103:** 2547, 1999.

92. A. B. Kaiser, *Phys. Rev. B.,* **57:** 1418, 1998.

93. P. M. Ajayan, *Chem. Rev.,* **99:** 1787, 1999.

94. S. Paulson, M. R. Falvo, N. Snider, A. Helser, T. Hudson, A. Seeger, R. M. Taylor, R. Superfine, and S. Washburn, *Appl. Phys. Lett.,* **75:** 2936, 1999.

95. L. X. Benedict, V. H. Crespi, S. G. Louie, and M. L. Cohen, *Phys. Rev. B.,* **52:** 14935, 1995.

96. Y. H. Lee, D. H. Kim, H. Kim, and B. K. Ju, *J. Appl. Phys.,* **88:** 4181, 2000.

97. S. Roche, F. Triozon, and A. Rubio, *Appl. Phys. Lett.,* **79:** 3690, 2001.

98. Y. Yosida, *J. Phys. Chem. Solids,* **60:** 1, 1999.

99. C. A. Grimes, E. C. Dickey, C. Mungle, K. G. Ong, and D. Qian, *J. Appl. Phys.,* **90:** 4134, 2001.

100. A. B. Kaiser, *Adv. Mater.,* **13:** 927, 2001.

101. A. B. Kaiser, *Phys. Rev. B.,* **57:** 1418, 1998.

102. K. Kaneto, M. Tsuruta, G. Sakai, W. Y. Cho, and Y. Ando, *Synth. Met.,* **103:** 2543, 1999.

103. P. J. Paplo, E. Graugnard, B. Walsh, R. P. Andres, S. Datta, and R. Reifenberger, *Appl. Phys. Lett.,* **74:** 323, 1999.

104. N. I. Sinitsyn, Y. V. Gulyaev, G. V. Torgashov, L. A. Chernozatonskii, Z. Y. Kosakovskaya, Y. F. Zalharchenko, N. A. Kiselev, A. L. Musatov, A. I. Zhbanov, S. T. Mevlyut, and O. E. Glukhova, *Appl. Surf. Sci.,* **111:** 145, 1997.

105. S. Cxie, W. Li, Z. Pan, B. Chang, and L. Sun, *Mater. Sci. Eng. C.,* **A286:** 11, 2000.

106. H. Ago, K. Petritsch, M. S. P. Shaffer, A. H. Windle, and R. H. Friend, *Adv. Mater.,* **11:** 1281, 1999.

107. B. I. Yakobson, C. J. Barbee, and J. Bernhole, *Phys. Rev. Lett.,* **76:** 2511, 1996.

108. M. Tracy, T. Ebbesen, and J. Gibson, *Nature,* **381:** 678, 1996.

109. C. F. Cornwell, and L. T. Wille, *Solid State Communication,* **101:** 555, 1997.

110. D. S. Portal, E. Artacho, and J. M. Soler, *Phys. Rev. B.,* **59:** 12678, 1999.

111. D. H. Roberetson, D. W. Brenner, and J. J. W. Mintmir, *Phys. Rev. B.,* **45:** 592, 1992.

112. N. Yao, and V. Lordi, *J. Appl. Phys.,* **84:** 1939, 1998.

113. A. Krishnan, E. Dujardin, T. W. Ebbesen, P. N. Yianilos, and M. M. J. Tracy, *Phys. Rev. B.,* **58:** 14013, 1998.

114. J. Salvetat, G. Andrews, D. Briggs, J. Bonard, R. R. Bacsa, A. J. Kulik, T. Stockli, N. A. Burnham, and L. Forro, *Phys. Rev. Lett.,* **82:** 944, 1999.

115. J. P. Lu, *Phys. Rev. Lett.,* **79:** 1297, 1997.

116. B. I. Yakobson, C. J. Brabec, and J. Bernholc, *Phys. Rev. Lett.,* **76:** 251, 1996.

117. C. Q. Ru, *Phys. Rev. B.,* **62:** 10405, 2000.

118. Z. Xin, Z. Jianjun, and O. Zhong, *Phys. Rev. B.,* **62:** 13692, 2000.

119. C. A. Cooper, and R. J. Young, *Journal of Raman Spectroscopy,* **30:** 929, 1999.

120. G. Goze, L. Vaccarini, L. Henrard, P. Bernier, E. Hernandez, and A. Rubio, *Synth. Met.,* **103:** 2500, 1999.

121. O. Lourie, H. D. Wagner, Y. Zhang, and S. Iijima, *Adv. Mater.,* **11:** 931, 1999.

122. R. B. Pipes, and P. Hubert, *Comp. Sci. Tech.,* **62:** 419, 2002.

123. M. Yu, B. S. Files, S. Arepalli, and R. S. Ruoff, *Phys. Rev. Lett.,* **84:** 5552, 2000.

124. M. M. J. Tracy, T. W. Ebbesen, and T. M. Gibson, *Nature,* **381:** 680, 1996.

125. E. W. Wong, P. E. Sheehan, and C. M. Lieber, *Science,* **277:** 1971, 1997

126. D. A. Walters, L. M. Ericson, M. J. Casavant, J. Liu, D. T. Colbert, K. A. Smith, and R. E. Smalley, *Appl. Phys. Lett.,* **74:** 3803, 1999.

127. J. P. Salvetat, G. A. D. Briggs, J. M. Bonrad, R. Basca, A. J. Kulik, and T. Stockli, *Phys. Rev. Lett.,* **82:** 944, 1999.

128. D. A. Walters, L. M. Ericson, L. M. Gasavant, J. Liu, D. T. Collbert, and K. A. Smith, *Appl. Phys. Lett.,* **74:** 3803, 1999.

129. M. F. Yu, O. Lourie, M. Dyer, K. Moloni, and T. Kelly, *Science,* **287:** 637, 2000.

130. M. F. Yu, B. S. Files, S. Arepalli, and R. S. Ruoff, *Phys. Rev. Lett.,* **84:** 5552, 2000.

131. S. B. Sinnott, O. A. Shenderova, C. T. White, and D. W. Brenner, *Carbon,* **36:** 1, 1998.

132. F. Li, H. M. Cheng, S. Bai, and G. Su, *Appl. Phys. Lett.,* **77:** 3161, 2000.

133. K. Lozano, and E. V. Barrera, *J. Appl. Poly. Sci.,* **79:** 125, 2001.

134. D. Srivastava, M. Menon, and K. Cho, *Phys. Rev. Lett.,* **83:** 2973, 1999.

135. J. P. Lu, *J. Phys. Chem. Solids,* **58:** 1649, 1998.

136. O. Lourie, H. D. Wagner, Y. Zhang, and S. Ijima, *Adv. Mater.,* **13:** 312, 2000.

137. Y. Lu, and P. K. Liaw, *JOM,* **53:** 31, 2001.

138. R. A. Jishi, and G. Dresselhaus, *Phys. Rev. B.,* **26:** 4514, 1982.

139. E. Hernandez, C. Goze, P. Bernier, and A. Rubio, *Phys. Rev. Lett.,* **80:** 4502, 1998.

140. C. Q. Ru, *Phys. Rev. B.,* **62:** 10405, 2000.

141. J. P. Lu, *J. Phys. Chem. Solids,* **58:** 1649, 1997.

142. C. Q. Ru, *J. Appl. Phys.,* **87:** 7227, 2000.

143. G. Wegner, *Angew Chem. Int. Ed.,* **20:** 361, 1981.

144. J. H. Reynolds, *Chemtech,* **July:** 440, 1988.

145. T. A. Skotheim, *Handbook of Conducting Polymers,* Marcel Dekker, New York, 1986.

146. J. C. W. Chein, *Polyacetylene: Chemistry, Physics and Materials Science,* Academic press, New York, 1984.

147. J. L. Bredas, and G. B. Street, *Acc. Chem. Res.,* **18:** 309, 1985.

148. P. Burgmayer, and R. W. Murry, *J. Phys. Chem.,* **88:** 2515, 1984.

149. F. B. Kaufman, A. H. Schroeder, E. M. Engler, S. R. Kramer, and J. Q. Chambers, *J. Am. Chem. Soc.,* **102:** 482, 1980.

150. H. Shorakawa, E. J. Louis, A. G. Chiang, and A. J. Heeger, *J. chem. Soc. Chem. Commun.,* **16:** 579, 1977.

151. A. Dall, G. Dascola, V. Varaca, and V. Bocchi, *Comp. Rend.,* **433:** 267c, 1968.

152. A. F. Diaz, and K. K. Kanazawa, *J. Chem. Soc. Chem. Commun.,* **14:** 635, 1979.

153. R. A. Bull, F. F. Fan, and A. J. Brad, *J. Electrochem. Soc.,* **129:** 1009, 1982.

154. P. Burgmayer, and R. W. Murray, *J. Am. Chem. Soc.,* **104:** 6139, 1982.

155. K. Naoi, and W. H. Smyrl, *J. Electrochem, Soc.,* **138:** 440, 1997.

156. J. F. Dandreaux, M. E. Galvin, and G. E. Wnek, *J. Phys.,* **44:** 135, 1983.

157. I. Kminek, and J. Trekoval, *Makromol. Chem. Rapid. Commun.,* **5:** 53, 1984.

158. F. S. Bates, and G. L. Baker, *Macromolecules,* **16:** 704, 1983.

159. M. Aldissi, *Synth. Met.,* **13:** 87, 1986.

160. M. E. Galvin, and G. E. Wnek, *Poly. Bull.,* **13:** 109, 1985.

161. M. Sato, S. Tanaka, and K. Kaeriyama, *J. Chem. Soc. Chem. Commun.,* **873:** 1986.

162. D. J. Kim, S. H. Kim, T. Zyung, J. J. Kim, I. Cho, and S. K. Choi, *Macromolecules,* **29:** 3657, 1996.

163. J. C. W. Chien, G. E. Wenk, F. E. Karasz, and J. A. Hirsch, *Macromolecules,* **14:** 479, 1981.

164. W. Deits, P. Cukor, M. Rubner, and H. Jopson, *Synth. Met.,* **4:** 199, 1982.

165. Z. Yang, F. E. Karasz, and H. J. Geise, *Polymer,* **35:** 392, 1994.

166. Z. Yang, I. Sokolik, and F. E. Karasz, *Macromolecules,* **26:** 1188, 1993.

167. Z. Yand, B. Hu, and F. E. Karasz, *Pure Appl. Chem.,* **A35:** 233, 1998.

168. Z. Yang, F. E. Karasz, and H. J. Geise, *Macromolecules,* **26:** 6570, 1993.

169. G. G. Malliaras, J. K. Herrema, J. Wildeman, R. H. Wieringa, R. E. Gill, S. S. Lampoura, and G. Hadziioannou, *Adv. Mater.,* **10:** 721, 1993.

170. A. Hibere, P. F. Hutten, J. Wildeman, and G. Hadziioannou, *Macromol. Chem. Phys.,* **198:** 2211, 1997.

171. G. G. Malliaras, J. K. Herrema, J. Wildeman, R. E. Gill, S. S. Lampoura, and G. Hadziioannou, *High Speed Optoelectronics SPIE Proc.,* San Diago, 1993.

172. S. Destri, M. Cattellani, and A. Bolognesi, *Makromol. Chem. Rapid. Commun.,* **5:** 353, 1985.

173. A. Bolognesi, M. Catellani, S. Destri, W. Porzio, S. Melle, and E. Pedemonte, *Makromole, Chem.,* **187:** 1287, 1986.

174. A. Bolognesi, M. Catellani, and S. Destri, *Mol. Cryst. Liq. Cryst.,* **117:** 29, 1985.

175. A. Bolognesi, M. Catellani, S. Destri, and W. Porzio, *Polymer,* **27:** 1128, 1986.

176. C. N. Rao, B. C. Satishkumar, A. Govindaraj, and M. Nath, *Chemphyschem,* **2:** 78, 2001.

177. S. Arms, B. Vincent, and J. W. White, *J. Chem. Soc. Chem. Commun.,* **201:** 1525, 1986.

178. O. A. Sakid, and G. G. Wallace, *Electoanal.,* **5:** 555, 1993.

179. Y. P. Lin, and G. G. Wallace, *J. Electroanal, Chem.,* **247:** 145, 1988.

180. M. D. Imisides, and G. G. Wallace, *J. Electroanal, Chem.,* **246:** 181, 1988.

181. W. Ulmana, and Wller, *J. Anal. Chem.,* **58:** 2979, 1986.

182. O. Sakid, and G. G. Wallace, *Anal. Chim. Acta.,* **279:** 209, 1993.

183. J. Heinze and M. Dietrich, *Materials Science Forum,* **42:** 63, 1989.

184. R. Roy, *Mater. Res. Soc. Symp. Proc.,* **286:** 241, 1993.

185. D. J. Birchall, *Mater. Res. Soc. Symp. Proc.,* **286:** 297, 1993.

186. S. C. Sang, Y. K. Yang, P. J. F. Harris, and M. L. H. Green, *Nature,* **372:** 159, 1994.

187. T. W. Ebbesen, *J. Phys. Chem. Solids,* **57:** 951, 1996.

188. P. M. Ajayan, and S. Iijima, *Nature,* **361:** 333, 1993.

189. P. M. Ajayan, T. W. Ebbesen, T. Ichihashi, S. Iijima, K. Tanigaki, and H. Hiura, *Nature,* **362:** 522, 1993.

190. N. Ikemiya, J. Umemoto, S. Hara, and K. Ogino, *ISIJ. Int.,* **33:** 156, 1993.

191. M. S. P. Shaffer, and A. H. Windle, *Adv. Mater.,* **11:** 937, 1999.

192. D. H. Everett, *Basic Principles of Colloid Science,* Royal Society of Chemistry, London, 1988.

193. S. Fan, M. G. Chapline, N. R. Franklin, T. W. Tombler, A. M. Cassel, and H. Dai, *Science,* **283:** 512, 1999.

194. L. S. Schadler, S. C. Giannaris, and P. M. Ajayan, *Appl. Phys. Lett.,* **73:** 3842, 1998.

195. S. S. Wong, E. Joselevich, A. T. Woolley, C. L. Cheung, and C. M. Lieber, *Nature,* **394:** 52, 1998.

196. S. T. Tans, A. R. M. Verschueren, and C. Dekker, *Nature,* **393:** 49, 1998.

197. J. Kong, N. R. Franklin, C. Zhou, M. G. Chapline, S. Peng, K. Cho, and H. Dai, *Science,* **278:** 622, 2000.

198. Y. Fan, M. Burghard, and K. Kern, *Adv. Mater.,* **14:** 130, 2002.

199. J. Lefebvre, R. D. Antonov, M. Radosavljevic, J. F. Lynch, M. Llaguno, and A. T. Johnson, *Carbon,* **38:** 1745, 2000.

200. B. McCarthy, J. N. Coleman, R. Czerw, A. B. Dalton, M. Panhuis, A. Maiti, A Drury, P. Bernier, J. B. Nagy, B. Lahr, H. J. Byrne, D. L. Carroll, and W. J. Blau. *J. Phys. Chem. B.,* **106:** 2210, 2002.

201. C. Stephane, T. P. Nguyen, M. Lamy de la Chapelle, S. Lefrent, C. Journet, and P. Bernier, *Synth. Met.,* **108:** 139, 2000.

202. A. Koshio, M. Yudasaka, M. Zhang, and S. Iijima, *Nano. Lett.,* **1:** 361, 2001.

203. S. Curran, A. P. Davey, J. Coleman, A. Dalton, B. McCarthy, S. Maier, A. Drury, D. Gray, M. Brennan, K. Ryder, M Lamy de la Chapelle,

C. Journet, P. Bernier, H. J. Byrne, D. Carroll, P. M. Ajayan, S. Lefrant, and W. Blau, *Synth. Met.,* **103:** 2559, 1999.

204. A. Stra, J. F. Stoddart, D. Steuerman, M. Diehl, A. Boukai, E. W. Wong, X. Yang, S. Chung, H. Choi, and J. R. Heath, *Angew. Chem. Int. Ed.,* **40:** 1721, 2001.

205. B. McCarthy, J. N. Coleman, R. Czerw, A. B. Dalton, D. L. Carroll, and W. J. Blau, *Synth. Met.,* **121:** 1225, 2001.

206. S. P. Shaffer, and A. H. Windle, *Adv. Mater.,* **11:** 937, 1999.

207. R. Czerw, Z. Guo, P. M. Ajayan, Y. Sun, and D. L. Carroll, *Nano. Lett.,* **1:** 423, 2001.

208. A. B. Kaiser, *Adv. Mater.,* **13:** 927, 2001.

209. T. Gennett, A. C. Dillon, J. L. Alleman, K. M. Jones, F. S. Hasoon, and M. J. Heben, *Chem. Mater.,* **12:** 599, 2000.

210. M. Lapkowski, *Mater. Sci.,* **1:** 7, 1991.

211. M. T. Nguyen, M. Leclerc, and A. F. Diaz, *Chem. Rev.,* **3:** 186, 1995.

212. G. Zotti, E. Sciennza, *Technologia,* **77:** 156, 1995.

213. B. Zhao, H. Hu, S. Niyogi, M. E. Itkis, M. A. Hamon, P. Bhowmik, M. S. Meier, and R. C. Hadon, *J. Am. Chem. Soc.,* **123:** 11673, 2001.

214. K. D. Ausman, R. Piner, O. Lourie, and R. S. Ruoff, *J. Phys. Chem. B.,* **104:** 8911, 2000.

215. J. L. Bahr, J. Yang, D. V. Kosynkin, M. J. Bronilowski, R. E. Smalley, and J. M. Tour, *J. Am. Chem. Soc.,* **123:** 6536, 2001.

216. W. Luo, and W. Wu, *New Journal of Chemistry,* **17:** 471, 1993.

217. Y. Iidda, and M. Yoshii, *Electronics and communications in Japan,* **80:** 1, 1997.

218. S. Subramoney, *Adv. Mater.,* **10:** 1157, 1998.

219. A. B. Kaiser, *Phys. Rev. B.,* **57:** 1418, 1998.

220. A. A. Maarouf, C. L. Kane, and E. J. Mele, *Phys. Rev. B.,* **61:** 11156, 2000.

221. R. Gaal, J. P. Salvetat, and L. Forro, *Phys. Rev. B.,* **61:** 7320, 2000.

222. M. Burghard, V. Krstic, G. S. Duesberg, G. Philipp, J. Muster, and S. Roth, *Synth. Met.,* **103:** 2540, 1999.

223. H. Stahl, J. Appenzeller, R. Martel, Ph. Avouris, and B. Lengeler, *Phys. Rev. Lett.,* **85:** 5186, 2000.

224. J. Tersoff, *Appl. Phys. Lett.,* **74:** 2122, 1999.

225. R. S. Lee, H. J. Kim, J. E. Fischer, A. Thess, and R. E. Smalley, *Letters to Nature,* **388:** 255, 1997.

226. A. B. Kaiser, Y. W. Park, G. T. Kim, E. S. Choi, G. Dusberg, and S. Roth, *Synth. Met.,* **103:** 2547, 1999.

227. J. N. Coleman, S. Curran, A. B. Dalton, A. P. Davey, B. McCarthy, W. Blau, and R. C. Barklie, *Phys. Rev. B.,* **58:** R7492, 1998.

228. J. N. Coleman, S. Currant, A. B. Dalton, A. P. Davewy, B. McCarthy, W. Blau, and R. C. Barklie, *Synth. Met.,* **102:** 1174, 1999.

229. E. Kymakis, I. Alexandrou, and G. A. J. Amaratunga, *Synth. Met.,* **127:** 59, 2002.

230. J. M. Benoti, B. Corraze, S. Lefrant, W. J. Blau, P. Bernier, and O. Chauvet, *Synth. Met.,* **121:** 1215, 2001.

231. J. N. Barisci, G. G. Wallace, and R. H. Baughman, *J. Electrochem. Soc.,* **147:** 4580, 2000.

232. J. N. Barisci, G. G. Wallace, and R. H. Baughman, *Electrochemica Acta,* 4**6:** 509, 2000.

233. C. Niu, E. K. Sichel, R. Hoch, D. Moy, and H. Tennent, *Appl. Phys. Lett.,* **70:** 1480, 1997.

234. I. W. Chiang, B. E. Brinson, A. Y. Huang, P. A. Willis, M. J. Bronikowski, J. L. Margrave, R. E. Smalley, and R. H. Huang, *J. Phys. Chem. B.,* **105:** 8297, 2001.

235. M. Yudasaka, H. Kataura, T. Ichihashi, L. C. Qin, S. Kar, and S. Iijima, *Nano. Lett.*, **1:** 487, 2001.

236. L. Dai, and W. H. Mau, *Adv. Mater.,* **13:** 899, 2001.

237. R. Bandyopadhyaya, E. Native-Roth, O. Regev, and R. Yerushalmi-Rozen, *Nano. Lett.,* **2:** 25, 2002.

238. Q. Zhao, M. D. Frogley, and H. D. Wagner, *Comp. Sci. Tech.*, **62:** 147, 2002.

239. Q. Zhao, J. R. Wood, and H. D. Wagner, *J. Poly. Sci. B. Poly. Phys.,* **39:** 1492, 2001.

240. K. Lozano, J. Bonilla-Rios, and E. V. Barrera, *J. Appl. Poly. Sci.,* **80:** 1162, 2001.

241. I. Alexandrou, E. Kymakis, and G. A. J. Amaratunga, *Appl. Phys. Lett.,* **80:** 1435, 2002.

242. D. H. Napper, *Polymeric Stabilization of Colloidal Dispersions,* Orlando, Florida, 1993.

243. A. B. Dalton, W. J. Blau, G. Chambers, J. N. Colman, K. Henderson, S. Lefrant, B. McCarthy, C. Stephan, and H. J. Byrne, *Synth. Met.,* **121:** 1217, 2001.

244. H. S. Woo, R. Czerw, S. Webster, D. L. Carroll, J. W. Park, and J. H. Lee, *Synth. Met.,* **116:** 369, 2001.

245. M. Eckermann, *Characterization and Optimization of Carbon Nanotube Actuators,* Honor Degree Thesis, University of Wollongong, 2001.

246. S. Niyogi, H. Hu, M. A. Hamon, P. Bhowmik, B. Zhao, S. M. Rozenzhak, J. Chen, M. E. Itkis, M. S. Meier, and R. C. Haddon, *J. Am. Chem. Soc.,* **123:** 733, 2001.

247. H. Kataura, Y. Kumazawa, Y. Maniwa, I. Umezu, S. Suzuki, Y. Ohtshuka, and Y. Achiba, *Synth. Met*., **103:** 2555, 1999.

248. P. J. Boul, J. Lie, E. T. Mickelson, C. B. Huffman, L. M. Ericson, I. W. Chiang, K. A. Smith, D. T. Colbert, R. H. Hauge, J. L. Margrave, and R. E. Smalley, *Chem. Phys. Lett.,* **310:** 367, 1999.

249. M. in Het Panhuis, S. Benrezzak, A. B. Dalton, M. Tahhan, A. I. Minett, W. J. Blau, R. H. Baughman, J. N. Barisci, and G. G. Wallace, submitted on 5 / 1 / 2002 at the ICSM 2002 conference, China.

250. M.Yadasaka, H. Kataura, T. Ichighashi, L. V. Qin, S. Kar, and S. Iijima, *Nano. Lett.,* **1:** 487, 2001

251. A. B. Dalton, C. Stephan, J. N. Coleman, B. McCarthy, P. M. Ajayan, P. Bernier, W. J. Blau, and H. J. Byrne, *J. Phys. Chem. B.,* **104:** 10012, 2000

252. G. S. Duesberg, W. J. Blau, H. J. Byrne, J. Muster, M. Burghard, and S. Roth, *Chem. Phys. Lett.,* **310:** 8, 1999

253. A. M. Rao, S. Bandow, E. Richter, and P. C. Eklund, *Thin Solid Films,* **331:** 141, 1998.

254. F. Li, H. M. Cheng, Y. T. Xing, P. H. Tan, and G. Su, *Carbon,* **38:** 2041, 2000.

255. R. Satio, T. Takeya, T. Kimura, and G. Dresslhaus, *Phys. Rev. B.,* **57:** 4145, 1998

256. H. H. Gommans, J. W. Alldredge, T. Tashiro, J. Park, J. Magnuson, and A. G. Rinzler, *Appl. Phys.,* **88:** 2509, 2000

257. J. Hwang, H. H. Gammans, H. Tasgiro, R. Haggenmuller, K. I. Winey, J. E. Fisher, D. B. Tanner, and A. G. Rinzler, *Phys. Rev. B.,* **62:** R13310, 2000

258. H. Ajiki, and T. Ando, *J. Appl. Phys. Part 2-lett,* **34:** 107, 1994

259. Z. Yu, and L. Brus, *J. Phys. Chem. B.,* **105:** 1123, 2001.

260. M. Radosavljevic, J. Lefebvre, and A. T. Johnson, *Phys. Rev. B.,* **64:** 1, 2001.

261. L. Kavan, P. Rapta, L. Dunsch, M. J. Bronikowski, P. Willis, and R. E. Smalley, *J. Phys. Chem. B.,* **105:** 10764, 2001.

262. R. H. Baughman, C. Cui, A. A. Zakhidov, Z. Iqbal, J. N. Barisi, G. M. Spinks, G. G. Wallace, A. Mazzoldi, D. Derossi, A. G. Rinzler, O. Jaschinski, S. Roth, and M. Kertsz, *Science,* **284:** 1340, 1999.

263. M. Gao, L. Dai, R. H. Baughman, G. M. Spinks, and G. G. Wallace, *Electroactive Polymer Actuators and Devices,* **3987:** 2000.

264. A. Mazzoldi, D. Derossi, and R.H. Baughman, *Electroactive Polymer Actuators and Devices,* **3987:** 2000.

265. U. Hubler, P. Jess, H. P. Lang, H. J. Guntherodt, J. P. Salvetat, and L. Forro, *Carbon,* **36:** 697, 1998.

266. A. Volodin, M. Ahlskog, E. Seynaeve, C. V. Haesendonck, A. Fonseca, and J. B. Nagy, *Phys. Rev. Lett.,* **84:** 3342, 2000.

267. T. Hertel, R. E. Walkup, and P. Avouris, *Phys. Rev. B.,* **58:** 13870, 1998.

268. M. F. Yu, M. J. Dyer, and R. S. Ruoff, *J. Appl. Phys.,* **89:** 4554, 2001.

269. D. Qian, E. C. Dickey, R. Andrews, and T. Rantell, *Appl. Phys. Lett.,* **76:** 2868, 2000.

270. T. Hertel, R. Martel, and P. Avouris, *J. Phys. Chem. B.,* **102:** 910, 1998.

271. I. Musa, M. Baxendale, G. A. J. Amaratunga, and W. Eccleston, *Synth. Met.,* **102:** 1250, 1999.

272. B. E. Kilbride, J. N. Coleman, D. F. O'Brien, and W. J. Blau, *Synth. Met.,* **121:** 1227, 2001.

273. S. B. Lee, T. Katayama, H. Kajii, H. Araki, and K. Yoshino, *Synth. Met.,* **121:** 1591, 2001.

274. Y. Lin, A. M. Rao, B. Sadanadan, E. A. Kenik, and Y. P. Sun, *J. Phys. Chem. B.,* **106:** 1294, 2002.

275. R. Czerw, Z. Guo, P. M. Ajayan, Y. Sun, and, D. L. Carroll, *Nano. Lett.,* **1:** 423, 2001.

276. J. E. Riggs, D. B. Walker, D. L. Carroll, and Y. P. Sun, *J. Phys. Chem. B.,* **104:** 7071, 2000.

277. S. Ijjima, *Nature,* **354:** 56, 1991.

278. X. Gong, J. Liu, S. Baskaran, R. D. Voise, and J. S. Young, *Chem. Mater.,* **12:** 1049, 2000.

279. C. A. Cooper, and R. J. Young, *Journal of Raman Spectroscopy,* **30:** 929, 1999.

280. H. Ago, T. Kugler, F. Cacialli, W. R. Salaneck, M. S. P. Shaffer, A. H. Windle, and R. H. Friend, *J. Phys. Chem. B.,* **103:** 8116, 1999.

281. J. N. Coleman, A. B. Dalton, S. Curran, A. Rubio, A. P. Davey, A. Drury, B. McCarthy, B. Lahr, P. M. Ajayan, S. Roth, R. C. Barklie, and W. J. Blau, *Adv. Mater.,* **12:** 213, 2000.

282. S. A. Curran, P. M. Ajayan, W. J. Blau, D. L. Carroll, J. N. Coleman, A. B. Dalton, A. P. Davey, A. Drury, B. McCarthy, S. Maier, and A. Strevens, *Adv. Mater.,* **10:** 1091, 1998.

283. A. B. Dalton, H. J. Byrne, J. N. Coleman, S. A. Curran, A. P. Davey, and B. W. J. Blau, *Synth. Met.,* **102:** 1176, 1999.

284. S. Curran, A. P. Davey, J. Coleman, A. Dalton, B. McCarthy, S. Maier, A. Drury, D. Gray, M. Brennan, K. Ryder, M. Lamy de la Chapelle, C. Journet, P. Bernier, H. J. Byrne, D. Carroll, P.M. Ajayan, S. Lefrant, and W. Blau, *Synth. Met.,* **103:** 2559,1999.

285. B. Zhao, H. Hu, S. Niyogi, M. E. Itkis, M. A. Hamon, P. Bhowmik, M. S. Meier, and R. C. Hadon, *J. Am. Chem. Soc.,* **123:** 11673, 2001.

286. K. D. Ausman, R. Piner, O. Lourie, and R. S. Ruoff, *J. Phys. Chem. B.,* **104:** 8911, 2000.

287. L. W. Chiang, B. E. Brinson, R. E. Smalley, J. L. Margrave, and R. H. Hauge, *J. Phys. Chem. B.,* **105:** 1157, 200

288. J. L. Bahr, J. Yang, D. V. Kosynkin, M. J. Bronilowski, R. E. Smalley, and J. M. Tour, *J. Am. Chem. Soc.,* **123:** 6536, 2001.

289. E. Frackowiak, K. Metenier, V. Bertagna, and F. Beguin, *Appl. Phys. Lett.,* **77:** 2421, 2000.

290. G. Z. Chen, M. S. P. Shaffer, D. Coleby, G. Dixon, W. Zhou, D. J. Fray, and A. H. Windle. *Adv. Mater,* **12:** 522, 2000.

291. I. Alexandrou, E. Kymakis, and G. A. J. Amaratunga, *Appl. Phys. Lett.*, **80:** 1435, 2002.

292. S. Lefrant, I. Baltog, M. Lamy de la Chapelle, M. Baibarac, G. Louarn, C. Journat, and P. Bernier, *Synth. Met.,* **101:** 184, 1999.

293. J. Fan, M. Wan, D. Zhu, B. Chang, Z. Pan, and S. Xie, *J. Appl. Poly. Sci.,* **74:** 2605, 1999.

294. J. Fan, M. Wan, D. Zhu, B. Chang, Z. Pan, and S. Xie, *Synth. Met.,* **102:** 1266, 1999.

295. H. Ago, K. Petritsch, M. S. P. Shaffer, A. H. Windle, and R. H. Friend, *Adv. Mater.,* **11:** 1281, 1999.

296. K. Fu, W. Huang, Y. Lin, L. A. Riddle, D. L. Carroll, and Y. Sun, *Nano. Lett.*, **1:** 439, 2001.

297. J. E. Riggs, Z. Guo, D. L. Carroll, and Y. Sun, *J. Am. Chem. Soc.,* **122:** 5879, 2000.

298. M. S. P. Shaffer, X. Fan, and A. H. Windle, *Carbon,* **36:** 1603, 1998.

299. Y. Lin, A. M. Rao, B. Sadanadan, E. A. Kenik, and Y. Sun, *J. Phys. Chem. B.,* **106:** 1294, 2002.

300. C. Bower, R. Rosen, L. Jin, J. Han, and O. Zhou, *Appl. Phys. Lett.,* **74:** 3317, 1999.

301. B. Z. Tang, and H. Xu, *Macromolecules,* **32:** 2569, 1999.

302. A. B. Dalton, W. J. Blau, G. Chembers, J. N. Coleman, K. Henderson, S. Lefrant, B. McCarthy, C. Stephan, and H. J. Byrne, *Synth. Met.,* **121:** 1217, 2001

303. Z. Jia, Z. Wang, C. Xu, J. Liang, B. Wei, D. Wu, and S. Zhu, *Mater. Sci. Eng. A.,* **271:** 395, 1999.

304. G. L. Hwang, and K. C. Hwang, *Nano. Lett.*, **1:** 435, 2001.

305. C. Ho, I. D. Raistrick, and R. A. Huggins, *J. Electrochem. Soc.,* **127:** 243, 1980.

306. M. Hughes, M. S. P. Shaffer, A. C. Renouf, C. Singh, G. Z. Chen, D. J. Fray, and A. H. Windle, *Adv. Mater,* **14:** 382, 2002.

307. C. Downes, J. Nugent, P. M. Ajayan, D. J. Duquette, and K. S. V. Santhanam, *Adv. Mater.,* **11:** 1028, 1999.

308. J. Tamm, A. Hallik, A. Alumaa, and V. Sammelselg, *Electrochemica Acta,* **42:** 2929, 1997.

309. V. Georgakilas, K. Konstantinos, M. Prato, D. M. Guidi, M. Holzinger, and A. Hirsch, *J. Am. Chem. Soc.,* **124:** 760, 2002.

310. R. H. Baughman, C. Cui, A. A. Zakhidov, Z. Iqbal, J. N. Barisci, G. M. Spinks, G. G. Wallace, A. Mazzoldi, D. De Rossi, A. G. Rinzler, O. Jaschinski, S. Roth and M. Kertesz, *Science,* **284:** 1340, 1999.

311. J. P. Salvetat, G.A.D. Briggs, J. M. Bonard, R.R. Bacsa, A.J. Kulik, T. Stockli, N.A. Burnham and L. Forro, *Phys. Rev. Lett.,* **82:** 944, 1999.

312. J. D. W. Madden, and G. M. Spinks, private communication.

313. G. M. Spinks, G. G. Wallace, C. Carter, D. Zhou, L. S. Fifield, C. Kincaid, and R. H. Baughman, *SPIE Smart Materials and Structures*, Newport Beach, March 2001.

314. T. E. Herod, and J. B. Schlenoff, *Chem. Mater*., **5:** 951, 1993.

315. M. Tahhan, V. T. Truong, G. M. Spinks, and G. G. Wallace, *Smart Mater. Struct.,* **12:** 626, 2003.

316. C. L. Arnantia, C. Sampedro, M. A. Goicolea, Z. G. Balugera, E. Rodriguze, and R. J. Barrio, *Electroanalysis,* **11:** 1222, 1999.

317. M. Gao, S. Huang, L. Dai, G. G. Wallace, R. Gao, and Z. Wang, *Angew. Chem. Int. Ed.,* **39:** 3664, 2000.

318. W. Zhou, X. C. Ma, Z. Y. Yuan, and E. G. Wang, *Surf. Interface Anal.,* **32:** 236, 2001.

319. J. H. Chen, Z. P. Huang, D. Z. Wang, S. X. Yang, W. Z. Li, J. G. Wen, and Z. F. Ren, *Synth. Met.,* **125:** 289, 2002.

320. S. Kazaoui, N. Minami, N. Matsuda, H. Kataura, and Y. Achiba, *Appl. Phys. Lett.,* **78:** 3433, 2001.

321. S. Kazaoui, N. Minami, H. Kataura, and Y. Achiba, *Synth. Met.*, **121:** 1201, 2001.

322. H. T. Chiu, and J. S. Lin, *J. Mater. Sci.,* **27:** 319, 1990.

323. J. Tamm, A. Hallik, A. Alumaa, and V. Sammelselg, *Electrochemica Acta,* **42:** 2929, 1997.

324. G. A. Wood, and J. O. Iroh, *Poly. Eng. Sci.*, **36:** 2389, 1996.

325. G. A. Wood, and J. O. Iroh, *Eur. Poly. J.,* **33:** 107, 1997.

326. S. W. Feldberg, *J. Am. Chem. Soc.,* **106:** 4671, 1984.

327. J. Heinze, and M. Dietrich, *Materials Science Forum,* **42:** 63, 1989.

328. T. Osaka, K. Naoi, S. Ogano, and S. Nakamura, *J. Electrochem. Soc.,* **134:** 2096, 1987.

329. M. Shim, N. W. S. Kam, R. J. Chen, Y. Li, and H. Dai, *Nano. Lett.,* **2:** 285, 2002.

330. R. J. Chen, S. Bangsaruntip, K. A. Drouvalakis, N. W. S. Kam, M. Shim, Y. Li, W. Kim, P. J. Utz, and H. Dai, *Proc. Natl. Acad. Sci.,* **100:** 4984, 2003.

331. M. P. Mattson, R. C. Hadden, and A. M. Rao, *J. Mol. Neurosci.,* **14:** 175, 2000.

332. Z. Guo, P. J. Sadler, and S. C. Tang, *Adv. Mater.,* **10:** 701, 1998.

333. O. P. Matyshevska, A. Y. Kavlash, Y. V. Shtogun, A. Benilov, Y. Kiryizov, K. O. Gorchinsky, E. V. Bukaneva, Y. I. Prylutskyy, and P. Scharff, *Mater. Sci.,* **C15:** 249, 2001.

334. S. E. Baker, W. Cai, T. L. Lasseter, K. P. Weidkamp, and R. J. Hamers, *Nano. Lett.,* **2:** 1413, 2002.

335. S. Kumar, H. Doshi, M. Srinivasarao, J. O. Park, and D. A. Schiraldi, *Polymer,* **43:** 1701, 2002.

336. R. Andrews, D. Jacques, A. M. Rao, T. Rantell, F. Debyshire, Y. Chen, J. Chen, and R. C. Haddon, *Appl. Phys. Lett.,* **75:** 1329, 1999.

337. B. Vigolo, A. Penicaud, C. Coulon, C. Sauder, R. Pailler, C. Journet, P. Bernier, and P. Poulin, *Science,* **290:** 1331, 2000.

338. B. Vigolo, A. Penicaud, C. Coulon, C. Sauder, R. Pailler, C. Journet, P. Bernier, and P. Poulin, *Mat. Res. Soc. Symp. Proc.,* **633:** A1211, 2001.

339. P. Launois, A. Marucci, B. Vigolo, P. Bernier, A. Derre, and P. Poulin, *Journal of Nanoscience and Nanotechnology,* **1:** 125, 2001.

340. B. Vigolo, P. Poulin, M. Lucas, P. Launois, and P. Bernier, *Appl. Phys. Lett.,* **81:** 1210, 2002.

341. A. B. Dalton, S. Collins, E. Munoz, J. M. Razal, V. H. Ebron, J. P. Frerairs, J. N. Coleman, B. G. Kim, and R. H. Baughman, *Nature,* **423:** 703, 2003.

342. A. Neimark, S. Ruetsch, K. Kornev, P. Ravikovitch, S. Badaier, M. Maugey, and P. Poulin, *Nano. Lett.,* **3:** 419, 2003.

343. Z. Guo, P. J. Sadler, and S. C. Tsang, *Adv. Mater.,* **10:** 701, 1998.

344. J. N. Barisci, M. Tahhan, G. G. Wallace, S. Badaire, T. Vaugien, M. Maugey, and P. Poulin, *Adv. Func. Mater.,* **14:** 133, 2004.

345. M. Zheng, A. Jagota, E. D. Semke, B. A. Diner, R. S. Mclean, S. R. Lustig, R. E. Richerdson, and N. G. Tassi, *Nat. Mater.,* **2:** 338, 2003.

346. E. Buzaneva, A. Karlash, K. Yakovkin, Y. Shtogun, S. Putselyk, D. Zherebetskiy, A. Gorchinskiy, G. Popova, S. Prilutska, O. Matyshevska, Y. Prilutskyy, P. Lytvyn, P. Scharff, and P. Eklund, *Mater. Sci. Eng. C.,* **19:** 41, 2002.

347. O. P. Matyshevska, A. Y. Karlash, Y. V. Shtogun, A. Benilov, Y. Kirgizov, K. O. Gorchinskyy, E. V. Buzaneva, Y. I. Prylutskyy, and P. Scharff, *Mater. Sci. Eng. C.,* **15:** 249, 2001.

348. Y. A. Kim, T. Matusita, T. Hayashi, M. Endo, and M. S. Dresselhaus, *Carbon,* **39:** 1747, 2001.

Appendix A

Published Papers

‘Articles below removed for copyright reasons, please refer to the citation

1- Carbon nanotubes and polyaniline composite actuators

2- Properties of carbon nanotubes fibers spun from DNA-stabilized dispersions